CFD modelling and investigation of two-stroke dual-fuel marine engines with high pressure gas admission

By

Renyou Yang

A thesis submitted in fulfilment of the requirements for the degree

of Doctor of Philosophy

Department of Naval Architecture, Ocean and Marine Engineering

The University of Strathclyde, Glasgow, United Kingdom

July 2018

Statement

Abstract

Due to their durability, cost-effectiveness and high efficiency, the large two-stroke marine engines are widely used by the merchant ships. However, as the conventional two-stroke diesel engines suffer from the high pollutants emissions, the dual fuel versions burning natural gas and pilot fuel to initiate combustion is an alternative, which can considerably reduce the engine environmental footprint. The application of the high pressure and direct injection of the natural gas can remarkably benefit the emissions. In order to understand in-depth the full-cycle operating processes in a two-stroke dual fuel marine engine with high-pressure gas direct injection, the related CFD models were customized and developed by the use of ANSYS Fluent, and validated by employing available experimental data. Subsequently, the parametric investigation of the dual fuel injection was conducted and the recommended sets of design parameters are identified. Furthermore, the internal processes in the whole cycle of the engine dual fuel and the diesel operating mode were analysed and compared.

The spray process of the liquid/pilot fuel was modelled and validated by the available experimental data, taking into account the variable Thermophysical liquid fuel properties with the ambient conditions. Aiming to develop the models for the high-pressure gas injection, the conserving-equation sources approach was developed, considering the effects of the barrel-shaped shocks patterns near the nozzle exit. The derived CFD models were validated by the published measured penetrations of nitrogen injection under two pressure ratios values.

As the diffusion flame dominates in the high-pressure direct injection (HPDI) gas combustion, the non-premixed dual fuel combustion model was developed, in which the pilot fuel combustion was treated as the ignition kernel. Based on the measurements in the rapid compression and expansion machine (RCEM), the derived heat release rate (HRR) and the NO emission was used to validate the CFD results. By comparing the results of the two investigated non-premixed combustion models, the steady flamelet diffusion model was recommended, where the reaction rates of Hanson and Salimian (1984) for the extended Zeldvich mechanism were applied.

In order to determine the injection and geometric parameters of dual fuel operation in the marine engine S60ME, the parametric research of HPDI, combustion processes was conducted with the aim to maintain the power level and reduce the NO and CO_2 emissions. The investigated parameters included the dual fuel injection timing, the gas injection duration, the lateral angle of gas nozzle, the holes number of gas injector, and the different inclination angle for each gas hole.

Based on the results of the conducted parametric study, the dual fuel design parameters for the marine engine S60ME were recommended. By using the developed dual fuel combustion models, the whole-cycle processes in the large two-stroke marine dual fuel engine were investigated, by comparing the diesel model operating mode. The results indicated that the NO and CO_2 emissions for the dual fuel mode were lower than that of the diesel mode by 31% and 21% respectively. The diffusion flame for the diesel mode was located downstream the liquid vapour plumes, whilst the dual fuel mode exhibited the high-temperature flame in the vicinity of the stoichiometric surface of the gas plumes. Moreover, the diesel mode achieved the higher flame temperature than the dual fuel mode. Due to the lower carbon dioxide (CO_2) for the duel fuel combustion, the scavenging efficiency for the dual fuel mode was 4.2% higher than that of the diesel mode.

Acknowledgements

The work in the PhD thesis was significantly supported by the excellent colleagues. First, I would like to thank my supervisors, Dr. Gerasimos Theotokatos and Prof. Dracos Vassalos, for their continuous supports and recommendation during my PhD experience at the University of Strathclyde. With attribution to their patience and the guidance, my professional knowledge and skills had been further developed, as well as the research management and organization. The regular meeting with the supervisors was extremely beneficial of my academic career and completing the PhD work.

A special acknowledgement is to the Faculty of the Naval Architecture, Ocean and Marine Engineering (NAOME) in the University of Strathclyde. Due to the financial support of NAOME (the tuition fee) and the European Commission through the research project JOULES (the stipend) (http://www.joules-project.eu), I can pay the tuition fee and maintain the living in the PhD time. Thank to the administrators in the department, who always gave me the quick and convenient help in the university lives and the academic credits in the PG Cert RPD Class.

All the CFD simulations presented in thesis were operated on the ARCHIE-WeSt supercomputers. I also would like to appreciate the administrators to provide the adequate computational resources to complete the investigation.

Finally, I am deeply grateful to my family and my parents, for their ongoing support of my full-time PhD education. Over the past four years, my wife Lei Chen took care of my daughter alone in China. Without my wife's support and unconditional dedication, I could not concentrate on and finish the PhD work. Sincerely love to you.

Publications

1. R. Yang, G. Theotokatos & D. Vassalos (2016). Numerical investigation of the gas injection process in large marine DF engines. International Conference on Maritime Safety and Operations, Glasgow, UK, 13th – 14th October 2016.

Contents

List of Figures

List of Tables

Abbreviations

AHRR: Actual Heat Release Rate

ATDC: After Top dead Centre

BC: Black Carbon

BDC: Bottom Death Centre

BOG: Boil-off Gas

BSFC: Brake Specific Fuel Consumption

℃A: Crank Angle Degree

CA: Crank Angle

CFD: Computational Fluid Dynamics

CI: Compression Ignition

CMC: Conditional Moment Closure Model

CN: Cetane Number

DF: Dual Fuel

ECA: Emissions Controlled Areas

ECU: Electronic Control Unit

ED: Eddy Dissipation Model

EGR: Exhaust Gas Recirculation

EOS: Equation of State

EQ: Equilibrium Ratio

EPFM: the Eulerian Particle Flamelet Model

EVC: Exhaust Valve Close

EVO: Exhaust Valve Open

GHRR: Gross Heat Release Rate

GID: Gas Ignition Delay

HC: Hydrocarbon

HHV: Higher Heating Value

HPDI: high-pressure and direct-injection

HR: Heat Release

HRR: Heat Release Rate

IFC: Infinitely Fast Chemistry Model

IMEP: Indicated Mean Effective Pressure

IMO: International Maritime Organization

ISO: International Organization for Standardization

ITTC: International Towing Tank Conference

KHRT: Kelvin-Helmholtz and Rayleigh-Taylor Model

LDV: Laser-Doppler Velocity Apparatus

LES: Large Eddy Simulation

LHV: Lower Heating Value

LNG: Liquefied Natural Gas

LPT: Lagrangian Particle Tracking Approach

MN: Methane Number

MW: Molecular Weight

NHPT: n-Heptane

NOx: Nitrogen Oxides

ON: Octane Number

PDF: Possibility Density Function

PLIF: Planar Laser Induced Fluorescence

PM: Particulate matter

RCEM: Rapid Compression Expansion Machine

RNG: Re-Normalisation Group Method

RIT: Relative Injection Timing

SEZM: Super-Extended Zeldovich Mechanism

SCR: Selective Catalytic Reduction

SGC: Specific Gas Consumption

SMCR: Specified Maximum Continuous Rating

SPC: Scavenging Ports Closing

SPOC: Specific Pilot Oil Consumption

SPO: Scavenging Ports Opening

SSD: Stochastic Secondary Droplet

SSE: Standard State Enthalpy

TAB: Taylor Analogy Breakup

TDC: Top dead Centre

UN: European Union

VOF: Finite Volume Technique

Chapter 1 Introduction

1.1 Background

1.1.1 Ship Emissions Control

In 2008, International Maritime Organization (IMO) revised a standard of sulphur content of the marine fuel, which was admitted by European Union (UN). The Emissions Controlled Areas including Baltic Sea, the North Sea and the English Channel were established, where SOx of ship operation have to be less than 0.1% from 1 January 2015. This measure is also considered in the other coastal area around most of developed countries. Complying with the IMO marine fuel standard [1], the sulphur content will be decreased from 3.5% in 2012 to 0.5% in 2020 globally. Moreover, the stringent regulations in NOx emissions from marine diesel engines are also included. The "Tier III" emission limits for engines installed on a ship constructed on or after 1 January 2016 operating in the Established Controlled Areas (ECAs) and "Tier II" outside such area were issued by IMO [1]. Apart from the above-mentioned pollutants, the limitations of ship exhaust such as carbon dioxide (CO_2), carbon monoxide (CO) and unburned hydrocarbon (HC) are also proceeded by the international and national authorities, due to their contributions to the global warming and harm to the human health.

Primarily consisting of methane up to 95%, the combustion characteristics of natural gas are governed by the methane properties, such as high octane number (ON). High octane number means a relatively highly auto-ignition temperature, and therefore it is suitable for high compression ratio engines, which requires the ignition energy to enable combustion. Such characteristics of high resistance to auto ignition, in turn, can effectively extend the upper load limit of dual fuel engine, which also allows the optimization of compression ratios for the improvement of engine efficiencies. With attribute to the low carbon-hydrogen ratio of natural gas, the carbon dioxides emission for the dual fuel mode can be considerably reduced. The sulphur is almost completely removed during the natural gas liquefaction process, which results in almost elimination of the sulphur oxides. Natural gas can be ignited and burned over the wide flammability range, which can be beneficial of reducing the NOx emissions. In addition to the low emissions of gas pollutants, the very low particulate matters, no visible smoke and no sludge deposits, lead the dual fuel engine become the prospective technology. Meanwhile, due to the high ON number and low burning rate of the natural gas, one of the main challenges regarding dual fuel engine is to avoid the methane slip.

1.1.2 Categorisation of Dual Fuel Marine Engines

For two-stroke marine engine, there are possible two methods of introducing the natural gas into the cylinder of compression-ignition (CI) engine. One is to inject the natural gas, and then mixed into the scavenge air at the mid-stroke cylinder position during the compression stroke, shown in Figure 1.1.

The internal operation is based on pre-mixed lean-burn Otto process, where the gas is ignited by pilot liquid fuel in the prechamber. The main merits include the low NOx and CO_2 emissions, low particulate matters, and even lower wall heat losses, lower pilot fuel amount. The investigation showed that this dual fuel operation has the very low emissions meeting IMO Tier III without additional technologies [2]. However, the knock was still detected in terms of the pressure in-cylinder history [2].

The second is based on Diesel cycle, where the gas is compressed to a high pressure about 300 bar and injected into the engine combustion chamber through the gas injectors, and then ignited by the advanced pilot fuel near top dead centre (TDC). This technology has been developed by MAN Diesel & Turbo, sketched in Figure 1.2. This technology has the same engine power to the conventional diesel engine and similar fuel supply system and lubrication system, which means that both of operation processes are interchangeable. Compared to the diesel operation, Kjemtrup [3] indicated that the dual fuel operation has the lower NOx and CO_2 emissions by 25% and 20% respectively, and near zero PM levels. Further, such technique can avoid knock and misfire problems, and has very low methane slip, while it requires the EGR or SCR to meet the IMO Tier III NOx regulations.

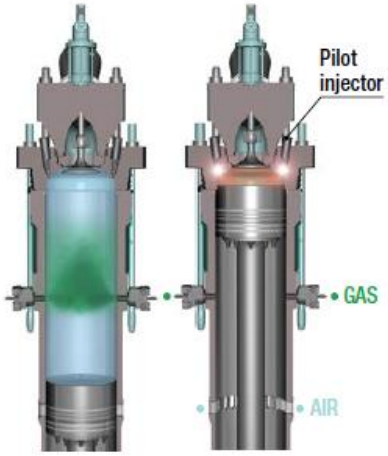

Figure 1.1 Wärtsilä's 2-stroke DF principle with gas admission (left) and ignition (right) [4]

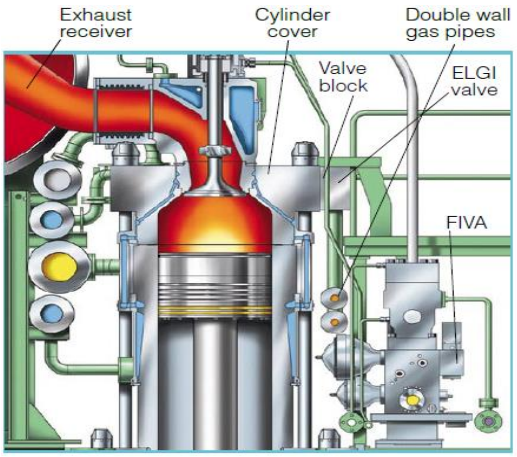

Figure 1.2 ME-GI 2-stroke diesel engine in MAN Diesel & Turbo [5]

1.2 Operating Characteristics of Dual Fuel Engines

1.2.1 Main Fuel Properties

Several important parameters are adopted to feature the fuel properties associated with the combustion process.

Octane number (ON) denotes the volume percentage of ISO octane in a combustible mixture (including ISO octane and normal heptane) [6]. 100 ON implies 100% octane and 0% heptane, and 0% octane and 100% heptane corresponds to 0 ON. The higher octane number implies the

higher compression that the fuel can withstand before detonating (igniting), which is often used to measure the fuel performance to resist the knock tendency.

Cetane number (CN) is the fraction of cetane ($C_{16}H_{34}$) and 1- methylnaphthalene ($C_{11}H_{10}$) in a mixture [6], which signifies the easy ignition under compression. Likewise, the cetane number is generally applied to characterise the fuel ability in the compression ignition (CI) engine.

Table 1.1 shows the chemical properties of the common fuels in the diesel engine at standard atmospheric conditions. It can be found that the natural gas mainly composed of methane is much lighter than the other two liquid fuels.

Table 1.1 Chemical properties of common fuels at standard atmospheric conditions [7]

Fuels	Diesel	Gasoline	Natural Gas(Methane)
Chemical formula	$C_nH_{1.8n}$	$C_nH_{1.87n}$	CH_4
Density (kg/m^3)	827-840	750	0.725
LHV (MJ/kg)	42.5	44.0	45.0
Octane Number	—	95	120
Cetane Number	52	—	—
Auto-ignition temperature (℃)	250	280	650

The Lower Heating Value (LHV) of natural gas comes closely to other two conventional fuels listed in Table 1.1, which is marginally higher than the diesel by 6%. It means that less natural gas needs to be supplied for the same heat release.

High octane number (ON) means a relatively highly auto-ignition temperature. Consequently, it is beneficial of natural gas to work in compression ignition (CI) engine, where the gas in the combustion chamber needs to be ignited by the pilot oil or spark plug. The merit of such high resistance to auto ignition is to extend the load limit of the engine and let the gas burn over a wide flammability range, so that the nitrogen oxides and soot emissions can be significantly reduced. Meanwhile, the poor ignition of the fuel often causes the incomplete combustion under the part loads, due to the flammability limit of lean air/methane mixture and low burning rate of natural gas in the chamber. Such slow burning speed of natural gas provides more time for the heat transfer to the gas, resulting in a tendency to knock in the premixed mixture combustion of CI engine [8].

In addition to the benefits of the NOx and PM emissions, natural gas has a lower carbon dioxides production than other two fuels in Table 1.1, due to the lower carbon-hydrogen ratio.

1.2.2 Engine Performance and emissions of Dual Fuel Engine with High Pressure Gas Injection

In DF engines with the low pressure gas injection, the natural gas is entirely mixed with the air before ignition. Therefore, the burning rate and flame propagation speed of the combustible mixture is controlled by the chemical kinetics. In the high-pressure and direct-injection (HPDI) gaseous engine, the natural gas highly pressurized in the nozzles is directly injected into the combustion chamber near top dead centre (TDC), and then is ignited by the pilot fuel. Despite the premixed combustion occurring in the early stage of the gas injection, the mixing-limited and diffusion flame still dominate. As a consequence, the performance and pollutant emissions in HPDI gaseous engine are remarkably different to the premixed combustion engine fuelled by the same gas fuel. Due to the realization of the prevailing diffusion combustion in the CI engine, the knock tendency that cannot be avoided in the premixed engine is substantially reduced, which means that the HPDI gas injection is considerably compatible to the high compression ratio designs. As a result of the small amount of the pilot fuel and the inherent properties of natural gas, HPDI gaseous engine ignited by advancing the pilot fuel injection can be regarded as a prospective dual fuel operation in the reduction of the pollutant emissions (including the NOx, CO_2 and PM), as well as retaining the same level of engine power rate.

Figure 1.3 and Table 1.4 compare the heat release rate (HRR), accumulated heat release (HR) and pollutant emissions from the diesel mode and the (HPDI) dual fuel mode in RCEM. The rapid compression expansion machine (RCEM) was developed by Imhof et al. [9] in the Kyushu University of Japan, which has a 200mm ×66mm ×80mm (Length × Width ×Height) combustion chamber and 240mm-diameter cylinder. The experiments revealed that the heat release by the diesel and dual fuel modes are similar and the NOx emissions had a notable reduction by at least 26%.

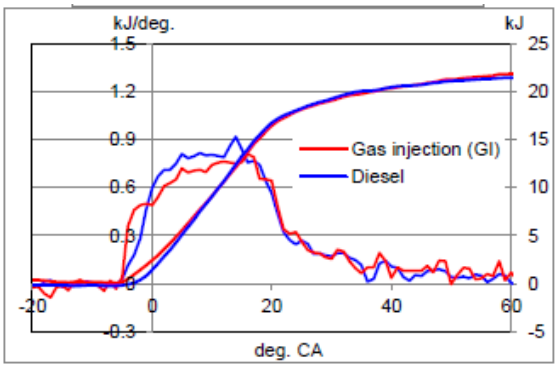

Figure 1.3 Comparison of HRR and HR in RCEM under the diesel and dual fuel modes [9]

Table 1.2 Comparison of emissions in RCEM under the diesel and dual fuel modes [9]

Fuel	GI	Diesel
CO [ppm]	8~10	44
HC [ppm]	69~87	21
NOx [ppm]	346~393	531

The HPDI technology is also employed by a large 2-stroke marine engine of MAN Diesel & Turbo. Figure 1.4 compares heat release rates varied with the gas/pilot ratio in the shop tests of 8L70ME-C-GI engine under 75% and 100% load. It depicted that dual fuel operation had a higher maximum heat release rate than the normal diesel mode. The corresponding pressure curves against crank angle

under different loads shown in Figure 1.5 indicated that the in-cylinder pressure in the dual fuel mode almost coincided with that of the diesel mode. It was demonstrated that the engine output does not derate for the HPDI application to large 2-stroke marine engine, which implied that there was no knock or misfiring problems in the whole load range. The cyclic variation of shop tests in 4T50ME-X engine illustrated in Figure 1.6 signified that the HPDI gas engine had a slightly improvement in the cycle-to-cycle stability.

In the two-stroke marine engine 5S60ME-C8.5-GI primarily fuelled by natural gas, ICEAS [5] reported that about 15% of the mass of the natural gas could be saved, compared to the diesel operation. The lower fuel consumed and low carbon-hydrogen ratio of methane means that the lower CO_2 is emitted. It is estimated that CO_2 emission approximately can be reduced by 20% for the same power rate with the normal diesel engine.

Kjemtrup [3] drew the following conclusions by use of HPDI technology in the normal marine engine, concerning the pollutant emissions.

a. There was very low methane slip in the whole engine load envelope;

b. Extremely low carbon monoxide (CO) was produced, which magnitude was the same level to the diesel mode.

c. NOx emissions could be reduced by 25%, which level was 1~3% lower than the IMO Tier II requirements;

d. Installation of EGR to the HPDI gas engine could substantially benefit the NOx emissions, which strictly complied with IMO TIII level;

e. Similar to the normal diesel, adding the EGR to dual fuel engine could reduce the maximum HRR, raise the late-stage heat release and increase the fuel consumption.

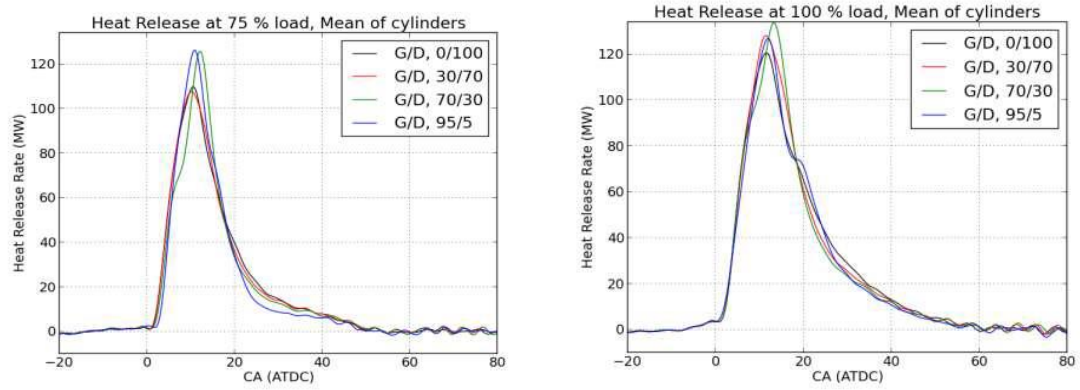

Figure 1.4 Heat release rate curves varied with the different gas/diesel ratios under 75% and 100% engine loads in the shop test engine 8L70ME-C-GI [3]

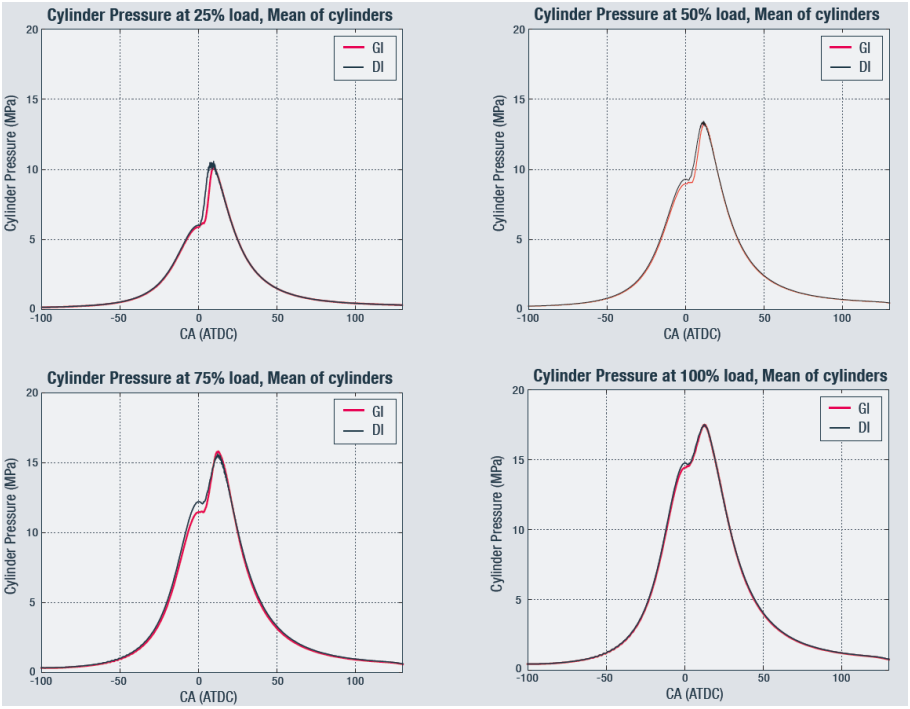

Figure 1.5 Cylinder pressure curves under 25% ~100% loads for MAN B&W L70ME-GI engine supplied by the diesel and dual fuel [10]

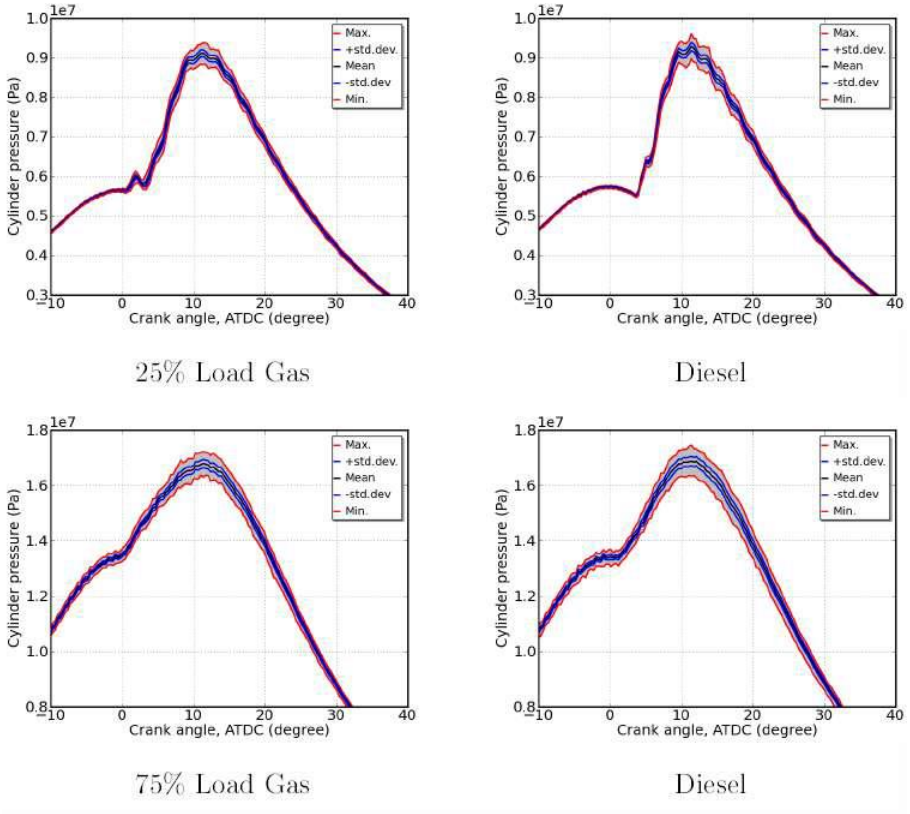

Figure 1.6 Pressure variations of shop test engine 4T50ME-X experiencing 500 consecutive cycles [3]

1.3 Research Motivation

It has been demonstrated that the application of the natural gas to the marine engine can notably benefit our environment. Investigation of the large two-stroke DF engine with the low-pressure gas injection in the middle stroke of cylinder indicates that 25%-30% CO_2 and 85%-90% NOx can be reduced, as well as the very low particulate matters (PM) and no sludge deposits [2,11]. However, the drawbacks also have been observed, such as the derated engine power and the methane slip at part load, due to the knock tendency and misfiring problems [2]. Another kind of 2-stroke marine engine is to directly inject natural gas into the combustion chamber and then ignited by the advanced pilot fuel. Apart from the lower CO_2, lower fuel mass required and significant reductions in PM, about 25% decrease of NOx emissions, substantially low methane slip and CO product can be achieved, without degradation of the engine power [3,10]. In conjunction with the EGR technology, the 2-stroke marine dual fuel engine with high-pressure directly gas injection (HPDI) can comply with the IMO Tier III standard.

It is well-known that the engine performance and emissions are strongly dependent of the internal operations of the engine. Due to the high pressure, high temperature in the cylinder, it is extremely high challenge to measure the operating processes, including the fuel injection, combustion and scavenging processes. Consequently, limited experiment is conducted in this area. The CFD method is advantaged of exploring and capturing such complicated physics, as well as the pollutant emissions. Meanwhile, the natural gas has been demonstrated to be promising in the reduction of the pollutant emissions. But, limited number of publications about the natural gas used to two-stroke engine can be found. Based on the above-mention gaps, the large two-stroke marine engine with high pressure direct gas injection will be investigated numerically, with focus on the development of the CFD models, improvement of the dual fuel combustion and emissions, and understanding in-depth the internal processes operated by dual fuel.

Chapter 2 Literature Review

2.1 Introduction

In high-pressure direct-injection (HPDI) dual fuel (DF) engines, the natural gas is directly injected into the engine chamber near top dead centre (TDC). Due to the high resistance to auto-ignition of the natural gas, the pilot fuel requires to be injected in advance, in order to ignite the subsequently injected gas. This kind of dual fuel engine does not degrade the engine power, avoids the knock problems, and generates the lower pollutant emissions, compared to the diesel engine.

In this thesis, the HPDI technology applied to a large two-stroke marine dual fuel engine will be numerically investigated. The literature review consists of two parts, including the CFD models associated with HPDI engines and the investigation of HPDI DF engines. In terms of the critical review, the research gap will be summarized and the aim and objectives, methodology and innovations will be illustrated.

2.2 CFD models of HPDI engines

In the diesel engine, the critical operations include the liquid fuel injection, combustion, and scavenging processes. The associated mathematical models have been developed by several researchers, such as the breakup models of liquid spray [12, 13, 14, 15, 16, 17] and the non-premixed combustion models [18, 19, 20, 21, 22].

Compared to the diesel engine, the main differences of the operating processes in the HPDI DF engine include the high-pressure gas injection and the related gaseous combustion. In this section, the models in these two areas are reviewed.

2.2.1 High-Pressure Gas Injection Models

Due to the high compressibility and the pressure ratio between the gas injector nozzle and the engine chamber, the underexpanded flow near the nozzle exit can be observed, which provides the special challenges of the mathematical approaches to compute the related characteristics and its effects on the flow. Before the reviews of the gas jet models, the high-pressure gas injection regime will be described.

2.2.1.1 Gas Injection Regime

(1) Underexpanded Flow near the Nozzle exit

Based on the continuity equation, momentum conservation, energy equation and the ideal gas equation of state in the isentropic compression of inviscid flow, the following relationship can be derived:

$$\frac{P_0}{P} = \left(1 + \frac{\gamma-1}{2}M^2\right)^{\gamma/(1-\gamma)} \quad (2.1)$$

Where, P_0 and γ denote the stagnation pressure and the specific heat ratio of the injected gas. And, M is the local Mach number in the nozzle flow.

When the stagnation pressure P_0 in the methane injection is theoretically 1.86 times of the ambient pressure P_a, the gas can smoothly jet into the environment. Hence, if the pressure ratio P_0/P_a is higher than 1.86, the additional underexpanded flow takes place after leaving the gas nozzle, in order to match the ambient pressure. Therefore, the nozzle exit looks like the throat in a converging-diverging duct, where supersonic flow outside the nozzle surrounded by the barrel shock and normal shock wave is produced, as well as the expansion waves attached in the nozzle lip and their reflections as compression waves from the flow boundary, sketched in Figure 2.2. The interaction of these compression waves forms the barrel-shaped shock pattern, which subsequently is reflected in the Mach disk.

The right graph in Figure 2.1 shows the shadowgram of the experiment [23], where the typical characteristics of underexpanded gas jet near the nozzle exit have been captured. The experiment was conducted in Mach number equal to 1.50 (the gas was not methane), where the Mach disk was found at axial station approximately 1.0D (diameter of the gas nozzle). Expansion waves attached at the nozzle lip, are caused by the ambient pressure lower than the exit pressure. As a consequence, the widened gas jet diameter can be expected, as well as the barrel shock and the resulting reflected shock wave.

Figure 2.2 provides the velocity map in four transverse sections measured by Laser-Doppler velocity (LDV) apparatus in an under-expanded free jet [24]. The associated sharp velocity reduction by the normal shock wave was clearly visible. This velocity valley gradually disappears downstream of the normal shock wave.

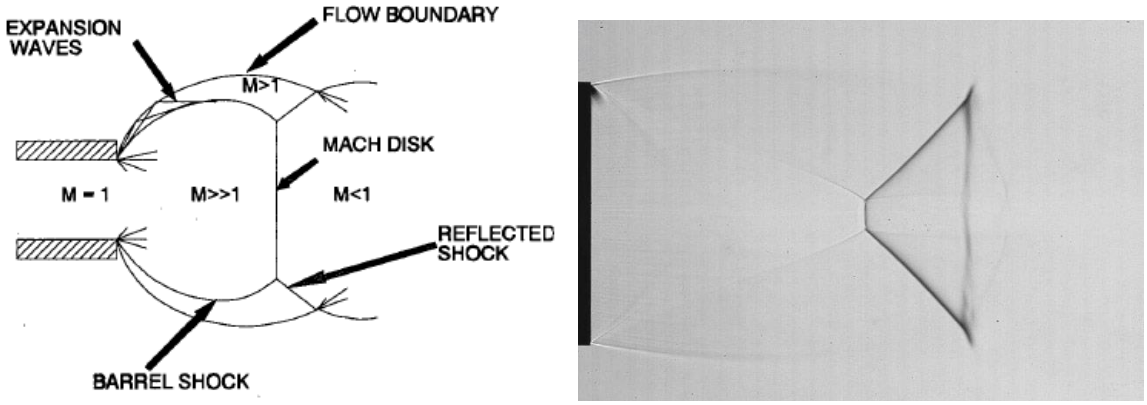

Figure 2.1 Underexpanded supersonic jets at nozzle exist. Left: schematic graph [25]; Right: experimental visualization [23]

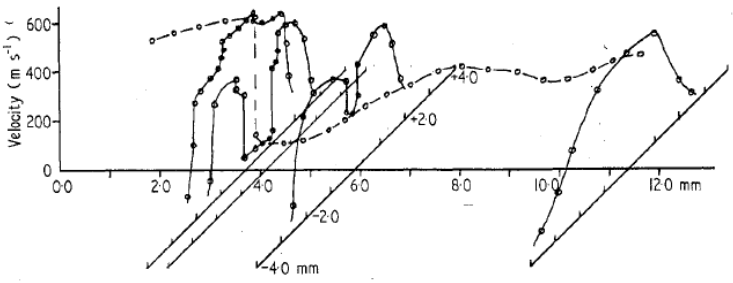

Figure 2.2 Velocity distributions with axial profile measured by LDV [24]

(2) Turbulent Free Jet in the Surroundings

As the high-pressure gas is injected into the engine combustion chamber, the gas travels away from the nozzle and entrains the surrounding air, as depicted schematically in Figure 2.3. The propagation and evolution of the gas jet can be described by the model of Turner [26], which shows a steady-state region behind the transient vortex region in the right graph of Figure 2.3. The gas jet penetration Z_t can be calculated as follows [27]:

$$Z_t = \Gamma \left(\dot{M}_n/\rho_a\right)^{1/4} t^{1/2} \tag{2.2}$$

where $\dot{M}_n$ is the gas jet momentum rate at nozzle exit, which can be calculated by using the relationship between the total pressure, density and the local Mach number. The penetration of gas transient jet is function of the square-root of the travelling time. In equation (2.2), the constant Γ is equal to 3.0 proposed by Ouellette [27]. By analysing the incompressible transient jets, Hill [28] derived the following equation for calculating the constant Γ.

$$\Gamma^4 + \frac{6K_s(1-s)^2}{\sqrt{\pi}(2-s)s^3}\Gamma^2 - \frac{24}{\pi(2-s)s^3} = 0 \tag{2.3}$$

where the entrainment coefficient K_s is equal to 0.32. When the jet width s normalized by the gas penetration Z_t is equal to 0.20~0.30, the pure constant Γ approximates 3.0.

Regarding the underexpanded compressible gaseous jet, the following constant Γ solution was recommended by Hill [28].

$$\left(\frac{Z_t}{d\sqrt{\frac{\rho_n}{\rho_0}}}\right) = \Gamma\sqrt{\frac{\pi}{4}}\left(\frac{U_0 t}{d\sqrt{\sqrt{\frac{\rho_n}{\rho_0}}}}\right)^{1/4} \tag{2.4}$$

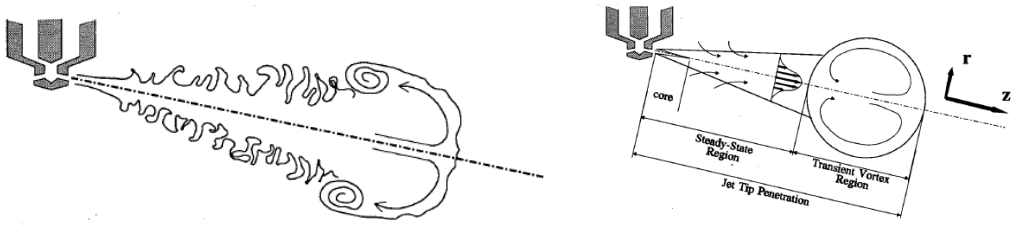

Figure 2.3 Turbulent transient jet structure [25]

Using the transient vortex ball model of Turner [26] to the directly-injected and high-pressure gas jet in the chamber, Hajialimohammadi [29] predicted that the transient vortex-ball approach overestimated the gas jet penetration, compared to the experiments. The reason is that there exists pressure drop in the nozzle flow, which is induced by the expansion wave travelled in the high-pressure side of the nozzle. Hence, the shock tube theory was adopted by Hajialimohammadi [29] to estimate the effective pressure P_E.

$$1+\left(\frac{a_0}{a_\infty}\right)\left(\frac{k_a-1}{k_h-1}\right)-\left[\left(\frac{a_0}{a_\infty}\right)\left(\frac{k_a-1}{k_h-1}\right)\right]\left(\frac{P_E}{P_0}\right)^{\frac{k_h-1}{2k_h}}-\left(\frac{P_0}{P_\infty}\right)^{\frac{k_a-1}{2k_a}}=0 \tag{2.5}$$

Replacing the effective pressure P_E to the total pressure P_0 for the calculation of momentum rate at nozzle exit in equation (2.1), the solution of gas jet penetration was created [29].

$$Z_t = \Gamma\,(d_n U_n)^2\left[\frac{\pi}{4}\frac{P_E}{P_\infty}\frac{R_\infty T_\infty}{R_0 T_0}\left(\frac{2}{k_h+1}\right)^{\frac{1}{k_h-1}}\right]^{1/4} t^{1/2} \tag{2.6}$$

Combined with the shock tube theory and vortex-ball model of Turner (1962), the results could be noticeably improved for the prediction of high-pressure gas jet penetration, despite of some disparity near the start of gas injection [29].

2.2.1.2 Gas Injection Models

(1) Gas Sphere Spray

In the research of Choi [30], the gas in the nozzle was regarded as the liquid parcels. Consequently the liquid spray model implemented by KIVA can be directly employed, where the evaporation process of

liquid droplets is defined as the diffusion of the gaseous sphere. It is assumed that the phase change from the liquid to the gas in the model does not activate the energy exchange inside the nozzle. The core region near the nozzle exit is considered as the inviscid region, the diameter of which is equal to the nozzle diameter. The corresponding core length is assumed to be the 12.5 times the nozzle radius, which highly affects the spray penetration.

The turbulent parameters involving the turbulent intensity I_n, turbulent kinetic energy k and dissipation rate ε in the core region need to be determined, which are estimated by using the following equations:

$$I_n = 0.12U_g \tag{2.7}$$

$$k = \frac{3}{2}I_n^2 \tag{2.8}$$

$$\varepsilon = 0.5\, k^{1.5}/d_n \tag{2.9}$$

Unlike the results of Choi [30] who set the gas sphere inside the nozzle, Hessel [31] designated the gas injection origin near the nozzle exit in the chamber, by use of the liquid spray module supplied by KIVA 3V. This treatment is beneficial of the reduction of computing mesh, due to the ignorance of the mesh fined inside and around the nozzle exit. Also, it is convenient for the parametric investigation of the gas injector, due to not re-meshing the model.

A similar work was done by Vångö [32], who called it as Lagrangian particle tracking (LPT) approach. Based on the open code Openfoam, the liquid properties and the corresponding thermo-physics are set to gaseous behavior.

(2) Gas Injection Modelling

The simulation of the real gas nozzle mounted to the end wall of the chamber highly challenges, due to the requirement of the high-resolution grids, in order to precisely calculate the underexpanded jet in the vicinity of the nozzle exit.

Owing to the limits of computational capacity in the past decades, "parabolized" Navier-Stokes (PNS) equations reduced from the completely Navier-Stokes (NS) equations aligned along streamlines had become popular. Under the assumption that the gradients normal to the streamline surface is much greater than that paralleled to the surface and the relatively thin disturbance, some high-order terms in the NS equations are neglected, formed as the PNS equations, which can be used to efficiently compute the complicated 3-D steady high-Mach viscous flow, as well as the inviscid flow. In addition, the hypothesis of axisymmetric flow with no swirling, quiescent gaseous environment, ignoring of the buoyancy forces were made by Chuech [33], where the turbulent sonic underexpanded free jets were

simulated. Compared to the experiment, this approach in conjunction with the divergent nozzle approximation and compressibility-corrected k-ε turbulence model matched well the mean flow field variables and their fluctuations. Its drawback was that it could not provide the information in the near-field region, where the barrel-shaped shocks were dominated.

Cumber [34] used the density-weighted (Favre) averaging axisymmetric and steady-form conservation equations augmented by the ideal gas state to compare the standard k-ε and compressibility-correction k-ε turbulence models in the solution of underexpanded flow. In order to reduce the computational effort in solving the barrel-shaped shocks and Mach disk, the adaptive finite-volume grid algorithm in a 2-D rectangular mesh was applied. With respect to the location and the diameter of the Mach disk in the near-field inviscid jet, the computational results agreed well with the experiment. In the subsonic flow far-downstream, the closure of the compressibility-correction k-ε turbulence model was regarded to reasonably agree with the experiment in the distributions of the mean jet gas velocity and mass faction.

Through the modifications of boundary conditions in KIVA-II, Ouellette [25, 27] implemented the interface set between the nozzle exit and chamber wall to simulate the gas injection, shown in Figure 2.4. Similar to the gas sphere approach, the gas injection boundary conditions including the velocity, temperature and density, must be specified before simulation, as well as the kinetic energy and turbulent length scale.

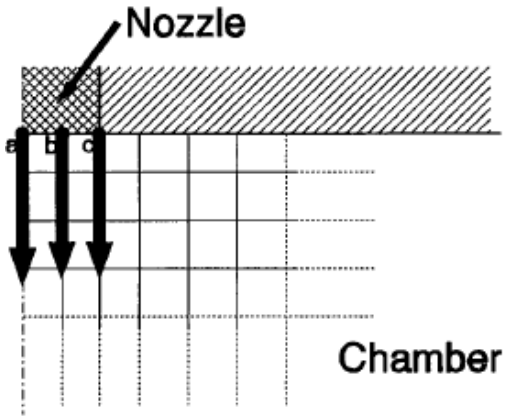

Figure 2.4 Gas nozzle/chamber interface model in KIVA [25]

In order to consider the effects of the barrel-shaped shocks in the coarse grids, the pseudo-diameter concept was used to account for the actual gas injector parameters.

$$d_{ps} = d_n \left(\frac{\rho_n}{\rho_{ps}}\right)^{1/2} \left(\frac{U_n}{U_{ps}}\right)^{1/2} \tag{2.10}$$

$$\rho_{ps} = \frac{P_{ch}}{RT_0}\left(\frac{\gamma+1}{2}\right) \tag{2.11}$$

$$U_{ps} = \sqrt{\frac{2\gamma}{\gamma+1} RT_0} \tag{2.12}$$

where the subscripts "s" and "n" represent the pseudo-diameter concept and nozzle exit. Thereafter, the diameter d_{ps}, gas jet density ρ_{ps} and the gas velocity U_{ps} in the interface between the nozzle exit and chamber wall can be estimated.

Jennings and Jeske [35, 36] directly modified the end wall boundary conditions where the gas nozzle exit was located. Due to chocked flow inside the nozzle, the mass flow rate was considered to be constant, and the corresponding velocity was equal to the sonic speed. The exit pressure and temperature was calculated by the underexpanded flow approach. By use of the finite volume method to discretize the continuity, momentums, enthalpy, transport of gas species and closure by the two-equation k-ε turbulence model, the natural gas mixing with air prior to combustion was simulated. And the significance of the turbulence on the evolution of gas plume was demonstrated.

Gribben [37] employed a 2-D axisymmetric model to investigate the shock-reflection hysteresis in the variable-pressure chamber. Here, the laminar axisymmetric Navier–Stokes equations were simplified to solve this problem, in which the convective terms and diffusive terms were discretized by the Osher's scheme and MUSCL scheme respectively. The influence of the varying back pressure in the near-region shocks and resulting flow field was investigated.

Li [38] compared the standard k-ε turbulence model and inviscid approach with the pressure ratio changing from 3 to 80 in the cylinder chamber with a 1 inch diameter nozzle, based on the CFD software ANSYS Fluent. In order to reduce the computational cost, the 2-D axisymmetric model was employed to explore the complex phenomena of transient free jet. By employing an extremely high-density grid, the primary characteristics including the barrel-shaped shocks at high pressure ratio and the repeating diamond-shaped shocks at relatively low pressure ratio near the nozzle exit were distinctly simulated, as shown in Figure 2.5. The comparison of the results from the inviscid model and k-ε model demonstrated that the inviscid assumption in the near-field region is reasonable. The variations of the size and position of Mach disk and pressure rise caused by the shock with the increasing gas injection pressure were also investigated by Li [38].

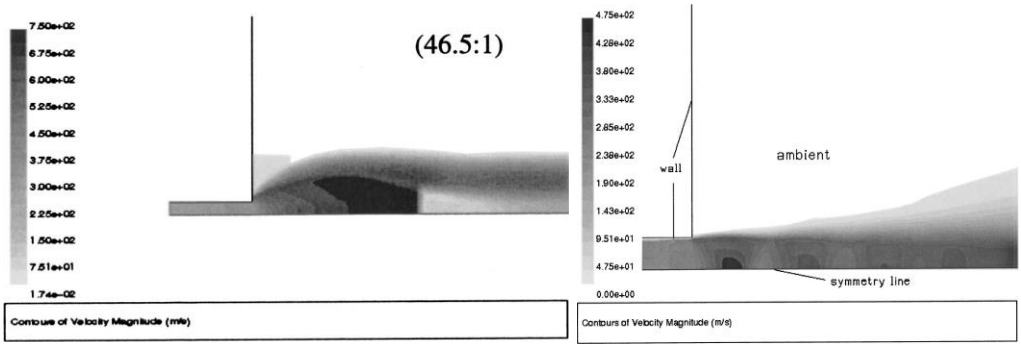

Figure 2.5 Velocity contour. Left: pressure ratio 46.5; Right: pressure ratio 3.0. [38]

Likewise, Hajialimohammadi [39] modelled a 2-D axisymmetric constant vessel including the gas nozzle geometry to capture the underexpanded jet in detail, based on the RANS method closed by Realized k-ε turbulence model in ANSYS Fluent. The calculated axial jet penetration agreed well with the experiment.

The AVL FIRE software was used by Yadollahi and Boroomand [40] to investigate the 3-D transient gas injection and mixing with air in the CNG direct injection engine. In the model, the cylindrical gas nozzle was directly modelled at the end of the chamber, where the "transition layer" meshing generation was employed, in order to reduce the mesh number far away from the underexpanded region. The variation of tip penetration injected by natural gas with the injection time was validated by measurements.

2.2.2 HPGI Gas Combustion Models

In a large two-stroke dual fuel engine, the ambient air and pilot liquid separately enter the engine chamber. The pilot fuel is injected firstly and subsequently auto-ignited near the top dead centre (TDC), owing to the hot compressed air. The high-pressure gas is also directly injected into the chamber, which rapidly ignites caused by the flame kernel created by the pilot fuel. In the combustion chamber, the main gas injection and combustion take place instantaneously. The diffusive combustion dominates for both the pilot fuel and main gas, despite the initial rapid pre-mixed combustion.

2.2.2.1 Combustion Regime

As the natural gas is directly injected into the high-pressure chamber, it requires the ignition source to ignite, due to its high Octane number. It is difficult for the fixed spark plug to create the precise ignition event at the designated time, whilst both reliable ignition timing and location can be supplied by the pilot fuel [41]. Generally speaking, the gaseous combustion by means of the high-pressure direct injection into the chamber near the top dead centre (TDC) will experience three phases: high-pressure gas injection, the gaseous combustion during the gas injection, and combustion after the gas injection.

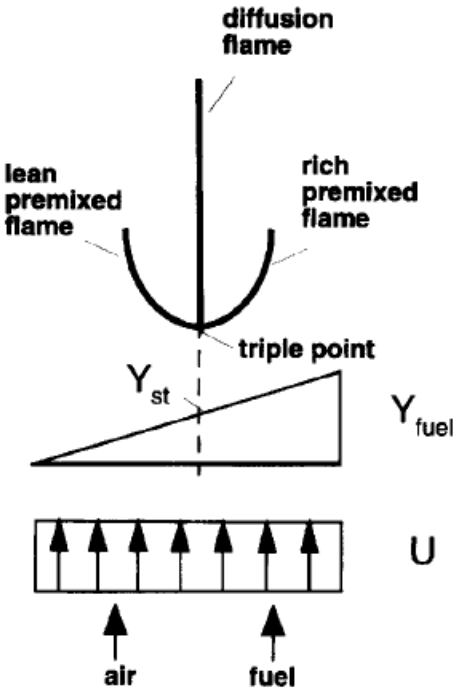

Figure 2.6 Striple flame structure stabilized by uniform velocity profile and linear fuel concentration [42]

The high-pressure gas injection acts as the transient vortex ball of Turner [26]. As the gas is injected into the

chamber, an underexpanded flow characterized by the barrel-shape shocks near the nozzle exit occurs. Far from the nozzle exit, the pattern of gas jet resembles a travelling vortex ball with a steady-state tail. In this model, the surrounding air is not entrained into the leading ball but the following tail.

The pilot fuel will ignite the natural gas along the sides of the quasi-steady tail rather than in the vortex-ball region [43]. In subsequence, the flame propagates through the flammable mixture on the periphery of the gas jet. Once the outer mixture is consumed, the gaseous combustion comes into the non-premixed diffusion flame [41]. It means that the reaction zone occurs in the thin flame surface appoximately close to the stiochoimetric air-fuel ratio. In the vicinity of the nozzle exit, the flame is lifted, owing to the extremly high flow strains. Shortly downstream, the triple flame takes place in such "lift" flame, with attribute to the propagation of flame through the fuel concentration gradient depicted in Figure 2.7. Muniz et al. [42] demonstrated that the triple point is located in the stoichiometric point with the maximum flame speed along the flame centreline. Moreover, the long and thin trailing diffusion flame is produced along the downstream of triple point, with attribute to the massive fuel and oxidizer diffuse towards the centreline. On the sides of triple point, the lean premixed and rich premixed flames takes place respectively, both of which 'anchor' the non-premixed flame [42].

After the injector needles close, the gas injection does not supply the momentum to the jet, whilst the steady-state gas jet heading a vortex ball occurs as a "puff" jet [41]. Ouellette and Hill [27] indicated that puff jet penetration is proportional to one-fourth root of the time, which implies that the travelling speed has a considerable decline. The flame in the tail spreads around the fuel cloud during the mixing process, until the combustion stops.

In addition, the pilot injection also plays an important role in the behaviour of the gas fuel combustion. In case where the pilot fuel does not ignite until close the end of the gas injection, the gas fuel combustion will follow the partially premixed cloud rather than the triple flame dominated by non-premixed combustion in the quasi-steady jet as it was demonstrated by Mctaggart-Cowan [41].

2.2.3.2 HPGI Gas Combustion Models

In the laminar flame, the reaction rates in the source terms of the species transports are determined by Arrehenius expressions, according to the following equation:

$$R_{fuel} = -A\rho^2 Y_{fuel} Y_{ox} e^{-E/RT} \tag{2.13}$$

With respect to the turbulent combustion, the Favre-mean reaction rates are not equal to the product of each mean variable in equation (2.14), but involve the related fluctuations and the couplings.

$$\tilde{R}_{fuel} \neq -A\rho^2 \tilde{Y}_{fuel} \tilde{Y}_{ox} e^{-E/R\tilde{T}} \tag{2.14}$$

Hence, the problem of decoupling the interaction between the turbulence and combustion is the key for the simulation of the turbulent combustion. Until now, there is no general expression of the mean reaction rates that entirely couple the turbulent mixing, molecular diffusion and chemistry kinetics. Hence, the combustion model has to be reduced. As the above description, the mixing-limited and the non-premixed combustion prevail in the HPDI gaseous engine. Therefore, the non-premixed combustion models will be introduced briefly in the following.

(1) Eddy Dissipation (ED) Model

Eddy dissipation model was developed by Magnussen and Hjertager[18]. In the diffusion flame, the chemical reaction takes place very fast, and the reaction rate is dominated by the intermixing on the molecular level of the fuel and oxygen eddies. Namely, the rate of combustion is determined by the dissipation rate of the eddies in the turbulent field. Owing to the turbulent characteristics of the species concentration, the fluctuation and mean concentration can be related to the dissipation rate. Hence, the mean reaction rate can be expressed by:

$$\tilde{R}_{fuel} = A\,\frac{\varepsilon}{k} min(\tilde{c}_{fuel}, \frac{\tilde{c}_{O2}}{r_f}) \tag{2.15}$$

As the fuel and oxidizer separately enter in the combustion chamber, the resulting eddies are assumed to be formed separately. In the lean fuel zone, the mean rate of combustion is calculated by the time-averaging fuel concentration $\tilde{c}_{fuel}$. With respect to the rich fuel zone, the mean oxygen $\tilde{c}_{O2}$ and its stoichiometric coefficient r_f determine the mean reaction rate.

Apparently, this model requires that the chemical reaction occurs in the scale of the micro-structure turbulence. Once the chemical timescale is higher than the Kolmogorov scale, the fuel combustion extinguishes.

(2) Infinitely Fast Chemistry (IFC) Model

Infinitely fast chemistry (IFC) approach is reasonably applied to the case where the diffusive time is generally much longer than the time scaled by chemical reaction. The one-step chemical reaction is adopted, according to the following equation:

$$F + O \rightarrow P \tag{2.16}$$

In the adiabatic state, the mass fraction of species Y_i and local temperature T can be calculated by the mixture fraction Z. Therefore, in conjunction with the presumed PDF shape, the mean scalars in the flow can be calculated by using the following equations as reported in Jin [44]:

$$\tilde{Y}_i = \int_0^1 Y_i(Z) P(Z; \vec{x}, t) dZ \tag{2.17}$$

$$\tilde{T} = \int_0^1 T(Z)P(Z;\vec{x},t)dZ \tag{2.18}$$

At present, two shapes of PDF are popular in the non-premixed combustion, including double Delta function and the β –function PDF, which are provided by the following equations respectively [45]:

$$P(Z) = \begin{cases} 0.5, & Z = \tilde{Z} - \sqrt{\widetilde{Z''^2}} \\ 0.5, & Z = \tilde{Z} + \sqrt{\widetilde{Z''^2}} \\ 0.0, & elsewhere \end{cases} \tag{2.19}$$

$$P(Z) = \frac{Z^{\alpha-1}(1-Z)^{\beta-1}}{\int Z^{\alpha-1}(1-Z)^{\beta-1}dZ} \tag{2.20}$$

Where,

$$\alpha = \tilde{Z}\left[\frac{\tilde{Z}(1-\tilde{Z})}{\widetilde{Z''^2}} - 1\right] \tag{2.21}$$

$$\beta = (1-\tilde{Z})\left[\frac{\tilde{Z}(1-\tilde{Z})}{\widetilde{Z''^2}} - 1\right] \tag{2.22}$$

It can be observed that the Delta-shape PDF in equation (2.19) is very simple and easy to calculate, whilst it is apparently less precise than the β-function expressed by equation (2.20) [45].

It is expected that IFC approach can illustrate qualitative information about the global flame structure, as well as the maximum heat release rate of the fuel combustion.

(3) Non-Premixed Equilibrium Model

It is impossible of the fuel combustion that only one or multi-steps chemical reactions take place. Generally, there are dozens, even hundreds of the intermediate products and radicals that can be produced during the fuel combustion, which involves thousands of chemical reactions. In that way, the IFC approach cannot effectively represent such complicated phenomena, however the IFC also can be regarded as a reduced Equilibrium model.

Under constant pressure and temperature, the chemical reactions occur toward the decrease of the mixture Gibbs free energy, according to the second law of thermodynamics. When the Gibbs free energy reduces to its minimum value, the reaction reaches at equilibrium. Given by the mixture fraction and total enthalpy in the non-adiabatic state, the mass fraction for the involved species and temperature can be calculated in terms of the minimum Gibbs free energy. Similar to the IFC approach, integrated by the presumed PDF shape, the mean scalars and their variations in the turbulent system can be obtained. The detailed theory is described in section 3.4.3.

(4) Steady Diffusion Flamelet Model

The flamelet concept was applied by Peters [19] to describe the non-equilibrium effects of the turbulent diffusion combustion, in which the reaction domain was regarded as the thin burning layer. In addition, the turbulent flame brush was structured as the ensemble of laminar flamelets dominated by the diffusion process.

Compared to the equilibrium model, laminar flamelet model can compute the non-equilibrium chemical reaction by involving the scalar dissipation rate χ_{st} at the stoichiometric flame layer, which represents the aerodynamic straining of the turbulent flame. When the dissipation rate χ_{st} is equal to zero, it implies that the equilibrium combustion occurs.

The detailed chemical kinetics is considered through the embedded laminar flamelet model such as the counter-flow laminar combustion. ANSYS Fluent [45] indicated that this model cannot be used to accurately simulate the low chemical reaction, such as the NOx formation and low-temperature CO oxidation.

The fundamental and related equations of the steady diffusion flamelet model are described in section 3.4.4.

(5) Unsteady Flamelet Model

According to the steady diffusion flamelet model, due to its "quasi-steady" characteristics, the laminar flamelet database integrated by the PDF shape can be tabulated, as a function of the mean mixture fraction and its fluctuation, the scalar dissipation rate and the total enthalpy in the non-adiabatic system, before the CFD simulation. This can significantly reduce the computational cost of the communication between the CFD code and laminar flamelet database. However, if the diffusion flame involves the strongly instantaneous state or long residence times, only a single flamelet cannot precisely express the actual chemistry kinetics, for example the split-injections and the NOx formation. This requires a number of laminar flamelets created simultaneously solved with the flow in the main CFD code. It can be expected that when each grid cell embeds one laminar flamelet, a huge computational efforts is required. The alternative is to divide the whole computational domain into several subzones. In each subzone, the statistically averaged scalars in the laminar flamelet model are considered. The turbulent flame in each subzone can be represented by one flamelet at each time step. Hence, the model computational expense will be considerably reduced.

Based on this concept, Barths et al. [22] developed the Eulerian Particle Flamelet Model (EPFM). Here, the different marker particles were introduced into the chamber, each of which represented one flamelet. Therefore, the different flamelet histories can be related to the pathway of the particle

travelling through the turbulent flow field. Then, the mean mass fraction of the i^{th} species in the turbulent flow is calculated by using the following equation,

$$\tilde{Y}_i(\vec{x},t) = \int_{\vec{x}_0}\int_0^1 \tilde{f}_{Z,\vec{x}_0}(Z,\vec{x}_0;\vec{x},t)Y_i(Z,\vec{x}_0;t)dZd\vec{x}_0 \quad (2.23)$$

Assuming that there were n marker particles in the initial n subzones in the turbulent flow, each subzone is represented by one flamelet. The mass fraction of species i in the subzone l is denoted by the following,

$$Y_i\left(Z,\vec{x}_{0,l},t\right) = Y_{i,l}(Z,t) \quad (2.24)$$

On the hypothesis of the statistical independence of the mixture fraction Z and the original locations $\vec{x}_0$ of the marker particles, the joint PDF can be produced by two marginal PDFs. In the whole domain, the sum of the mean mass fraction was integrated as follows.

$$\tilde{Y}_i(\vec{x},t) = \sum_{l=1}^{n}\tilde{I}_l(x,t)\int_0^1 \tilde{f}_{Z,\vec{x}_0}(Z,\vec{x},t)Y_{i,l}(Z,t)\,dZ \quad (2.25)$$

Where, the probability that particle l from initial subzone $\vec{x}_{0,l}$ travelled to the location $\vec{x}$ at time t was computed by,

$$\tilde{I}_l(x,t) = \int_{\vec{x}_{0,l}}\tilde{f}_{\vec{x}_0}(\vec{x}_0;\vec{x},t)d\vec{x}_0 \quad (2.26)$$

In the research of Barths et al. [22], the probability $\tilde{I}_l(x,t)$ was not solved by the Lagrangian method for tracking the particles, but by using the following Eulerian transport equation:

$$\frac{\partial\bar{\rho}\tilde{I}_l}{\partial t} + \nabla\cdot\left(\bar{\rho}\tilde{\vec{v}}\tilde{I}_l\right) - \nabla\cdot\left(\bar{\rho}\frac{\gamma_T}{Sc_T}\nabla\tilde{I}_l\right) = 0 \quad (2.27)$$

The communications between the CFD code and the flamelets are based on the concept of the representative interactive flamelet (RIF) shown in Figure 2.7.

When the detailed chemistry kinetics of the fuel was embedded to the Flamelet code such as the NOx formations, a more accurate prediction about NOx emissions can be achieved, comparing the case where the Zeldovich Mechanism is used.

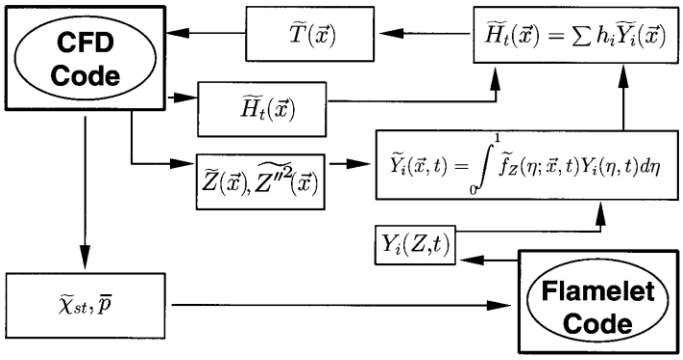

Figure 2.7 Road map of RIF concept [22]

(6) Conditional Moment Closure (CMC) Model

The Conditional Moment Closure (CMC) model was first developed by Bilger et al. [20] and Klimenko et al. [21] respectively. Compared to the Reynolds averaging and Favre mean approaches for the Navier – Stokes Equations in the turbulent flow, the variation of the scalars by CMC is further smaller than the conditional expectation, which implies the turbulent fluctuation averaged by CMC diminishes greatly. As a consequence, the interaction of the chemistry kinetics and turbulence is decoupled, in terms of the omissions of the higher order moments.

In the development of Bilger et al. [20], the conditional expectation or average of the scalar $Y(x,t)$ at a given value η can be calculated, according to the following equation:

$$Q(\eta,x,t) = \langle Y|\eta\rangle = \langle Y(x,t)|Z(x,t)=\eta\rangle = \int_{-\infty}^{+\infty} YP(Y|Z(x,t)=\eta)\,dY \qquad (2.28)$$

Then, the variation $Y''(x,t)$ can be defined,

$$Y(x,t) = Q(Z,x,t) + Y''(x,t) \qquad (2.29)$$

Consequently, the conditional mean Navier-Stokes equation on the mixture fraction $Z(x,t)$ equal to η can be derived, according to the following equation:

$$\langle\rho|\eta\rangle\frac{\partial Q}{\partial t} = -\langle\rho|\eta\rangle\langle\vec{u}|\eta\rangle\cdot\nabla Q + \langle\rho|\eta\rangle\frac{\langle\chi|\eta\rangle}{2}\frac{\partial^2 Q}{\partial\eta^2} + \langle\rho|\eta\rangle\langle\dot{\omega}|\eta\rangle + e_Q + e_Y \qquad (2.30)$$

The five terms in the right side of equation (2.30) represent the convection, turbulent mixing, the chemical reaction source, contributions from molecular diffusion, and the turbulent flux of the reactive species to a “porous particle”. Here, the “porous particle” denotes that the constant mixture fraction Z valued to η travels with the conditional-mean velocity $\langle\vec{u}|\eta\rangle$.

Bilger et al. [20] indicated the e_Q in equation (2.30) could be ignored in the flow of the high Re number, whilst e_Y needs to be estimated:

$$e_Y \approx -\frac{\nabla\cdot\left[\langle\rho|\eta\rangle\left\langle u''Y''|\eta\right\rangle_{P(\eta)}\right]}{P(\eta)\langle\rho|\eta\rangle} \tag{2.31}$$

Owing to the small conditional variation of the scalar including species mass fraction, temperature and the density, the conditional-average scalar can be directly used to calculate the mean chemical reaction rate in the governing equations (2.30), under the assumption of first order CMC. Therefore, the following equation is used to calculate:

$$\langle\dot{\omega}|\eta\rangle \approx \dot{\omega}(\langle T|\eta\rangle, \langle Y_i|\eta\rangle, \langle\rho|\eta\rangle) \tag{2.32}$$

With regard to the probability density function in equation (2.28) used to evaluate the conditional-mean scalar, the above-mentioned double Delta function or the β –function PDF shapes still can be used.

It is inferred that the CMC method requires an expensively computational resource in the direct solution of the governing equations [44]. However, due to the rigorous theory, CMC method is compatible with all kinds of the fuel combustion, which drives its comprehensive development. For example, the higher order CMC closure had been developed by Cha et al. [46] and Kim [47], in order to precisely predict the fuel extinction and re-ignition. Han et al. [48] investigated the ignition and mixing controlled combustion in detailed chemistry in a direct injection diesel engine, by use of the CMC model in conjunction with the RIF concept.

2.3 Investigation of Flow and Combustion Processes in Marine Engines

Rare investigation about two-stroke HPDI dual fuel engine can be collected in publications. Therefore, the research about the processes in the 2-stroke marine diesel engines and 4-stroke HPDI dual fuel engines are reviewed respectively.

2.3.1 Numerical investigation of the 2-stroke diesel engine

In this section, the numerical investigations including the closed-cycle and scavenging processes are focused on, because the experimental publications cannot be found.

The commercial CFD software STAR-CCM+ Version 10 was employed by Pang et al. [49] to investigate the diesel fuel combustion and soot formation processes at full load in the two-stroke, low-speed marine diesel engine 4T50ME-X from MAN Diesel & Turbo. The test in a constant volume chamber was used to validate the CFD models, where the four skeletal n-heptane mechanisms, the standard k-ε turbulence model and the KHRT breakup model were compared. In order to match both liquid and vapour penetrations measured in the experiments, the constant C_1 in the standard k-ε model is modified from the defaulted value of 1.44 to 1.55, and the constant B_1 in KHRT model, which determines the liquid core length is recommended to be equal to 25. In terms of the ignition delay and

lift-off length measured under the four different chamber pressures, the skeletal n-heptane mechanism consisting of 30 species with 68 reactions was suggested. Plotted by the equivalence ratio against temperature, the results depicted the rich premixed core and the outer diffusion flame, where the maximum temperature was located in the diffusion flame. As the simulation of the closed-cycle of the 4T50ME-X diesel engine, the Zeldvich mechanism for the NO formation with the two different Arrhenius parameters were compared with the measurement. Both of Arrhenius parameters overestimated the NO emissions, where the result from the Arrhenius parameters proposed by Tao [50] was 1.8-times higher than the experiment, and the recommendation by Easley and Mellor [51] had a 1.5 times. In addition, the spatial and temporal distributions of intermediates CH_2O, OH, C_2H_2 were visualized, which respectively presented the low-temperature chemistry reaction zone, the high-temperature diffusion flame and the precursor of the soot formation.

Sun [52] focused on the validation of the CFD models employing the software package CONVERGE 2.3 in the 2-S marine diesel engine 6S35ME-B9, in which the KHRT breakup sprays model was used. By comparing the n-heptane and n-tetradecane chemical kinetics mechanisms, SAGE and CTC/shell combustion models, it was demonstrated that the n-heptane-SAGE model results were closer to the experimental measure of the pollutant emissions including NOx, HC, CO and CO_2, while the n-tetradecane-SAGE model was preferable for accurately predicting the maximum temperature. The SAGE model is a better choice to more accurately evaluate the maximum pressure in-cylinder.

Apart from the fuel injection and combustion processes, the scavenging process is also the critical engine process for two-stroke engines, which considerably affects the pollutant emissions and the engine efficiency. Obeidat et al. [53] applied the Large Eddy Simulation (LES) in CFD code Openfoam to model the scavenging process in a MAN B&W marine engine. The significant simplifications were made, including the uniform radial and tangential velocity replacing the real scavenging ports and the fixed piston positions at 0%, 25%, 50% and 75% locations defined by the coverage ratio of the intake ports. By comparison of the measured profiles of the axial velocity in the cylinder, the LES method was demonstrated to be feasible to simulate the scavenging flow in a two-stroke marine engine.

Using the ANSYS Fluent 6.3, Lamas and Vidal [54] calculated the scavenging process of one engine cylinder for the MAN B&W 7S50MC engine, where the cylinder, intake ports and exhaust duct were modelled. The model validation was based on the cylinder pressure, the mixing of the exhaust gas with the fresh air charge and the evolution of the swirling flow induced by the intake ports.

The dynamics of the turbulent swirling flow in the cylinder of the low-speed two stroke diesel engine was also investigated by Hemmingsen et al. [55] by means of the STAR-CCM+ software. In order to precisely evaluate the air charging and mixing processes, about 5.2 million cells was modelled and the Spalart-Allmaras and SST k-ω turbulence models were compared, using the measurements of the

axial, radial and tangential velocities. The λ^2 criterion colored by the axial velocity visualized the flow structure and evolution of the vortex cores and rings.

Sigurdsson [56, 57] simulated the scavenging processes in a large two-stroke, low-speed, and uniflow-scavenged marine engine, by using the commercial software STAR-CD. The computational domains included the cylinder volume, scavenge ports, scavenge box and exhaust duct, where the 12 ° sector zone was adopted simplified by the periodic conditions. The heat release rate derived from the experiment was added to the energy equation as a source term to simulate the effects of the fuel injection and combustion, in which the peak pressure was 14% lower than the experimental result. This was primarily caused by the disparity of the assumed ideal gas and the real gas states. The sensitivity involving the turbulence models and mesh resolutions indicated that the RNG k-ε turbulence model and the finest mesh were recommended, in terms of the maximum tangential velocity at top dead centre (TDC). Also, the angular and axial momentum, the mixing process of the fresh air and the remaining gas in-cylinder, and the scavenging parameters were evaluated, as well as heat transfer through the cylinder wall and piston.

2.3.2 Investigation of the Flow and Scavenging Processes in 4-Stroke HPDI Dual Fuel Engine

2.3.2.1 Experimental Research

Due to the high auto-ignition temperature and the anti-knock properties of methane, natural gas, which primarily consists of the methane, is compatible with the CI engine. Douville [58] conducted the experimental investigation of the high-pressure, directly-inject (HPDI) natural gas combustion ignited by diesel pilot fuel in the cylinder, and the engine performance, emissions and combustion characteristics of engine fuelled by the diesel and natural gas were investigated. Due to the temperature near the top dead centre (TDC) in the diesel engine lower than the auto-ignition temperature of natural gas, the pilot fuel was required for ignition. The potential of such dual fuel engine that had the higher thermal efficiencies in high loads and lower pollutant emissions over the entire range of engine load was demonstrated by the experiments.

Larson [59] payed more attention to measure the influence of the injection pressure, the dual fuel injection timing, the exhaust pressure and boost pressure of the cylinder on the emissions including the nitrogen oxides (NOx), carbon monoxide (CO), particulate matter (PM) and total hydrocarbons (HC). Here, the change of dual fuel injection timing included the absolute injection timing and the relative injection timing between the pilot and gas injection.

The comprehensive experiments on a single-cylinder 4-stroke heavy-duty engine were conducted by McTaggart-Cowan [41, 60]. In order to understand in-depth the gaseous combustion and pollutant productions, the changes of the injection pressure varied with engine speed and loads, gas composition (including ethane, propane and methane), gas dilution (inert nitrogen) and hydrogen

addition were investigated. Apart from the pollutant emissions, the effects of all these additives with the methane on the combustion characteristics including efficiency, combustion variability, gaseous-fuel ignition delay, burn duration were also tested and analysed [61, 62].

A new type of HPDI injector tested by Brown [63], where the pilot diesel was injected into a gas/diesel reservoir in the nozzle (Figure 2.8), and then the pilot and gas were co-injected into the cylinder. Also, the two sizes of reservoir volume in the injector were compared in experiments, as well as the single and double gas injections in both reservoir volumes. The double gas injections mean that the HPDI engine had both the pilot/gas mixing injection and the pure gas injection.

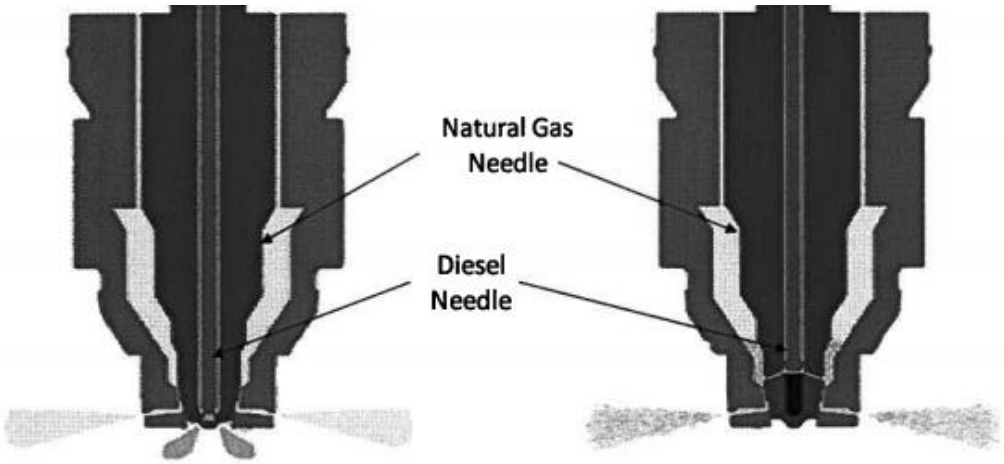

Figure 2.8 Comparison of the cross-section geometry of a HPDI normal dual fuel injectors and co-injector nozzle [63]

The internal combustion processes in the HPDI dual fuel engine were also investigated in the an extensive number of experiments [64, 65], focusing on the injection parameters and the diesel/gas mass ratio. Li et al. [64] studied the effects of the injection interval between the pilot and gas, the pilot fuel injection duration and the pilot fuel injection pressure on the ignition delay, the heat release rate, the brake specific fuel combustion (BSFC) and the cyclic variation of cylinder pressure, as well as the cylinder pressure and its first and second derivatives. The effects of the HPDI gaseous injection changing with the diesel injection pressure and gas injection start on the gaseous emissions including the CO, NOx and THC were studied by Zhang et al. [65]. Besides the different diesel / gas fuel ratio injected into the engine cylinder were compared by Zhang et al. [65].

A single cylinder test engine called Rapid Compression Expansion Machine (RCEM) shown in Figure 2.9 was used to compare the dual fuel and the diesel operating modes [9]. The RCEM is a one-shot firing machine, in which the single-hole gas injector and single-hole pilot/ diesel injector are installed. Not only the comparison of the diesel mode and dual fuel mode, but also the change of the pilot injection timing, gas injection pressure and reduction of oxygen in the charged air, were investigated. The pressure in-cylinder, carbon monoxide (CO), unburned (HC) and NOx were measured and the heat released rates are evaluated, as well as the flow and flame visualizations.

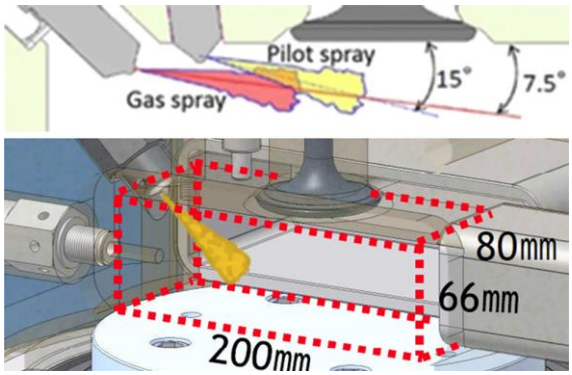

Figure 2.9 Schematic of the RCEM [9]

2.3.2.2 CFD Modelling of HPDI Gaseous Combustion

The combustion processes in HPDI dual fuel engine following injection consist of three phases: the preparation of combustible mixture (ignition delay), premixed combustion and mixing limited combustion (non-premixed combustion).

Ouellette [25] used the ignition delay τ_i, which was derived from the shock-tube experiments conducted by Tsuboi and Wagner [66], to evaluate the reaction rate.

$$\tau_i = 4 \cdot 10^{-15}[CH_4]^{0.32}[O_2]^{-1.02}e^{\frac{222}{RT}} \tag{2.33}$$

Under the assumption of homogeneous conditions and neglibible heat diffusion from the ignition locations, the reaction rate of methane in the period of ignition delay can be estimated,

$$RR_{ign} = \left(\frac{C_v}{-LHV}\right)\left(\frac{\Delta T}{T}\right)_{\tau_i}\left(\frac{P}{R_{mix}W_{CH4}}\right)\left(\frac{1}{\tau_i}\right) \tag{2.34}$$

As an approximation, 1% changes of the temperature $(\Delta T / T)_{\tau_i}$during the ignition delay causes a pre-exponential constant A in the order of 10. Substituting equation (2.33) to (2.34), the reaction rate of methane during ignition delay can be derived,

$$RR_{ign} = A[CH_4]^{-0.32}[O_2]^{1.02}[N_2] \quad e^{\frac{-222}{RT}} \tag{2.35}$$

where the concentration of nitrogen $[N_2]$ is derived from the pressure expression, in terms of the ideal gas equation of state. Now, the order of the pre-exponential constant A changes to 1.0×10^5.

Between the ignition and high-temperature schemes, the mixing-limited or chemistry-limited combustion cannot be determined. Therefore, the reaction rate can be averaged by the considering

ignition reaction RR_{ign} and the higher temperature reaction rate RR_{hts} over a transition temperature change ΔT.

$$RR_k = \frac{(T_c - T_{ib})}{\Delta T} RR_{hts} + \frac{(T_{ib} + \Delta T - Tc)}{\Delta T} RR_{ign} \quad (2.36)$$

Where, T_c denotes the local temperature and the transition criterion temperature T_{ib} is designated about 1700 K.

When the methane experiences the non-premixed combustion, Ouellette [25] employed the eddy-dissipation model to simulate the methane combustion, described in Section 2.2.3.2. With respect to the chemical reactions, the two-step mechanism was used by Ouellette [25], considering the intermediate carbon monoxide (CO).

Li [67] separated the dual fuel combustion into diesel pilot ignition and natural gas combustion. The pilot ignition delay was computed by employing the Shell model [68], which can be used to simulate the auto ignition in any volumetric combustion except for the purely premixed process. The natural gas combustion was modelled by considering the characteristic-time combustion approach, where the reaction rate was reduced by the following equation:

$$\frac{dY_i}{dt} = -\frac{Y_i - Y_i^*}{\tau_c} \quad (2.37)$$

where Y_i denotes the mass fraction of species i. Y_i^* can be calculated by equilibrium model varied with the local temperature in-cylinder. The characteristic time τ_c is determined by the minimum of the chemical kinetic time and turbulent mixing time.

The simulation of dual Fuel combustion in HPDI engine was also conducted by Lee [69], where the direct chemistry solver (SAGE) was adopted, embedded with chemical mechanism of Patel [70]. Also, the SAGE solver was applied by Li [71] to investigate the hydrogen addition to the HPDI dual fuel engine. Both published papers [69, 71] did not provide any information about this chemistry solver. The commercial CFD software CONVERGE [72] indicated that the SAGE solver called a delta PDF to simulate the various combustion modes including premixed, non-premixed, partially premixed and multiple fuels.

By means of the ECFM-3Z combustion model included in the commercial CFD software AVL-FIRE, Wang et al. [73] modelled the influence of injection rates on the combustion and emissions of a 4-stroke HPDI dual fuel engine.

The description of ECFM-3Z was reported in Colin and Benkenida [74] and its principles are illustrated in Figure 2.10. Each computational cell splits into three zones including unmixed fuel zone (F), mixed zone (M) and unmixed air zone (A).

The fuel flame consists of three regimes including auto-ignition, premixed flame and diffusion flame. The three delta-shape PDFs were applied to express such structure, according to the following equation:

$$P(Z) = a\delta(Z) + b\delta(Z - \bar{Z}_M) + c\delta(Z - 1) \quad (2.38)$$

where $\bar{Z}_M$ denotes the mean value of the mixture fraction in the mixed zone. The three terms in equation (2.38) represent the unmixed air zone, mixed zone and unmixed fuel zone respectively. The simplified CMC method was adopted to closure the Z space.

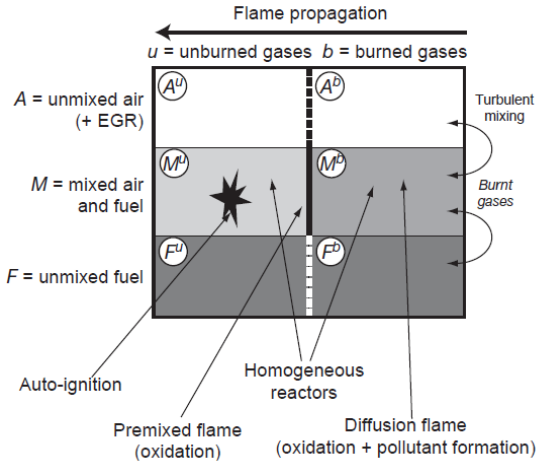

Figure 2.10 Sketch of ECFM-3Z combustion model [74]

2.3.2.3 Parametric Investigations

As the high-pressure natural gas is directly injected into the engine combustion chamber, due to the excellent anti-knock and the low emissions characteristics, the natural gas is a promising fuel alternative for the CI engine. However, the natural gas high auto-ignition temperature and low flame propagating speed are considered as drawbacks. To improve the combustion quality and reduce emissions, including the injection parameters and fuel additions, comprehensive parametric investigations are required and have been reported in the literature.

(1) Injection Parameters

The relative injection timing (RIT) denotes the time interval between the pilot injection end and gas injection starts. Larson [59] showed that RIT considerably influences the engine emissions. In the shop test of 4-stroke dual fuel engine conducted by Larson [59], the minimum pollutant emissions were observed at RIT of 1.8 ms. Similar measurements were made by Duggal [75], where it was conducted that the increase of RIT deteriorated the gas combustion quality, resulting in the unacceptable emissions and fuel consumption level.

In the RCEM test regarding the advanced pilot injection timing under the same gas injection parameters, the RIT of -3.8 ℃A instead of -2.3 ℃A led to a 20% NOx increase [9]. For an RIT change from -2.3 ℃A to +0.8 ℃A, the emissions were reduced marginally [9]. Lee [69] numerical analysis showed that small RIT could cause the increase of the NOx emissions, whilst IMEP was not considerably affected.

The other critical injection parameter is the pilot fuel or gas fuel injection timing. Advancing injection timing could increase the peak pressure and the pressure rise, due to the earlier start of combustion [64]. However, the higher maximum HRR required the injection timing of the pilot fuel or gas fuel to be retarded [64]. The experiment of Zhang [65] demonstrated that the advancing injection timing can benefit the peak pressure, while maximum HRR varied diversely. With regard to the emissions, the earlier injection timing can reduce the HC emissions, as well as improve the combustion and thermal efficiency. The effect of injection timing on CO production was influenced by the engine speed. CFD by Gao [76] indicated that advancing gas fuel injection timing could increase the IMEP, as well as the NOx and CO emissions.

In the experiments of the modified Cummins ISX four-stroke engine, Larson [59] reported that the relationship between the injection timing, the NOx emissions and efficiency could be effectively indicated by the timing of 50% cumulative heat release (HR50), where the specific fuel consumption was approximated as a function of HR50 approximately. The NOx emissions were almost independent of the equivalence ratio. Other emissions including the CO, HC and PM were significantly affected by the equilibrium ratio and the engine speed, apart from the injection timing.

Higher pressure gas injection can increase the gas tip penetration and momentum exchange, as well as the mixing and air entrainment. This apparently influences the gas combustion and the related pollutant emissions. Larson's experiment [59] in a 4-stroke HPDI gaseous engine showed that the correlation between NOx, efficiency and HR50 was not affected by the injection pressure, whilst the CO and HC emissions were varied with the injection pressure and the equivalence ratio. When Li [64] conducted the experiments in a 4-stroke turbocharged HPDI gaseous engine, and concluded that raising the injection pressure was able to increase the peak pressure, the maximum pressure rise and the maximum HRR, but the combustion stability became worse. Regarding the same engine experiment, Zhang [65] further demonstrated that the higher combustion quality and thermal efficiency could be achieved through boosting the gas injection pressure, which was beneficial of the reduction of the HC emissions. The same trends regarding the peak pressure and maximum temperature was numerically computed by Gao [76], whilst the NO emission was found to be independent of the gas injection pressure.

Wang [73] focused on the numerical investigation of the pilot fuel and gas injection profiles shown in Figure 2.11 by use of the commercial software AVL-FIRE. Generally, there are three locally peak pressure points observed in the cylinder pressure diagrams, which are respectively caused by the cylinder compression, the pilot fuel combustion and gas fuel combustion. It was concluded that the pilot injection end rate more significantly affected the cylinder pressure and temperature than the pilot injection start rate. The smaller pilot injection end rate could be beneficial for the NO and soot emissions. Similarly, the in-cylinder temperature was more sensitive to the gas injection end rate than

the start point, nevertheless both of them had an opposite influence on the temperature. With regard to the NO and soot emissions, a trade-off between them was observed, caused by the profiles of the gas injection rate. It was expected that the gas inclined angle played a more important role in the engine performance and emissions, due to the possible impingement of the gas on the piston bowl. Calculations of Wang [73] depicted that the +/- 5 °variations of the gas inclined angle could increase at least 2 times of the CO production. As the higher change up to +/- 15 °, the CO emission was elevated around 20~35 times.

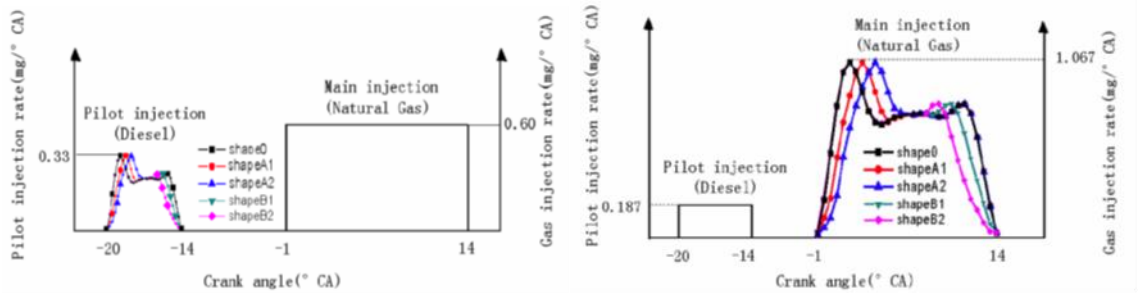

Figure 2.11 Injection profiles of pilot and gaseous fuels [73]

The direct chemistry solver SAGE was used by Lee [69] to investigate the dual fuel injection direction and holes number of injectors (Figure 2.12), where the inclined angle variation from -15 °to 15 °, in comparison with the base case, and for various holes number from 4 to 7. The calculations showed that the IMEP did not change much, despite of the variation of the pilot fuel inclined angle. However, the CO would rise due to the inefficiently burning of gas inside the bowl. Changes of the holes numbers showed that the IMEP and NOx emissions almost held constant, whilst the CO production had a moderate change, the 5-holes injector exhibited the minimum CO emissions.

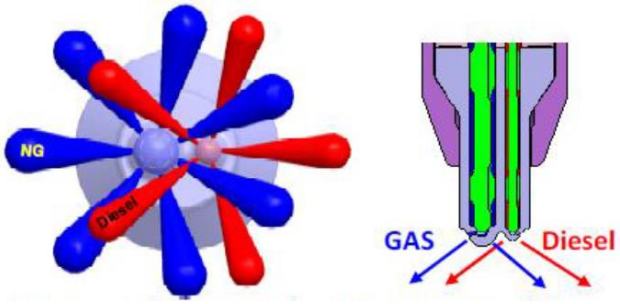

Figure 2.12 Sketch of the twin fuel injector used to the HPDI gaseous engine [69]

(2) Fuel Composition

• Ethane and Propane Additions

Natural gas primarily consists of methane, which mass fraction is within 70% and 95% [62]. Apart from the methane CH_4, the natural gas includes the ethane C_2H_6 and propane C_3H_8, as well as very limited sulphur.

McTaggart-Cowan [62] described that the ignition delay was not influenced by the heavy hydrocarbons in natural gas including ethane and propane, when the temperature was above 1400K. But, at the low temperature range, the increase of ethane and propane fraction in the natural gas, led to a more ignitable fuel, which resulted in the reduction of the ignition delay. The shorter ignition delay caused the reduced premixed combustion at the early combustion process, which means that the diffusion combustion period was prolonged. As a consequence, the combustion duration of natural gas was increased accordingly. However, in case where the addition of ethane or propane fraction is higher than the moderate level, the ignition delay will not further reduce, and the ignition experiences the stoichiometric combustion [41].

The HC emissions are mainly produced by the unreacted fuel. The experiment of McTaggart-Cowan [41, 62] showed that the addition of ethane and propane in the methane could benefit the late combustion, and consequently reduced the HC emissions. Similarly, the CO production also reduced, but the formation route is quite different, because the CO is a by-product of the partial combustion. Further investigation demonstrated that this was possibly due to the improvement of mixing or increase of the radical contents at gas reaction zone, through the comparison of the pure methane and fuel additions of ethane and propane in experiments [62].

With regard to the NOx emissions, it seemed that it was not noticeably affected by the compositions of these heavy hydrocarbons [41]. Either ethane or propane would lead to a substantial increase in PM and black carbon (BC) emissions, primarily owing to the formation of the intermediate species C_2H_2 and C_2H_5 [41, 62].

• Hydrogen Addition

Natural gas has a low flame propagating speed in the non-premixed combustion process. The addition of hydrogen not only improves the diffusion flame stability but also benefits the mixing process. Moreover, the hydrogen added to the gas increased the flame thickness under partially-premixed conditions, due to its higher diffusivity. Consequently, the ignition delay of natural gas reduced and the combustion duration was prolonged [62]. At low loads, the addition of hydrogen could significantly raise the heat release rate, possibly owing to the enhanced chemical kinetics [41]. At high loads, the overall combustion rate was not notably affected by the hydrogen addition, which implied that the overall combustion process was dominated by the diffusion process [61]. In summary, due to the improvement of flame stability for the addition of hydrogen, the cyclic variations had been considerably reduced [61].

Moreover, the experiments [61] demonstrated that increase 10% concentration of hydrogen in the mixture can reduce the 15%-20% HC and CO emissions, attributed to the improvement of the combustion stability. The PM emission including black carbon (BC) could be reduced by 10%. Due to

the lower carbon-energy ratio as the increase of the hydrogen addition, the carbon dioxide CO_2 reduced by 3.5% at high load and 5% at low loads. Also, the NOx emissions were raised by 10% for 10% increment of hydrogen addition, due to the higher flame temperatures and higher radicals H, OH and O concentrations.

Li [71] compared the effects of hydrogen-addition way on thermal efficiency and emissions using the SAGE solver including the volume-equivalent (VE) principle and energy-equivalent (EE) principle. In the VE cases, the volume ratio of the injected hydrogen and the total fuel changed from 10% to 40%. To maintain the same heat release, the gas injection durations in VE cases were suitably prolonged. The EE cases referred to that the energy of injected hydrogen was varied between 10% and 40% of the total energy. The 3D simulation showed that the variations of the in-cylinder maximum pressure and the maximum HRR were influenced by the hydrogen-addition approach in the gas fuel. According to the volume-equivalent principle, the maximum pressure and maximum HRR reduced. However, the opposite trends observed in the hydrogen addition based on the energy-equivalent principle. Based on the VE principle, the CO production reduced for the hydrogen addition lower than 10%, whilst the increase of the CO emissions was observed for the further increase of the hydrogen under the gas injection pressure 180 bar. By means of the energy-equivalent method, raising the hydrogen-methane blend ratio in the gas fuel could continuously reduce the CO production. The NOx emissions decreased with the increase of the VE hydrogen addition in the gas fuel, whilst the opposite variation was found in the EE cases. Both hydrogen-addition approaches can benefit the reduction of the soot emissions.

• Fuel Dilution

When the nitrogen is used to dilute the methane, a higher gas injection rate is required, in order to retain the same fuel energy. In the 4-stroke HPDI dual fuel engine tested by McTaggart-Cowan [41], if the 40% nitrogen was added to the methane, more than twice pumping work needed to be supplied. Hence, the nitrogen dilution can increase the jet penetration and air entrainment. The primary effect of the nitrogen addition is to the decrease the gaseous fuel mixture heating value, but the chemical kinetics is not influenced, even at very high N_2 concentration [62].Therefore, the slower initial flame speed but faster and more stable combustion at late stage were observed.

The improvement of the momentum exchange and the mixing of gas jet with the surroundings caused by the nitrogen addition could also effectively reduce the gas ignition delay (GID), which is associated with the methane number (MN). McTaggart-Cowan [62] demonstrated that 1% reduction of MN was able to decrease 0.75% in GID. The maximum HRR is approximately affected by GID in a linear relationship. In magnitude, 1% change of GID could cause the 1% change of maximum HRR, except for the case of the high nitrogen dilution. McTaggart-Cowan [62] explained that the peak HRR took place in the premixed combustion process, and the less fuel available in the premixed

combustion for the shorter ignition delay, led to the reduction of maximum HRR. The lower and longer heat release rates were found in the nitrogen addition, which indicated that the diffusion flame prevailed.

Regarding the pollutant emissions, due to the improvement of the late-stage combustion in the case of nitrogen dilution, the unburned HC reduced. The opposite variation can be found in CO production, which caused by the interaction of gas jet and piston bowl due to the higher gas jet penetration.

2.4 Research Gaps

Based on the literature review conducted, the following research gasps are identified:

- The underexpanded flow near the nozzle exit caused by the high-pressure gas jet can significantly influence the gas penetration and its entrainment with the chamber air. Most of the researchers numerically calculate such complicated flow, based on the 2D model, due to the limitation for high grid resolution. In the 3D simulation in the HPDI engine, the gas combustion processes and pollutant formations are focused on. Apparently, it is high challenge that both the gas jet and the resulting combustion are accurately evaluated by using CFD in three dimensions.
- The dual fuel combustion with the high pressure direct gas injection is dominated by the non-premixed combustion process. Recently, some commercial software such as AVL-FIRE [73] has been employed to investigate the 4-stroke dual fuel engine. It seems that the solution procedure of dual fuel is not clearly described, in which the detailed chemical reactions will vary with the crank angle, due to the separate injection of the pilot and gas fuel.
- Most of the previous studies separately calculate the closed-cycle and scavenging processes of the marine engines. In terms of the limited number of the published studies, the CFD shows that a remarkable variation of the peak pressure with comparison with the experimental results. The accurate prediction of the internal processes in the whole cycle of marine engine should be beneficial for investigating the evolution of the involved processes and the interaction between the closed and open cycles.
- Recently, the two-stroke HPDI dual fuel engines started to be used in the merchant ships. However, the researchers rarely reported such internal processes, due to their complicated physics and the limitations of the apparatuses. CFD method is suitable for the understanding in depth of the operating processes and the engine components design in large two-stroke dual fuel engines, as well as two-stroke diesel engines.
- With respect to the HPDI dual fuel marine engine, limited studies involving the parametric investigation of the operating processes by CFD or the experiment can be found, especially concerning the geometry of the gas injector.

- The composition of the natural gas includes the methane, ethane, propane and a slight amount of nitrogen and sulphur, etc. The natural gas properties remarkably affect the injection, combustion and pollutant emissions. Apart from the experiments conducted by McTaggart-Cowan [62], limited research about the effects of the natural gas composition has been undertaken. Likewise, the detailed chemical kinetics and the associated combustion performance such as the ignition delay, combustion duration, flame speed and the combustion quality have not been investigated so far.

2.5 Aim & Objectives

The overall objective of the PhD work is to investigate the full-cycle of marine two-stroke dual-fuel engines operating with high pressure gas injection and pilot liquid fuel for initiating combustion as well as to study the engine in-cylinder processes by using Computational Fluid Dynamics (CFD) modelling.

The following specific objectives are set:

- Select the appropriate CFD tools based on the literature review.
- Identify the additional sub-models as well as the CFD model characteristics required for the specific application.
- Develop, customise and validate an appropriate sub-model for representing the high pressure direct gas injection process.
- Develop and validate a sub-model for representing the dual fuel non-premixed combustion process.
- Parametric investigation of the HPGI and combustion processes to define recommended geometric parameters for reducing fuel consumption and pollution emissions.
- Investigate the engine in-cylinder processes in a full cycle and compare the diesel mode and the dual fuel operating mode.
- Analyse the derived results to obtain a better understanding of the influence of the dual fuel non-premixed combustion process on the engine performance parameters and the emissions formation.

2.6 Innovation

The following novel elements are covered in this thesis:

- The conserving-equation sources approach for the HPDI gas injection is developed.
- Modelling the dual fuel diffusion flame model in a two-stroke marine engine is carried out.
- Parametric investigation is conducted by CFD method, including the effects of dual fuel injection angle, duration and orifice number on the engine performance and pollutant emissions.

- Numerically investigate the full-cycle operating processes in a large two-stroke marine engine, both for the dual fuel and normal diesel modes.

2.7 Research Methodology

After the introduction of the dual fuel engine and the literature reviews, the computational tools ANSYS Fluent will be described in the next chapter. Based on the objective of thesis and the limits of the ANSYS Fluent, the new modules will be developed and validated by the existing experiments (Chapter 5), with focus on the high-pressure gas direct injection and the dual fuel non-premixed combustion. Subsequently, the developed and customized CFD tool is used to conduct the parametric investigation of the gas injection parameters on the closed-cycle operating processes in the two-stroke HPDI dual fuel marine engine. Followed by the recommended design sets from the parametric investigation, the full-cycle processes for the dual fuel and diesel modes are compared, including the fuel injection, fuel combustion, exhaust gas blowing down and the scavenging processes. Based on the above investigation, the conclusions are summarized and the further work is proposed.

The research methodology is illustrated in Figure 2.13.

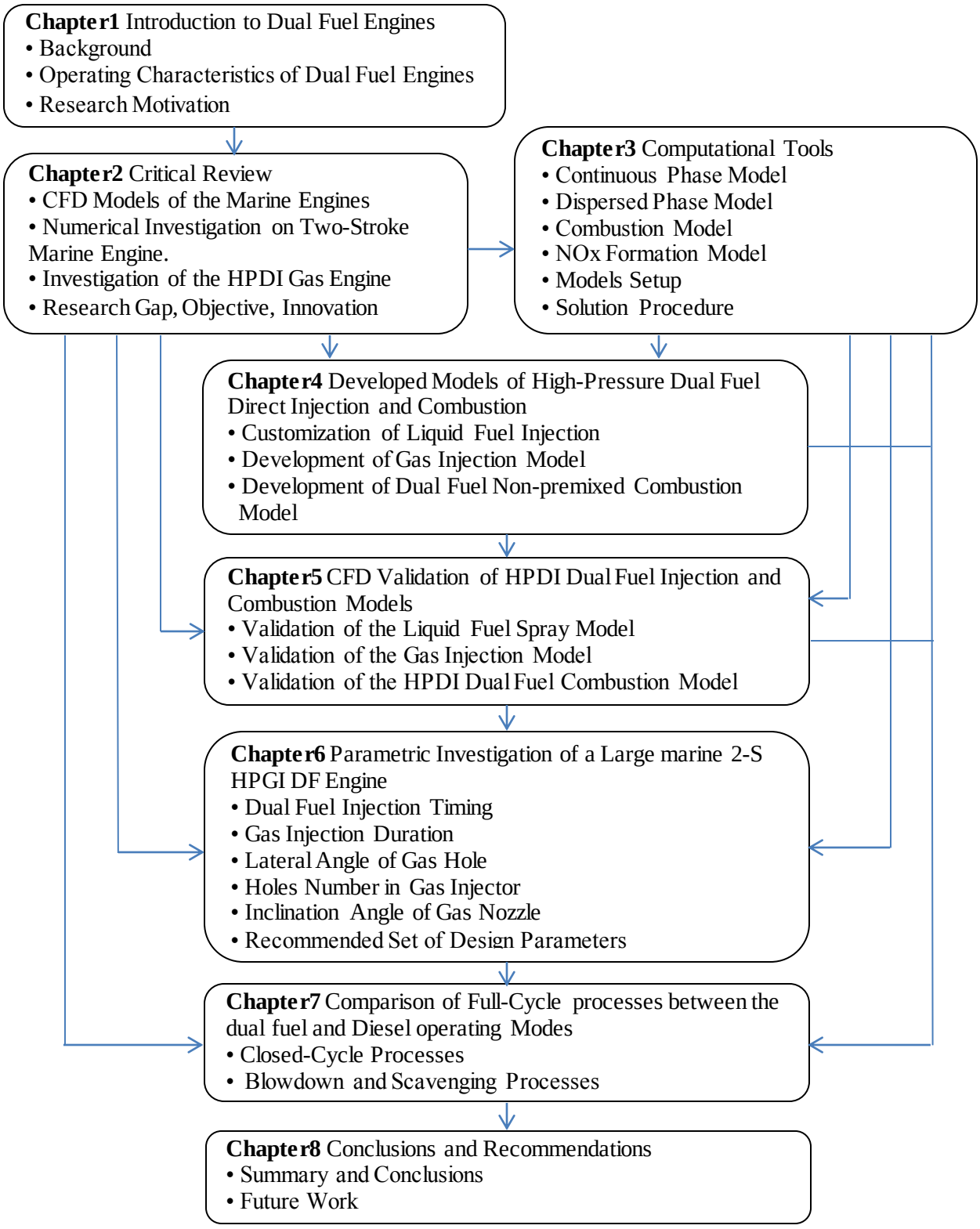

Figure 2.13 Flowchart of the research methodology

Chapter 3 CFD Software

3.1 Introduction of CFD Models

For developing CFD models of the full-cycle operating processes in the HPDI dual fuel engine, four sub-models need to be combined in CFD software ANSYS Fluent. These include the continuous phase model, the dispersed phase model, the combustion model and the NOx Formation. The interrelations between them are illustrated in Figure 3.1.

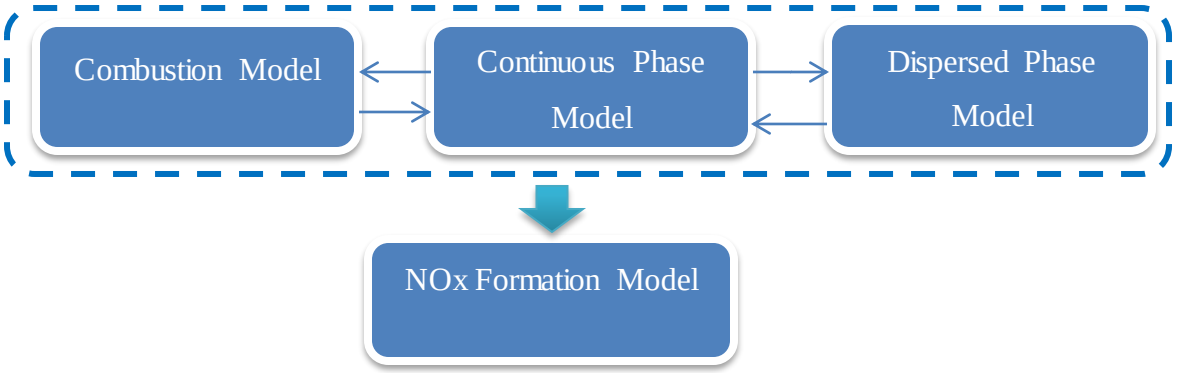

Figure 3.1 the relationship of each sub-model

Due to the high compressibility of the fluid in the high-pressure and high-temperature combustion chamber as well as the high-pressure gas injection, the Favre mean approach [77] is adopted to treat the mean and fluctuated terms of the turbulent flow, where the variables are averaged by using the working medium density, according to the following equation:

$$\frac{1}{\tilde{\rho}} = \frac{1}{\Delta t}\int_{t}^{t+\Delta t}\frac{1}{\rho}dt \tag{3.1}$$

$$\tilde{\varphi} = \frac{1}{\Delta t\tilde{\rho}}\int_{t}^{t+\Delta t}\rho\varphi dt, \tag{3.2}$$

where $\varphi = [1, P, T, H, Z, Y_i, u_i]$ represent the pressure, the temperature, the enthalpy, the mixture fraction, the mass fraction of species and the velocity components in the flow fields in a Cartesian coordinate respectively.

3.2 Continuous Phase Modelling

3.2.1 Continuity Equation

The equation for conservation of mass can be described by the following equation:

$$\frac{\partial\tilde{\rho}}{\partial \mathrm{t}} + \frac{\partial}{\partial x_i}(\tilde{\rho}\tilde{u}_i) = S_m + S_U \tag{3.3}$$

Where, the source term S_m denotes the mass added to the continuous phase from the dispersed droplets due to the fuel vaporization. S_U is the user defined function, which needs to program for the simulation of dual fuel combustion as the mass source of high-pressure injected gas.

3.2.2 Momentum Conservation Equations

The Favre-averaged equations of the momentum conservation in the inertial reference frame are the following:

$$\frac{\partial}{\partial t}(\tilde{\rho}\tilde{u}_i)+\frac{\partial}{\partial x_j}(\tilde{\rho}\tilde{u}_i\tilde{u}_j)=-\frac{\partial \tilde{p}}{\partial x_i}+\frac{\partial}{\partial x_j}\left[\mu\left(\frac{\partial \tilde{u}_i}{\partial x_j}+\frac{\partial \tilde{u}_j}{\partial x_i}-\frac{2}{3}\delta_{ij}\frac{\partial \tilde{u}_l}{\partial x_l}\right)\right]+\frac{\partial}{\partial x_j}\left(-\tilde{\rho}\widetilde{u_i' u_j'}\right)+\tilde{\rho}g_i+F_i+F_U \tag{3.4}$$

where F_i is the external body forces driven by the dispersed phase, and F_U is the user defined function that represents the momentums sources caused by the high-pressure gas injection.

Employing the Boussinesq hypothesis [77], the Reynolds stresses are solved by using the following equation:

$$-\tilde{\rho}\widetilde{u_i' u_j'}=\mu_t\left(\frac{\partial \tilde{u}_i}{\partial x_j}+\frac{\partial \tilde{u}_j}{\partial x_i}\right)-\frac{2}{3}(\tilde{\rho}k+\mu_t\frac{\partial \tilde{u}_k}{\partial x_k})\delta_{ij} \tag{3.5}$$

In order to close these equations, the turbulence model needs to be introduced to calculate the turbulent kinetics k and the corresponding viscosity μ_t.

3.2.3 Turbulence Model

The RNG k-ε turbulence model [78] is applied to compute the turbulent viscosity in equation (3.5),

$$\frac{\partial}{\partial \mathrm{t}}(\tilde{\rho}k)+\frac{\partial}{\partial x_i}(\tilde{\rho}k\tilde{u}_i)=\frac{\partial}{\partial x_j}\left(\alpha_k\mu_t\frac{\partial k}{\partial x_j}\right)+G_k+G_b-\tilde{\rho}\varepsilon-Y_M+S_k \tag{3.6}$$

$$\frac{\partial}{\partial \mathrm{t}}(\tilde{\rho}\varepsilon)+\frac{\partial}{\partial x_i}(\tilde{\rho}\varepsilon\tilde{u}_i)=\frac{\partial}{\partial x_j}\left(\alpha_\varepsilon\mu_t\frac{\partial \varepsilon}{\partial x_j}\right)+C_{1\varepsilon}\frac{\varepsilon}{k}(G_k+C_{3\varepsilon}G_b)-C_{2\varepsilon}\tilde{\rho}\frac{\varepsilon^2}{k}-R_\varepsilon+S_\varepsilon \tag{3.7}$$

$$\mu_t=\tilde{\rho}C_\mu\frac{k^2}{\varepsilon} \tag{3.8}$$

In these equations, G_k represents the turbulent production caused by the mean velocity gradients, which is calculated by using the following equation:

$$G_k=-\rho\,\widetilde{u_i' u_j'}\,\frac{\partial \tilde{u}_j}{\partial x_i}=\mu_t S^2 \tag{3.9}$$

where $S = \sqrt{2S_{ij}S_{ij}}$, and $S_{ij} = \frac{1}{2}(\frac{\tilde{u}_i}{x_j} + \frac{\tilde{u}_j}{x_i})$.

G_b is the generation of turbulent kinetic energy due to buoyancy, which is calculated by:

$$G_b = \beta g_i \frac{\mu_t}{Pr_t}\frac{\partial \tilde{T}}{\partial x_i} \tag{3.10}$$

where $Pr_t = 1/\alpha$, and α is determined by:

$$\left|\frac{\alpha - 1.3929}{\alpha_0 - 1.3929}\right|^{0.6321} + \left|\frac{\alpha + 2.3929}{\alpha_0 + 2.3929}\right|^{0.3679} = \frac{\mu_{mol}}{\mu_{eff}} \ll 1 \text{ with } \alpha_0 = k/\mu C_p \tag{3.11}$$

Y_M denotes the contribution of the fluctuating dilatation in compressible turbulence to the overall dissipation rate, and it is given by the following equation:

$$Y_M = 2\tilde{\rho}\varepsilon M_t^2 \tag{3.12}$$

The turbulent Mach number is defined as:

$$M_t = \sqrt{k/a_S^2} \tag{3.13}$$

where a_S is the sound speed, calculated by ideal gas formula:

$$a_S = \sqrt{\gamma R\tilde{T}} \tag{3.14}$$

R_ε in equation (3.7) is given by the following equation:

$$R_\varepsilon = \frac{C_\mu \rho \eta^3 (1 - \eta/\eta_0)}{1 + \beta\eta^3}\frac{\varepsilon^2}{k} \tag{3.15}$$

where $\eta = Sk/\varepsilon$.

The turbulent source terms $S_k$and S_ε of the turbulence equations (3.6) and (3.7) will be specified in the gas injection process, considering the turbulence induced by the gas injection near the nozzle exit.

3.2.4 Energy Equation

Due to the strongly compressible flow coupling the rapid chemical process and heat transfer through the cylinder wall, the energy equation must be introduced to calculate the mean in-cylinder temperature. As the non-premixed combustion model is employed, the total enthalpy *H* replacing the internal energy of the mixture is calculated, based on the energy conservation, according the following equation:

$$\frac{\partial}{\partial t}(\tilde{\rho}\tilde{H}) + \frac{\partial}{\partial x_i}(\tilde{\rho}\tilde{u}_i\tilde{H}) = \frac{\partial}{\partial x_i}\left(\frac{k_t}{C_p}\frac{\partial \tilde{H}}{\partial x_i}\right) + S_h \tag{3.16}$$

where the mean total enthalpy $\widetilde{H}$ is defined by:

$$\widetilde{H} = \sum \tilde{Y}_j \widetilde{H}_j = \sum \tilde{Y}_j \left[\int_{T_{ref,j}}^{\tilde{T}} C_{p,j} dT + h_j^0 (T_{ref,j}) \right] \tag{3.17}$$

where $\tilde{Y}_j$ denotes the mean mass fraction of species j, and $C_{p,j}$ is the specific heat ratio of species j at a constant pressure.

Because of the enthalpy of formation $h_j^0(T_{ref,j})$ of species j at the reference temperature $T_{ref,j}$ involved in the total enthalpy, the energy equation does not need to include the energy source term caused by the fuel burning.

S_h is the user defined source terms of the total enthalpy, which can be designated by the ignition source or the gas injection source as the required for CFD simulation of the dual fuel engines.

3.2.5 Species Transport Equation

To comply with the conservation for chemical species, the general species transport can be derived by the following equation:

$$\frac{\partial}{\partial t}(\tilde{\rho}\tilde{Y}_i) + \nabla \cdot (\tilde{\rho}\vec{\tilde{u}}\tilde{Y}_i) = -\nabla \cdot \vec{J}_i + R_i + S_i + S_{YU} \tag{3.18}$$

where Y_i is the local mass fraction of species i, R_i is the net rate of production of species i due to the chemical reaction and S_i is the evaporation rate from the dispersed phase such as the piloted fuel.The user defined source S_{YU} should be included in the species transport, such as the injected gas.

Considering the turbulent flow in the cylinder, the mass diffusion of each species $\vec{J}_i$ is calculated by the following equation:

$$\vec{J}_i = -\left(\tilde{\rho} D_{i,m} + \frac{\mu_t}{Sc_t}\right) \nabla \tilde{Y}_i - D_{T,i} \frac{\nabla \tilde{T}}{\tilde{T}} \tag{3.19}$$

where $D_{i,m}$ denotes the mass diffusion coefficient for species i in the mixture, which can be defined in the material properties. Thermal diffusion coefficient $D_{T,i}$also needs to set in the material properties. Other parameters include the turbulent viscosity μ_t and turbulent Schmidt number Sc_t, both of which are equal to 0.7 in ANSYS Fluent.

3.2.6 Peng-Robinson Equation of Gas State

The equation of state (EOS) in the air mixture is adopted to describe the interaction of the pressure, temperature and volume under the equilibrium state. When the working conditions of the mixture reach the supercritical state, the real gas EOS is regarded as the preferable model, such as Peng-Robinson EOS [79]. Regarding the internal processes taking place in the cylinder of a large 2-stroke

marine engine, the in-cylinder temperature and pressure are far from the fuel critical point. Jin [80] demonstrated that the Peng-Robinson EOS is suitable for the marine diesel engine CFD simulation.

The following equation is proposed:

$$P = \frac{RT}{V-b} - \frac{a(T)}{V(V+b)+b(V-b)} \tag{3.20}$$

The parameter a and b can be calculated by using the mixture composition:

$$a = \sum_{i=1}^{N}\sum_{j=1}^{N} X_i X_j \sqrt{a_i a_j} \tag{3.21}$$

$$b = \sum_{i=1}^{N} X_i b_i \tag{3.22}$$

where X_i is the molar fraction of species i (j) of the mixture with N components.

Each species parameters can be calculated by the following equation:

$$a_i = \left(0.457247\,\frac{R^2 T_{c,i}^2}{P_{c,i}}\right)\left\{1 + (0.37464 + 1.54226\omega_i - 0.26992\,\omega_i^2)\left[1 - \left(\frac{T}{T_{c,i}}\right)^{1/2}\right]\right\} \tag{3.23}$$

$$b_i = 0.07780\,\frac{RT_{c,i}}{P_{c,i}} \tag{3.24}$$

where the critical temperature$T_{c,i}$, the critical pressure $P_{c,i}$ and the acentric factor ω_i of the component i are determined by the species properties.

3.3 Dispersed Phase Modelling

This model is employed to represent the processes where the liquid droplets are injected into the engine combustion chamber. The involved processes can be simplified as shown in Figure 3.2.

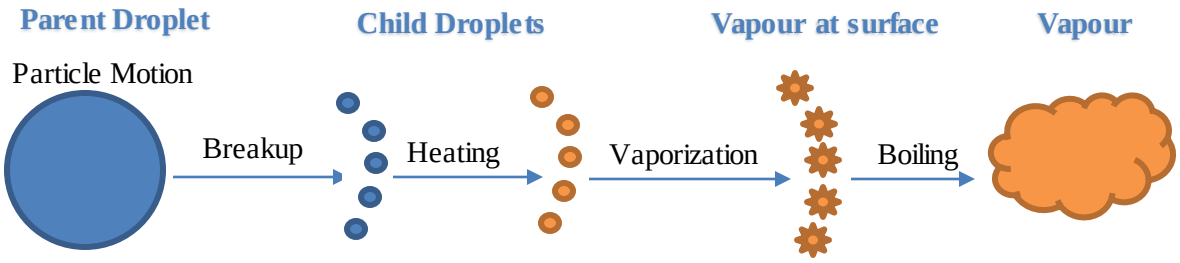

Figure 3.2 The physical evolution of the injected liquid droplet in the cylinder chamber

3.3.1 Droplet Motion Model

The force balance acting on each particle can provide the following equation of particle motion in the inertial reference frame:

$$\frac{\mathrm{d}\vec{u}_P}{\mathrm{d}t} = F_D\left(\vec{\tilde{u}} - \vec{u}_P\right) + \frac{\vec{g}(\rho_P - \tilde{\rho})}{\rho_P} + \vec{F}_{pg} + \vec{F}_{vm} \tag{3.25}$$

Where, the non-dimensional drag force F_D [81] is calculated as follows:

$$F_D = \frac{18\mu}{\rho_P d_P^2}\frac{C_D Re_P}{24} \tag{3.26}$$

The related Reynolds number is defined as:

$$\mathrm{Re}_P = \frac{\tilde{\rho} d_P |\vec{u}_P - \vec{\tilde{u}}|}{\mu} \tag{3.27}$$

where μ is the fluid viscosity of the continuous phase.

C_D is the drag coefficient of the particle, which is calculated by the following equation [82]:

$$C_D = C_{d,sphere}(1 + 2.632y) \tag{3.28}$$

$$C_{d,sphere} = \begin{cases} 0.424, & Re_d > 1000 \\ \frac{24}{Re_P}\left(1 + \frac{1}{6}{Re_P}^{2/3}\right), & Re_d \leq 1000 \end{cases} \tag{3.29}$$

Where, the droplet distortion y is derived by the following equation [83]:

$$\frac{\mathrm{d}^2 y}{\mathrm{d}t^2} = \frac{C_F}{C_b}\frac{\tilde{\rho}}{\rho_P}\frac{|u_P - \tilde{u}|^2}{r^2} - \frac{C_k \sigma_P}{\tilde{\rho} r^3} y - \frac{C_d \mu_P}{\tilde{\rho} r^2}\frac{dy}{dt} \tag{3.30}$$

The constant C_b is equal to 0.5, representing the breakup point where the distortion of the droplet is equal to the radius r of droplet [45]. The parameters C_F, C_k, and C_d are equal to 1/3, 8 and 5 respectively [82]. The surface tension σ_P and viscosity μ_P of the liquid droplets can be derived by using the liquid properties.

Another term in the right side of the equation (3.25) is the additional force $\vec{F}_{pg}$, caused by the pressure gradient in the fluid, which can be calculated by [45]:

$$\vec{F}_{pg} = \frac{\tilde{\rho}}{\rho_P}\vec{u}_P \nabla \vec{\tilde{u}} \tag{3.31}$$

The visual mass force $\vec{F}_{vm}$ arises from the acceleration of the fluid surrounding the droplets, which can be calculated by [45]:

$$\vec{F}_{vm} = C_{vm}\frac{\tilde{\rho}}{\rho_P}\left(\vec{u}_P\nabla\vec{\tilde{u}} - \frac{d\vec{u}_P}{dt}\right) \quad (3.32)$$

The visual mass factor C_{vm} can set at its default value of 0.5 [45].

3.3.2 Droplets Breakup Modelling

The two breakup models will be employed and their performances will be compared for the liquid fuel high-speed injection in the combustion chamber. They are KHRT breakup model and the Stochastic Secondary Droplet (SSD) Model.

3.3.2.1 KHRT Breakup Model

Concerning the high-pressure liquid fuel injected into the combustion chamber, the Kelvin-Helmholtz (KH) breakup mechanism dominates in the liquid core zone, driven by the instability of the disturbed waves along the flow direction on the surface of the liquid droplet. Due to the significant density difference of the injected liquid and surrounding air, the Rayleigh-Taylor (RT) wave also occurs on the liquid surface, which is the other factor resulting in the droplets breakup.

Commercial Software ANSYS Fluent [45] provides the KHRT breakup model that combines both mechanisms in the high-weber-number liquid sprayed into the freestream conditions. It assumes that the liquid core called "blobs" exists near the nozzle exit. Within the liquid core, the KH breakup model is employed; outside the liquid core, both KH and RT are involved.

(1) Liquid Core Estimation

The illustration of liquid core approximation is shown in Figure 3.3, where the length of liquid core is estimated, using the Levich theory [84] according to the following equation:

$$L = C_L d_0 \sqrt{\frac{\rho_P}{\tilde{\rho}}} \quad (3.33)$$

Where, the default value of Levich constant C_L is 5.7 [45], and the diameter d_0 is the minimum of the initial droplet diameter and inner diameter of the cone-shaped injection.

The blobs size is computed by [15]:

$$D_e = d_0\sqrt{C_a} \quad (3.34)$$

where C_a denotes the contraction coefficient. The half angle shown in Figure 3.3 needs to be set in the droplets injection properties.

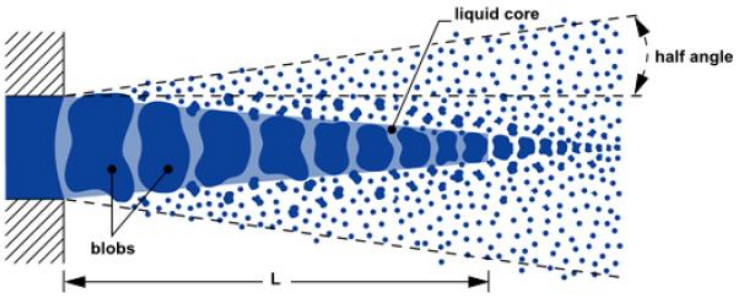

Figure 3.3 Liquid core approximation [45]

(2) KH Breakup Model

In order to estimate the radius of child droplets and the remaining parent droplets, the wavelength Λ_{KH} of the fastest-growing unstable surface wave, the maximum growth rate $\Omega_{KH}$and the breakup time τ_{KH} are calculated by using the following equations [85]:

$$\frac{\Lambda_{KH}}{a_{KH}} = 9.02\frac{(1+0.45Oh^{0.5})(1+0.4Ta^{0.7})}{(1+0.87We_g^{1.67})^{0.6}} \tag{3.35}$$

$$\Omega_{KH}\sqrt{\frac{\rho_P a_{KH}^3}{\sigma_P}} = \frac{(0.34+0.38We_g^{1.5})}{(1+Oh)(1+1.4Ta^{0.6})} \tag{3.36}$$

$$\tau_{KH} = \frac{3.726B_1\, a_{KH}}{\tau_{KH}\Omega_{KH}} \tag{3.37}$$

where a_{KH} is the radius of the parent droplets when the KH wave takes place and B_1 is the breakup time constant determined by the injector characterization.

The other parameters in the two equations are as follows:

$Oh = \sqrt{We_P}/Re_P$: Ohnesorge number;

$Ta = Oh\sqrt{We_g}$: Taylor number;

$We_P = \rho_P\left|\vec{u}_P - \vec{\tilde{u}}\right|^2 a_{KH}/\sigma_P$: Weber number of liquid oil injected;

$We_g = \tilde{\rho}\left|\vec{u}_P - \vec{\tilde{u}}\right|^2 a_{KH}/\sigma_P$: Weber number of the working medium surrounding the parent droplet;

$Re_P = \tilde{\rho}\left|\vec{u}_P - \vec{\tilde{u}}\right| a_{KH}/\mu$: Reynolds number of parent droplet.

(3) RT Breakup Model

The frequency of the fastest growing wave Ω_{RT} and the corresponding wavelength Λ_{RT} induced by RT mechanism on the droplet surface are predicted by the following equations [45]:

$$\wedge_{RT} = 2\pi\, C_{RT}/K_{RT} \tag{3.38}$$

$$\Omega_{RT} = \sqrt{\frac{2[-g_P(\rho_P-\tilde{\rho})]}{3\sqrt{3\sigma_P}(\rho_P+\tilde{\rho})}} \tag{3.39}$$

where g_P is the droplet acceleration along the droplet travelling, and the related wave number K_{RT} can be expressed by [45]:

$$K_{RT} = \sqrt{\frac{-g_P(\rho_P-\tilde{\rho})}{3\sigma_P}} \tag{3.40}$$

The breakup process occurs, when the generation time of RT wave on the droplet surface exceeds the breakup time τ_{RT} derived from the following equation [45]:

$$\tau_{RT} = \frac{C_\tau}{\Omega_{RT}} \tag{3.41}$$

The RT breakup time constant C_τ is set as 0.5, and C_{RT} has a value of 0.1, which are the default value [45].

(4) Droplet Breakup Process

In the liquid core area, the KH breakup mechanism prevails, where the radius of the smaller child droplet is proportional to the KH wave length on the liquid surface [85],

$$r_{KH} = B_0 \wedge_{KH} \tag{3.42}$$

Subsequently, the change rate of the parent droplet radius is provided by the following equation [85]:

$$\frac{da_{KH}}{dt} = -\frac{(a_{KH}-r_{KH})}{\tau_{KH}}, \quad r_{KH} \le a_{KH} \tag{3.43}$$

The constant B_0 is equal to 0.61 which is its default value [45].

Outside the liquid core domain, both mechanisms are considered for breakup. With respect to RT wave formed in the normal direction on the droplet surface, breakup takes place only when the wave generation time is larger than the breakup time τ_{RT}. The newly-formed droplet is created with the radius derived by the following equation [45]:

$$r_{RT} = \pi\, C_{RT}/K_{RT} \tag{3.44}$$

The remaining radius of the parent droplet is calculated by equation (3.43), where KH parameters are substituted by RT parameters.

When the smaller child droplets are formed, their properties involving material, temperature, position and velocity magnitude are the same to the corresponding parents results. Their velocity vectors are

randomly orthogonal to the travel direction of parents. The resulting parents velocities need to be updated by conserving the momentum.

3.3.2.2 Stochastic Secondary Droplet (SSD) Model

Owing to the complexity of the droplets breakup process, the probability of parent droplets breaking into the smaller ones is considered to be independent from the parent droplets size. And the child droplets size is computed by the analytical solutions from the Fokker-Planck equation [16].

The following two parameters namely the critical radius r_C and the breakup time t_{bu} determine whether the secondary breakup occurs [16]:

$$r_C = \frac{We_{cr}\,\sigma_P}{\rho\,|\vec{u}_P - \vec{\tilde{u}}|^2} \tag{3.45}$$

$$t_{bu} = B\sqrt{\frac{\rho_P}{\rho}}\frac{r}{|\vec{u}_P - \vec{\tilde{u}}|} \tag{3.46}$$

where the critical Weber number We_{cr} needs to be specified with its default value of 6, and breakup constant B is recommended to be equal to $\sqrt{1/3}$ [16].

The breakup time can increase corresponding to the droplets which radius is larger than the critical radius r_C in equation (3.45). When the breakup time of the parent droplets exceeds the local critical breakup time t_{bu}, the breakup occurs. At this moment, the new parcels are produced, and the associated parent parcels disappear.

Considering the j^{th} parcels which will breakup in time (t+Δt), the radius distribution function of newly created parcels can be determined, based on the stochastic sampling procedure, according to the following equation [16]:

$$\frac{N(r,t+\Delta t)_j}{N(t+\Delta t)_j} = \frac{1}{2}\left[1 + erf\left(\frac{lnr - lnr_j - \langle\xi\rangle}{\sqrt{2\langle\xi^2\rangle}}\right)\right] \tag{3.47}$$

where $N(t+\Delta t)$ is the total number of breaking droplets, $N(r, t+\Delta t)$ is the number of the droplet radius less than r and r_j is the parent droplets radius.

The model parameter $\langle\xi\rangle$ is equal to 0.1 [16], whereas the corresponding parameter $\langle\xi^2\rangle$ can be calculated by using the following equation [16]:

$$\langle\xi^2\rangle = -\langle\xi\rangle \ln(We_{cr}/We_j) \tag{3.48}$$

where We_j is the Weber number of initial j^{th} parcels calculated by [16]:

$$We_j = \rho_j\left|\vec{u}_j - \vec{\tilde{u}}\right|^2 r_j/\sigma_j \tag{3.49}$$

Complying with the mass conservation, the equation (3.47) can be applied to calculate the radius distribution of the newly-formed parcels, which is independent of their parents' droplets size.

The velocity vector of the new parcel is calculated by the parents' data and a W_{bu}. The direction of this additional velocity W_{bu} is randomly orthogonal to the relative velocity vector $(\vec{u}_j - \vec{\tilde{u}})$ of the parent droplets, whereas its magnitude is proportional to the parent droplets radius and breakup frequency shown below [16]:

$$|W_{bu}| = r_j / t_{bu} \tag{3.50}$$

3.3.3 Inert Heating or Cooling

When the droplet temperature T_P is lower than the vaporization temperature T_{vap}, and the current mass of the particle is also lower than the mass $(1 - f_{v,0})m_{P,0}$ (where $f_{v,0}$ is the volatile fraction), the inert heating or cooling process occurs.

The droplet temperature is derived by using the following equation that is derived by applying the energy balance in the droplet [45]:

$$m_P C_P \frac{dT_P}{dt} = hA_P\left(\tilde{T} - T_P\right) + \varepsilon_P A_P \sigma(\theta_R^4 - T_P^4) \tag{3.51}$$

where $\tilde{T}$ is the local mean temperature of the continuous phase, whereas the convective heat transfer coefficient h is calculated by the following equation [86,87]:

$$Nu = \frac{hd_P}{k_\infty} = 2.0 + 0.6Re_P^{1/2}Pr^{1/3} \tag{3.52}$$

Prandtl number of the continuous phase is defined as:

$$\mathrm{Pr} = C_p\mu / k_\infty \tag{3.53}$$

where k_∞ is thermal conductivity of the continuous phase.

The second term on the right side of the equation (3.51) can be ignored, when the radiation is far less than the convective heat transfer at the droplet surface.

3.3.4 Droplet Vaporization

Droplet vaporization law could be applied to the conditions when the droplet temperature is among the vaporization temperature T_{vap} and boiling temperature T_{bp}, until the droplet volatile fraction is completely consumed. It must be noticed that, once the vaporization starts, it will keep going even when the droplet temperature T_P is below T_{vap}, except for the case where T_P falls below the dew point.

The change rate of the droplet mass m_P is calculated by the following equation [88, 89]:

$$\frac{\mathrm{d}m_P}{\mathrm{dt}} = k_c A_P \tilde{\rho} \ln(1 + B_m) \tag{3.54}$$

where A_P is the surface area of the liquid droplet. The mass transfer coefficient k_c is estimated by using the following Sherwood number correlation [86, 87]:

$$Sh_{AB} = \frac{k_c d_P}{D_{i,m}} = 2.0 + 0.6 Re_P^{1/2} Sc^{1/3} \tag{3.55}$$

The Schmidt number is calculated by:

$$Sc = \mu / \tilde{\rho} D_{i,m} \tag{3.56}$$

The Spalding mass number B_m is expressed by:

$$B_m = \frac{\tilde{Y}_{i,S} - \tilde{Y}_{i,\infty}}{1 - \tilde{Y}_{i,S}} \tag{3.57}$$

where, $\tilde{Y}_{i,S}$ and $\tilde{Y}_{i,\infty}$ represent the vapour mass fraction at the droplet surface and in the bulk gas respectively. $Y_{i,S}$ is determined by saturated vapour pressure P_{sat} at the droplet temperature T_P according to the following equation:

$$\tilde{Y}_{i,S} = \frac{M_{wi} P_{sat}(T_P)}{\tilde{\rho}_s R T_P} \tag{3.58}$$

where M_{wi} and $\tilde{\rho}_s$ are the molecular weight of the vapour and the density in the vicinity of the droplet surface respectively. R is the gas universal gas constant, for the fuel vapour.

When evaporation continues, the latent heat h_{fg} varies as follows:

$$h_{fg} = -\int_{T_P}^{T_{bp}} C_{P,g} dT + h_{f,bp} + \int_{T_P}^{T_{bp}} C_{P,p} dT \tag{3.59}$$

where $C_{P,g}$ and $C_{P,p}$ are the specific heat of gaseous and liquid phase of the vapouring species respectively, and $h_{f,bp}$ is the latent heat at the boiling temperature T_{bp}.

The droplet temperature changes according to the following equation [45]:

$$m_P C_{P,p} \frac{dT_P}{dt} = h A_P \left(\tilde{T} - T_P\right) - \frac{dm_P}{dt} h_{fg} + \varepsilon_P A_P \sigma_P (\theta_R^4 - T_P^4) \tag{3.60}$$

The last term in the right side of the equation (3.60) represents the radiative effects and can be neglected.

The Nu number is adopted to evaluate the convective heat transfer coefficient h [89].

$$Nu = \frac{hd_P}{k_\infty} = \frac{\ln(1+B_m)}{B_m}(2.0 + 0.6Re_P^{1/2}Pr^{1/3}) \quad (3.61)$$

The heat transfer between the droplets and continuous gas phase is also the energy source for the consequent solution of energy equation.

3.3.5 Droplet Boiling

When droplet temperature is greater than the boiling point T_{bp}, the droplet boiling law is employed to calculate the droplet diameter time derivative [90]:

$$\frac{\mathrm{d}(d_P)}{\mathrm{dt}} = \frac{4k_\infty}{\rho_P C_{p,\infty} d_P}(1 + 0.23\sqrt{Re_P})ln\left[1 + \frac{C_{p,\infty}(\tilde{T}-T_P)}{h_{fg}}\right] \quad (3.62)$$

The model requires that continuous phase temperature $\tilde{T}$ exceeds the boiling temperature T_{bp}, where the droplet temperature remains constant and equal to the boiling point T_{bp} during the boiling process. $C_{p,\infty}$ is the heat capacity of the continuous phase mixture.

3.4 Combustion Modelling

After modelling the dispersed phase and continuous phase, the variables in the flow fields can be substituted into the combustion models, as shown in Figure 3.4. In thesis, two non-premixed combustion models including the equilibrium combustion model and the steady Diffusion flamelet model are employed for the modelling of the marine Diesel and HPDI DF engine combustion and their results are compared.

Before the introduction of the combustion models, the mixture fraction and assumed Probability Density Function (PDF) will be described.

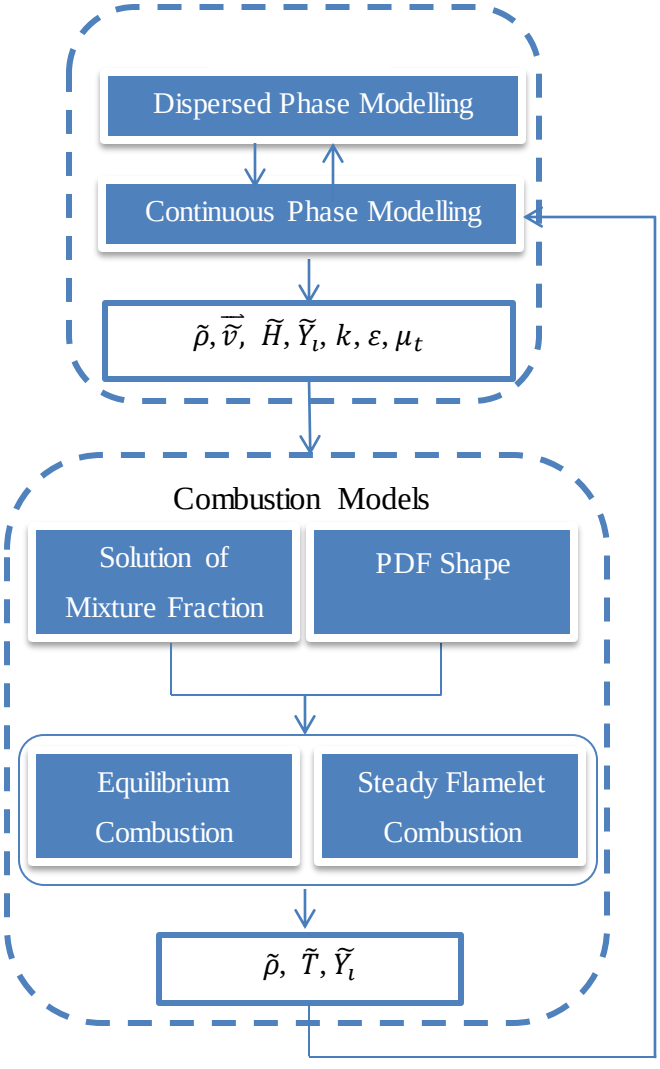

Figure 3.4 Code structure for the combustion modelling

3.4.1 Mixture Fraction Solution

The fuel combustion process can create dozens of products. For N species, the N-1

species transport equations need to be solved, which are substantially time-consuming during the computational iteration. The conserved scalar can overcome this problem, due to its merits of the non-source solution. In other words, the temporal and spacial distributions for each species can directly be determined by the individual boundary conditions, when the conserved scalar is solved.

Mixture fraction known as one of the important conserved scalars is often adopted to simulate the non-premixed combustion to eliminate the complexity of chemistry problems.

In term of the elemental mass fraction, the mixture fraction can be defined as [91]:

$$Z = \frac{Y_i^E - Y_{i,ox}^E}{Y_{i,fuel}^E - Y_{i,ox}^E} \tag{3.63}$$

Where Y^E is the elemental mass fraction. Subscript *i* represents the element *i*, and subscript "ox "and "fuel" denote the mass fraction of element *i* in the oxidizer and fuel injection respectively.

On the hypothesis of the same mass diffusion for each species in engine, the transport equations of Favre-averaged mixture fraction $\tilde{Z}$and its variation $\widetilde{Z^{\prime 2}}$ can be expressed as follows [92]:

$$\frac{\partial}{\partial t}\left(\tilde{\rho}\tilde{Z}\right) + \nabla \cdot \left(\tilde{\rho}\vec{\tilde{v}}\tilde{Z}\right) = \nabla \cdot \left(\frac{\mu_t}{\sigma_t}\nabla\tilde{Z}\right) + S_m + S_{user} \tag{3.64}$$

$$\frac{\partial}{\partial t}\left(\tilde{\rho}\widetilde{Z^{\prime 2}}\right) + \nabla \cdot \left(\tilde{\rho}\vec{\tilde{v}}\widetilde{Z^{\prime 2}}\right) = \nabla \cdot \left(\frac{\mu_t}{\sigma_t}\nabla\widetilde{Z^{\prime 2}}\right) + C_g\mu_t\left(\nabla\widetilde{Z^{\prime 2}}\right) - C_d\tilde{\rho}\frac{\varepsilon}{k}\widetilde{Z^{\prime 2}} + S_{user} \tag{3.65}$$

Due to the conservation of atomic mass, there are no source terms caused by the fuel combustion in equations (3.64) and (3.65). S_m is the source term from the dispersed liquid droplets. S_{user} is defined by user, such as the source of natural gas injection. Other constants include σ_t, C_g and C_d with the default value of 0.85, 2.86 and 2.0 respectively [45].

3.4.2 PDF Shape

It is well known that the laminar combustion is dominated by the chemical kinetics, in which the chemical reaction rate can be computed by the following Arrehenius expression:

$$R_{fuel} = -A\rho^2 Y_{fuel} Y_{ox} e^{-E/RT} \tag{3.66}$$

As regards the turbulent combustion, the key to reasonably calculate the turbulent combustion process is to predict the mean chemical reaction rate. After Favre means the variables ρ, Y_{fuel} , Y_{ox} and T in equation (3.66), the several variations matrix for each variable and the interactions between them will inevitably be formed. Concerning the flow variables, they can be closed by the turbulence model. For the variables related to the combustion, the new method should be introduced to solve this complicated physics involving turbulence, molecular diffusion and chemical kinetics.

The Probability Density Function (PDF) denoted as $P(f)$ is used to solve the interaction between the turbulence and the fuel combustion. In specific, the density-weighted variables representing the flow and combustion also can be integrated by using the PDF shape to calculate the mean and fluctuation caused by turbulence and combustion.

$$\tilde{Z} = \int_0^1 ZP(Z)dZ \tag{3.67}$$

$$\widetilde{Z'^2} = \int_0^1 Z^2 P(Z)dZ - \tilde{Z}^2 \tag{3.68}$$

Several PDF shapes had been used to research the turbulence-chemistry interaction, including β-function and truncated Gaussian function. In this thesis, the β-function PDF shape is used to compute the mean and variation of mixture fraction. Therefore, the PDF is calculated according to the following equation:

$$P(Z) = \frac{Z^{\alpha-1}(1-Z)^{\beta-1}}{\int_0^1 Z^{\alpha-1}(1-Z)^{\beta-1}dZ} \tag{3.69}$$

Where,

$$\alpha = \tilde{Z}\left[\frac{\tilde{Z}(1-\tilde{Z})}{\widetilde{Z'^2}} - 1\right] \tag{3.70}$$

$$\beta = (1-\tilde{Z})\left[\frac{\tilde{Z}(1-\tilde{Z})}{\widetilde{Z'^2}} - 1\right] \tag{3.71}$$

3.4.3 Non-Premixed Equilibrium Combustion Model

Due to the effects of the strong convection and diffusion, both the chemical time and spacial scale are smaller than the turbulent (Kolmogorov) micro-scale. It is feasible that most of the non-premixed combustion can be regarded as the infinitely rapid chemistry, namely local equilibrium. Consequently, the chemistry methodology can be simplified significantly due to the elimination of the variables related to the chemical kinetics. The solution process is shown in Figure 3.5.

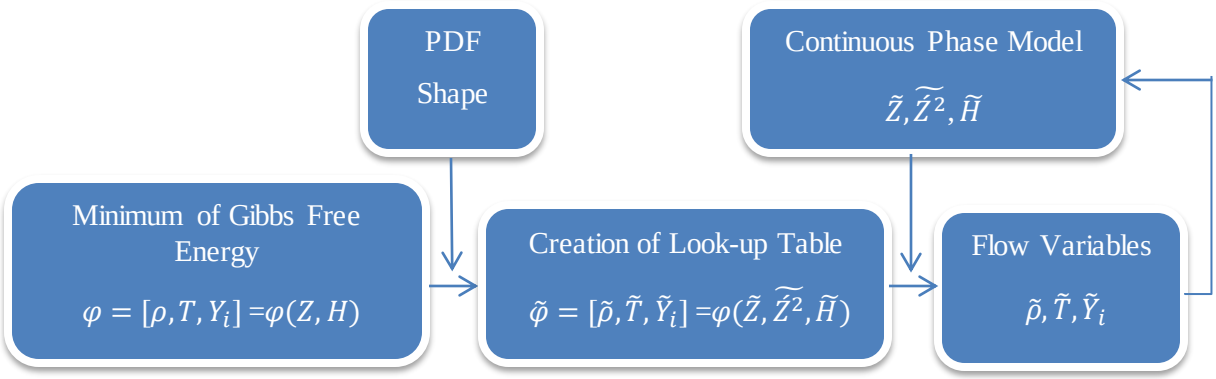

Figure 3.5 Road map for the solution of non-premixed equilibrium model

3.4.3.1 Minimum of Gibbs Free Energy

Under constant pressure and temperature, the chemical reactions occur toward the decrease of the Gibbs free energy of the mixture, as dictated by the second law of thermodynamics. When the Gibbs free energy gets its minimum value, the reaction reaches equilibrium.

The Gibbs free energy G is defined as,

$$G = E + PV - TS \tag{3.72}$$

where $E = E(S, V, n_i)$ is the internal energy; S is the entropy; and n_i is the mole number of species i.

Subsequently, the derivation of the Gibbs free energy G is calculated by:

$$dG = -SdT + VdP + \sum_{i=1}^{N} \mu_i dn_i \tag{3.73}$$

Where,

$\mu_i = \frac{\partial G}{\partial n_i}\Big|_{S,V,n_{i\neq j}}$ denotes the chemical potentials of species i.

At equilibrium, the Gibbs free energy G reaches its minimum, which means that the RHS of equation (3.73) is equal to zero.

Assuming the constant temperature and pressure at each time step, the last term in the right side of the equation (3.73) is equal to zero.

$$\sum_{i=1}^{N} \mu_i dn_i = 0 \tag{3.74}$$

The corresponding chemical reaction is as follows:

$$\sum_{i=1}^{N} \nu_i' \mathcal{M}_i \overrightarrow{\leftarrow} \sum_{i=1}^{N} \nu_i'' \mathcal{M}_i \tag{3.75}$$

where ν_i'' is the stoichiometric coefficient for product i; ν_i' is the stoichiometric coefficient for reactant i; $\mathcal{M}_i$ denotes species i.

Combining the chemical equation (3.75), the mass conservation provides the following equation:

$$\frac{dn_i}{(\nu_i''-\nu_i')} = \frac{dn_j}{(\nu_j''-\nu_j')} \tag{3.76}$$

In term of the EOS of the ideal gas and the partial pressure law, substituting equation (3.76) to (3.74), the equation for calculating the temperature of the mixture is as follows,

$$\prod_{i=1}^{N}(C_i)^{\nu_i''-\nu_i'} = e^{-\sum_{i=1}^{N}(\nu_i''-\nu_i')\mu_i^0/RT}\left(\frac{P^0}{RT}\right)^{\sum_{i=1}^{N}(\nu_i''-\nu_i')} \tag{3.77}$$

where C_i=n_i/V is the mole concentration of species i; P^0 is equal to 1atm; and μ_i^0 is the Gibbs free energy of pure species i under the standard atmosphere P^0 and temperature T.

The calculation procedure of Gibbs free energy at equilibrium state is shown in Figure 3.6.

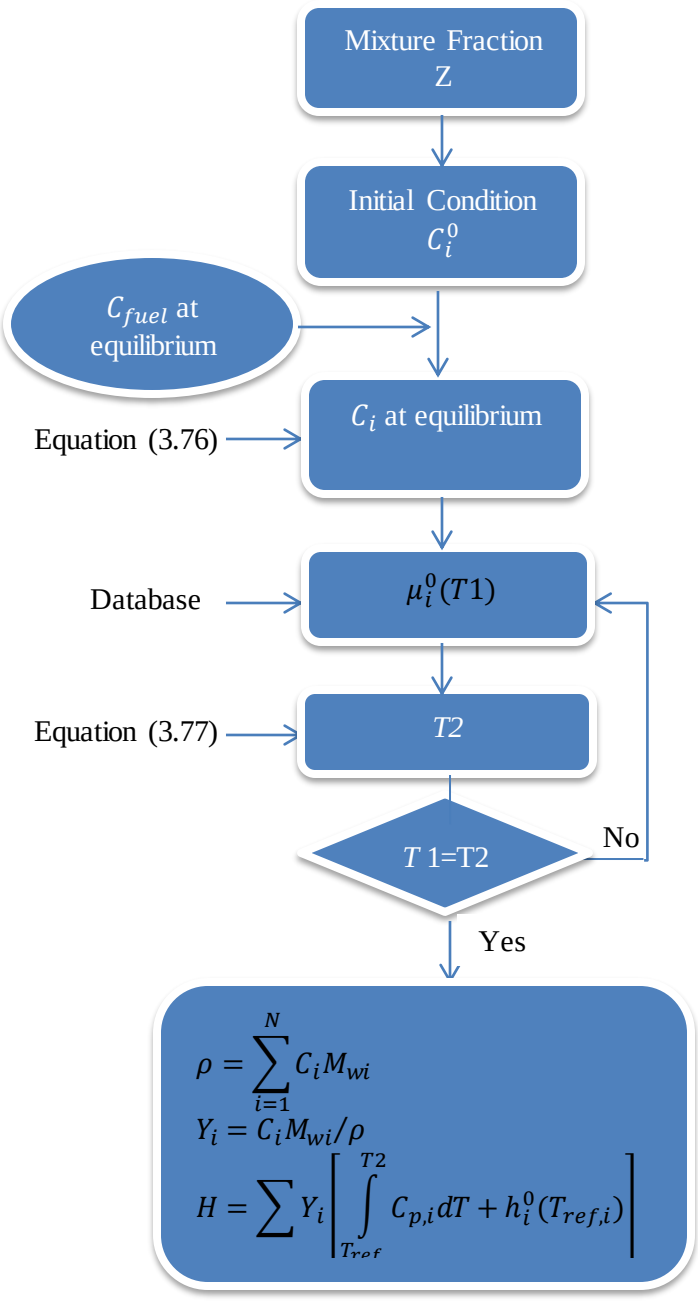

Figure 3.6 Flowchart for the calculation of Gibbs free energy at equilibrium state

As inputting the variable mixture fraction Z and the remaining mole concentration C_{fuel} at equilibrium, the relationship between the density ρ, mass fraction Y_i of species i, temperature T and mixture fraction Z, total enthalpy H can be tabulated.

3.4.3.2 Creation of Look-up Table

In such non-adiabatic reacting system, the PDF shape is the function of the mixture fraction Z and total enthalpy H. Assuming that these two variables are independent, the joint PDF can be separated by using the following equation:

$$P(Z,H) = P(Z)P(H) \tag{3.78}$$

In a diesel engine, the heat loss due to the heat transferring through the combustion chamber walls has limited effects on the fluctuation of the turbulent enthalpy, which is ignored in the total enthalpy ($H \approx \widetilde{H}$). Then, the equation (3.78) is simplified as follows:

$$P\left(Z,\widetilde{H}\right) = P(Z) \tag{3.79}$$

Integrating the results from the laminar chemical kinetics at equilibrium (Session 3.4.3.1), the mean density $\tilde{\rho}$, the temperature $\tilde{T}$ and the mass fraction $\tilde{Y}_i$ of species i are computed by the following equations:

$$\frac{1}{\tilde{\rho}} = \int_0^1 \frac{1}{\rho} P(Z)\, dZ \tag{3.80}$$

$$\tilde{Y}_i = \frac{1}{\tilde{\rho}} \int_0^1 \rho\, Y_i(Z,\widetilde{H}) P(Z) dZ \tag{3.81}$$

$$\tilde{T} = \frac{1}{\tilde{\rho}} \int_0^1 \rho\, T(Z,\widetilde{H}) P(Z) dZ \tag{3.82}$$

The mean mixture fraction $\tilde{Z}$ and the variation $\widetilde{Z''^2}$ for the PDF shape $P(f)$ in equation (3.69) are estimated by using equations (3.67) and (3.68).

All these data at equilibrium are tabulated as a function of $\tilde{Z}$, $\widetilde{Z''^2}$ and $\widetilde{H}$, based on the minimum of Gibbs free energy. Interpolation is employed by using $\tilde{Z}$, $\widetilde{Z''^2}$ and $\widetilde{H}$ calculated by the CFD code, to estimate the variables including mean density, temperature and species mass fraction which are provided input to the CFD Code, as shown in Figure 3.5. This iteration between the CFD and the tabulation works until the CFD results reach the convergence.

Due to the calculation of look-up table in advance and the avoidance of the complicated chemistry calculation, this method can substantially reduce the computational expense. It is effectively used to the fast combustion process.

3.4.4 Steady Diffusion Flamelet Model

The concept of the laminar flamelet was introduced by William [93], and further developed by Peters [19] who applied this concept to the turbulent combustion. Generally, the reaction rate in the diffusion combustion is very fast, whilst it is not infinitely fast, which means that a thin reaction layer is expected. In such scale, the turbulent flame brush can be viewed as the ensemble of the discrete, and the steady turbulent flamelets. Peters [19] reported that the combustion occurs in the vicinity of the stoichiometric flame surface.

By means of the coordinate transformation of the Crocco-type [19], the new coordinate system was introduced, which was fixed on the stoichiometric surface. The mixture fraction Z and the other two coordinates Z_2, Z_3 orthogonal to Z in the Z space are created. The balance equations are the following [45]:

$$\rho\frac{\partial Y_i}{\partial t}=\frac{\rho}{2}\chi\frac{\partial^2 Y_i}{\partial Z^2}+\dot{w}_i-R(Y_i) \tag{3.83}$$

$$\rho\frac{\partial T}{\partial t}=\frac{\rho}{2}\chi\frac{\partial^2 T}{\partial Z^2}-\sum_{i=1}^{n}\frac{h_i}{C_p}\dot{w}_i+\frac{1}{C_p}\left(\frac{\partial P}{\partial t}+q_R\right)-R(T) \tag{3.84}$$

In equations (3.83) and (3.84), the operator *R* involving the derivatives of the transformed coordinates Z_2, Z_3 can be omitted, because it is of the lower order than the other terms due to the thin reaction zone. Subsequently, the species transform equations and conserved energy equation become one-dimension in the mixture fraction Z space.

The new parameter called scalar dissipation rate χ is introduced in the governing equations, which is related to the mixture fraction Z, and is provided by the following equation [45]:

$$\chi=2D|\nabla Z|^2 \tag{3.85}$$

Due to the coordinates transformation, the convective terms in the governing equations disappear. The scalar dissipation rate at stoichiometric position χ_{st} is used to present the flame surface of the diffusive combustion, the inverse of which is characterized as the diffusion time. χ_{st} comes close to zero, implying the combustion approaches to the equilibrium state. Due to the increase of the aerodynamic strain, χ_{st} also increases, which means that the non-equilibrium state should be considered. When χ_{st} exceeds the critical point χ_q where the heat conduction from the reaction zone to both sides exceeds the heat release of the fuel combustion, the diffusion flame is quenched. In summary, the mixture fraction Z and the scalar dissipation rate χ are the fundamental parameters in the flamelet model, which shape the structure and behaviour of the diffusion flame.

The laminar flamelet database employs the counter-flow diffusion flame to express a flamelet in the flow, as illustrated in Figure 3.7. This laminar flame comprises of the opposed, axisymmetric fuel and oxidizer jets, where the mixture fraction at fuel jet and oxidizer jet are equal to 1.0 and 0.0 respectively.

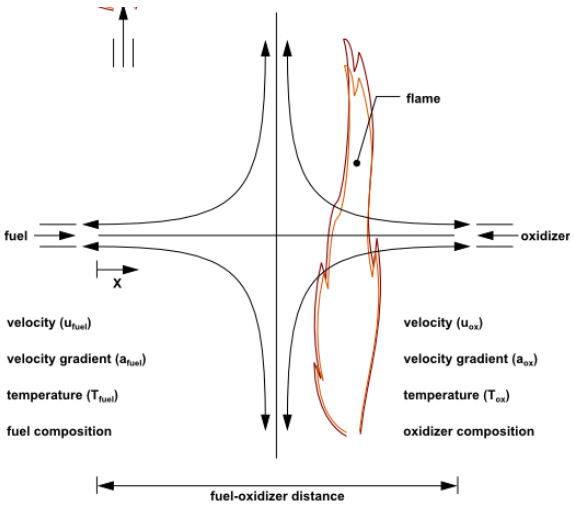

Figure 3.7 The schematic of the counter-flow diffusion flamelet [45]

Integrating by using the PDF shape for the mixture fraction Z and scalar dissipation rate χ in a laminar flamelet, the mean mass fraction of species and temperature in the turbulent flame can be calculated and tabulated against the mean and the variation of the mixture fraction and scalar dissipation rate in CFD code. Then, the following equations are used to calculate the mean species fraction and temperature in the turbulence flame.

$$\tilde{Y}_i = \int_0^{\infty} \int_0^1 Y_i(Z, \chi, \tilde{H}) P(Z) P(\chi) dZ d\chi \tag{3.86}$$

$$\tilde{T} = \int_0^{\infty} \int_0^1 T(Z, \chi, \tilde{H}) P(Z) P(\chi) dZ d\chi \tag{3.87}$$

In equations (3.86) and (3.87), the variation of the total enthalpy is neglected.

With respect to the scalar dissipation rate χ in CFD code, its mean value depends on the turbulent time scale and the variation of the mixture fraction in the diffusion flame, according to the following equation [19]:

$$\tilde{\chi} = C_{\chi} \frac{\varepsilon}{k} \widetilde{Z'^2} \tag{3.88}$$

The fluctuation of the scalar dissipation rate $\widetilde{\chi'^2}$ is ignored, as recommended by Peters [19].

Regarding the scalar dissipation PDF shape, Peters [19] reviewed that the distribution of χ is approximately lognormal, even at relatively low Reynolds number. Therefore, the following equation holds:

$$P(\chi) = \frac{1}{\chi \sigma \sqrt{2\pi}} exp\left[-\frac{1}{2\sigma^2} (ln\chi - \mu) \right] \tag{3.89}$$

Where, the parameters μ and σ can be computed from the first and second moment of χ.

$$\tilde{\chi} = exp\left(\mu + \frac{1}{2}\sigma^2 \right) \tag{3.90}$$

$$\widetilde{\chi'^2} = \widetilde{\chi}^2 [\exp(\sigma^2) - 1] \tag{3.91}$$

The communication between the CFD code and laminar flamelet code is illustrated in Figure 5.8.

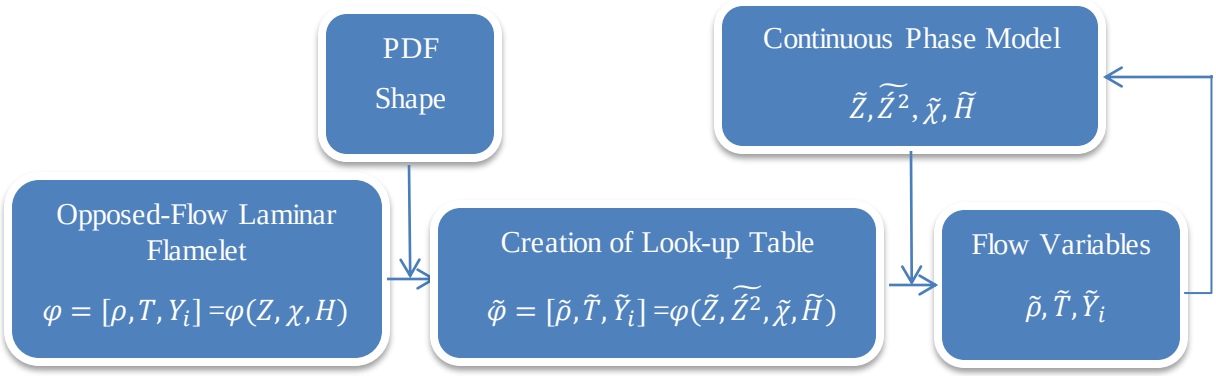

Figure 3.8 Flowchart for the solution of steady diffusion combustion model

3.5 NOx Formation Modelling

NOx formation takes place at a non-equilibrium state, and is strongly affected by the temperature. As the NOx production rate is far lower than the fuel burning rate, the NOx formation generally can be viewed as the post process of the fuel combustion.

NOx emissions mainly consist of the nitric oxide (NO) [45]. In thesis, the two NO mechanisms will be introduced: extended Zeldovich mechanism and NO formation from intermediate N_2O.

3.5.1 NOx Transport Equations

Similar to the species transport, the NOx transport equation involves the unsteady, the convective, the diffusion and the source terms:

$$\frac{\partial}{\partial t}\left(\tilde{\rho}\tilde{Y}_i\right) + \nabla \cdot \left(\tilde{\rho}\vec{\tilde{u}}\tilde{Y}_i\right) = \nabla \cdot \left(\tilde{\rho}\mathcal{D}\nabla\tilde{Y}_i\right) + S_{Y_i} \tag{3.92}$$

where $\tilde{Y}_i$ is the mass fraction of NOx species, including NO and N_2O; $\mathcal{D}$ is the effective diffusion coefficient; and S_{Y_i} is the NOx formation rate, determined by the NOx mechanism.

3.5.2 Extended Zeldovich Mechanism

Considering the phenomena taking place during the combustion process in a diesel engine, the target species amount related to the NOx production is the NO. There are two ways to form this pollutant: by oxidization of N_2 higher than 1800K, and in the fuel-rich zones or near stoichiometric conditions [94].

The following chemical reactions are known as the extended Zeldovich mechanism:

$$O + N_2 \rightleftharpoons N + NO \tag{3.93}$$

$$N + O_2 \rightleftharpoons O + NO \tag{3.94}$$

$$N + OH \rightleftharpoons H + NO \tag{3.95}$$

The source term in equation (3.92) resulted from thermal NO formation is written as:

$$S_{thermal,NO} = M_{w,NO} \frac{d[NO]}{dt} \tag{3.96}$$

where $M_{w,NO}$ is the molecular weight of NO, and the time derivative of NO molar concentration is calculated by the following equation:

$$\frac{d[NO]}{dt} = 2k_{f,1}[O][N_2] \frac{\left(1 - \frac{k_{r,1}k_{r,2}[NO]^2}{k_{f,1}[N_2]k_{f,2}[O_2]}\right)}{\left(1 + \frac{k_{r,1}[NO]}{k_{f,3}[OH] + k_{f,2}[O_2]}\right)} \tag{3.97}$$

In equation (3.97), the constants $k_{f,1}$, $k_{f,2}$, and $k_{f,3}$ are the forward reaction rates in the three chemical reactions respectively, which are calculated by the following equation [95]:

$$k_{f,1} = 1.8 \times 10^8 e^{-38370/\tilde{T}} \tag{3.98}$$

$$k_{f,2} = 1.8 \times 10^4 \tilde{T} e^{-4680/\tilde{T}} \tag{3.99}$$

$$k_{f,3} = 7.1 \times 10^7 e^{-450/\tilde{T}} \tag{3.100}$$

The corresponding reverse rates are provided by Hanson and Salimian [95]:

$$k_{r,1} = 3.8 \times 10^7 e^{-425/\tilde{T}} \tag{3.101}$$

$$k_{r,2} = 3.81 \times 10^3 \tilde{T} e^{-20820/\tilde{T}} \tag{3.102}$$

$$k_{r,3} = 1.71 \times 10^8 e^{-24560/\tilde{T}} \tag{3.103}$$

To solve the equation (3.97), the O radical concentration needs to be estimated. The following equation holds [96]:

$$[O] = 3.97 \times 10^5 \tilde{T}^{-1/2} [O_2]^{1/2} e^{-31090/\tilde{T}} \tag{3.104}$$

Considering the third reaction (3.95) at partial equilibrium, the OH concentration is provided by the following equation [97, 98]:

$$[OH] = 2.129 \times 10^2 \tilde{T}^{-0.57} e^{-4595/\tilde{T}} [O]^{1/2} [H_2O]^{1/2} \tag{3.105}$$

3.5.3 NO Formation from Intermediate N_2O

This mechanism was proposed by Melte and Pratt [94] under elevated pressures and oxygen-rich conditions. It is of a relative importance for the compression ignition engines where the relatively low

temperature partially reduces the NO formation through the Zeldovich mechanism [94]. This mechanism can couple the Zeldovich mechanism.

The mechanism can be divided into two reaction formulas [94]:

$$N_2 + O + M \rightleftharpoons N_2O + M \tag{3.106}$$

$$N_2O + O + M \rightleftharpoons 2NO \tag{3.107}$$

where M represents the third body, leading to the preferable mechanism at an elevated pressure. The O radical is only derived from the dissociation of molecular oxygen at equilibrium [94]:

$$\frac{1}{2}O_2 \rightleftharpoons O \tag{3.108}$$

The rate of NO produced by employing the intermdediate N_2O is calculated by using the following equation [94]:

$$\frac{\mathrm{d}[NO]}{\mathrm{dt}} = 2\left(k_{f,5}[N_2O][O] - k_{r,5}[NO]^2\right) \tag{3.109}$$

Assuming that N_2O is at the quasi-steady state conditions, its concentration can be obtained by [94]:

$$[N_2O] = \frac{k_{f,4}[N_2][O][M] + k_{r,5}[NO]^2}{k_{r,4}[M] + k_{f,5}[O]} \tag{3.110}$$

Where the forward and reverse reaction rate constants are the following [94]:

$$k_{f,4} = 4.44 \times 10^{32}\tilde{T}^{-8.358}e^{-28234/\tilde{T}} \tag{3.111}$$

$$k_{r,4} = 4.00 \times 10^{8}e^{-28234/\tilde{T}} \tag{3.112}$$

$$k_{f,5} = 2.90 \times 10^{7}e^{-11651/\tilde{T}} \tag{3.113}$$

$$k_{r,5} = 1.45 \times 10^{-29}\tilde{T}^{9.259}e^{-11651/\tilde{T}} \tag{3.114}$$

3.6 Models Setup

In the thesis, the ANSYS Fluent will be customized and developed to investigate the large 2-stroke HPDI dual fuel marine engine and diesel engine. The whole CFD procedure includes the pre-processing, the CFD modelling and the post-processing. The function of the pre-processing is to mesh the fluid domains with the compatible boundary conditions; some of the auxiliary surfaces should be also set. Post-processing is used to obtain the calculated parameters to analyse the derived results and draw the conclusions by means of the visualizations, monitors and UDFs (user defined functions). The most complicated part is the CFD modelling, which is used to solve the governing equations at

the given mesh, considering the boundary and initial conditions. Figure 3.9 briefly illustrates the operations for the numerical investigation of the full-cycle internal processes in a dual fuel engine with the high-pressure directly gas injection, where the development of the gas injection model and dual fuel combustion model will be described in Chapter 4 and Chapter 5.

3.6.1 Setup of the Continuous Phase Model

• Initial conditions used to provide the compatible initial flow field parameters for iterations, include the pressure, the temperature, the velocity components, the turbulent kinetic energy and the dissipation rate, the mean and variations of the mixture fraction and the NO mass fraction.

• Boundary conditions determine the non-reaction and non-injection solution, for which the wall conditions, the inlet pressure and the outlet pressure need to be provided.

• Species properties define Thermophysical properties for each species at reference conditions, such as the density, the specific heat ratio, thermal conductivity, the viscosity, the molecular weight, and the parameters associated with the chemical reaction.

• Mixture properties provide the associated chemical equations and thermodynamic formulas in the mixture between the involved species, including the density, specific heat ratio, thermal conductivity, viscosity, and others.

3.6.2 Setup of Dispersed Phase Model

• Droplets Injection parameters include the injection type, fuel type, evaporating species, injection location, injection direction, spray angle, injection velocity and injection flow rate as function of crank angle, as well as the related breakup model and aerodynamics.

• Thermophysical properties of the liquid / pilot fuel include the density, the specific heart capacity, the viscosity, the latent heat, the vaporization temperature, the boiling temperature, the binary diffusivity, the saturation vapour pressure, the droplet surface tension and the vaporization model, all of which were programmed in C++ and then hooked to the main solver by UDF.

3.6.3 Setup of the Combustion Model

• The species and the associated boundaries determine the involved intermediates and their productions in the skeleton chemical mechanism, as well as the mass fractions and temperature of the injected fuel and oxidizer contained in the combustion chamber.

• The chemical kinetics mechanism involves the reactions equations and the reaction rates expressed by using the standard Arrhenius formula when the steady flamelet diffusion model is activated. For the non-premixed combustion of n-heptane, 28 species and 52 chemical reactions [45] are involved,

apart from the inert species nitrogen (N_2), as presented in Appendix A. With respect to the methane combustion, the skeletal mechanism includes 17 species and 58 reactions [99], which are listed in Appendix B.

• Thermophysical properties for each species including the specific heat capacity, the enthalpy and the entropy also need to be imported into the solver, which are expressed as the polynomials varied with the temperature ranging between 273 K and 5000 K, depicted in Appendix C.

• When the steady flamelet diffusion model is activated, the laminar flamelet in the 2D axisymmetric counter-flow diffusion combustion needs to be calculated under different dissipation rate χ.

• With the implementation of the non-premixed equilibrium model, the look-up table of the scalars including the density, the mass fraction of species and the temperature as function of the mean and fluctuation of mixture fraction and total enthalpy is created by means of the minimum Gibbs free energy. For the steady flamelet diffusion model, the look-up table is determined by the laminar flamelet of the 2D counter flow integrated by the β-shape PDF function, in which the relationship between these scalars and the mean and variation of mixture fraction, total enthalpy and dissipation rate is tabulated.

3.6.4 Implementation of Dynamic Mesh

• The layering method is to automatically mesh the fluid domain caused by the piston and exhaust valve moving, where the grid splits and collapses are controlled by the pre-designated split factor and collapse factor respectively.

• The engine parameters determine the piston moving history, where the engine speed, crank period, crank radius, connecting rod length and starting crank angle need to be provided.

• Exhaust valve profile is used to define the exhaust valve position and the related computational domains, which is created and inputed.

• The dynamic zones are defined in the fluid domains with the dynamic mesh and the moving boundaries such as the piston and valve, where not only the motion profiles, but also the grid size in the adjacent zone needs to be defined.

• The auxiliary surfaces must be created during the pre-processing and be compatible with the requirements of the main solver. The two types of the auxiliary surfaces applied to the full-cycle operating processes of the engine, including the “interior” surfaces and “interface” surfaces. The “interior” surfaces are used to control and improve the auto-meshing topology in the dynamic zones. The function of the “interface” is to connect the two computational domains, in which the sharing surface has the different grid distribution for the adjacent zone.

• Auto-adjustment time step is used to change the time step during the critical processes for improvement of CFD stability and convergence, such as the combustion process, the operating process of the exhaust valve open and close, and the scavenging ports open and close.

• NO reaction rates in the NOx formation model are to determine the rate constants in the extended Zelodvich mechanism, which is achieved through UDF programmes.

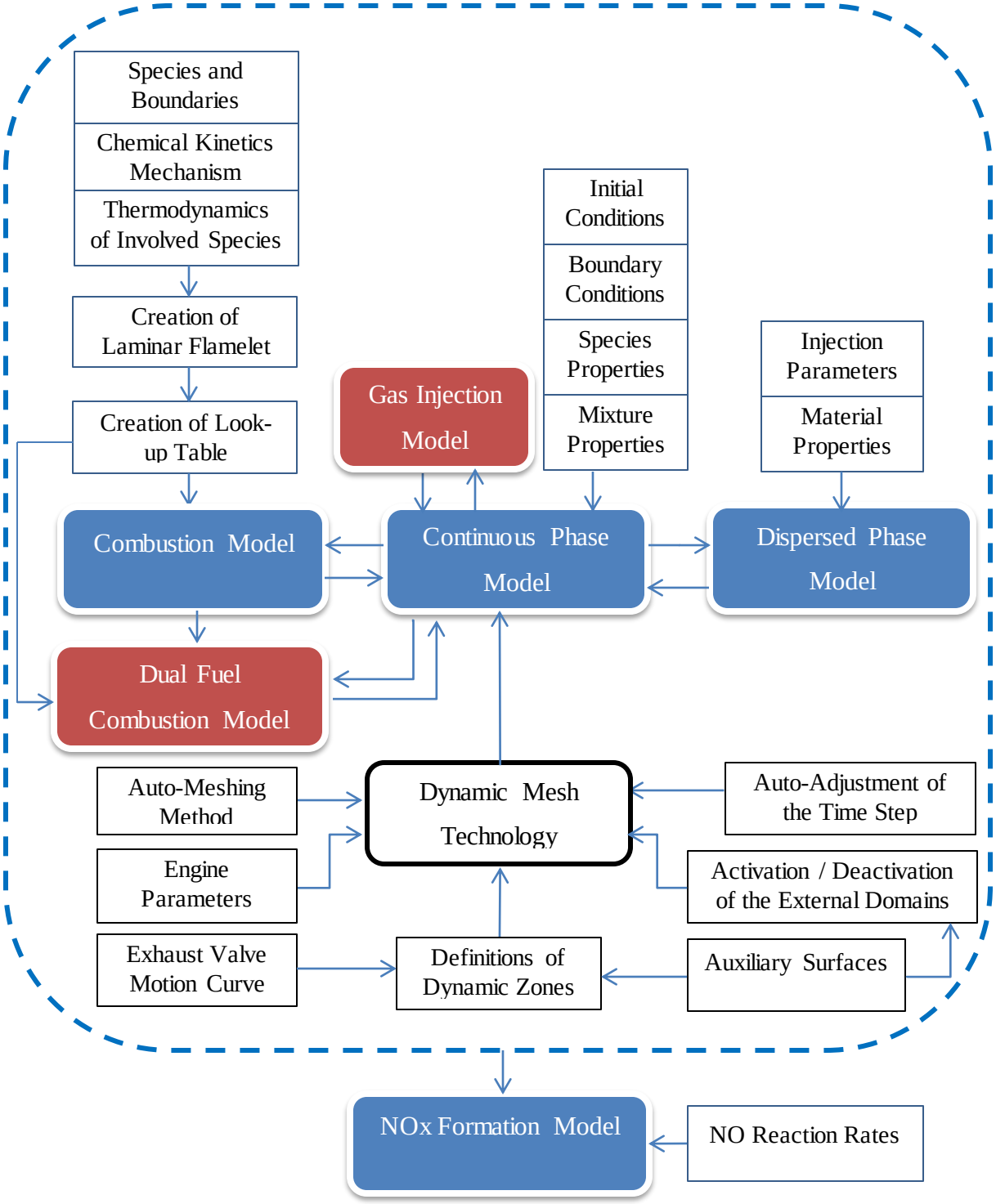

Figure 3.9 Flowcharts of the CFD modelling for the whole-cycle operating processes in dual fuel engine

3.7 Solution Procedure

Once the governing equations and the initial and boundary conditions are established, as well as the related models involved in the simulations of the investigated marine engine, the whole mathematical system of equations can be solved by iteration. Due to the strongly turbulent and compressible flow in the engine chamber, the Favre-averaged N-S equations are employed, which are closed by the RNG k-ε turbulence model. The finite volume method is used to integrate the equations in each cell, in which the mass conservation is automatically complied with. These integrated equations are discretized by the second-order schemes, such as the second-order upwind in the convective terms, the central-differential scheme in the diffusion terms and the second-order implicit scheme in the time derivatives. The pressure-velocity coupling in the discretized equations is solved by the SIMPLE algorithms, embedded with the initial and boundary conditions. In order to improve the stability, compatibility and robustness of the solution, the relaxation factors are introduced. The involved variables in the turbulent flow include the means and variations of the density, the temperature, the pressure, the species mass fraction, the turbulent kinetic energy and the dissipation rate.

Chapter 4 Models Development of High-Pressure Dual Fuel Direct Injection and Combustion

4.1 Introduction

In a 2-stroke high pressure direct gas injection (HPDI) duel fuel marine engine, the pilot fuel is first injected into the combustion chamber and starts burning soon after. Subsequently, a large amount of high-pressure gas is directly injected into the engine chamber and ignited by the pilot fuel. The accurate prediction of the pilot sprays, the gas fuel injection and the associated combustion processes is quite important for the evaluation of dual fuel engine performance and emission parameters. In the chapter, the dual fuel injection and combustion models employed to the HPDI engine will be developed, based on the commercial CFD software ANSYS Fluent.

4.2 Customization of Liquid Fuel Injection

The internal operations in the HPDI engine include the liquid fuel injection process. In this section, the main purpose is to develop and customize the liquid fuel injection model in ANSYS Fluent.

4.2.1 Liquid Fuel Properties

When the fuel combustion takes place in the engine chamber and the piston moves, the environment inside the chamber changes accordingly. The properties of the droplets are varied with the in-cylinder pressure and temperature, due to the heat transfer between the droplets and the surroundings. The properties associated with the droplets breakup processes include the density, the specific heat ratio, the viscosity, the saturation vapour pressure, the latent heat of evaporation, the boiling temperature, the binary diffusion and the droplet surface tension, all of which are evaluated in Appendix D.

4.2.2 Liquid Spray Model

On the basis of the liquid injector characterization, the atomizer model with cone region is used to simulate the initial injection process as the liquid fuel leaves the nozzle exit, illustrated in Figure 4.1. A number of parameters are defined to characterize the initial conditions of the liquid spray, including: injection centre, orifice diameter, spray axis and spray angle, as well as the droplets parameters (droplets diameter, spray velocity and mass flow rate).

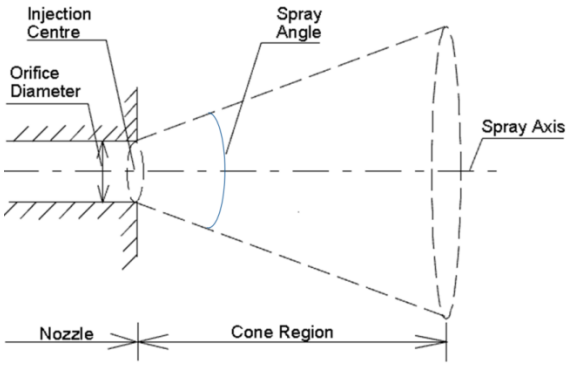

Figure 4.1 The sketch of initial liquid injection

The orifice diameter determines the length of the liquid core by 'blobs' (Figure 3.3) in Levich theory [84], when the liquid breakup model KHRT is employed. The breakup regime in the liquid core is ruled by the Kelvin-Helmholtz waves [100], where the child droplets are shed from this domain. Therefore, this parameter significantly affects the liquid penetration as the KHRT model is adopted.

The injection centre and spray axis indicate the location and direction of liquid sprays. Spray angle is an important parameter affecting the spray process. Wakuri et al. [101] showed that the vapour penetration was considerably affected by spray angle. The spray angle also is closely related to the air entrainment and droplets evaporation [102]. This variable should be calculated in terms of the nozzle geometry and density ratio between the injected liquid and ambient air [17].

The droplet diameter is apparently affected by the nozzle geometry. For the atomizer, the droplet diameter is initialized by the orifice diameter.

The injection rate profiles including the spray velocity U_l and mass flow rate $\dot{m}_l$ are calculated by the Bernoulli equation, accounting for the head loss through orifice.

$$U_l = C_v U_b = C_v \sqrt{2(P_l - P_a)/\rho_l} \tag{4.1}$$

$$\dot{m}_l = C_d A_l \sqrt{2\rho_l (P_l - P_a)} \tag{4.2}$$

Theoretical Bernoulli velocity U_b is defined from the total injection pressure P_l of liquid fuel and the chamber pressure P_a, under the assumption of the incompressible flow in the nozzle.

The relationship of the discharge coefficients characterizing the internal flow losses in the nozzle is expressed by,

$$C_d = C_v C_a \tag{4.3}$$

Where, C_a denotes the area contraction coefficient representing the equivalent area loss caused by the bubbles of cavitation and the non-uniform flow profile at the nozzle exit [103]. The velocity coefficient C_v denotes the velocity loss in the nozzle, which is the ratio of the actual mean velocity to the Bernoulli velocity in the nozzle.

4.2.3 Implementation of Liquid Spray Model

Based on the commercial CFD software ANSYS Fluent, the liquid fuel spray model will be developed and customized.

The liquid spray and breakup models are implemented in the discrete phase module, where the cone-shape droplet injection type is activated and the associated parameters are set accordingly. Due to the

variable liquid spray velocity and injection rate, the related files need to be created and added to the liquid spray model.

As the engine combustion chamber conditions changes with the piston moving, the liquid fuel properties will be varied, shown in Appendix D. These variable parameters cannot be directly set in ANSYS Fluent. As a consequence, the macro can be used to define these variables by using C++, and hooked to the materials of the injected droplet.

4.3 Development of a Gas Injection Model

Simulating the high-pressure gas injection into the engine combustion chamber is a quite challenging task, due to the high compression ratio and the strong interactions between the injection process and gas turbulence within the cylinder, leading to an expansion wave propagating forward the high-pressure side in the gas nozzle and under-expanded sonic flow downstream near the gas nozzle exit. Consequently, a high-pressure gas injection model should be developed for adequately representing the involved phenomena under the feasible grid density, accounting for the pressure loss induced by the expansion wave and the effects of the barrel-shaped shocks pattern in the vicinity of the nozzle exit.

4.3.1 Gas Injection Model

As the gas is directly injected into the engine chamber under high pressure, an under-expanded flow close to the gas nozzle exit will be inevitably generated. In order to precisely capture the barrel-shaped shocks pattern, a number of 15-20 grid points across the orifice are required in the simulation of 2-D axisymmetric high-pressure gas injection as reported by Li [38]. Hajialimohammadi [39] recommended 10 cell layers across the nozzle diameter in the investigation of turbulent free jet by using 2D axisymmetric model. The same grid distribution close to the gas nozzle exit was also reported by Yadollahi and Boroomand [40]. Apparently, such high-density mesh distributed inside the chamber will result in a large quantity of grid nodes, which is extremely time-consuming for the simulation of the 3D gas injection and combustion. In addition, the advanced pilot liquid fuel is required for the dual fuel combustion, which is not compatible for the high-resolution grids due to the limits of the Lagrangian- Eulerian approach. As a consequence, a feasible gas injection model under the relative coarse mesh needs to be developed, considering both the gas fuel and pilot liquid injection process, as well as the dual fuel combustion process.

4.3.1.1 Estimation of Gas Injection Velocity

The transient vortex-ball model developed in Turner [26] has been used by many researchers to estimate the high-pressure gas injection penetration and the corresponding air entrainment [29, 39]. Analytical results showed that the vortex-ball theory overpredicted the gas jet penetration [39].

Hajialimohammadi [29] further indicated that the overprediction was due to the ignorance of pressure drop inside the nozzle caused by the expansion wave propagating upstream Subsequently, the shock tube theory was used by Hajialimohammadi [29] to estimate such pressure drop, and the corresponding effective pressure replacing the stagnation pressure of gas injection to predict the tip penetration.

In this section, the pseudo-diameter concept shown in Figure 4.2 [25] will be employed to estimate the effects of the barrel-shaped pattern on the gas injection. On the hypothesis of the perfect gas, no mixing and the same Mach number in the underexpansion region, the gas velocity U_n at the nozzle exit is the same to the gas velocity U_{ps} at the pseudo-diameter position [25]. The pseudo diameter is calculated by,

$$d_{ps0} = d_n \sqrt{\left(\frac{2}{\gamma_g+1}\right)^{\gamma_g/(\gamma_g-1)} \left(\frac{P_0}{P_a}\right)} \tag{4.4}$$

Where, P_a denotes the chamber pressure, and γ_g is the specific heat ratio of the injected gas.

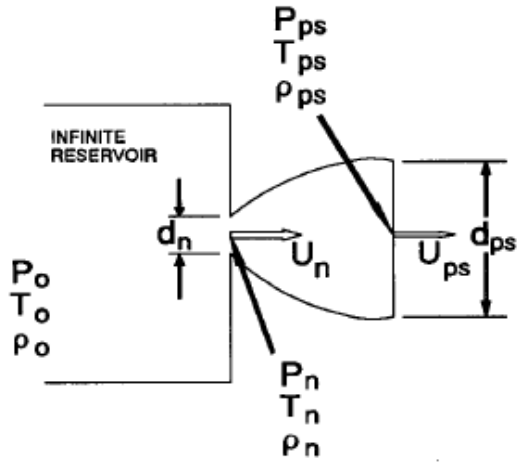

Figure 4.2 Pseudo-diameter concept for underexpansion model [25]

The pressure drop caused by the expansion wave travelling toward the high-pressure side in the nozzle will be estimated by using the shock tube theory, as proposed in Hajialimohammadi [29].

Based on the mass, momentum, energy and the gas state equations of the 1-D compressible flow in the shock tube theory, the gas injection velocity U_g and the pseudo diameter d_{ps} can be estimated by the following equations, in conjunction with the pseudo-diameter concept:

$$U_g = \frac{2\sqrt{\gamma_g R_{mg} T_g}}{\gamma_g-1}\left[1-\left(\frac{P_6}{P_g}\right)^{(\gamma_g-1)/2\gamma_g}\right] = (P_6 - P_\infty)\sqrt{\frac{2}{\rho_\infty\left[\left(\gamma_\infty+1\right)P_6+\left(\gamma_\infty-1\right)P_\infty\right]}} \tag{4.5}$$

$$d_{ps} = d_n\sqrt{\frac{P_6}{P_a}} \tag{4.6}$$

The derivation is detailed in Appendix E.

4.3.1.2 Estimation of Gas Flow Rate

In terms of the compressible flow in the converging-diverging nozzle, when the exit pressure is lower than P_{e3}, the corresponding mass flow rate of gas jet is choked, shown in Figure 4.3. The pressure P_{e3} refers to the point that the Mach number is precisely equal to 1.0 at throat, in front of or behind of which the subsonic flow occurs. The point of 0.528 P_0 is that the high-pressure methane is smoothly injected into the engine chamber without any shocks. The gas injection rate of the chocked flow can be evaluated by the following equation:

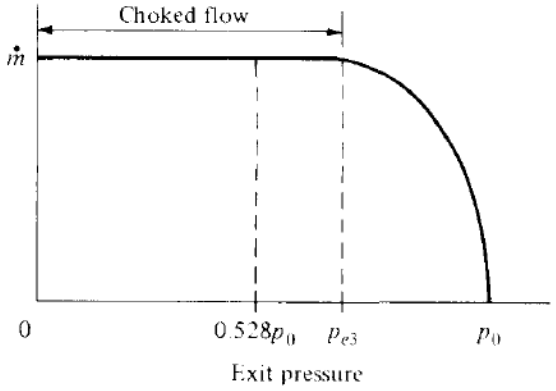

Figure 4.3 Mass flow rate of gas in the nozzle varied with the exit pressure [104]

$$\dot{m}_g = \frac{1}{4}\pi d_n^2 \rho_g \sqrt{\gamma_g R_{mg} T_g}\left(\frac{2}{\gamma_g+1}\right)^{\frac{2\gamma_g-1}{2(\gamma_g-1)}} \tag{4.7}$$

4.3.1.3 Conserving-Equation Sources Approach

The governing equations in CFD code include the mass, momentum, energy and species equations. When the Navier-Strokes equations are averaged, the resulted Reynolds Stresses have to be calculated, which are closed by the turbulence model. In this research, RNG k-ε turbulence model is employed including the transport equations of the turbulent kinetic energy and turbulent dissipation rate. As the non-premixed combustion model is employed, the conserved scalar mixture fraction will be used as the species variable in the transport equation. Considering the same phase of the injected gas with the engine chamber, it is decided that the introduction of the injected gas into the chamber will be carried out through the addition of the source terms in these conserving equations. The parameters transferring between the conserving-equation sources approach for the gas injection and CFD models is illustrated in Figure 4.4 and Table 4.1. Compared to the conventional approaches such as the real gas injector geometry and modification of the boundary condition at the gas nozzle exit, the conserving-equation sources method is very convenient for the parametric investigation of the gas injector, without changing the computational mesh and the boundary conditions.

Before the calculation of the conserving-equation sources, the engine combustion chamber pressure P_a in CFD code needs to be evaluated for the estimation of gas injection velocity, mass flow rate and pseudo diameter, by using the following equation:

$$P_a = \frac{\iiint_\Omega \tilde{\rho}\tilde{P}dV}{\iiint_\Omega \tilde{\rho}dV} \tag{4.8}$$

Where, Ω is the transient volume of the combustion chamber varied with the piston position.

Subsequently, the associated conserving-equation sources can be calculated by using the following equation:

$$S_U = \sum \dot{m}_g / \delta V_g \tag{4.9}$$

$$\vec{F}_U = \sum U_g \dot{m}_g \vec{n}_g / \delta V_g \tag{4.10}$$

$$S_h = \sum \left(\int_{T_{ref}}^{T_g} C_{Pg} dT + h_{0g} \right) \dot{m}_g / \delta V_g \tag{4.11}$$

$$S_Z = \sum \dot{m}_g / \delta V_g \tag{4.12}$$

where, $\vec{n}_g$ denotes the normal direction for each hole of the gas injector, and h_{0g} is the formation enthalpy of the injected gas at the reference temperature T_{ref}. The volume δV_g at nozzle exit is related to the pseudo diameter, and is calculated by using the following equation:

$$\delta V_g = \frac{1}{6} \pi d_{ps}^3 \tag{4.13}$$

According to Choi [30], the sources of turbulence kinetic energy and dissipation rate in the chamber induced by the high-pressure injected gas at nozzle exit are calculated by the following equation:

$$S_k = 1.5 \left(U_g^{'} \right)^2 \rho_{ps} / dt \tag{4.14}$$

$$S_\varepsilon = 0.5 \left[1.5 \left(U_g^{'} \right)^2 \right]^{1.5} \rho_{ps} \Big/ (d_n \cdot dt) \tag{4.15}$$

Where, dt is the current time step in the CFD simulation, the turbulent intensity $U_g^{'}$ is associated with the gas injection velocity U_g, based on the following equation [30]:

$$U_g^{'} = 0.12 U_g \tag{4.16}$$

In addition, the injected gas density ρ_{ps} can be calculated by mass flow rate (equation (4.7)) and gas injection velocity U_g (equation (4.5)), as follows:

$$\rho_{ps} = \rho_g \frac{P_a}{P_6} \frac{\sqrt{\gamma_g R_{mg} T_g}}{U_g} \left(\frac{2}{\gamma_g + 1} \right)^{\frac{2\gamma_g - 1}{2(\gamma_g - 1)}} \tag{4.17}$$

Table 4.1 Parameters transferred in gas injection model

Parameters	Sym.	Unit	Governing Equation Sources
Combustion Chamber Pressure	P_a	Pa	—
Mass Source	S_U	kg/s/m^3	Equation 3.3
Momentum Sources	$\vec{F}_U$	N/m^3	Equation 3.4
Energy Source	S_h	w/m^3	Equation 3.16
Turbulent Kinetic Energy Source	S_k	kg/s^3/m	Equation 3.6
Turbulence Dissipation Rate Source	S_ε	kg/s^4/m	Equation 3.7
Mixture Fraction Source	S_{user}	kg/m^3/s	Equation 3.64

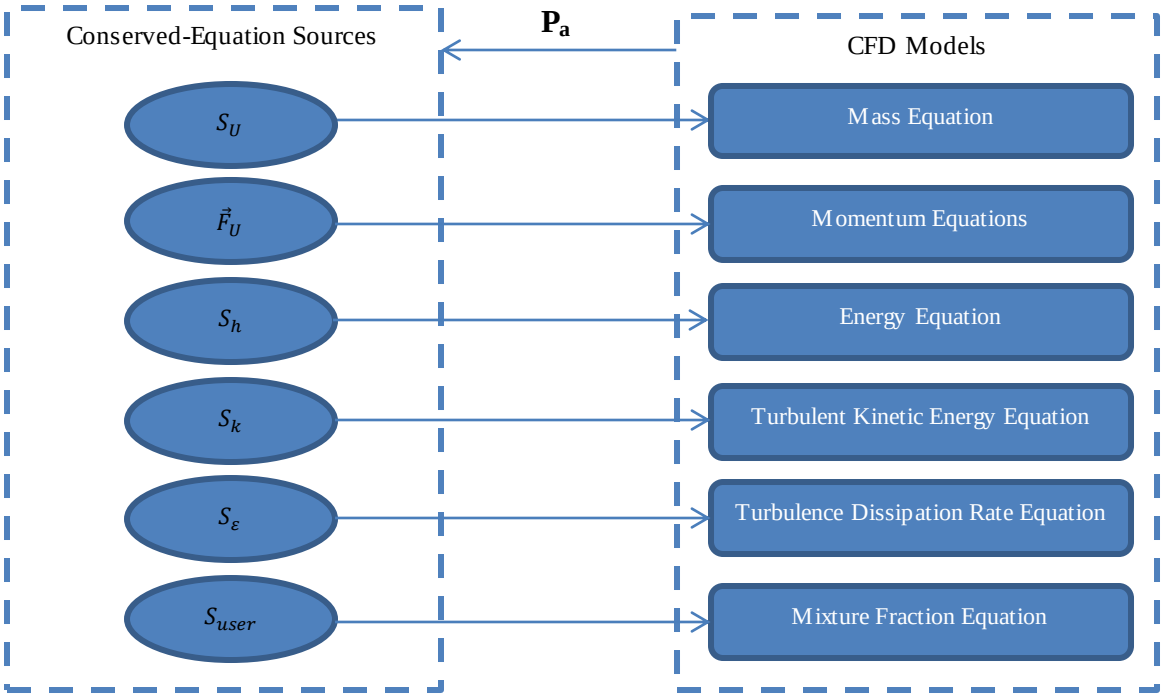

Figure 4.4 The relationship between the gas injection model and CFD models

4.3.2 Implementation of Gas Injection Model

C++ is used to program the conserving-equation sources and hooked to the computational domains in ANSYS Fluent. The macro DEFINE_SOURCE is adopted to define each source in the conserved equations to represent the initial gas injection conditions. Before the additions of the conserving-equation sources, the engine combustion chamber pressure P_a should be calculated, and subsequently the initial gas injection volume, gas injection velocity and the associated gas injection rate are estimated at each iteration by using the macro DEFINE_ADJUST.

4.4 Development of Dual Fuel Non-Premixed Combustion Model

In the non-premixed combustion concept, the fuel and oxidizer streams separately access the combustion chamber. In the presented work, the dual fuel combustion processes are separated to the

following parts: pilot fuel injection, mixing and combustion, and main gas injection, mixing and combustion. Based on the above descriptions, both the pilot fuel combustion and gas combustion are dominated by the non-premixed combustion process.

4.4.1 Pilot Fuel Combustion and Ignition Kernel

4.4.1.1 Pilot Fuel Combustion

Two non-premixed combustion models will be compared, including the equilibrium model and steady diffusion flamelet model, both of which were described in Section 3.4. Both models require the creation of the look-up tables in advance; the equilibrium model is based on the minimum Gibbs free energy and steady flamelet model is in terms of the laminar flamelet in the counter-flow diffusion flame. The β-function PDF-shape (equation 3.69) is used to decouple the turbulence-chemistry interaction. The pure n-heptane will be injected as the pilot fuel, where 28 species are involved in the diffusive combustion. The skeleton chemical kinetics in the laminar flamelet includes 52 chemical reactions, which are listed in Appendix A.

4.4.1.2 Creation of Ignition Kernel

The purpose of the simulation of the pilot fuel combustion is to obtain the information of the ignition kernel, including the location, radius, temperature distribution and the main products, as well as the evaporating heat of pilot fuel.

The function of the pilot fuel is to ignite the gas combustion as an ignition kernel, which can be viewed as a flame ball, as shown in Figure 4.5.

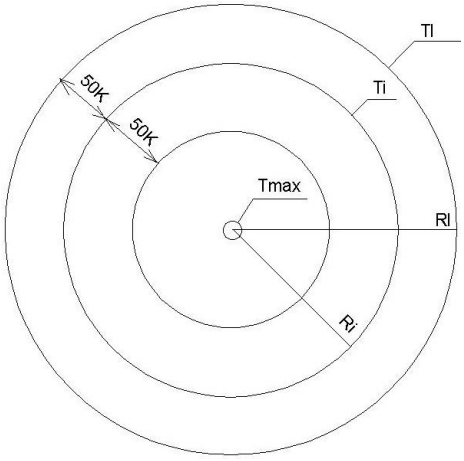

Figure 4.5 Ignition kernel shaped by the spherical flame. Tmax: maximum local temperature in the combustion chamber; Tl: flame-edge temperature; Rl: flame ball radius

By means of the temperature distribution simulated by the pilot fuel combustion, the associated ignition location $\vec{x}_l$, the radius R_i and the temperature distribution $\overline{T}_{ir}$ inside the ignition kernel against crank angle can be estimated, according to the following equations:

$$\vec{x}_l = \frac{\iiint_{T_l}^{T_{max}} \vec{x}\tilde{\rho} dV}{\iiint_{T_l}^{T_{max}} \tilde{\rho} dV} \tag{4.18}$$

$$R_i = \sqrt[3]{\frac{3}{4\pi} \iiint_{T_i}^{T_{max}} dV} \tag{4.19}$$

$$\overline{T}_{ir} = \frac{50}{R_{i+50} - R_i}(r - R_i) + T_i \ , r \in [R_{i+50}, R_i] \tag{4.20}$$

Where, R_{i+50} denotes the combustion-volume radius of the temperature greater than $T_i + 50$ K.

4.4.2 Gaseous Diffusion Combustion

As the high-pressure gas is directly injected into the chamber and subsequently entrained with the combustion chamber working medium (mostly air), the generated combustion kernel caused by the pilot fuel ignites the gaseous fuel mixture. The combustion is dominated by the limited mixing and the diffusion flame. There are two non-premixed combustion models will be applied to simulate such processes, including the equilibrium model [45] and steady diffusion flamelet model [19]. Due to the ignition kernel substituting the pilot fuel, the gaseous combustion can be simulated by the single mixture fraction approach in both two non-premixed combustion models, which considerably reduce the complexity of the applied methodology.

In terms of the location, the radius and the temperature distribution of the ignition kernel derived from the equations (4.18) - (4.20), the energy-equation source caused by the pilot fuel combustion can be estimated by the following equation:

$$S_{ig} = \sum_k Y_k \left[\int_{T_{local}}^{\bar{T}_{ir}} C_{P,k} dT \right] \tag{4.21}$$

Where, Y_k and $C_{P,k}$ are the mass fraction and the corresponding specific heat capacity under constant pressure of the species k in the cells respectively. T_{local} is the local temperature in the region of the ignition kernel.

In addition, the pilot fuel also causes the heat transfer due to the evaporation of its liquid droplet and the products of species CO_2 and H_2O from the combustion of the prepared mixture. This process will be simulated by the liquid spray model, in which the spray velocity, spray angle and material properties are the same to the pilot fuel. The spray flow rate of the species CO_2 and H_2O is calculated by using the following equation:

$$\dot{m}_{Pi} = C_i C_d A_l \rho_l \sqrt{2(P_l - P_a)/\rho_l} \tag{4.22}$$

Where, $\dot{m}_{Pi}$ corresponds to the evaporating species CO_2 and H_2O, respectively. And the proportionality factor C_i can be determined by:

$$C_i = \begin{cases} \frac{1}{1+9m/44n}, for\ CO_2 \\ \frac{1}{1+44n/9m}, for\ H_2O \end{cases} \tag{4.23}$$

Where, n and m denote the atomic number of carbon and hydrogen in the pilot fuel respectively.

Apart from the nitrogen N_2, the 16 species and 58 chemical reactions will be involved in the methane combustion, as reported in Rasmussen et al. [105]. Both combustion models require the creation of the look-up tables before the simulation, in order to reduce the computational cost. In the non-premixed equilibrium model, the mean scalars including the species mass fractions, density and temperature are dependent on the mean mixture fraction and mean enthalpy and the associated fluctuation, which will be tabulated in advance in terms of the minimum Gibbs free energy and β-shaped PDF. In the steady flamelet model, the methane combustion mechanism with 58 chemical reactions (as shown in Appendix B) [99] in the 2D counter-flow laminar flamelet is computed, and then integrated and tabulated by using the β-shaped PDF to achieve the interaction between the combustion and turbulence. Compared to the equilibrium model, the scalar dissipation rate χ is introduced into the look-up table to account for the effects of the flow strain in the steady diffusion flamelet.

4.4.3 Implementation of Dual Fuel Combustion Models

In the presented thesis, the simulation of the pilot fuel and gaseous combustion processes are separated. Before the calculation of the dual fuel combustion, the look-up table should be created. The boundary conditions in the fuel and oxidizer streams are defined. And the involved species and the related thermos-physical properties are hooked to ANSYS Fluent for the non-premixed equilibrium combustion model. With regard to the steady diffusion flamelet model, the fuel combustion mechanism and the species thermos-physical properties need to be added. In conjunction with the β-shaped PDF, the required the look-up table is generated.

When the pilot fuel is injected into the engine combustion chamber, the corresponding combustion occurs. The macro DEFINE_EXECUTE_AT_END is used to monitor the variables of ignition kernel each time step, including the location, the radius and the temperature distribution inside the flame ball. As a consequence, the energy-equation sources are added to the simulation of the gaseous combustion by C++ programing the equation (4.21) in the macro DEFINE_SOURCE. During the introduction of the ignition kernel to the gaseous combustion, pilot spray model is also added in which the evaporating species are the CO_2 and H_2O respectively, and the associated spray velocity and flow rate are the same to the pilot fuel.

4.5 Conclusions

Based on the commercial CFD software, the liquid fuel injection model, the gas injection model and the dual fuel non-premixed combustion model operated in the HPDI engine are developed and customized.

The main innovations are described as follows:

a. For the development and customization of the liquid spray model, the liquid fuel properties varied with the high-pressure and high-temperature environment are modelled, as described in Appendix D.

b. Combining the shock tube theory with the pseudo-diameter concept, the conserved- equation sources approach is developed to simulate the high-pressure gas direct injection into the engine combustion chamber, accounting for the effects of the expansion fan inside the gas nozzle and the barrel-shaped shocks patterns close to the nozzle exit.

c. The dual fuel non-premixed combustion model is developed, considering the ignition kernel, the species additions and the heat loss caused by the advanced pilot fuel combustion and evaporation.

Chapter 5 CFD Validation of HPDI Dual Fuel Injection and Combustion Models

5.1 Introduction

In this chapter, the validation of the CFD models developed in Chapter 4 is conducted, including the liquid fuel injection model, the high-pressure gas injection model and the dual fuel non-premixed combustion model. The grid convergence is studied, where the compatible grid resolution is recommended both for the liquid and gas fuel injection. Thereafter, the liquid/gas tip penetration in two different cubic-shaped chambers is used to validate the liquid sprays and gas injection models respectively, as well as the spatial and temporal distributions of the vapour and temperature in liquid spray process. Based on a suitable grid density, the rapid compression and expansion machine (RCEM) [9] is used to validate the dual fuel combustion model, as well as the extended Zeldovich mechanism.

5.2 Validation of the Liquid Fuel Spray Model

Engine Combustion Network [106] had developed the cubic chamber to perform experiments on the diesel fuel sprays. Several laboratories had also conducted the experimental uncertainties and played the comparison to minimize the experimental errors. In this section, some characterization of the baseline n-heptane sprays experiment is adopted to improve and validate the employed liquid spray model.

5.2.1 Existing Experimental Introduction

The n-heptane sprays experiment was conducted at SANDIA in 1997 [107]. In the experiment, the cubic combustion chamber with the characteristic size of 108 mm was used to validate a previously developed CFD model, with a focus on the liquid fuel penetration, and the spatial and temporal distributions of the vapour concentration and temperature in the chamber.

Figure 5.1 provides the schematic cross-section of the cube-shaped combustion vessel. The one-hole axial injector of 0.1 mm orifice diameter located in the centre of one side of the cubic vessel is used to inject the liquid fuel. The injection pressure difference between the injector hole and the chamber pressure is equal to 150 MPa. The total mass of the injected fuel is 17.8 mg with the injection duration 6.8 ms.

A fan with 8 blades is installed in the normal centre of the vessel top with a distance of 15 mm from the fan bottom to side wall, which functions are to mix the ambient air and keep the temperature uniform at the start of fuel injection. Based on the velocity visualization in the chamber tested by

Sieber [107], the mean swirl velocity induced by the mixing fan was estimated to 0.7 m/s. Considering the magnitude of the working medium velocity in the cubic vessel is far less than the spray velocity, the deflection caused by the working medium velocity on the liquid fuel sprays in the chamber can be neglected.

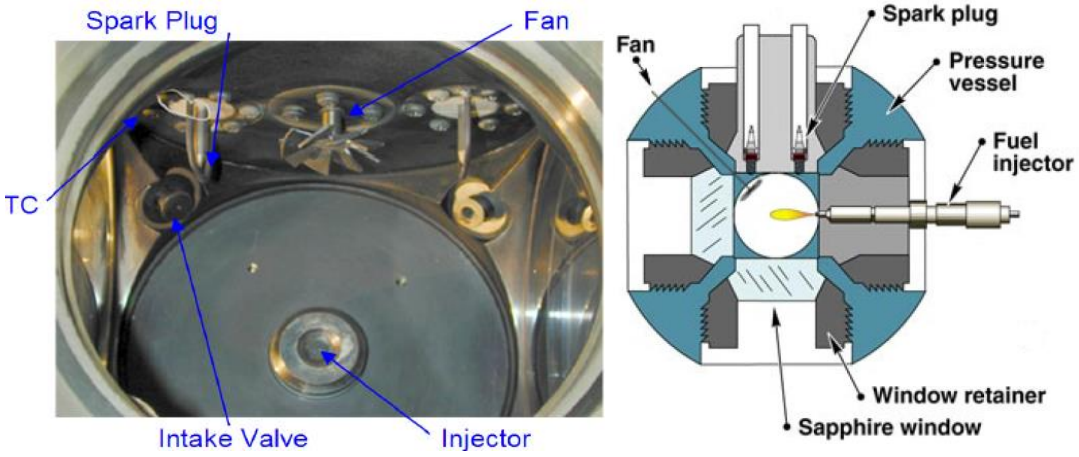

Figure 5.1 Schematic cross section of cube-shaped combustion vessel [106]

The high-pressure and high-temperature environment before fuel injection in the vessel is obtained by the premixed gas mixture combustion. The vessel is first filled by the specified-density gas mixture, which is subsequently ignited by two spark plugs. Consequently, the high-pressure and temperature environment is formed. When the chamber conditions in the vessel meets the experimental requirements resulting from the heat transfer through the vessel walls, the diesel fuel injection starts. Concerning the investigation of liquid fuel (NHPT) sprays, the obtained experimental conditions at the start of injection including the chamber temperature and pressure, as well as the bulk density and mixture composition are listed in Table 5.1.

Table 5.1 Conditions at diesel injection start and reactants composition in the mixture

Parameters		Sym.	Unit	—
Nominal Ambient Temperature		T_N	K	1000K
Nominal Ambient Density		ρ_N	Kg/m^3	14.8
Ambient Compressibility Factor		Z_g	—	1.01
Composition at diesel injection time	O_2	X_{O2}	%	0.0
	N_2	X_{N2}	%	89.71
	CO_2	X_{CO2}	%	6.52
	H_2O	X_{H2O}	%	3.77
Reactants prior to spark ignition	C_2H_2	X_{C2H2}	%	3.20
	H_2	X_{H2}	%	0.50
	O_2	X_{O2}	%	8.25
	N_2	X_{N2}	%	88.05

5.2.2 Liquid Fuel Properties

The liquid fuel NHPT comprised of 100% n-heptane is used to investigate the liquid fuel injection process. The properties related to the liquid fuel breakup and the evaporation include the density, the specific heat ratio, the viscosity, the saturation vapour pressure, the latent heat, the boiling temperature, the binary diffusion and the surface tension. All these parameters are a function of the SANDIA chamber environment, illustrated in Appendix D.

5.2.3 Estimation of the Liquid Fuel Injection Velocity and Injection Rate

By means of the equations (4.1) and (4.2), the liquid fuel injection velocity and mass flow rate in the cubic chamber of SANDIA can be estimated, illustrated in Figure 5.2. When all the parameters in the injector model are calculated at the start of liquid fuel injection time, the DPM model is subsequently activated and the evaporation rate of the fuel is estimated and used in the sources of the mass, momentum, species, energy and mixture fraction equations.

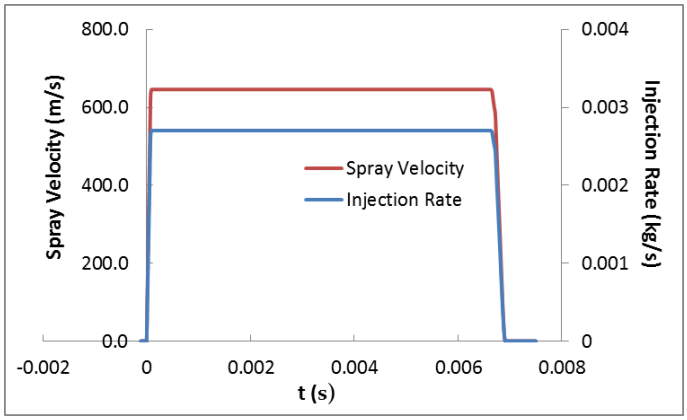

Figure 5.2 Liquid spray velocity and injection rate in the cube-shaped vessel at SANIDA

5.2.4 Validation of the Liquid Spray Model

5.2.4.1 Grid Convergence Study

Before the CFD simulation, the mesh size should be investigated and determined for the diesel fuel sprays. In ANSYS Fluent, the Eulerian-Lagrangian approach is adopted to calculate the interaction between the dispersed phase and continuous phase. In the liquid fuel spray, it is not viable for the mesh refinement as much as possible. One reason is that such an approach has the volume limitations in the cell occupied by the liquid. The higher resolution implies the higher liquid volume fraction in the refined cell, which will violate the hypothesis of the Eulerian-Lagrangian approach [108]. In ANSYS Fluent User Guide [109], the volume fraction of droplet in each cell must be very low, generally less than 10%, in order to ignore the effects of the droplet volume fraction on the continuous gas. Abraham [110] and Beard et al. [111] showed that the high volume fraction also could result in the numerical instabilities. When the stochastic approach is employed to the dispersed phase model

such as the collision model and SSD breakup model, the number of parcels will have to increase as the cell is refined, in order to ensure that the stochastic approach is valid [112]. This causes the rapid increase of the computational cost. Apparently, too coarse resolution also can lead the numerical problems, including the inaccurately local solution, unresolved gradients, artificial diffusion and incorrect turbulent parameters.

Dam [17] numerically investigated the effects of the grid refinement in three directions respectively on the liquid penetration and evolution of the diesel droplets, by using KHRT breakup model in KIVA code. The grid size of 5 times the nozzle diameter was recommended, when the breakup model was not used. As the KHRT breakup is employed, such grid size was marginally small.

With respect to the grid convergence study in the cubic vessel at SANDIA, the three grid resolutions of 4 mm, 1 mm and 0.5 mm were compared by the liquid and vapour penetrations in Jin [88]. Implementing the KHRT breakup and evaporation models, the mesh size of 10 times the nozzle diameter was suggested, compromising the computational cost and the numerical accuracy.

In the present validation, the grid size of 10 times nozzle diameter will be employed to compare the KHRT and SSD breakup models. Figure 5.3 depicts the mesh topology in the cube-shaped SANDIA vessel, where the refined zone of 1 mm grid size shall cover the diffusion region of the fuel vapour and the coarse mesh is used in the domain occupied by the still air.

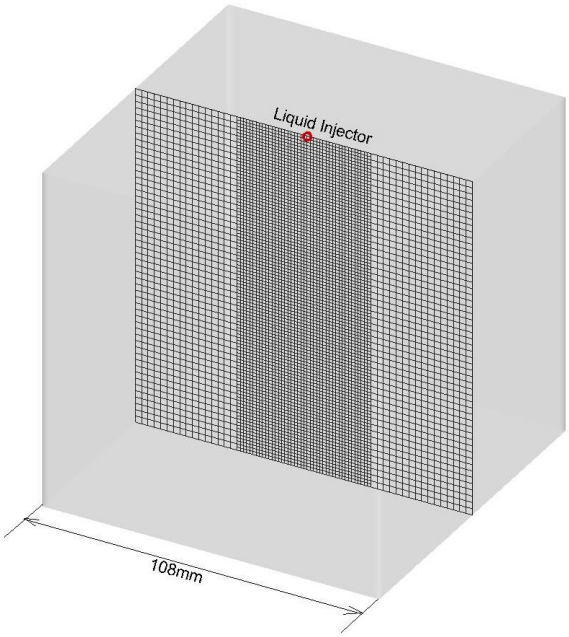

Figure 5.3 Geometry and grid distribution of cubic vessel at SANDIA

5.2.4.2 Validation of Droplet Breakup Model

The liquid spray velocity in the SANDIA chamber is higher than 600 m/s. In such high Weber number liquid spray process, the KHRT and SSD breakup models are recommended [17, 113].

(1) KHRT Breakup Model

Parameter B1 in KHRT as shown in equation (3.37) dominates the breakup time of droplet in the liquid core. ANSYS Fluent [45] recommended that the value of B1 should fall in the range between 1 and 60. B1 equal to 1.73 was recommended by Liu et al. [82], while Nordin [114] set constant B1 to 40. As a consequence, the constant B1values within the range 1.73 – 40 was used to model the injection process in SANDIA chamber. The derived results are shown in Figures 5.4 and 5.5.

Higher B1 values means that the parent droplet needs more time to break up into the children droplets under the same wave length on the droplet surface and wave growth rate, resulting in the larger overall mean diameter of droplets in the liquid core. As a consequence, the liquid penetration for the case where the constant B1 is equal to 40 is longer than that of B1 equal to 1.73. The results in the former case were closer to the experimental results.

Similarly, the higher liquid penetration can also provide a higher vapour penetration, which can be observed by the comparison of the corresponding results. The vapour penetration calculated when B1 is equal to 40 matches better the measurement results, compared with the results of B1 default value (1.73 proposed in ANSYS Fluent).

Figures 5.6 – 5.9 provide the spatial distributions of the mass fraction of fuel vapour and static temperature in the meridian plane at liquid injection time 0.68 ms and 0.90 ms respectively. The comparison of the model results reveal that the primary differences are observed in the vicinity of the nozzle exit and the region of the vapour tip. In the region near the nozzle exit shown in Figure 5.10, shorter breakup time due to the smaller B1 value results in the smaller and more children droplets to be created quickly, where the evaporation rate of droplets rises remarkably, thus leading to droplets temperature reduction. Therefore, the mean diameter of the droplets reduces, causing the reduction of the liquid and vapour penetration.

Compared to the measurements, the case where B1 is equal to 40 can overall obtain the closer results than the case where B1 is equal to 1.73 along the central spray direction, as well as in the transverse sections. Regarding the KHRT model for B1=1.73, apart from the disparity in the region of vapour penetration tip, the asymmetry can be clearly observed, while the experiment shows a approximately symmetric jet deployment (Figure 5.7).

In summary, the breakup constant B1 in KHRT breakup model has a profound effect on the evolution of the injected droplets and the associated vapour, which is determined by the liquid injector characterization. With respect to the SANDIA vessel, B1 equal to 40 is recommended as KHRT breakup model is employed, with comparison to the case of B1=1.73.

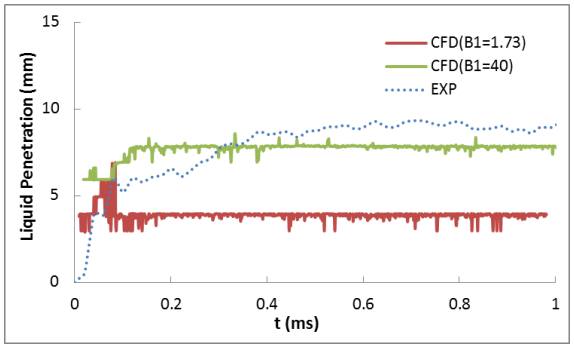

Figure 5.4 Liquid penetration derived from KHRT breakup model in SANDIA chamber

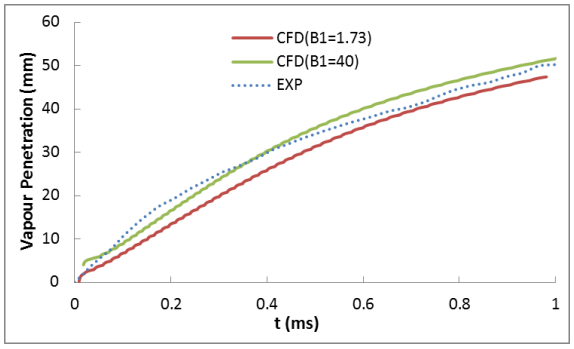

Figure 5.5 Vapour penetration derived from KHRT breakup model in SANDIA chamber

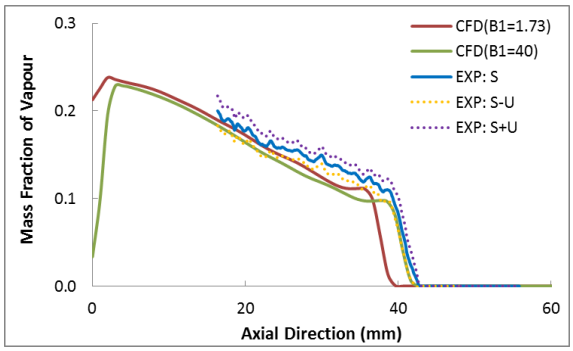

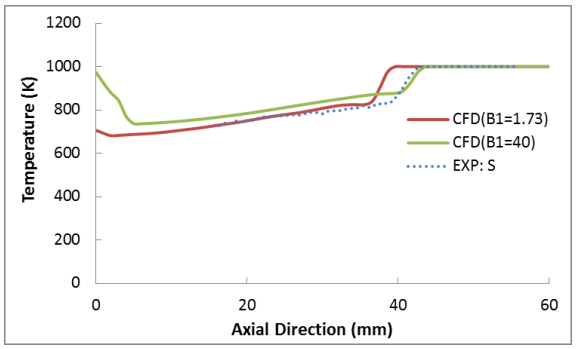

Figure 5.6 Vapour mass fraction and chamber temperature varied along the central line at liquid injection time 0.68 ms. EXP: S – experimental data; EXP: U – experimental uncertainty

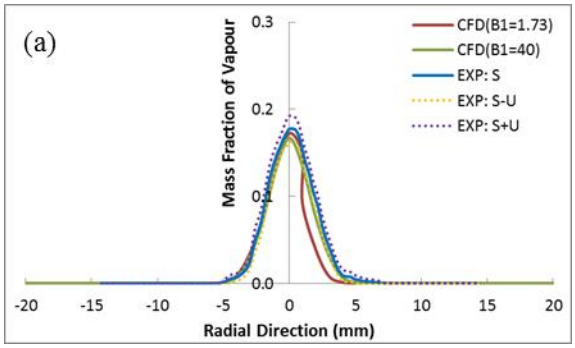

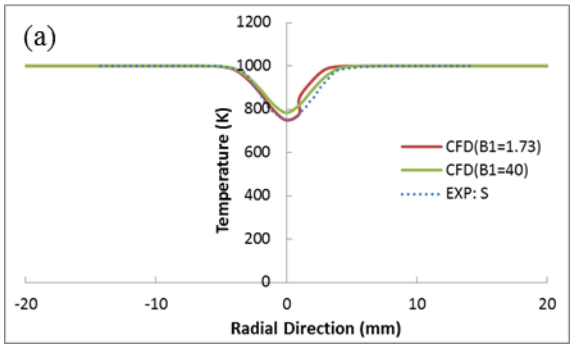

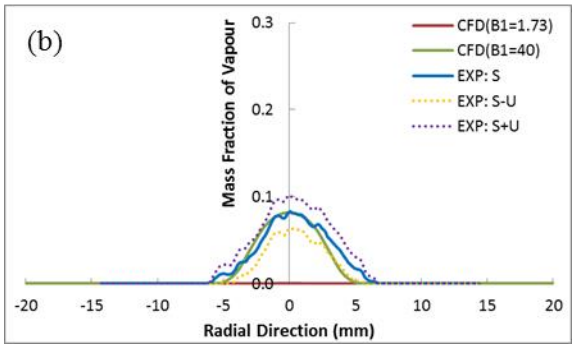

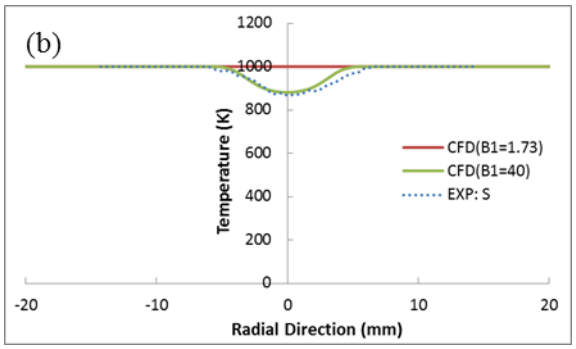

Figure 5.7 The variation of vapour mass fraction and chamber temperature at different cross section at liquid injection time 0.68 ms in the transverse sections z=20mm (a) and z=40mm (b). EXP: S – experimental data; EXP: U – experimental uncertainty.

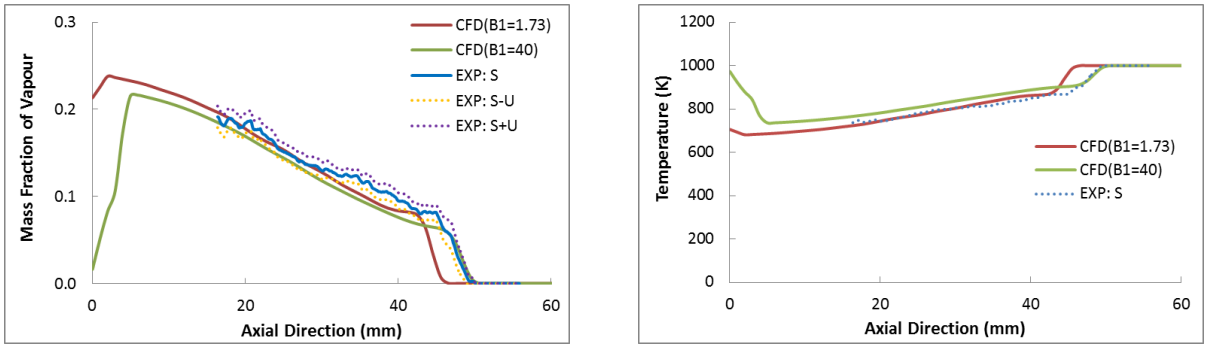

Figure 5.8 Vapour mass fraction and chamber temperature varied along the central line at liquid injection time 0.90 ms. EXP: S – experimental data; EXP: U – experimental uncertainty

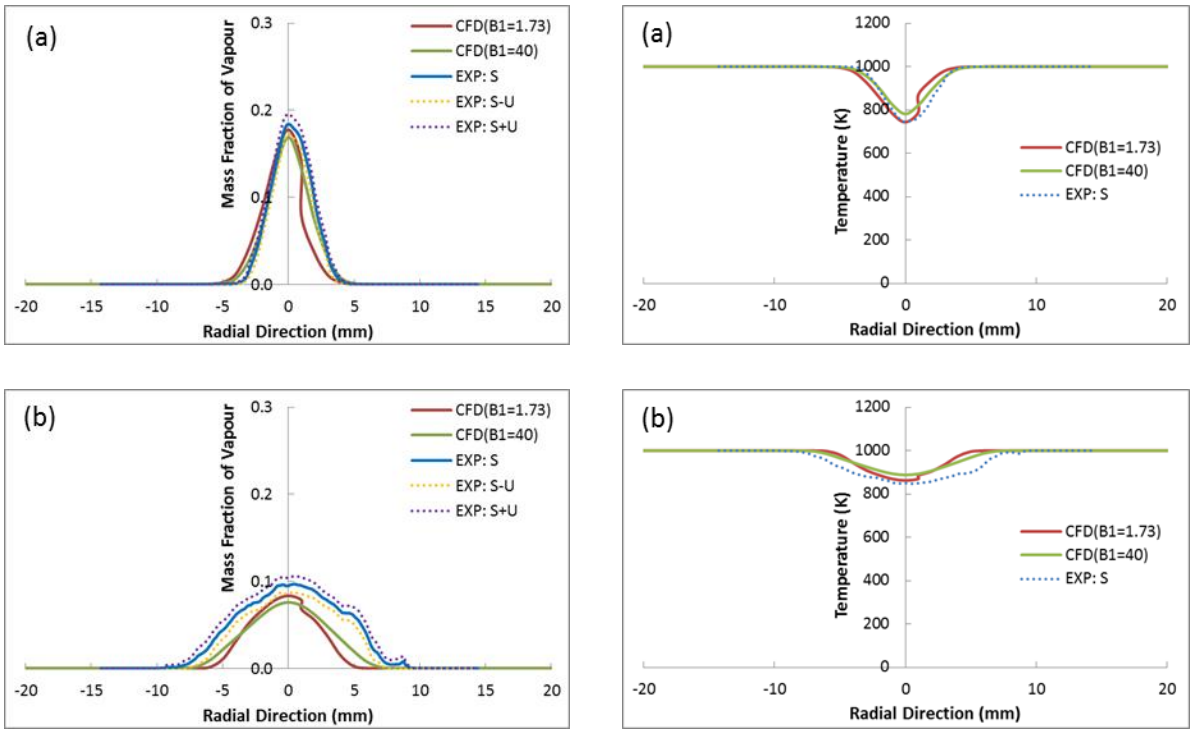

Figure 5.9 The variation of mass fraction and temperature at different cross section at liquid injection time 0.90 ms in the transverse sections z=20mm (a) and z=40mm (b). EXP: S – experimental data; EXP: U – experimental uncertainty.

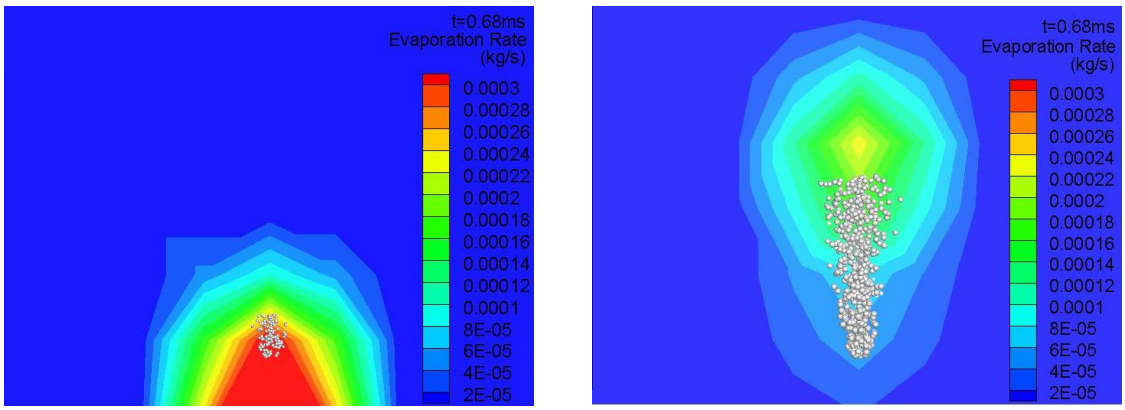

(a) B1=1.73 in KHRT model

(b) B1=40 in KHRT model

Figure 5.10 Evaporation rate of liquid fuel near the nozzle exit

(2) SSD Breakup Model

In SSD breakup model, the diameters of children droplets are independent from the size of the parent droplets. The model used the Fokker-Planck equation which is described by the equation (3.47) [16].

Figure 5.11 depicts that the fluctuation of liquid penetration computed by SSD breakup model is higher than that of KHRT model and the experimental data. As the diameters of newly created droplets as calculated based on the stochastic sampling procedure, various sizes of these droplets can be observed in Figure 5.13. A number of the children droplets have similar size to the parents droplets, whilst most of them are invisible in Figure 5.13(a). This causes the higher evaporation rate of droplets, compared to KHRT breakup model (B1=40), as well as the higher fluctuation in liquid penetration. However, the averaged liquid penetration predicted by SSD and KHRT models sufficiently coincides. Moreover, the vapour penetration evaluated by the SSD model also provides the similar results to the KHRT model. Compared to the measurements shown in Figure 5.12, the SSD breakup model can obtain consistent results for liquid and vapour penetrations, despite of the relatively higher fluctuation of liquid penetration.

Figures 5.14 - 5.17 describe the spatial distributions of mass fraction of fuel vapour and the chamber temperature calculated by the SSD breakup model for the SANDIA vessel for time instants 0.68 ms and 0.90 ms respectively. It can be clearly observed that the results simulated by SSD and KHRT (B1=40) breakup models adequately match, except for the region close to the nozzle exit. In the vicinity of nozzle exit, the SSD breakup model predicts a higher mass fraction of vapour and lower chamber temperature than the KHRT (B1=40) model, owing to the much smaller newly created droplets, as detailed in Figure 5.13. Similarly to the KHRT (B1=40) model, the results derived by the SSD breakup model agree well with the experimental measurements.

It is inferred that the SSD breakup model is more preferable than KHRT model in the following chapter, as some liquid injector parameters are uncertain. In other words, the SSD breakup model will be selected to investigate the liquid injection process in the Rapid Compression and Expansion Machine (RCEM) [115] and a large 2-stroke diesel engine [80] and dual fuel engine [5].

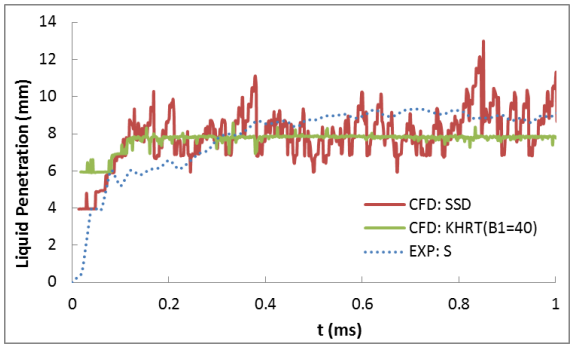

Figure 5.11 Comparison of liquid penetration from SSD breakup model and experiment in SANDIA vessel

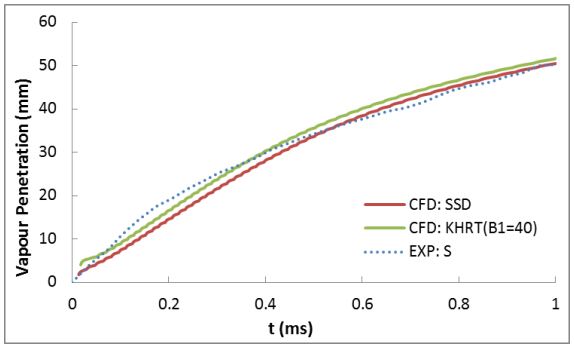

Figure 5.12 Comparison of vapour penetration from SSD breakup model and experiment in SANDIA vessel

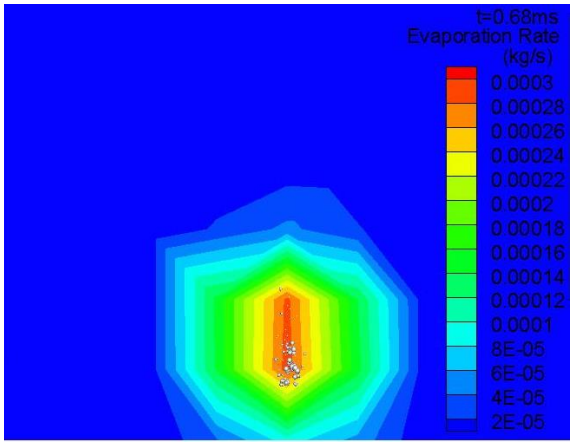

(a) SSD breakup model

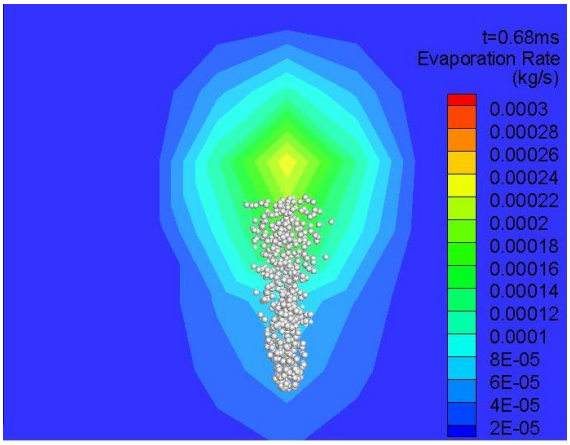

(b) KHRT breakup model with B1=40

Figure 5.13 Evaporation rate of liquid fuel near the nozzle exit

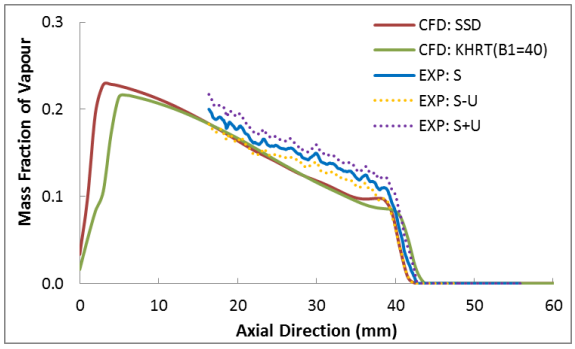

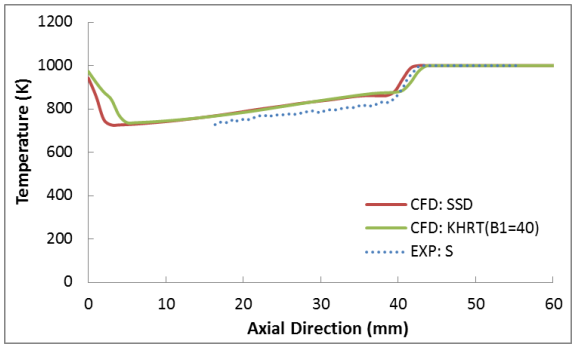

Figure 5.14 Vapour mass fraction and chamber temperature computed by SSD breakup model along the central line at time instant 0.68 ms. EXP: S – experimental data; EXP: U – experimental uncertainty

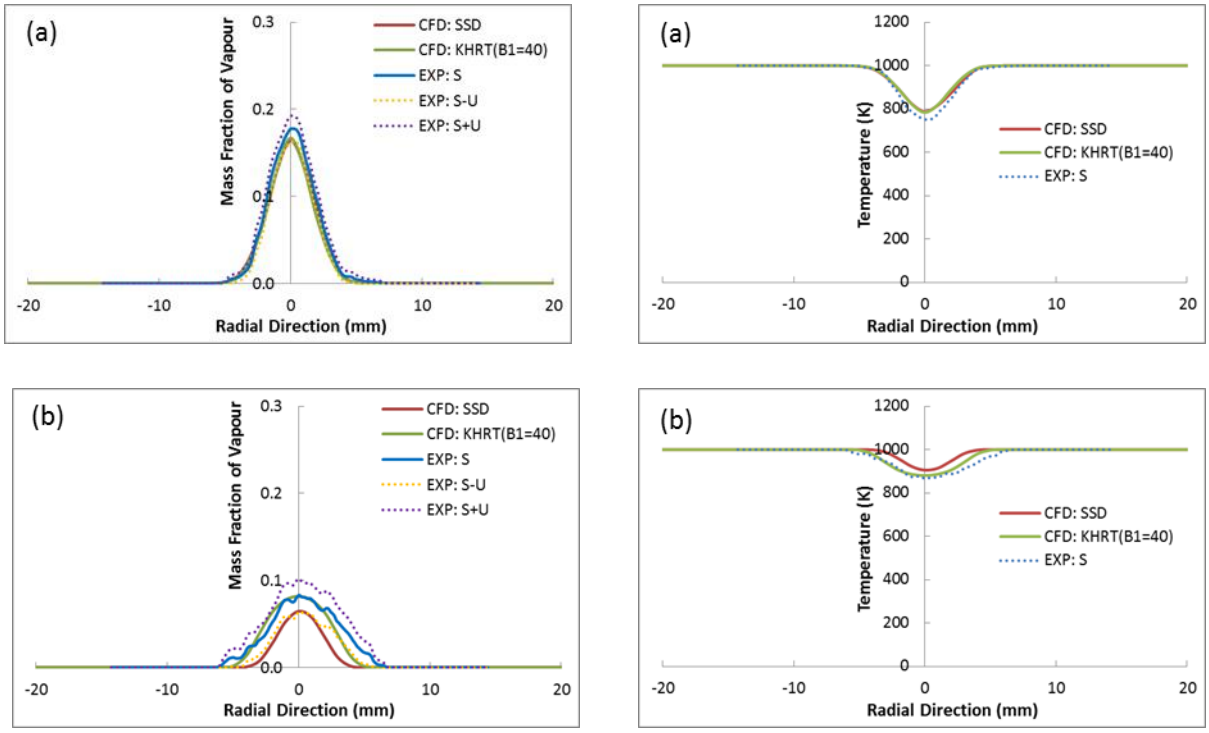

Figure 5.15 Variation of the vapour mass fraction and chamber temperature computed by the SSD breakup model in meridian plane in the transverse sections z=20 mm (a) and z=40 mm (b) at time instant 0.68 ms. EXP: S – experimental data; EXP: U – experimental uncertainty

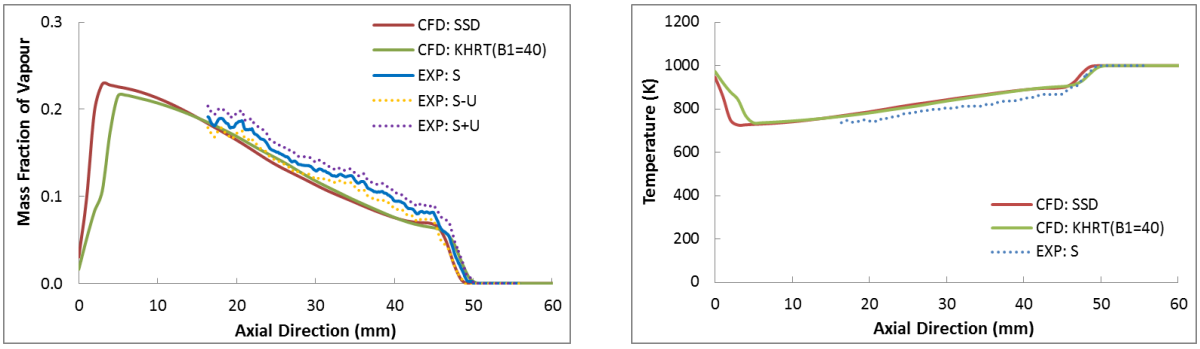

Figure 5.16 Vapour mass fraction and chamber temperature computed by SSD breakup model along the central line at time instant 0.90 ms. EXP: S – experimental data; EXP: U – experimental uncertainty

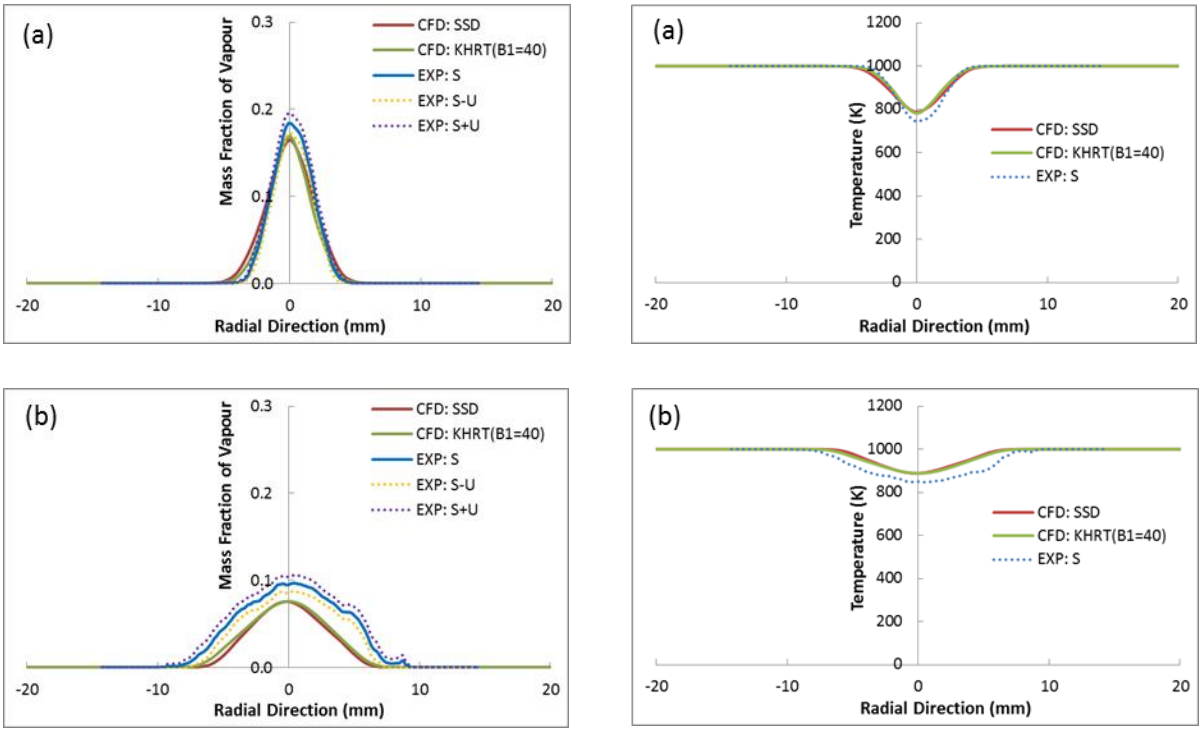

Figure 5.17 Variation of the vapour mass fraction and the chamber temperature computed by the SSD breakup model in the meridian plane in the transverse sections z=20 mm (a) and z=40 mm (b) at time instant 0.90 ms. EXP: S – experimental data; EXP: U – experimental uncertainty

5.3 Validation of the Gas Injection Model

Based on the generalized Richardson extrapolation recommended by ITTC [116], the grid convergence study is first conducted for the validation of the high-pressure gas injection model. Subsequently, the recommended grid resolution is selected to validate the high-pressure gas injection model against the existing experimental data [30].

5.3.1 Existing Experimental Introduction

The experimental study was performed by Choi [30], where a PLIF (planar laser induced fluorescence) system was used to study the gas injection process in a cube chamber. The compressed nitrogen was used in the experiment instead of the hazardous natural gas. Acetone was homogeneously mixed with the nitrogen flow in the nozzle as a function of fluorescence, due to the merits of very low boiling point, high saturation pressure and low toxicity. The injection system included a test injector, an acetone generator pressurised by high-pressure nitrogen, an electronic control unit (ECU), and a 14 V power supply. The experimental conditions and the dimension of the cube-shaped chamber are listed in Table 5.2.

Table 5.2 Experimental conditions for gas injection model validation

Parameters	Sym.	Unit	—
Injection Gas	—	—	Pure N_2
Nozzle Hole Diameter	d_g	mm	1.4
Injection Pressure	P_g	bar	10, 20
Injection Duration	t_g	ms	4
Ambient Pressure	P_a	bar	5
Ambient Temperature	T_a	K	293
Height of Cubic Chamber	H_C	mm	100
Length of Cubic Chamber	L_C	mm	80
Width of Cubic Chamber	B_C	mm	80

5.3.2 Validation of the High-Pressure Gas Injection Model

Pure Nitrogen (N_2) injection process into the cube chamber with the dimensions 0.08 m × 0.08 m × 0.1 m is simulated by the gas injection model with pressure ratio 2 and 4. The grid convergence study is performed to optimize the compatible grid resolution for the gas injection process investigation.

5.3.2.1 Grid Convergence Study

The grid resolution is of great significance to reduce the numerical errors and ensure the stability of the solution. In this section, the Richardson extrapolation [116] will be adopted to investigate the grid convergence index.

(1) Procedure Introduction

Richardson extrapolation is a method for obtaining a higher order estimate of the continuum value (value at zero grid spacing) from a series of lower order discrete values which is expanded in a power series expansion with integer powers of parameters such as grid size and the sum of the finite terms [116, 117]. In order to estimate the first n terms of the expansion, the 2n+1 solutions are required. It means that at least three solutions should be provided for the grid convergence study, only when the leading term can be evaluated.

In this research, the three grids are meshed, where the order of accuracy $<p_G>$ and error δ^*_{REG1} are calculated as recommended by ITTC CFD Uncertainty Procedure [116].

When estimating the errors and uncertainty of the grid point variables, both the convergence ratio $<R_G>$ and the order of accuracy $<p_G>$ can be based on the L2 norm of the solution changes, according to the following equations:

$$\langle R_G \rangle = \left\| \varepsilon_{G21} \right\|_2 / \left\| \varepsilon_{G32} \right\|_2 \tag{5.1}$$

$$\langle p_G \rangle = \frac{\ln\left(\left\|\varepsilon_{G21}\right\|_2 / \left\|\varepsilon_{G32}\right\|_2\right)}{\ln\left(r_G\right)} \tag{5.2}$$

$$\delta^*_{REG1} = \frac{\varepsilon_{G21}}{\ln\left(r_G\right)} \tag{5.3}$$

Where, ε_{G32} is the change of the coarse-medium solutions, and ε_{G21} is the change between the medium-fine results.

Under the monotonic convergence condition, the correction factor C_G is adopted to estimate the numerical errors δ^*_G caused by the grid resolution. According to the equations (5.4) and (5.5), this concept comes from the verification studies for 1D wave equation, 2D Laplace equation and Blasius boundary layer analytical benchmarking, accounting for the effects of the higher-order terms [116].

$$C_G = \frac{r_G^{\langle p_G \rangle} - 1}{r_G^{p_{est}} - 1} \tag{5.4}$$

$$\delta^*_G = C_G \delta^*_{REG1} \tag{5.5}$$

Where, p_{est} is estimated when the grid size goes to zero, the order of which is valued as 2.0 theoretically [117].

The grid uncertainty estimation is calculated by using the following equation,

$$U_G = \max\left[\left(2\left|1 - C_G\right| + 1\right), F_S\right]\delta^*_{REG1} \tag{5.6}$$

Where, the safety factor F_S=1.25 is recommended for careful grid studies [116].

(2) Estimation of Grid Convergence

A generalized Richardson Extrapolation Methodology requires that the grids for the convergence study should have the same mesh topology. In this section, the three structured and evenly distributed grids with a refinement ratio r_G equal to 2 had been created in the 2D axisymmetric gas Injection model, as illustrated in Figure 5.18. The gas jet tip penetration, the gas radial penetration, the injected gas diffusion profile at 1% nitrogen concentration, and the gas distribution at axis z/L=0.5 at the time 2 ms after the injection start are used to estimate the grid convergence index.

Based on the three solutions, the grid convergence index results are estimated, as shown in Table 5.3. The calculations imply that the monotonic convergence can be obtained with the grid refinement, according to the convergence ratio R_G. Consequently, the Richardson extrapolation can be used to

estimate the grid uncertainty U_G. By comparing the results shown in Figures 5.19 – 5.22, the mesh size 2 mm is inferred to be too coarse resulting in the point data far from the range of the grid uncertainty. When the grid density refines to 1 mm, the results are significantly improved, where most of flow data fall in the range of the grid uncertainty. This means that the gas spray model based on the grid resolution of mesh size 1 mm has effectively reduced the grid errors for the prediction of the gas jet penetration and evolution.

Table 5.3 Estimation of grid convergence index

	Gas Jet Tip Penetration	Gas Radial Penetration	Gas Profile at 1% Concentration	Gas Distribution at Axis z/L=0.5 at Injection Time 2ms
$<R_G>$	0.11	0.46	0.13	0.38
$<p_G>$	3.13	1.12	2.91	1.40
C_G	2.58	0.39	2.17	0.55

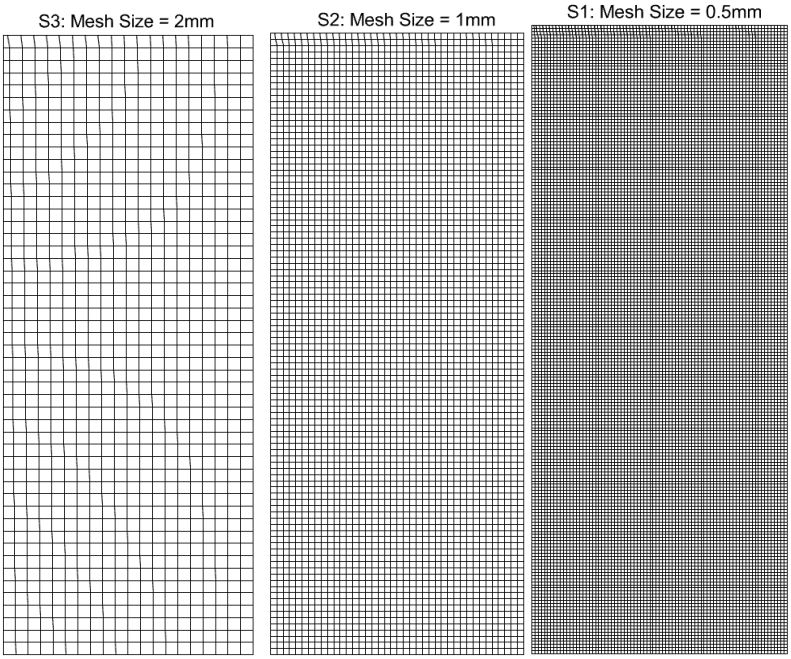

Figure 5.18 Three 2D axisymmetric meshes with a refinement ratio $r_G = 2$

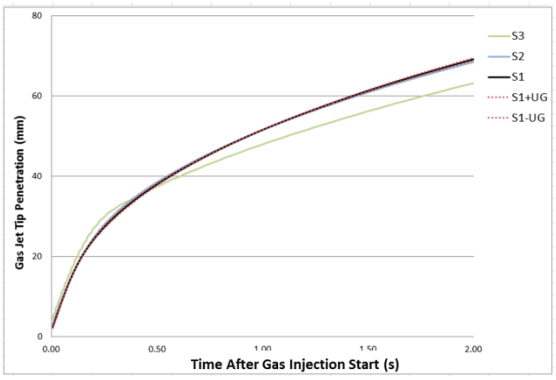

Figure 5.19 Grid convergence study for gas jet tip penetration

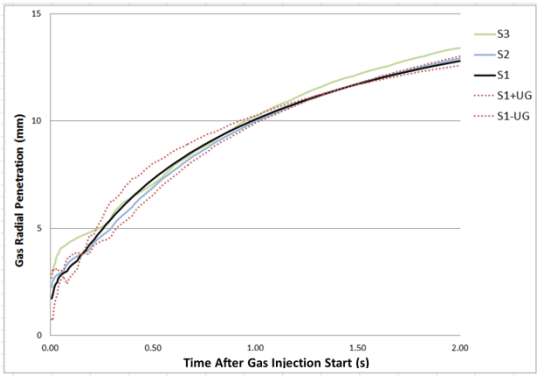

Figure 5.20 Grid convergence study for gas radial penetration

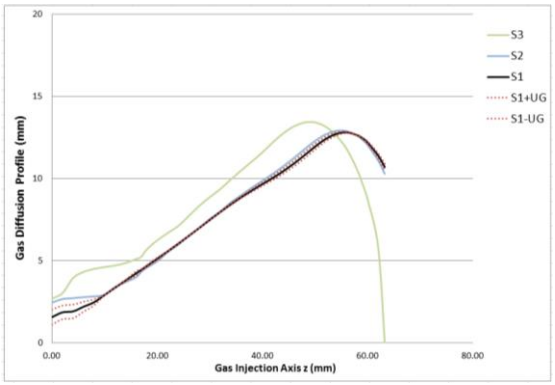

Figure 5.21 Grid convergence study for gas profile at 1% concentration

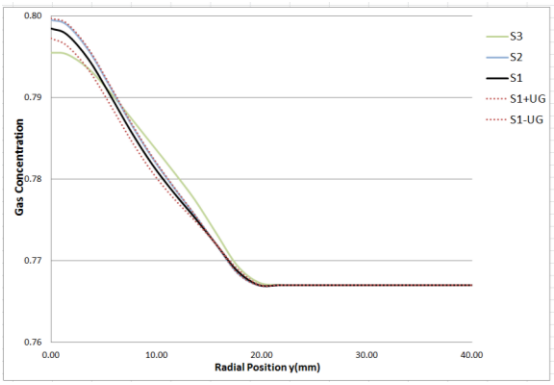

Figure 5.22 Grid convergence study for gas distribution in cross section z/L=0.5 at time 2ms after gas injection starts

5.3.3.2 CFD Validation

The experimental conditions used to the validation of the developed gas injection model are presented in Table 5.2. In terms of the grid convergence study, the 3D grid resolution is meshed to 1 mm^3 with grid number 0.64M, shown in Figure 5.23. Figure 5.24 compares the gas axial penetration derived from the model with the experimental results under pressure ratio 2 and 4, respectively. The results demonstrate that the CFD of the gas jet penetration coincides well with the measurement before the gas injection time 1.5 ms.It can be concluded that the conserving-equation sources approach can adequately predict the high-pressure gas jet penetration in the combustion chamber.

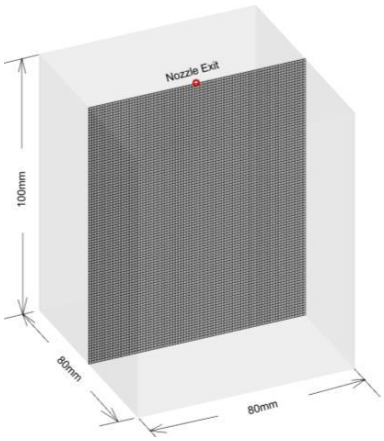

Figure 5.23 Gas chamber size for gas injection model validation

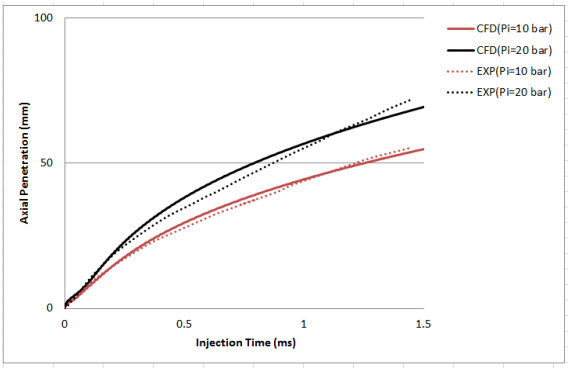

Figure 5.24 Gas tip penetrations under injection pressure 10 bar and 20 bar from the CFD and experiment. The experimental data is taken from [30]

5.4 Validation of the HPDI Dual Fuel Combustion Model

A rapid compression and expansion machine (RCEM) [9] is used to validate the CFD simulation on the HPDI dual fuel combustion process. The non-premixed dual fuel combustion model is validated, by comparing the derived and experimental results of the heat release rate (HRR) and NO emission for both the diesel and dual fuel modes.

5.3.1 Existing RCEM Description

RCEM is a single cylinder and one-shot firing test engine with the revolution 300 r/min, in which there is a cube clearance volume, as illustrated in Figure 5.25 [9]. The dimensions of the clearance volume are equal to 200 mm & 66 mm & 80 mm (Length & Width & Height), whereas the compression ratio and stroke are about 8.2 and 260mm respectively. The gas pressure booster can pressurize the natural gas up to 50 MPa, whereas the injection angle is set to 15° (Figure 5.25).The pilot fuel is injected prior to the gas fuel injection. The location of pilot injector is in front of the gas injector, and the corresponding spray angle is equal to 7.5°.

In one cycle, the intake valve is only open once, allowing for changing the cylinder with the pre-heated and pre-compressed air. Subsequently, the compression stroke, the fuels injection and combustion process take place. The exhausted mixture exits the cylinder at crank angle 60 °ATDC; a gas analyser is used to measure the exhaust gas compositions. Though the compression rate is relatively low, the pre-heated and pre-compressed air stored in a large tank is used that the in-cylinder pressure and temperature can reach the desired conditions and easily controlled accordingly.

Three groups of experiments were conducted by Imhof et al. [9], including the comparison of the diesel and dual fuel operations, the change of the pilot fuel injection timing and the reduction of the oxygen concentration in the charge air. In these experiments, the in-cylinder air temperature and pressure at the top dead centre (TDC) were 500 ℃ and 10 MPa respectively.

Table 5.5 provids the experiment conditions used to compare the HRR and NOx emissions under the diesel and dual fuel modes, respectively. The heat released by pilot fuel was approximately 3~4 % of the total heat released by both fuels combustion.

The pilot injection timing tests were listed in Table 5.6. The aim is investigating the effects of the change of the pilot injection timing on the heat release rate of dual fuel and the NOx productions.

Reducing the oxygen concentration in the charge air can significantly reduce the NOx emissions. Table 5.7 lists the experiment conditions of the oxygen concentration from 21.0% to 17.5% at the same air charge pressure and the same dual fuel injection parameters.

Table 5.4 Experimental conditions with the comparison of the diesel and dual fuel operations [9]

The diesel Mode		Dual Fuel Mode	
Nozzle Hole Diameter (mm)	0.5	Pilot Nozzle Hole Diameter (mm)	0.16
Injection Pressure (MPa)	100	Pilot Injection Pressure (MPa)	60
Injection Start/End (°ATDC)	-5.0/18.0	Pilot Injection Start/End (°ATDC)	-7.5/2.8
—	—	Gas Nozzle Hole Diameter (mm)	1.2
		Gas Injection Pressure (MPa)	30
		Gas Injection Start/End (°ATDC)	-6.0/18.0

Table 5.5 Experimental conditions of the changes of the pilot injection timing [9]

Parameters	Early	Normal	Late
Pilot Nozzle Hole Diameter (mm)	0.16	0.16	0.16
Pilot Injection Pressure (MPa)	50	50	50
Pilot Injection Start/End (°ATDC)	-8.0/-4.8	-6.0/-1.7	-4.4/0.2
Gas Nozzle Hole Diameter (mm)	1.0		
Gas Injection Pressure (MPa)	27.5		
Gas Injection Start/End (°ATDC)	-4.0/16.0		

Table 5.6 Experimental conditions with respect to the reduction of oxygen content in the ambient air [9]

Dual Fuel Mode		
Pilot Nozzle Hole Diameter (mm)	0.16	
Pilot Injection Pressure (MPa)	50	
Pilot Injection Start/End (°ATDC)	-8.0/-4.8	
Gas Nozzle Hole Diameter (mm)	1.0	
Gas Injection Pressure (MPa)	27.5	
Gas Injection Start/End (°ATDC)	-4.0/16.0	
Oxygen cont. charge air	21.0%	17.5%
Charge air pressure (MPa)	0.7	0.7

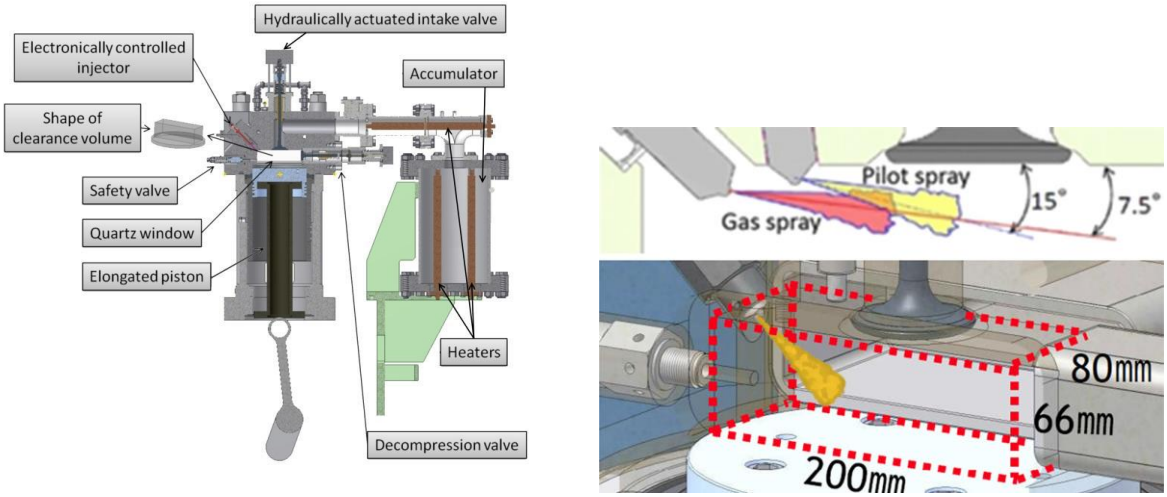

(a) Cross-sectional view of RCEM [9]

(b) Schematic diagram of cubic-shaped clearance volume [115]

Figure 5.25 Sketch of the RCEM

5.3.2 Validation of Dual Fuel Diffusion Combustion in RCEM

In this section, the RCEM measurements of the change of the fuel modes, the pilot fuel injection timing and the reduction of the oxygen concentration in the charge air are used to validate the dual fuel combustion model with the extended Zeldovich mechanism, in terms of the heat release rate and the NOx emissions. The developed dual fuel non-premixed equilibrium model and steady diffusion flamelet model are compared. The rate constants in the extended Zeldovich mechanism are derived from the Hanson and Salimian [95] and Heywood [118], respectively.

The n-heptane is selected as the liquid fuel on the diesel mode and pilot fuel on the dual fuel mode, which material properties needs to be modelled due to the variable temperature and pressure in the chamber shown in Appendix D. In addition, the methane will be used as the primary gas under the dual fuel operation.

5.3.2.1 Comparison of The diesel and Dual Fuel Modes

Using the in-cylinder pressure diagrams, the heat release rate (HRR) is determined by the first law of thermodynamics, as shown in the following equation [119]:

$$\frac{dQ}{dCA} = \frac{C_v}{R}\left(P\frac{dV}{d\theta} + V\frac{dP}{d\theta} - \frac{PV}{m}\frac{dm}{d\theta}\right) + P\frac{dV}{d\theta} \tag{5.7}$$

The HRRs varied with the crank angle and the NOx emissions at the ate expansion stroke will be used to validate the non-premixed combustion models under the diesel and the dual fuel modes.

Figures 5.26 and 5.27 depict the HRR curves calculated by non-premixed equilibrium model and steady flamelet model under dual fuel and diesel modes, respectively. Compared to the experimental data, both models can adequately predict the diesel and dual fuel non-premixed combustion processes. At the early stage of the fuel combustion, the higher slope of HRR under dual fuel mode than that of the diesel operation can be observed in experiment, which is also excellently captured by both combustion models. At late expansion stroke, the slightly discrepancy is observed, in which both models marginally overpredict the HRR under dual fuel mode and underestimate the HRR under the diesel mode. The noticeable peak HRRs of diesel and dual fuel also are sufficiently calculated by both combustion models. Comparatively, the steady flamelet approach seems to be closer to the experimental measurement for the diesel mode, and the non-premixed equilibrium model slightly overestimates the first peak HRR due to the underestimation of the initial part of combustion till the first peak of the HRR.

Table 5.7 lists the NO emissions experimentally measured and the derived CFD modelling results by using the two investigated non-premixed combustion models. It must be noted, the emissions are measured through sending them to the gas analyzer, while the CFD results correspond to the NO emissions prediction within the chamber at 60 °ATDC. At this CA point, CFD results indicate that the mass-averaged in-cylinder pressure is around 35 bar, corresponding to the mean of temperature 910 K - 950 K. All NOx species compositions are experimentally measured, whilst only NO is evaluated by the CFD model.

According to the experimental results, NOx emissions were reduced by 26% for the DF mode in comparison to the diesel mode. This trend can be simulated by non-premixed equilibrium model, despite of the significant discrepancy in magnitude. With respect to the steady flamelet approach, the

change of NO emission between the DF mode and diesel mode can be better computed than the equilibrium model.

The new specific rate constants in the extended Zeldovich mechanism recommended by Heywood [118] (shown in Table 5.8) are implemented and compared with the values of Hanson and Salimian [95] recommended by ANSYS Fluent [45]. Comparisons of the simulations in Table 5.7 depict that the change of the rate constants provided by Heywood [118] increases the NO prediction for the diesel mode and reduces the NO formation for the dual fuel mode. A larger discrepancy in NO produced by the new rate constants recommended by Heywood [118] is observed, compared with the results from the ANSYS defaulted rate constants derived from Hanson and Salimian [95] listed in Table 5.7.

Consequently, the ANSYS default values [95] for the rate constants in the extended Zeldovich mechanism will be used to evaluate the NO emissions in the next study. Regarding the non-premixed combustion model for the operating processes of the engine, the steady flamelet model will be used to investigate the change of pilot injection timing and oxygen reduction under dual fuel mode.

Table 5.7 Comparison of emissions under dual fuel and the diesel modes in RCEM vessel

	Rate Constants	Equilibrium Model		Steady Flamelet Model		Experiment	
		Diesel	Dual Fuel	Diesel	Dual Fuel	Diesel	Dual Fuel
NO (ppm)	Hanson and Salimian [95]	896	138	648	244	531	346-393
	Heywood [118]	1261	128	1061	153		

Table 5.8 Rate constants for extended Zeldovich mechanism

Reactions	Sym.	Unit	Rate Constants	
			Hanson and Salimian [95]	Heywood [118]
$O + N_2 \rightarrow N + NO$	$k_{f,1}$	m^3/(mol.s)	$1.8 \cdot 10^8 e^{-38370/T}$	$7.6 \cdot 10^7 e^{-38000/T}$
$N + NO \rightarrow O + N_2$	$k_{r,1}$	m^3/(mol.s)	$3.8 \cdot 10^7 e^{-425/T}$	$1.6 \cdot 10^7$
$N + O_2 \rightarrow O + NO$	$k_{f,2}$	m^3/(mol.s)	$1.8 \cdot 10^4 \tilde{T} e^{-4680/\tilde{T}}$	$6.4 \cdot 10^3 \tilde{T} e^{-3150/\tilde{T}}$
$O + N \rightarrow ON + O_2$	$k_{r,2}$	m^3/(mol.s)	$3.81 \cdot 10^3 \tilde{T} e^{-20820/\tilde{T}}$	$1.5 \cdot 10^3 \tilde{T} e^{-19500/\tilde{T}}$
$N + OH \rightarrow H + NO$	$k_{f,3}$	m^3/(mol.s)	$7.1 \cdot 10^7 e^{-450/T}$	$4.1 \cdot 10^7$
$H + N \rightarrow ON + OH$	$k_{r,3}$	m^3/(mol.s)	$1.7 \cdot 10^8 e^{-24560/\tilde{T}}$	$2.0 \cdot 10^8 e^{-23650/\tilde{T}}$

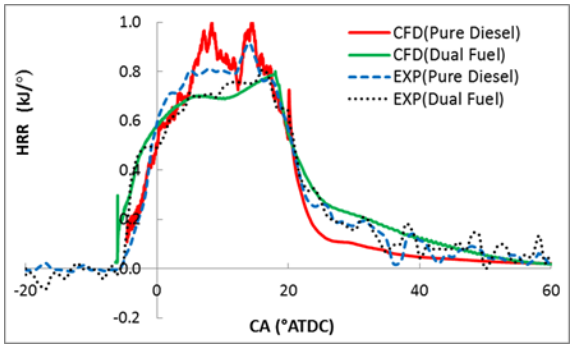

Figure 5.26 HRR computed by non-premixed equilibrium model and experiment under the diesel and dual fuel modes

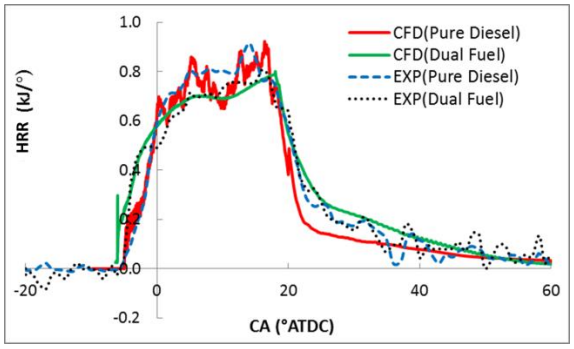

Figure 5.27 HRR computed by steady flamelet model and experiment under the diesel and dual fuel modes

5.3.2.2 Effects of Pilot Fuel Injection Timing on Dual Fuel Combustion

Under the same gas injection conditions, the effect of the change of pilot fuel injection timing listed in Table 5.5 on the HRR and NOx emissions will be investigated by means of CFD modelling and the derived results will be validated against the experimentally obtained measurements.

The characteristics of the ignition kernel caused by the change of the pilot fuel injection timing are listed in Table 5.9. By using the developed HPDI dual fuel combustion model (Chapter 4.4), the RCEM chamber pressure and the mass-averaged temperature affected by advancing or retarding the pilot fuel injection timing are illustrated in Figures 5.28 and 5.29. The results exhibit only slight deviation with the variation of the pilot fuel injection timing under the same gas injection condition. In addition, the resulting heat release rates (HRR) calculated by the dual fuel combustion model are shown in Figure 5.30. By comparing with the experimental result, CFD results match well in the early and normal pilot injection cases.

Regarding the late pilot injection timing case, there exists sharp rising of the peak HRR in the experimental results. When pilot injection start and main gas injection start significantly approach, the liquid fuel ignition is delayed due to the high dissipation rate and the lack of oxygen content within the ignition kernel, caused by the high-speed gas injection and the high concentration of gas fuel. The pilot fuel continuously accumulates, followed by the extremely rapid combustion in rich fuel mixture. The experimental HRR shown in Figure 5.30 depict that the ignition delay of pilot fuel was apparently prolonged and the highly peak HRR was obtained. Due to the separate simulation on the pilot fuel and main gas non-premixed combustion, such strong interaction between the main gas and pilot fuel cannot be captured by the steady flamelet model at present. In the case that the pilot fuel ignition is strongly influenced by the gas fuel, the current developed dual fuel combustion model has the limitations, and the double mixture fractions approach is proposed in conjunction with the variable gas mixture combustion mechanism.

The derived NO emission evaluated by the developed dual fuel combustion model and the extended Zeldovich mechanism with the default rate constants [95] of ANSYS Fluent are shown in Table 5.10.

For the normal pilot fuel injection timing, the variation of NO caused by advancing pilot injection timing can be adequately predicted by the steady flamelet model. For retarting the pilot fuel injection timing, there exists the reverse variation in the NO production observed in experimental and CFD results, because the severe interaction between the pilot fuel and main gas cannot be accurately simulated by the developed dual fuel combustion model in late case.

Table 5.9 Combustion characteristics for the different pilot injection timings in RCEM chamber

Pilot Injection Timing (°ATDC)		Ultra-high Temperature Zone (2400 K)		
Start	End	Duration (°)	R_{max}/R_P	CA at R_{Max} (°CAs)
-8.0	-4.8	19.03	0.0504	7.02
-6.0	-1.7	24.59	0.0555	8.85
-4.4	0.2	24.16	0.573	8.67

R_{max}: Maximum radius of the ignition kernel
R_P: Piston radius
°CAs: crank angle after pilot injection start.

Table 5.10 Comparison of emissions as the change of the pilot injection timing in RCEM

	NOx (ppm)		
	Early	Normal	Late
EXP	223	216	260
Flamelet	111	105	104

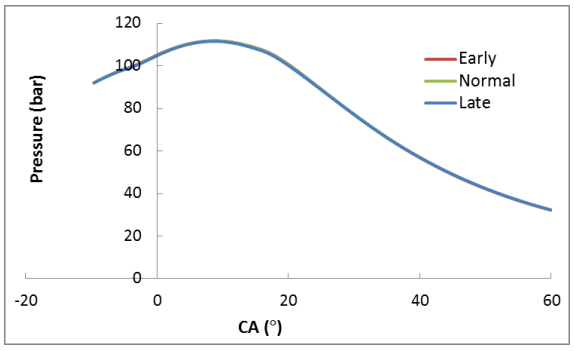

Figure 5.28 Mass-averaged pressure as the change of pilot injection timing in RCEM chamber

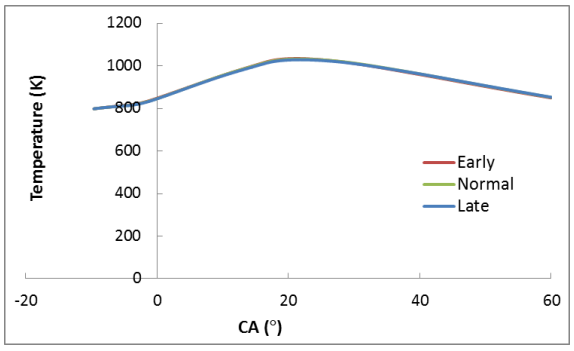

Figure 5.29 Mass-averaged temperature as the change of pilot injection timing in RCEM chamber

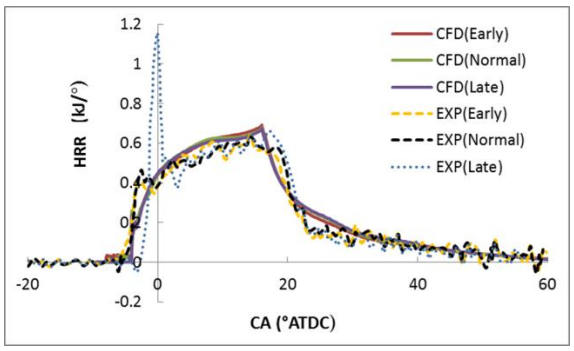

Figure 5.30 Comparison of HRR between the experiment and CFD as the change of pilot injection timing in RCEM chamber

5.3.2.3 Reduction of Oxygen Content in Charge Air

The two oxygen contents including normal condition 21.0% and reduced condition 17.5% in the charge will be simulated by the developed dual fuel combustion model with the extended Zeldovich mechanism and the results will be compared with the experimental measurements.

By using the developed dual fuel combustion model to simulate the dual fuel non-premixed combustion process, the derived mass-averaged pressure and temperature in chamber under normal and reduced oxygen content in the charge are estimated, as shown in Figures 5.31and 5.32.

The results indicate that the reduction of the oxygen content in the charge can result in the slight reductions of the RCEM chamber pressure and the mass-averaged temperature. This is due to the variation of the gas burning rate and the larger quantity of intermediate products, as illustrated in Figures 5.33 and 5.34. This trend can also be demonstrated by the heat release rate curves shown in Figure 5.35. Compared with the experimental results, the developed dual fuel combustion model can sufficiently predict the HRR variation, not only in magnitude but also in the variation caused by the reduced oxygen in the charge.

The slower gas burning rate and more intermediate products not only decrease the combustion temperature, but also the volume of the ultra-high temperature greater than 1800 K, shown in Figures 5.36 and 5.37. This is apparently beneficial of the suppression of NO formation, listed in Table 5.11.

Table 5.11 Comparison of emissions resulted from the oxygen reduction in experiment and steady flamelet model

	NOx emissions (ppm)	
	21%O_2	17.5% O_2
EXP	459-464	114
Flamelet Model (NO)	204	20

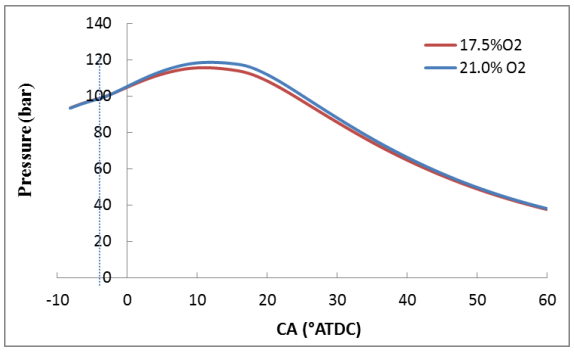

Figure 5.31 Mean pressure in RCEM chamber calculated by steady flamelet model under normal and reduced oxygen conditions

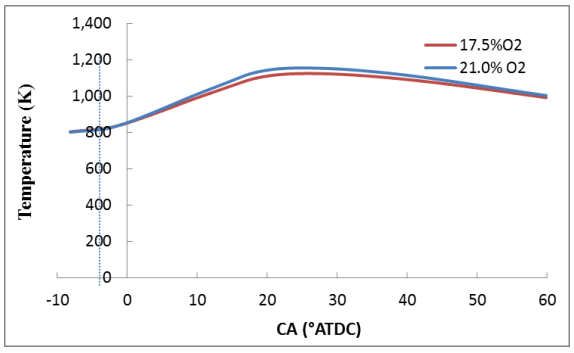

Figure 5.32 Mean temperature in RCEM chamber calculated by steady flamelet model under normal and reduced oxygen conditions

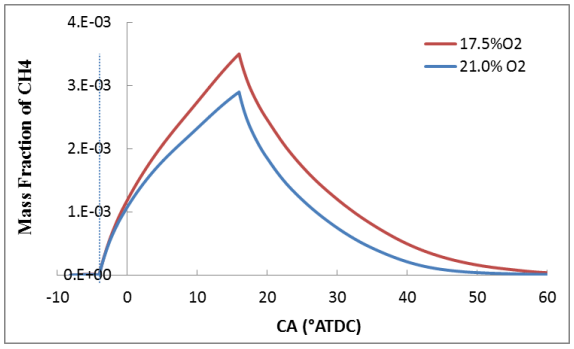

Figure 5.33 Mass fraction of methane in RCEM chamber calculated by steady flamelet model under normal and reduced oxygen conditions

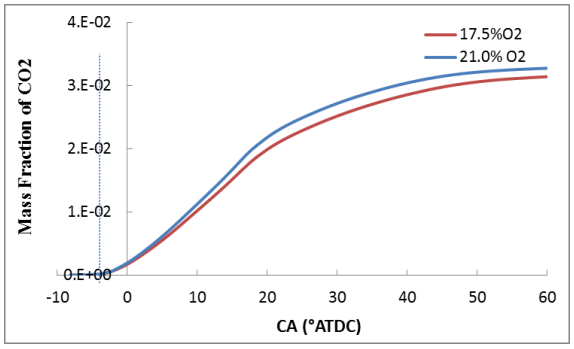

Figure 5.34 Mass fraction of carbon dioxide in RCEM chamber calculated by steady flamelet model under normal and reduced oxygen conditions

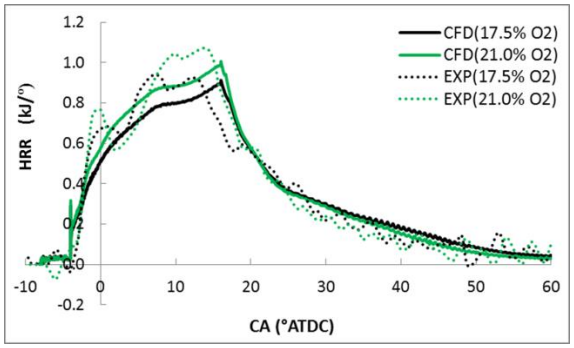

Figure 5.35 Comparison of HRR between the steady flamelet model and experiment under normal and reduced oxygen conditions

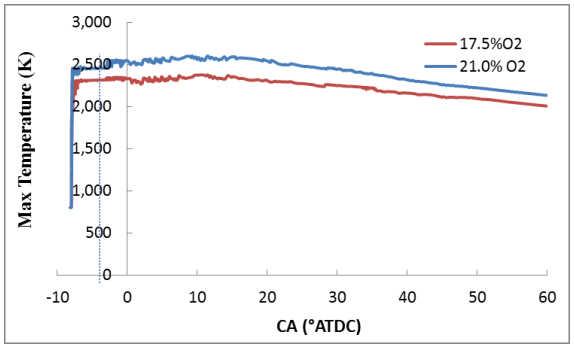

Figure 5.36 Max temperature in RCEM chamber calculated by steady flamelet model under normal and reduced oxygen conditions

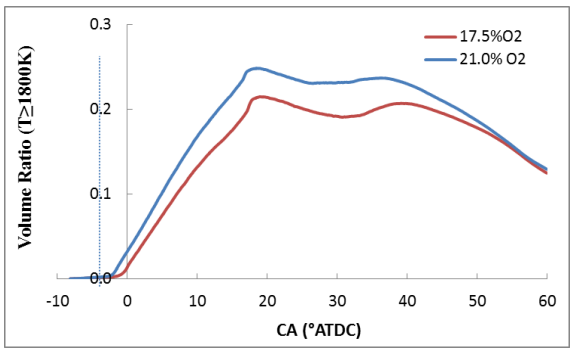

Figure 5.37 Volume ratio of local temperature greater than 1800K calculated by steady flamelet model under normal and reduced oxygen conditions

5.5 Conclusions

Regarding the HPDI dual fuel injection and combustion processes, the associated developed CFD models are validated, including the liquid fuel spray model, high-pressure gas injection model and the HPDI dual fuel combustion model. The liquid spray model with breakup model is validated, comparing with the experimental results in SANDIA vessel. With respect to the gas injection, the grid convergence study recommended by ITTC procedure, is conducted to investigate the grid resolution.

The high-pressure gas injection model is also validated, by using the N_2 jet tip penetration measured in the cube-shaped chamber. In terms of the measurement in RCEM, two developed non-premixed dual fuel combustion models are compared, as well as the rate constants in the extended Zeldovich mechanism.

The main findings are summarized as follows:

- The grid size of 10 times the nozzle diameter is recommended for modelling the liquid spray process in the high-pressure and high-temperature chamber, in order to compromise between the computational cost and accuracy.
- The grid resolution 1 mm adopted in the chamber can significantly reduce the grid errors for the prediction of the gas penetration and injection/ mixing evolution.
- The liquid fuel spray model can excellently evaluate the liquid fuel and the associated vapour penetration, and the temporal and spatial distributions of the vapour in SANDIA chamber.
- The gas injection model based on the conserving-equation sources can sufficiently predict the gas jet tip penetration, compared with the experimental results for the N_2 injection under a pressure ratio 2 and 4.
- By comparing the rate constants in the extended Zeldovich Mechanism provided by Hanson and Salimian [95] and Heywood [118], the former values are recommended to evaluate the NO formation.
- In terms of heat release rate (HRR) curves versus crank angle in RCEM chamber, the dual fuel combustion model embedded by the steady diffusion flamelet has been validated to precisely predict the non-premixed combustion process both on the diesel and dual fuel modes, except in the case that the starts of pilot fuel spray and main gas injection are very close, leading the sharply peak HRR in the early stage of high-pressure gas direct injection.

Chapter 6 Parametric Investigation of a Large 2-S HPDI DF Engine

6.1 Introduction

In this chapter, the validated CFD model employing the steady diffusion flamelet model and the extended Zeldovich mechanism will be applied to investigate the effects of the parameters of the pilot and main gas injection on the closed-cycle operation for a large 2-stroke dual fuel marine engine with the high-pressure direct gas injection (HPDI). The indicated mean effective pressure (IMEP) and the emissions including the NO, CO_2 and methane slip in these parametric cases will be numerically evaluated and compared. At the last, the recommended set of the design parameters of dual fuel injection will be addressed.

6.2 Engine Description

The 5S60-ME-C8.5-GI-TII marine engine from MAN Diesel & Turbo [5] will be investigated, which has a super long stroke and 60 cm bore for each cylinder (shown in Table 6.1). The fuel injection and exhaust valves are electronically controlled by appropriate control units. The sign "GI" implies that the gas injection mode can be adopted. With the postfix "TII", the designated engine complies with IMO Tier II emission regulations.

Prior to the gas direct injection, the pilot fuel firstly sprays into the dual fuel engine combustion chamber, which schematic graph is shown in Figure 6.1. Each cylinder has one gas control block to control the high-pressure gas supply through the gas channel to the gas injector. Different valves are required to separate the operation of the pilot fuel and main gas. Pilot or liquid fuel is activated by the multiway valve (FIVA), and the high-pressure gas is controlled by the ELGI valve.

Table 6.1 MAN Diesel & Turbo engine S60ME characteristics

Parameters	Sym.	Unit	—
Stroke	S	m	2.4
Bore	B	m	0.6
Crank Radius	R	m	1.2
Engine Speed (75% Load)	Nr	rpm	91.3
Engine Power (75% Load)	P_D	kW	7875

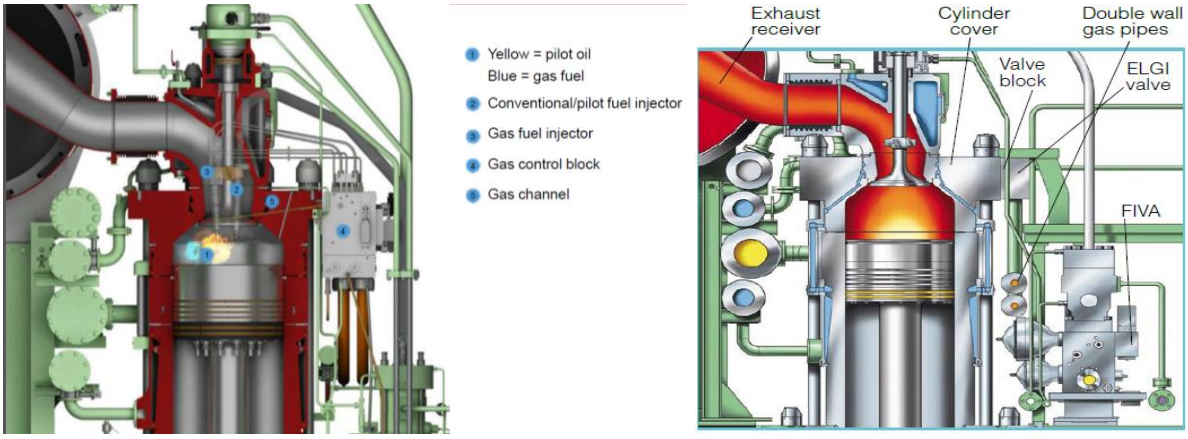

Figure 6.1 Sketch of large 2-stroke dual fuel engine made by MAN Diesel & Turbo [5]

6.2.1 Dual Fuel Injection

The pilot fuel pressurized by an oil fuel pressure booster is controlled by FIVA valve [5] to deliver the fuel oil into the combustion chamber. The ME hydraulic control oil system boosted at about 300 bar pressure also pressurizes the control oil to the ELGI valve, which switches on and off the gas fuel injection as illustrated in Figure 6.2.

In this chapter, the minimum pilot fuel mode [3] will be studied. In terms of CEAS engine data report of 5S60ME-C8.5-GI (methane) [5], the quantity of pilot fuel relatively increases with the reduction of the engine power, depicted in Figure 6.3. The main gas consumption (SGC) against engine load is nonmonotonic, where the lowest result takes place on 70% engine load. The two fuels make specific consumption listed in Table 6.2.

The three pilot injectors and three gas injectors are installed in each engine cylinder. In terms of the pilot oil pressure and gas fuel pressure curves shown in Figure 6.2, the pilot fuel and gas fuel injection timing and duration can be estimated. As an example for 75% SMCR, Table 6.3 provides the pilot fuel and gas fuel injection parameters at the conditions of 21 ℃ ambient air and 30 ℃ scavenge air coolant. It can be calculated that 0.642 g/rev of pilot fuel and 12.65 g/rev of natural gas are injected into the engine combustion chamber by each pilot injector and gas injector, respectively.

Table 6.2 The specific pilot oil consumption (SPOC) and specific gas consumption (SGC) under specified conditions [5]

Specified ambient conditions (ambient air: 21 ℃, scavenge air coolant: 30 ℃)				
Engine Load (% SMCR)	Power (kW)	Speed (r/min)	SPOC (g/kWh)	SGC (g/kWh)
100	10,500	100.5	5.5	138
75	7,875	91.3	6.7	132
50	5,250	79.8	8.7	132.9
25	2,625	63.3	13.9	134.9

Table 6.3 Dual fuel injection parameters at 75% engine load under Specified ambient conditions

Load (% SMCR)	Speed (r/min)	Pilot Fuel			Natural Gas		
		Fuel Consumption (g/rev)	Injection Start (°ATDC)	Injection End (°ATDC)	Fuel Consumption (g/rev)	Injection Start (°ATDC)	Injection End (°ATDC)
75	91.3	9.63	8.14	12.44	189.76	13.81	31.13

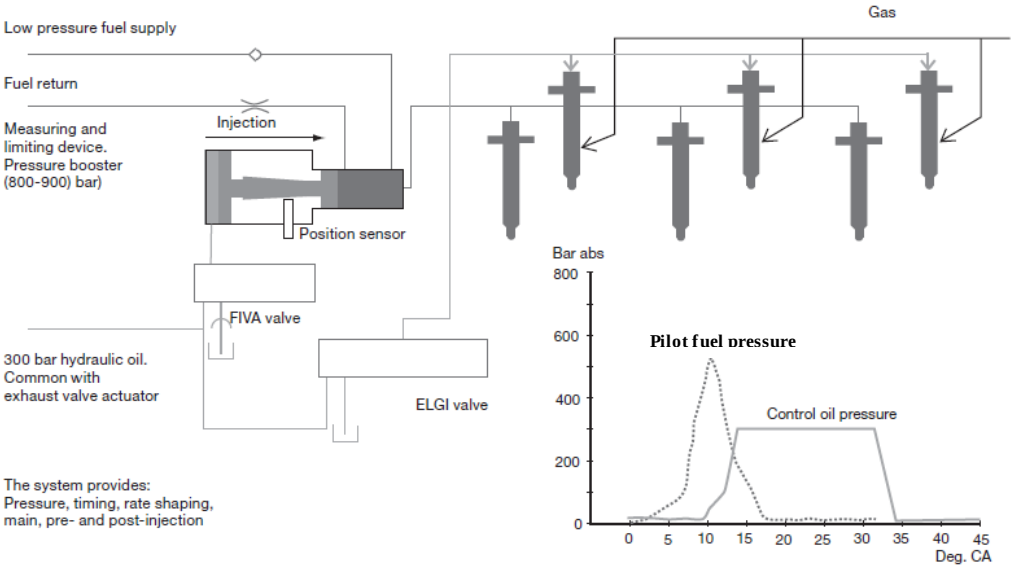

Figure 6.2 Dual Fuel Injection System [5]

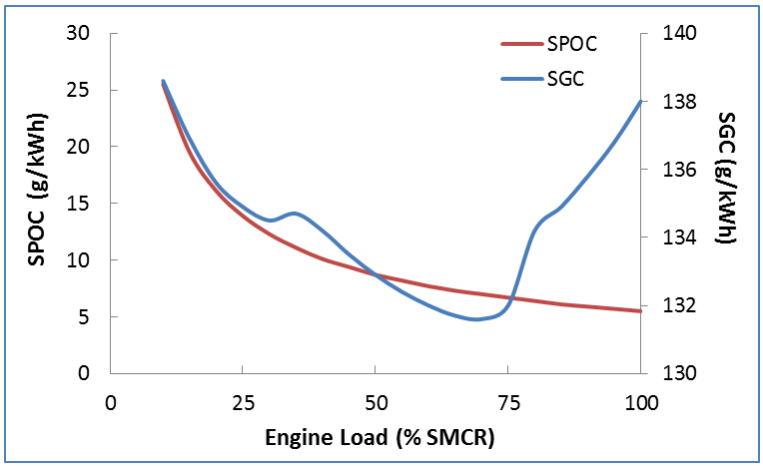

Figure 6.3 Specific pilot fuel consumption (SPOC) and specific gas consumption (SGC) varied with engine loads under dual fuel mode at ambient air 21 ℃ and scavenge air coolant 30 ℃ [5]

6.2.2 Fuel Properties

6.2.2.1 Pilot Fuel Properties

According to the engine manufacturer [5], GI engine when operating in DF mode achieves similar in-cylinder pressure histories compared to the diesel mode in the whole operating envelope. Consequently, the pilot fuel properties in the presented dual fuel engine can be modelled, based on the

internal environment under the diesel operation. Viewing liquid n-heptane as the pilot fuel, the boiling temperature can be calculated around 520 K [120] at 75% engine load. Other properties of the pilot fuel (n-heptane) under 75% load are demonstrated in Figures 6.4 ~ 6.7.

According to the Jin's results for the diesel operation [80], the initial spray cone angle (half angle) for the pilot fuel is also equal to 12° and the initial injection temperature is initialized by 323 K.

Thermophysical properties of the pilot fuel vapour can be found in Appendix C.

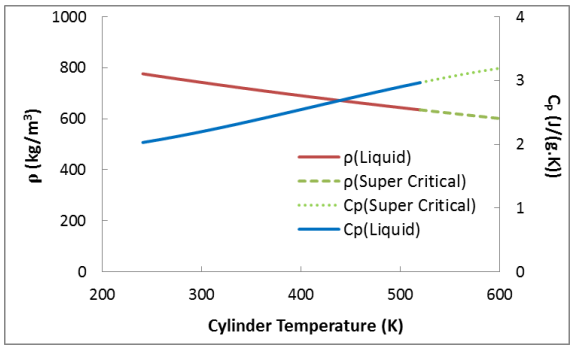

Figure 6.4 Density ρ and specific heat capacity CP of pilot fuel as a function of the cylinder temperature [121]

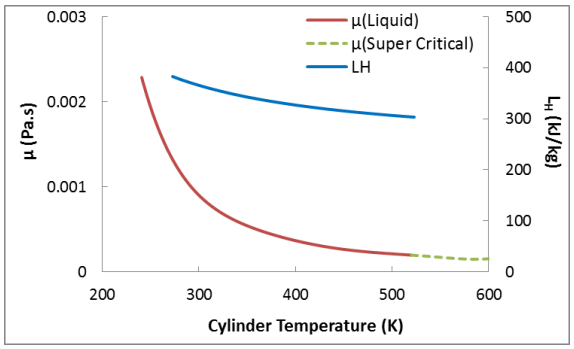

Figure 6.5 Liquid viscosity μ [121] and evaporation latent heat LH [122] of pilot fuel as a function of the cylinder temperature

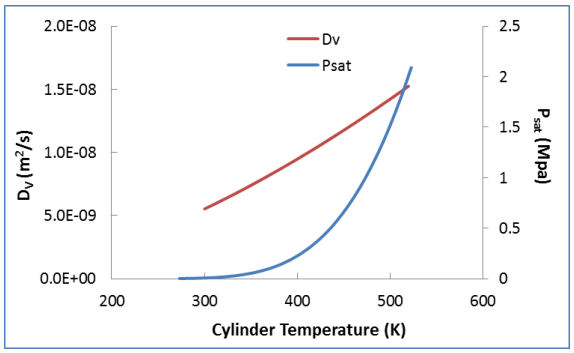

Figure 6.6 Binary Diffusion DV [123] and saturation pressure Psat [122] of pilot fuel as a function of the cylinder temperature

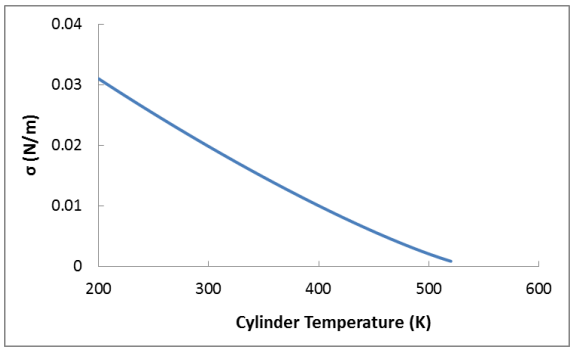

Figure 6.7 Droplet's surface tension σ as a function of the cylinder temperature under 75% dual fuel engine load [124]

6.2.2.2 Natural Gas Properties

MAN Diesel & Turbo [5] indicates that the gas supply system equalizes the gas pressure to 300 bar. Figure 6.8 illustrates the gas temperature about 45 ℃ before it is injected into the combustion chamber. The assumption that the natural gas primarily consists of methane (CH_4) is employed herein. Subsequently, the gas state equation is used to calculate its density.

Thermo-physic properties of the methane are detailed in Appendix C.

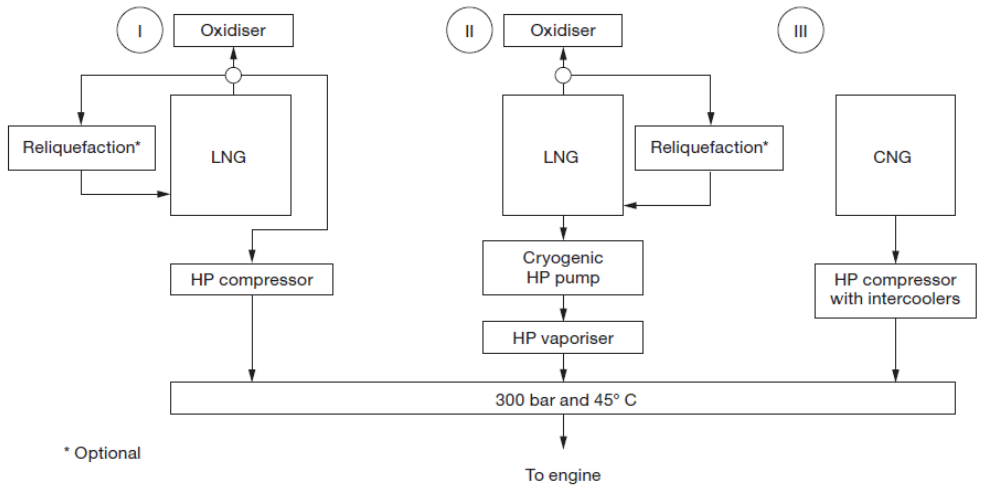

Figure 6.8 Three most commonly used gas supply systems to marine two-stroke HP GI engines [5]

6.2.3 Boundary conditions

6.2.3.1 Scavenge Air

In the large 2-stroke dual fuel marine engine 5S60ME-C8.5-GI [5], the turbocharger (TC) air consumption, the scavenge air cooler heat, the scavenge air pressure and the receiver temperature against engine load are presented in Figures 6.9 ~ 6.12. The related results under the typical engine loads are summarised in Table 6.4.

Table 6.4 The performance in scavenge air system at different loads of 5S60ME-C8.5-GI marine engine

Specified (Ambient Air: 21 ℃, Scavenge Air Coolant: 30 ℃)				
Load (%SMCR)	Turbocharger Air Consumption (kg/s)	Scavenge air pressure (bara)	Scavenge air receiver temperature (℃)	Scavenge air cooler heat (kW)
100	24	4	42	3830
75	19.7	3.19	37	2500
50	14.2	2.26	33	1190
25	8.9	1.46	37	300

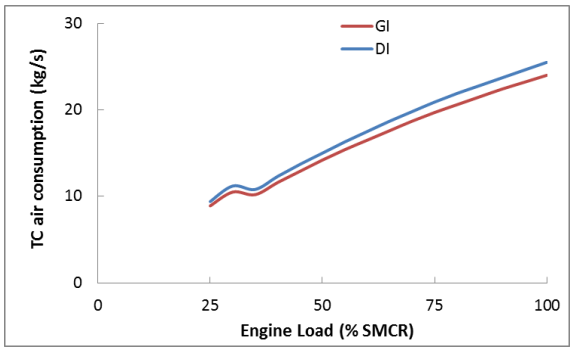

Figure 6.9 Turbocharger air consumption as a function of the engine load under dual fuel (GI) mode and the diesel (DI) mode at specified conditions

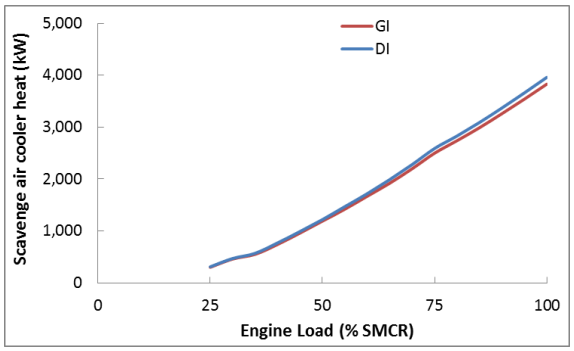

Figure 6.10 Scavenge air cooler heat as a function of the engine load under dual fuel (GI) mode and the diesel (DI) mode at specified conditions

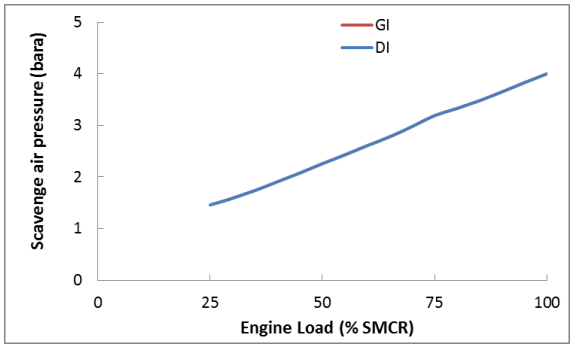

Figure 6.11 Scavenge air pressure as a function of the engine load under dual fuel (GI) mode and the diesel (DI) mode at specified conditions

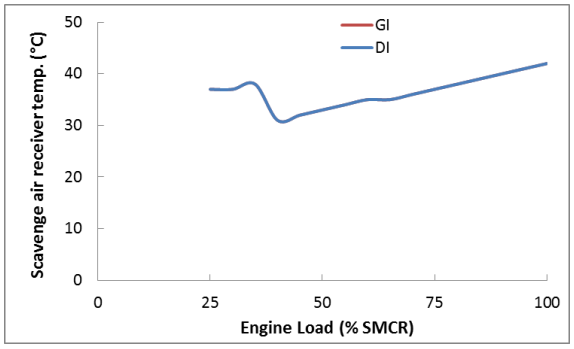

Figure 6.12 Scavenge air receiver temperature as a function of the engine load under dual fuel (GI) mode and the diesel (DI) mode at specified conditions

6.2.3.2 Exhaust Gas

After the exhaust valve opening, the in-cylinder gas will be discharged to the exhaust gas receiver, in which the fluctuating pressure will also be equalized, in order to provide the constant pressure to the turbocharger.

Figure 6.13 depicts the less exhaust gas drawn by dual fuel operation than the diesel, under the same engine load and ambient conditions. The higher temperature after turbocharger in dual fuel engine can be observed in Figure 6.14.

Table 6.5 Mass flow rate and temperature of exhaust gas after turbocharger of 5S60ME-C8.5-GI marine engine

Load (%SMCR)	Power (kW)	Mass Flow Rate (kg/s)	Temperature (K)
100	10500	24.5	241
75	7875	20	222
50	5250	14.4	236
25	2625	9	227

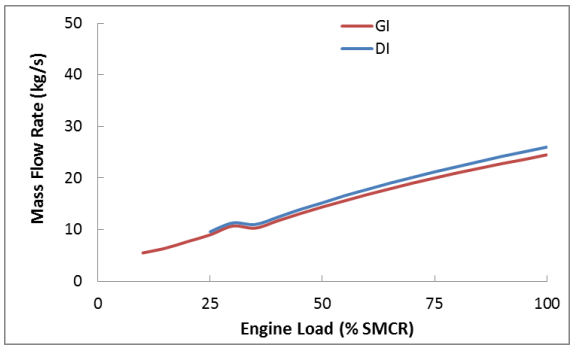

Figure 6.13 Comparison of mass flow rate of the exhaust gas from dual fuel (GI) engine and the diesel (DI) engine

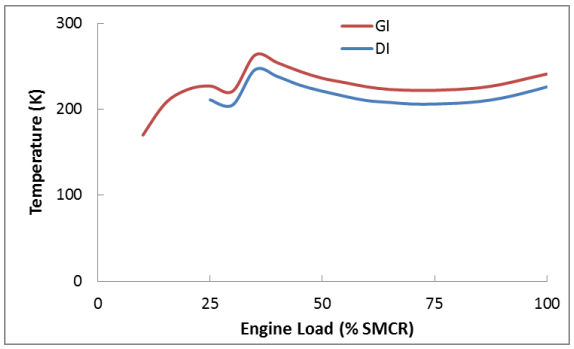

Figure 6.14 Comparison of temperature after turbocharger turbine integrated in dual fuel (GI) engine and the diesel (DI) engine

6.2.3.3 Walls Temperature

Before the CFD simulation, the walls temperature the marine engine S60ME including the scavenging ports, the exhaust stem, the exhaust duct, the exhaust valve and the piston need to be designated, which are derived from the shop test of the diesel mode [80], as shown in Table 6.6.

Table 6.6 Walls temperature for the marine engine 5S60ME under 75% load

Wall	Temperature (K)	Wall	Temperature (K)
Exhaust Duct	593	Exhaust Stem	823
Exhaust Valve	823	Cylinder	593
Piston	603	Scavenging Ports	315

6.3 CFD Running

By using the validated dual fuel injection and combustion model developing in ANSYS Fluent, the parametric investigation of the dual fuel injection will be performed. According to the grid convergence study in Chapter 5, the 1 mm grid size in the engine combustion chamber is adopted. The mesh number will be varied with the piston moving, where the 0.17 M will be estimated at TDC. The time step changes, according to the physical processes in the engine combustion chamber. Before the pilot fuel injection and the late expansion after 40 ° ATDC, the 0.1° CA time step will be used. During the pilot fuel injection and the high-pressure gas injection processes, the time step of 0.001° CA is required, as well as the moments of the scavenging ports and the exhaust valve opening and closing. For the gas fuel combustion after its injection, the 0.01° CA time step sets.

Before the parametric investigation, the internal operation simulation for the three whole cycles should be conducted, in order to achieve the converged results. Each whole-cycle calculation approximately costs 1 month in 16 CPUs on ARCHIE-WeSt supercomputer. With respect to the parametric investigation, the cases will run from -7° ATDC to 110° ATDC. The associated time consumption for each case is about 2 weeks in 16 paralleled CPUs.

6.4 Parametric Investigation of Dual Fuel Combustion

Aiming to obtain the recommended set of the dual fuel injection setting for the 75% engine load (cruising operation), the parametric investigation regarding the closed-cycle operation will be conducted numerically. The flowchart of the research is shown in Figure 6.15.

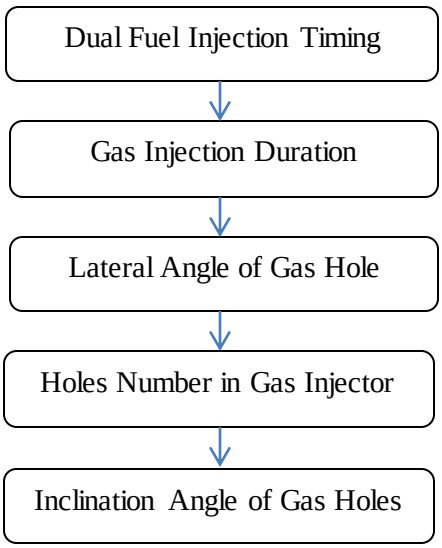

Figure 6.15 Flowchart of the parametric investigation

Before the parametric investigation, some variables including the longitudinal, lateral and vertical penetrations of the pilot spray or gas jet should be defined as depicted in Figure 6.16 and Table 6.7.

Given by the coordinates of the nozzle exit "I" and the tip location "K", the tip penetration in three directions can be calculated by the following equations:

$$IK" = [(x_i - x_K) \cdot \cos(\beta_i + \varphi_i) + (y_i - y_K) \cdot \sin(\beta_i + \varphi_i)] \cdot \cos\alpha_i + (z_i - z_K) \cdot \sin\alpha_i \quad (6.1)$$

$$KK' = (x_i - x_K) \cdot \sin(\beta_i + \varphi_i) - (y_i - y_K) \cdot \cos(\beta_i + \varphi_i) \quad (6.2)$$

$$K"K' = [(x_i - x_K) \cdot \cos(\beta_i + \varphi_i) + (y_i - y_K) \cdot \sin(\beta_i + \varphi_i)] \cdot \sin\alpha_i - (z_i - z_K) \cdot \cos\alpha_i \quad (6.3)$$

Where the subscript "i" replaced by “g” and “p” denotes the gas injector and the pilot fuel injector respectively.

Table 6.7 Symbols definitions of fuel penetration

	Unit	Sym.
Cartesian Coordinates	–	oxyz
Location of Nozzle Exist	–	I
Injection Direction	–	ID
Location of Tip Penetration	–	K
Longitudinal Penetration	m	IK”
Lateral Penetration	m	K’K
Vertical Penetration	m	K”K’
Inclination Angle	º	α_i
Lateral Angle	º	β_i
Installation Angle	º	φ_i
Coordinates of Nozzle Exit	m	x_i, y_i, z_i
Coordinates of Tip Penetration	m	x_K, y_K, z_K

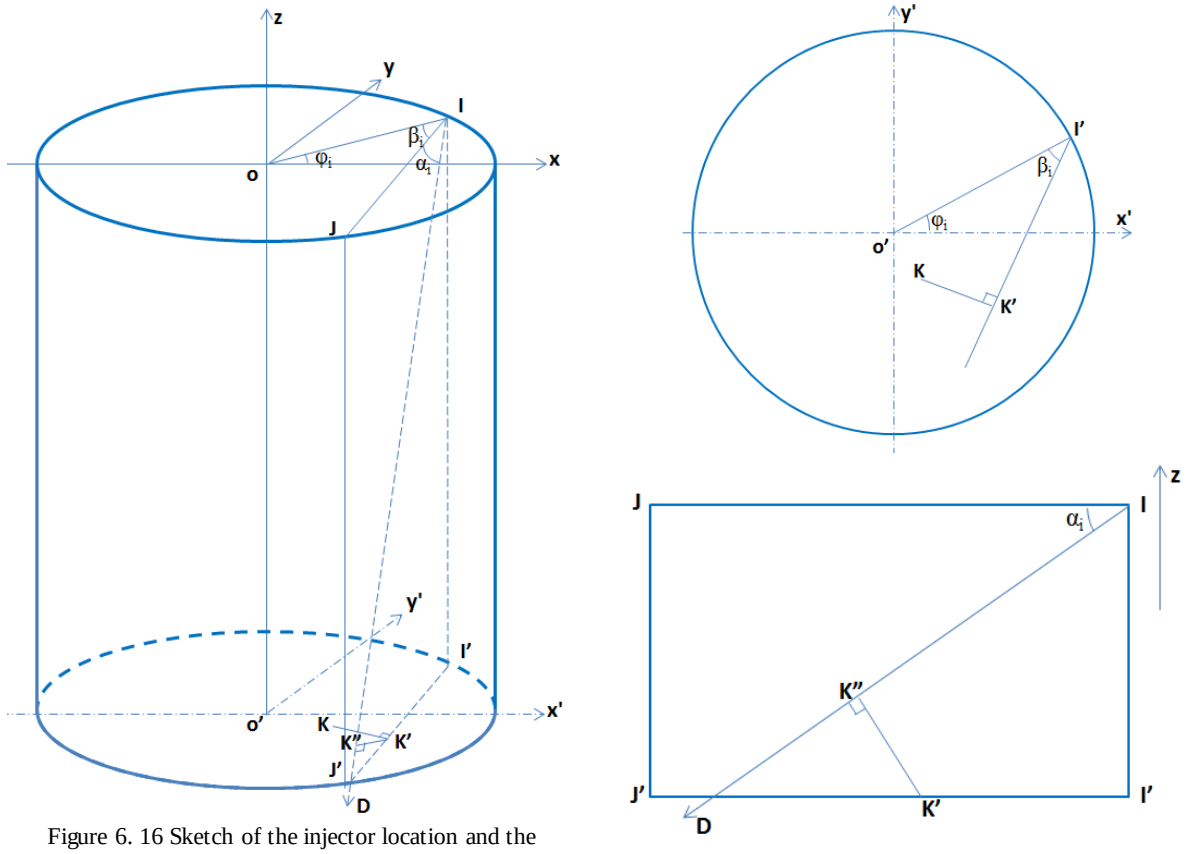

Figure 6. 16 Sketch of the injector location and the penetration

6.4.1 Effects of Dual Fuel Injection Timing

As shown in Table 6.8, the pilot and gas injection timings and duration in the case DF1 are derived from the pilot fuel injection pressure and gas injection pressure curves in Figure 6.2. The inclination angle of the gas injector is set at 15°, in order to avoid the gas accumulation near the cylinder top illustrated in Figure 6.17 [125]. The corresponding inclination angle of the pilot nozzle is also equal to 15 °.

The start of the pilot fuel spray in the second case DF2 is at the top dead centre (TDC), which has the same injection interval between the pilot spray end and the gas injection start to the case DF1. In the case DF3, the gas injection start is advanced to TDC, and the pilot spray is operated before TDC to maintain the same injection interval for the two fuels. As shown in Table 6.8, both pilot fuel and gas injection durations in the three cases are the same.

Table 6.8 Parameters of pilot and gas injection timing

	Pilot Injector			Gas Injector				
	Timing (°ATDC)	α_l (°)	β_l (°)	Timing (°ATDC)	Duration (°CA)	Holes Number	α_g (°)	β_g (°)
DF1	8.14~12.44	15	0	13.81~31.13	17.32	1	15	0
DF2	0.0~4.29	15	0	5.67~22.99	17.32	1	15	0
DF3	-5.67~-1.37	15	0	0~17.32	17.32	1	15	0

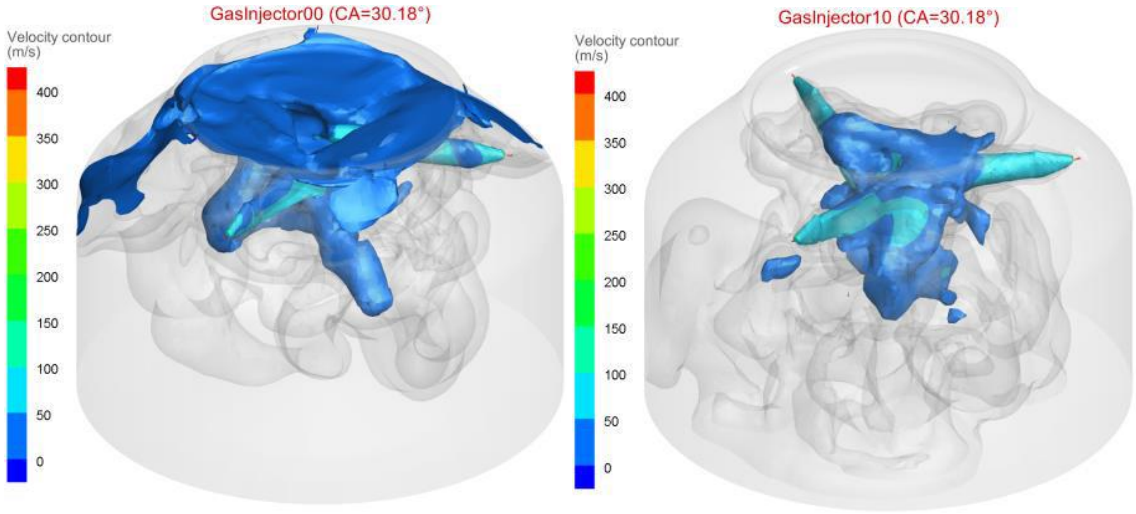

Figure 6.17 Gas distributions at crank angle 30.18 °. GasInjector00 (Left graph): Inclination angle 0 °; GasInjector10 (Right graph): Inclination angle 15 °. Colour Surface is at equivalence ratio ϕ=1.0; Dark grey is at ϕ=0.5; Light grey is at ϕ=0.1

6.4.1.1 Effect of Pilot Injection Timing on the Ignition Kernel

Figures 6.18 - 6.23 illustrate the parameters of the ignition kernel formed by pilot fuel combustion, including the location, volume, mean temperature and maximum temperature. The results at the start of the gas injection are summarised in Table 6.9.

As the piston moves towards TDC, the air density increases due to the in-cylinder increase. The advance of the pilot fuel injection timing decreases the longitudinal penetration of the ignition kernel as demonstrated in Figure 6.18. Due to the pre-swirling in the chamber primarily caused by the air inflow, the positive lateral penetration of ignition kernel is observed in Figure 6.19. Further retarding the pilot spray start from TDC benefits the reduction of lateral location of ignition kernel. The vertical location of ignition kernel slightly varies in the vicinity of the nominal site, which magnitude is lower than other two directions by at least one order of magnitude.

The volume of the ignition kernel is also affected by the pilot injection timing as depicted in Figure 6.21. At start of gas injection, DF3 generates the largest combustion kernel volume due to gas injection start closer to TDC, followed by DF2. DF1 has the lowest ignition volume, which result at the gas injection start is smaller of 33% than DF3.

With respect to the temperature of the ignition kernel, DF2 exhibits the highest mean temperature near the gas injection start, exceeding DF1 and DF3 by 43K and 31K respectively. With comparison of the maximum temperature, despite of the higher value in DF1 at the early stage of pilot fuel spray, it is significantly lower than DF3 by 103K at the gas injection start as listed in Table 6.9, due to the much further retarding the gas injection start from TDC in DF1.

Table 6.9 Comparison of ignition kernel at gas injection start varied with the pilot injection timing

	Ignition Location			V_{IG}/V_C	Ignition Temperature	
	2IK''/B	2K'K/B	2K''K'/B		T_{aver} (K)	T_{max} (K)
DF1	0.631	0.189	-0.026	0.00425	2443	2525
DF2	0.489	0.270	0.027	0.00539	2486	–
DF3	0.570	0.268	-0.037	0.00637	2455	2628

V_{IG}: Ignition volume where the temperature greater than 2400K;

V_C: Clearance volume;

T_{aver}: Mass-averaged Temperature in the ignition kernel;

T_{max}: Maximum temperature in the cylinder.

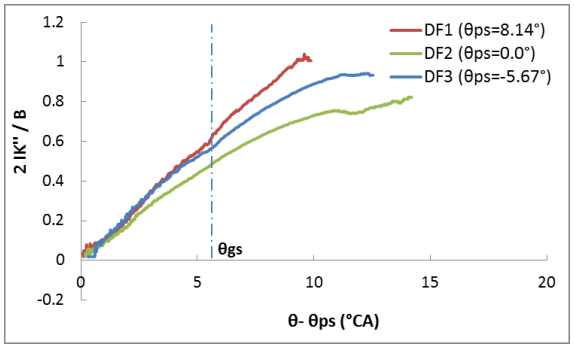

Figure 6.18 Longitudinal location of ignition kernel versus the pilot fuel injection timing.

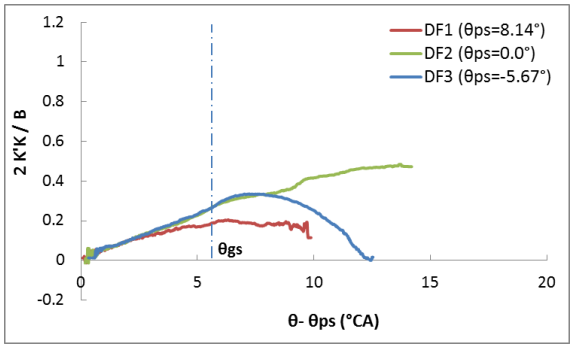

Figure 6.19 Lateral location of ignition kernel versus the pilot fuel injection timing

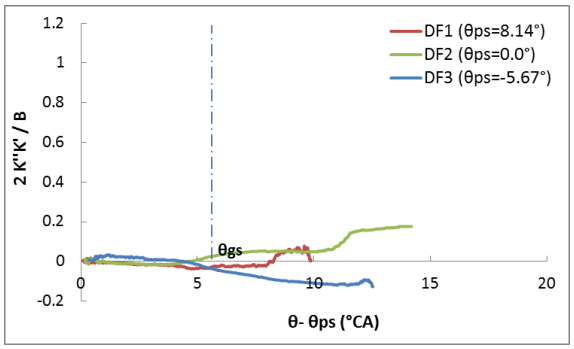

Figure 6.20 Vertical location of ignition kernel varied with the pilot fuel injection timing

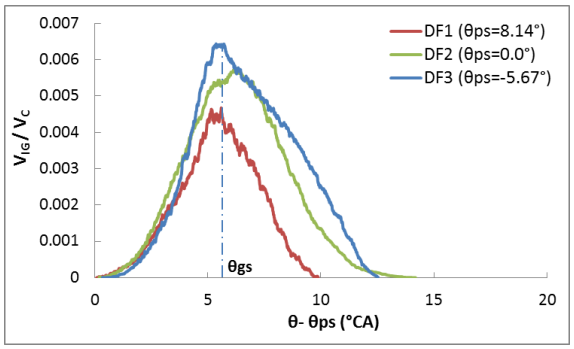

Figure 6.21 Ignition volume varied with the pilot fuel injection timing

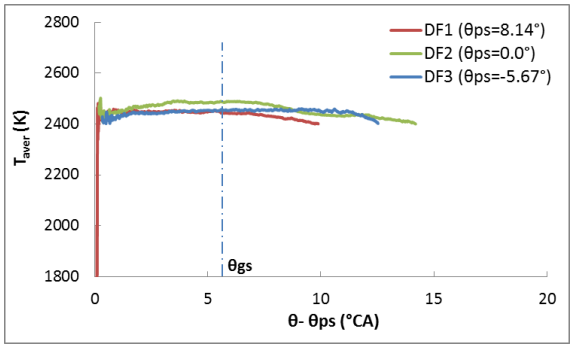

Figure 6.22 Mass-averaged temperature in the ignition kernel varied with the pilot fuel injection timing

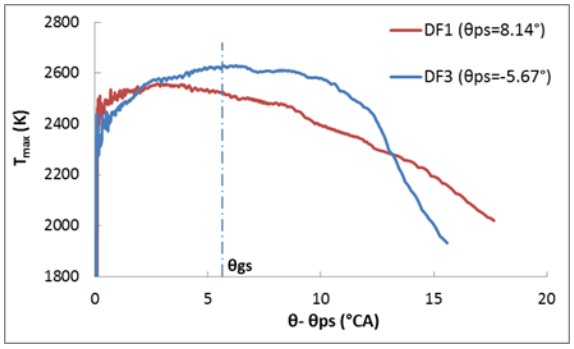

Figure 6.23 Maximum Temperature in-cylinder varied with the pilot fuel injection timing

6.4.1.2 Effect of the DF Injection Timing on the Gaseous Combustion

Figure 6.24 depicts that advancing the gas injection start at TDC (DF3) can substantially increase the in-cylinder pressure. The defined indicated work IMEPcc (equation (6.4)) by the mean pressure integrated by the cylinder volume from -7 °ATDC to 110 °ATDC can be raised by 14%, compared to the initial case DF1 with gas injection start 13.81 °ATDC. This is due to the improvement of the gaseous combustion process, leading the significant reduction in the incomplete combustion products as shown in Table 6.10. The effects of the pilot fuel and the gas fuel are clearly observed in Figure 6.25.

$$\text{IMEPcc} = \int_{-7^\circ}^{110^\circ} \text{PdV}/\Omega_S \qquad (6.4)$$

In equation (6.4), Ω_S denotes the swept volume for each engine cylinder.

As seen in Figure 6.26, retarding the gas injection timing leads to the reduction of the mean in-cylinder temperature. At the late expansion stroke after 50 °ATDC, the in-cylinder temperature of the DF3 is higher than that of DF2, as well as the heat release rate presented in Figure 6.27. Four peak HRRs are observed in Figure 6.27, where the former three peaks are associated with the pilot and gas fuel combustion. The last peak and the related valley at 40 °ATDC are caused by the change of the time step of CFD simulation for the decrease of the computational cost. The first valley HRR is apparently due to the completion of the pilot fuel combustion, followed by the second valley which results from the cold gas plumes impinging on the burning gas.

Methane concentration in-cylinder variation shown in Figure 6.28 indicates that retarding the gas injection timing increases the unburned methane. Based on the atomic conservation, the intermediates can be estimated by the fuel and carbon dioxide mass fraction shown in Figures 6.28 and 6.29. It is found that advancing the gas injection start at TDC can be significantly beneficial of the reduction of the intermediates.

As expected, the improvement of the gaseous combustion usually implies the higher combustion temperature in the cylinder, which will lead the increase of NO emission. However, DF2 produces the slightly lower NO emission than DF1. Based on the comparison of the in-cylinder maximum temperature curves and the high-temperature volume ratio greater than 2000K for cases DF1 and DF2 depicted in Figures 6.31 and 6.32, it can be inferred that the greater NO emission for DF1 is primarily attributed to the late continuous gas combustion.

Table 6.10 Engine performance and emissions affected by the DF injection timing

	IMEPcc (barabs)	Mass Fraction of NO (ppm)	Mass Fraction of CO (ppm)	Mass Fraction of Unburned HC (ppm)	Mass Fraction of CO_2 (ppm)
DF1	19.80	986	11526	304	54796
DF2	20.56	839	10641	211	54557
DF3	22.50	1109	5089	76	56251
Note: Emissions evaluated at 110 °ATDC before exhaust valve opens.					

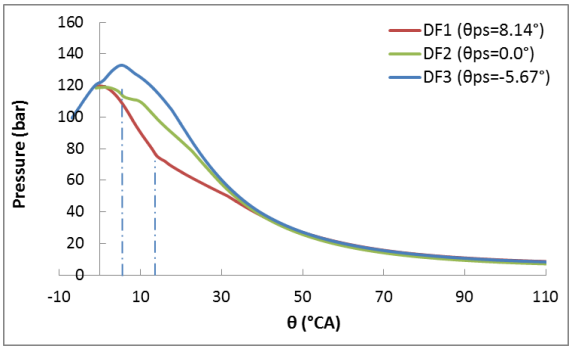

Figure 6.24 In-cylinder pressure affected the different DF injection timing in the closed cycle

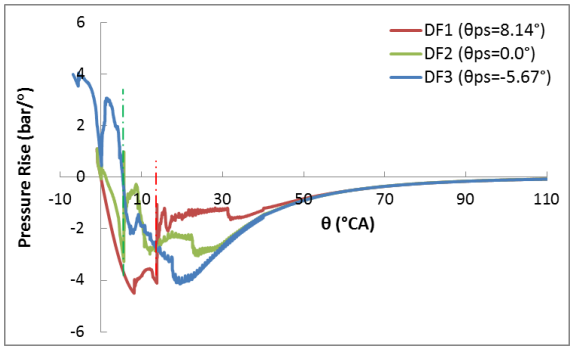

Figure 6.25 Pressure rise affected the different DF injection timing in the closed cycle

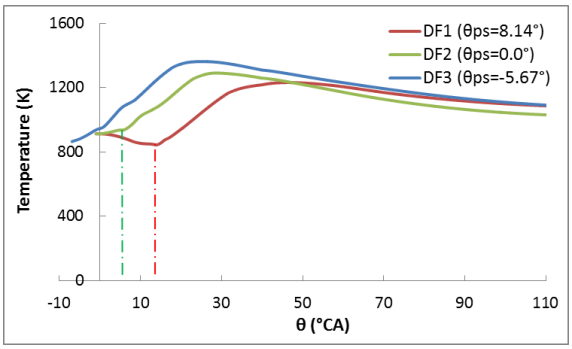

Figure 6.26 Mean temperature in-cylinder affected the different DF injection timing in the closed cycle

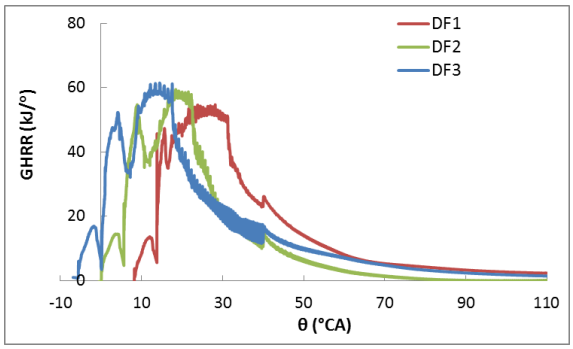

Figure 6.27 HRR affected the different DF injection timing in the closed cycle

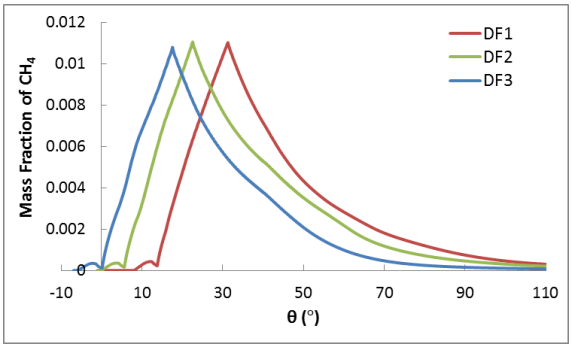

Figure 6.28 Mass fraction of methane affected the different DF injection timing in the closed cycle

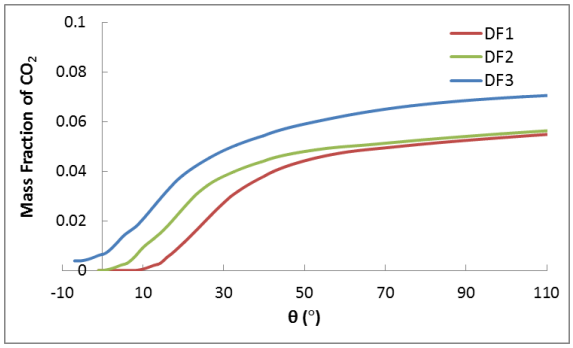

Figure 6.29 Mass fraction of carbon dioxide affected the different DF injection timing in the closed cycle

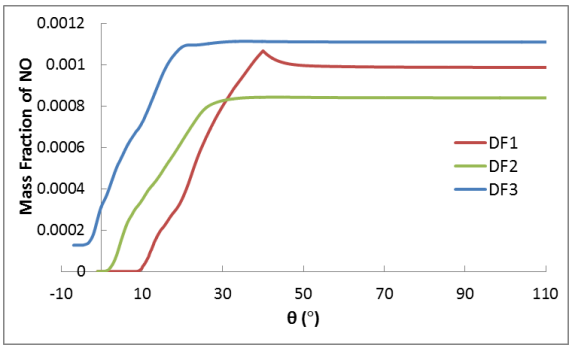

Figure 6.30 Mass fraction of nitric oxide affected the different DF injection timing in the closed cycle

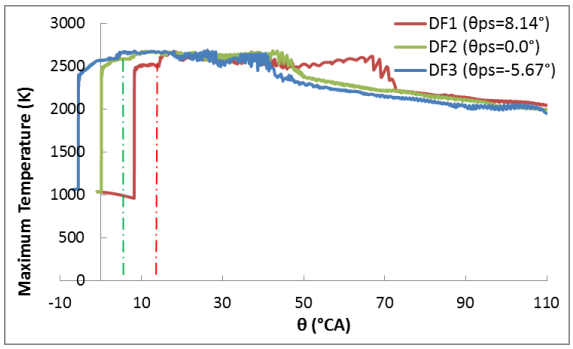

Figure 6.31 Maximum Temperature affected the different DF injection timing in the closed cycle

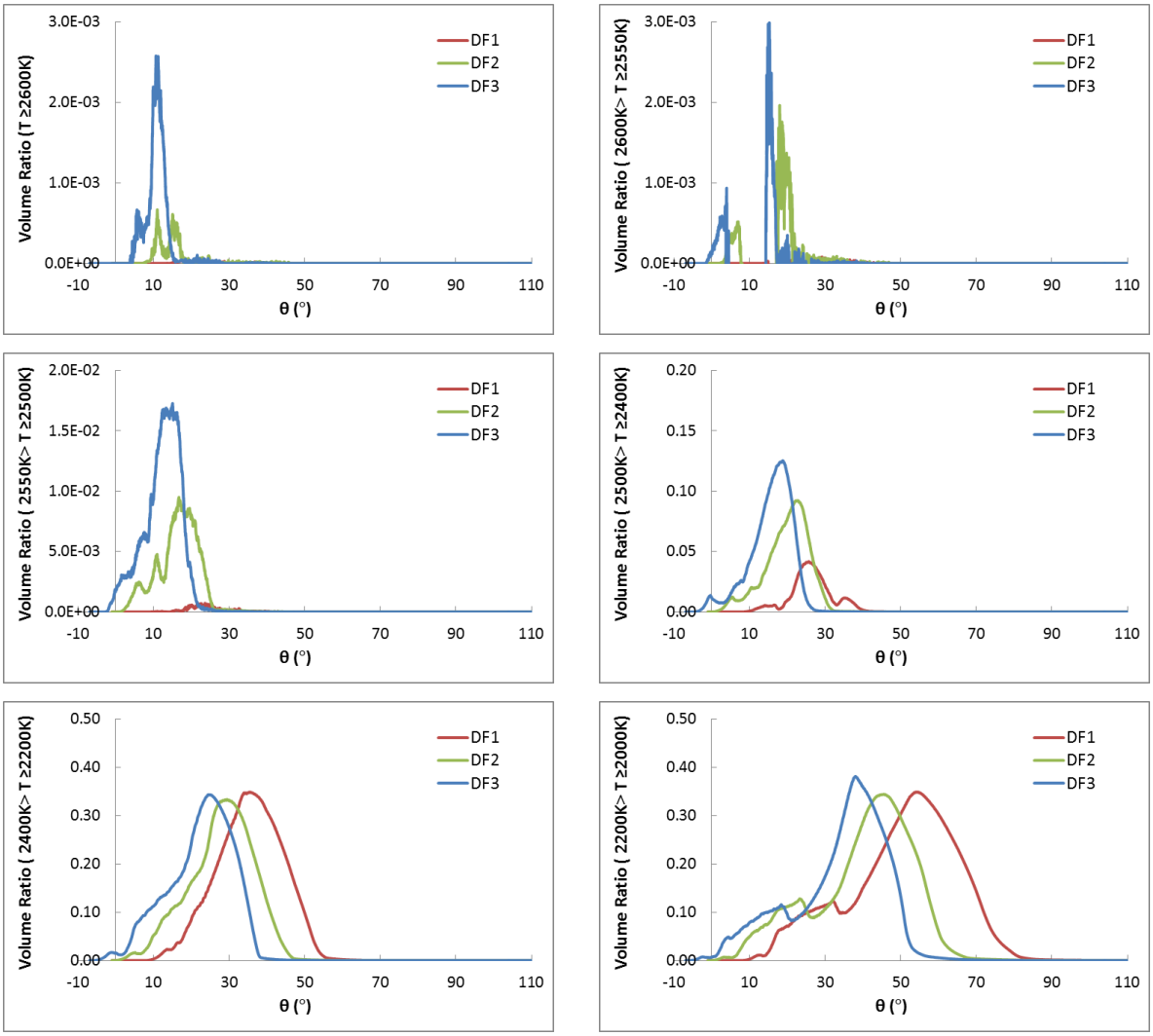

Figure 6.32 High-temperature volume ratio in-cylinder varied with the DF injection timing in the close cycle

6.4.2 Effects of the Gas Injection Duration

The three investigated cases where the gas injection duration changes from 11.24 ℃A to 17.32 ℃A listed in Table 6.11, will be compared.

Figure 6.33 demonstrates that shortening the gas injection duration can increase the in-cylinder maximum pressure and the corresponding indicated work IMEPcc shown in Table 6.12. The resulted pressure derivations with respect to crank angle (CA) are presented in Figure 6.34, which depict the higher pressure rise caused by the increase of the gas mass flow rate due to the reduction of the gas injection duration.

Apparently, the higher pressure and pressure rise resulted from the higher availability of the injected gas can lead to the higher in-cylinder mean temperature and heat release during the gas injection, shown in Figures 6.35 and 6.36. Owing to the cold gas plumes contacting the flame surface in the three cases, the deterioration of the gas combustion quality can be observed, in terms of the HRR

curves where the considerable reduction of the released heat is found after the early stage of gas burning at 6 ℃A.

Also, the higher injected gas flow rate can cause the more intermediate species and methane to be created during the combustion process, as well as the CO_2, shown in Figure 6.37 and Figure 6.38. Based on the atomic conservation, the intermediate species concentration can be estimated. Table 6.12 indicates that there is no notably change in the intermediate species produced by the incomplete combustion, which implies that the reduction of gas injection duration and the simultaneous increase of the gas flow rate do not remarkably improve the gas combustion quality and emissions.

The NO formation is associated with the high-temperature zone within the engine cylinder. It seems that DF6 with the shortest gas injection duration provides the longest combustion duration, in terms of the maximum temperature curved by the crank angle in Figure 6.40. With respect to the volume occupied by the high temperature gas greater than 2000 K, only slightly changes can be observed in Figure 6.41. Consequently, the three investigated cases almost have the same NO emissions, as inferred from the results presented in Table 6.12, where the maximum difference is about 5%.

Table 6.11 Parameters regarding the change of the gas injection duration

	Pilot Injector			Gas Injector				
	Timing (°ATDC)	α_l (°)	β_l (°)	Timing (°ATDC)	Duration (℃A)	Holes Number	α_g (°)	β_g (°)
DF4	-1.5~3.02	15	0	0.0~17.32	17.32	1	15	0
DF5	-1.5~3.02	15	0	0.0~14.46	14.46	1	15	0
DF6	-1.5~3.02	15	0	0.0~11.24	11.24	1	15	0

Table 6.12 Engine performance and pollutant emissions varied with the gas injection duration under dual fuel operation

	IMEPcc (barabs)	Mass Fraction of NO (ppm)	Mass Fraction of CO (ppm)	Mass Fraction of Unburned HC (ppm)	Mass Fraction of CO_2 (ppm)
DF4	22.30	1008	5938	149	69026
DF5	22.61	1059	5994	126	69541
DF6	22.62	1046	6013	120	68402

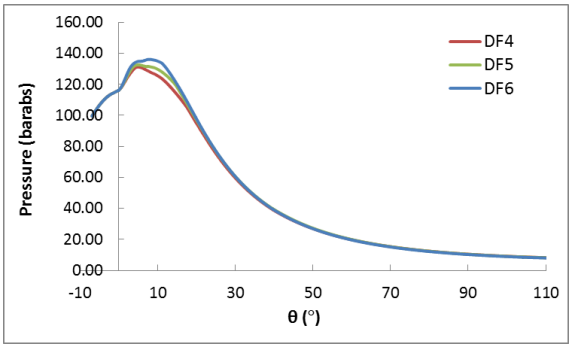

Figure 6.33 In-cylinder pressure curves under the different gas injection durations

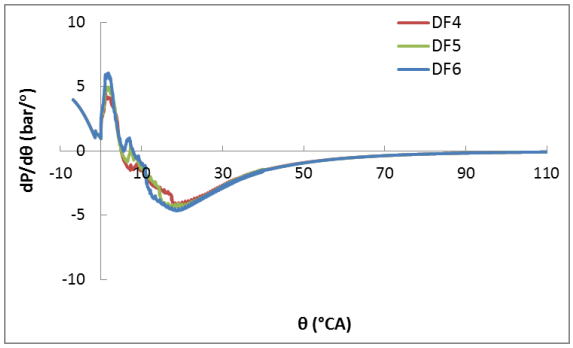

Figure 6.34 Pressure rises under the different gas injection durations

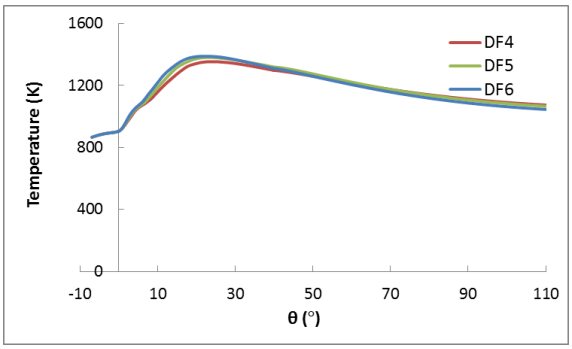

Figure 6.35 In-cylinder temperature curves under the different gas injection durations

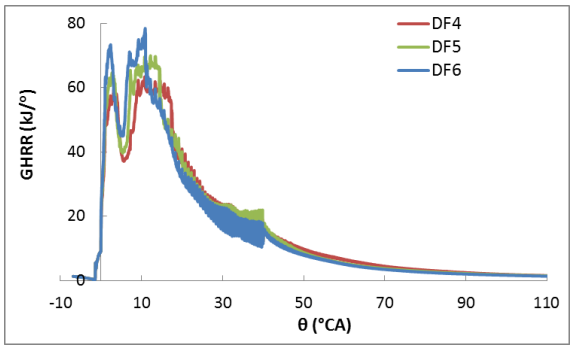

Figure 6.36 HRR curves under the different gas injection durations

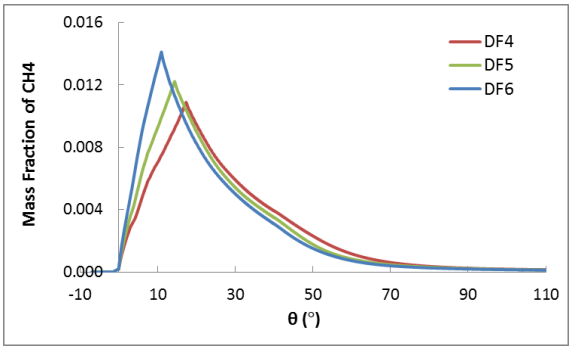

Figure 6.37 Mass fraction of methane in-cylinder under different gas injection duration

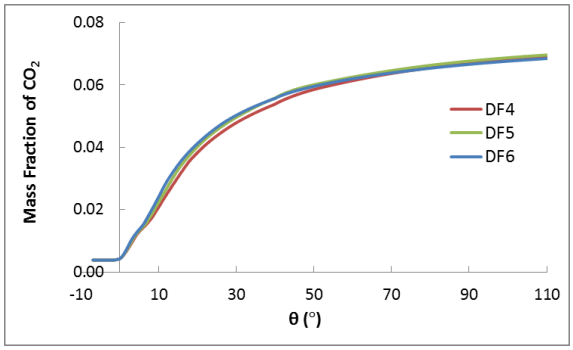

Figure 6.38 Mass fraction of carbon dioxide in-cylinder under different gas injection duration

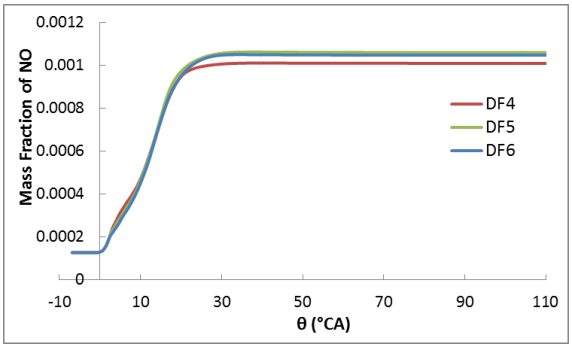

Figure 6.39 Mass fraction of nitric oxide in-cylinder under different gas injection duration

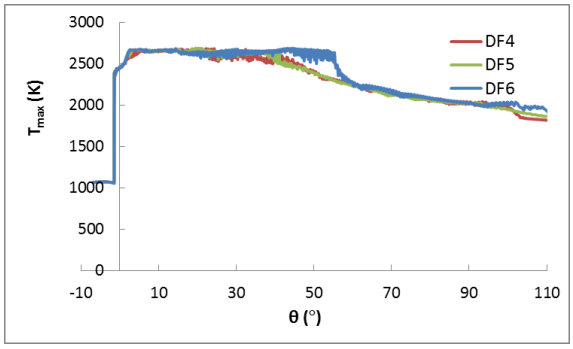

Figure 6.40 Maximum temperature against the crank angles under different gas injection duration

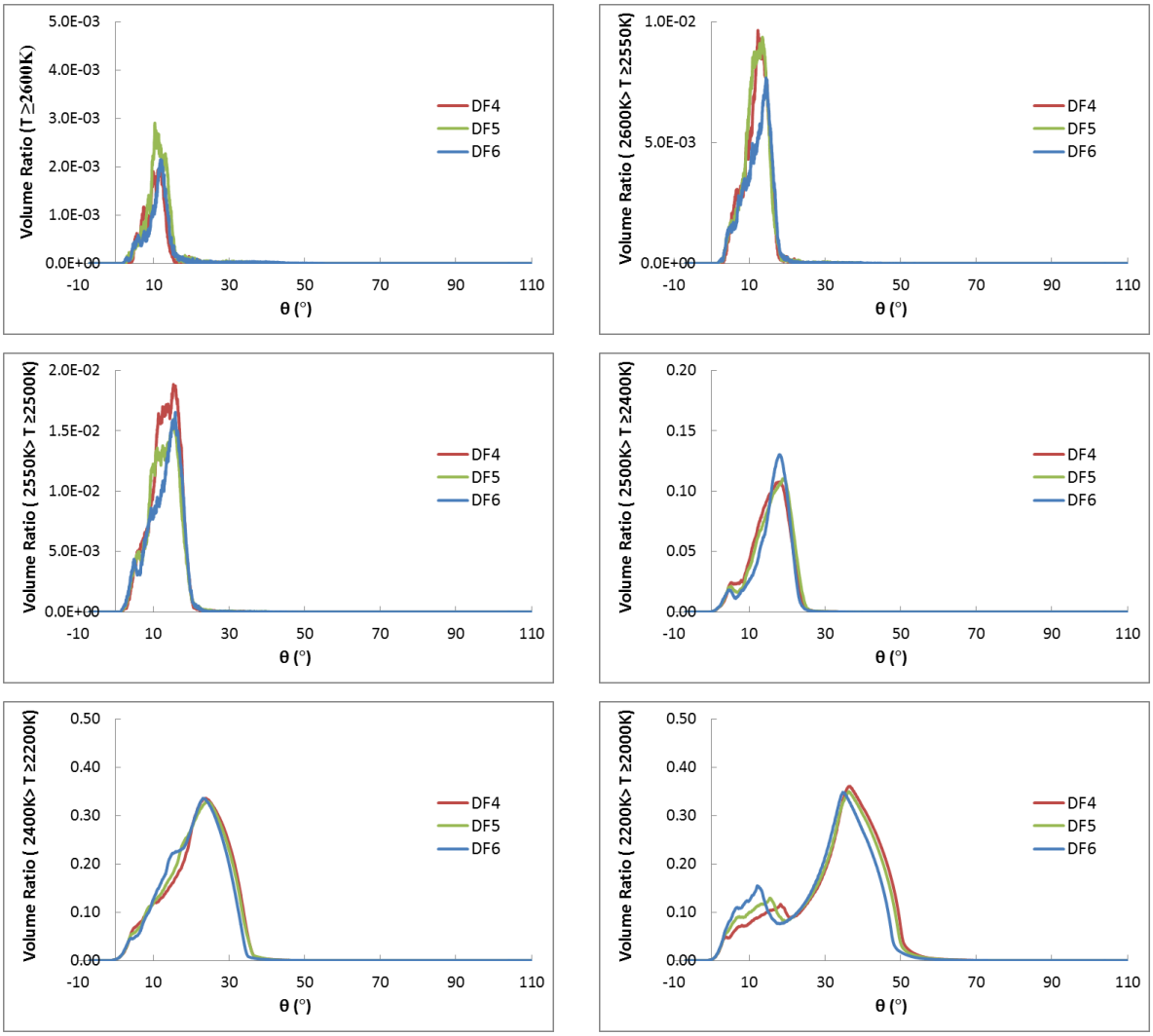

Figure 6.41 High-temperature volume ratio in-cylinder greater than 2000K under different gas injection duration

6.4.3 Change of Lateral Angle in Single-Hole Gas Injector

In order to avoid the injected gas stream to come in contact the diffusion flame surface as much as possibly, three cases with the different lateral angle in the one-hole gas injector are investigated, the parameters of which are presented in Table 6.13.

In terms of the pressure and the related pressure rise curves presented in Figures 6.42 and 6.43, it can be seen that the change of the gas injection direction can significantly raise the mean in-cylinder pressure, where the corresponding indicated work IMEPcc increases by 12% as the lateral angle of gas injector varied from 0 °to 30 °.

The increase of the in-cylinder pressure is attributed to the improvement of combustion quality, which apparently can increase the in-cylinder temperature as depicted in Figure 6.44. The HRR curves further demonstrate the improvement of gaseous combustion process, where the higher heat release peak occurs and the valley become more flattened as the larger lateral angle.

With regard to the unburned methane, the lower content can be observed in Figure 6.46, as the increase of the lateral angle of the gas nozzle. Hence, it can be expected that the more CO_2 and less intermediates are produced as the lateral angle of the gas nozzle changes to -30°, demonstrated in Figure 6.47 and Table 6.14.

Figure 6.48 depicts that the combustion duration is shortened as increasing the lateral angle of gas injector, attributed to the reduction of the intermediates dwelling in the cylinder. However, the NO formation rate is substantially increased, as indicated in Figure 6.49. This is the reason that the combustion chamber volume with the temperature greater 2400 K significantly increases, as demonstrated in Figure 6.50. At 110 °ATDC before the exhaust valve opening, the NO emission occupies 2282 ppm in the case DF8 with -30° lateral angle of gas injector, greater than that of the cases DF6 and DF7 by 1236 ppm and 418 ppm respectively.

Table 6.13 Cases parameters for the investigation of the gas injection direction

	Pilot Injector			Gas Injector				
	Timing (°ATDC)	α_l (°)	β_l (°)	Timing (°ATDC)	Duration (°CA)	Holes Number	α_g (°)	β_g (°)
DF6	-1.5~3.02	15	0	0.0~11.24	11.24	1	15	0
DF7	-1.5~3.02	15	0	0.0~11.24	11.24	1	15	-15
DF8	-1.5~3.02	15	0	0.0~11.24	11.24	1	15	-30

Table 6.14 Dual fuel engine performance and emissions varied with the gas injection direction

	IMEPcc (barabs)	Mass Fraction of NO (ppm)	Mass Fraction of CO (ppm)	Mass Fraction of Unburned HC (ppm)	Mass Fraction of CO_2 (ppm)
DF6	22.61	1046	6013	120	68402
DF7	24.58	1864	1419	8	77596
DF8	25.24	2282	18	0.0	79765

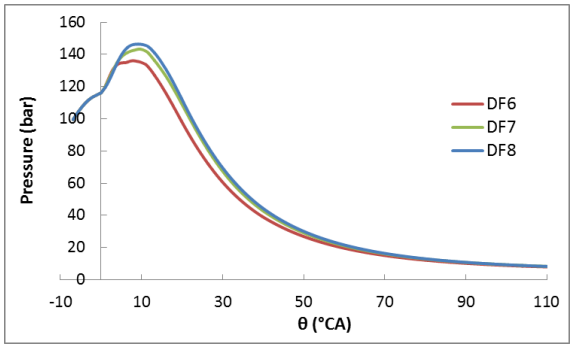

Figure 6.42 In-cylinder pressure variation for different lateral angles of single-hole gas injector

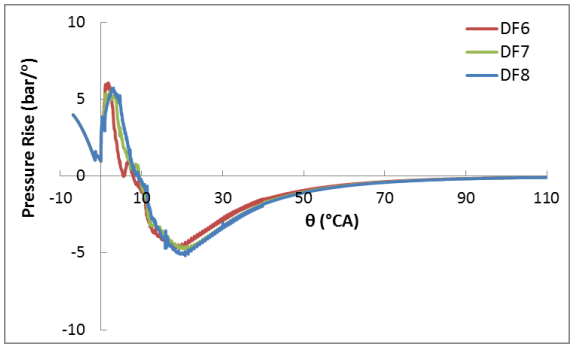

Figure 6.43 Pressure rise variation for different lateral angles of single-hole gas injector

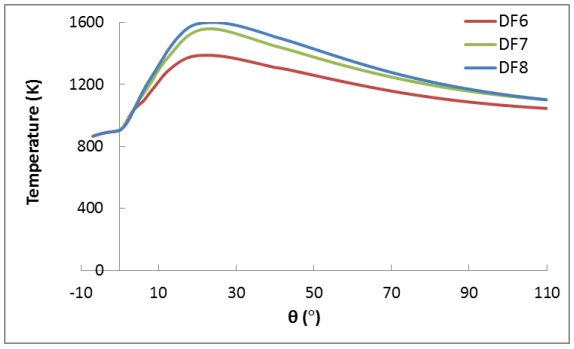

Figure 6.44 In-cylinder mean temperature variation for different lateral angles of single-hole gas injector

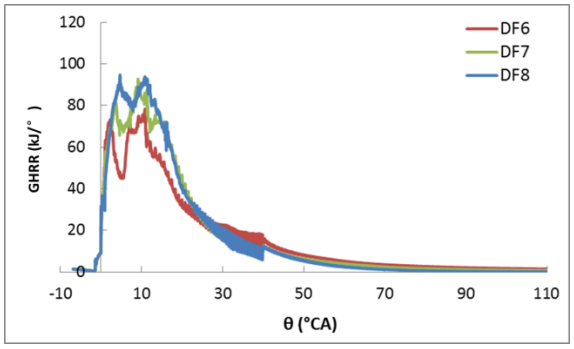

Figure 6.45 HRR for different lateral angles of single-hole gas injector

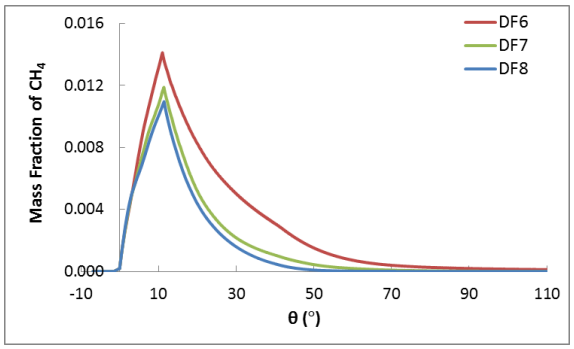

Figure 6.46 Mass fraction of methane variation for different lateral angles of single-hole gas injector

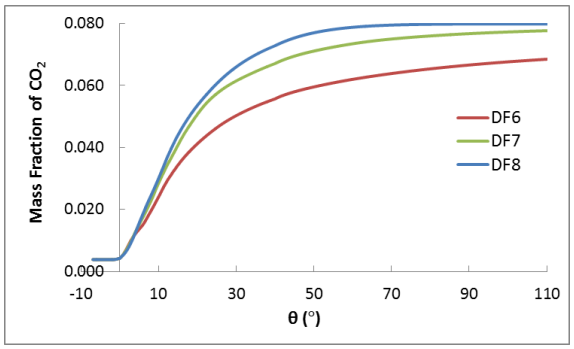

Figure 6.47 Mass fraction of carbon dioxide variation for different lateral angles of single-hole gas injector

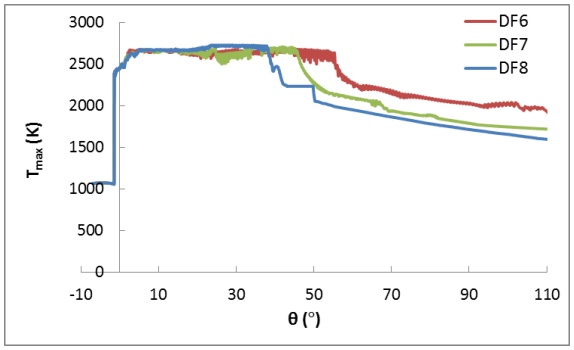

Figure 6.48 Maximum temperature variation for different lateral angles of single-hole gas injector

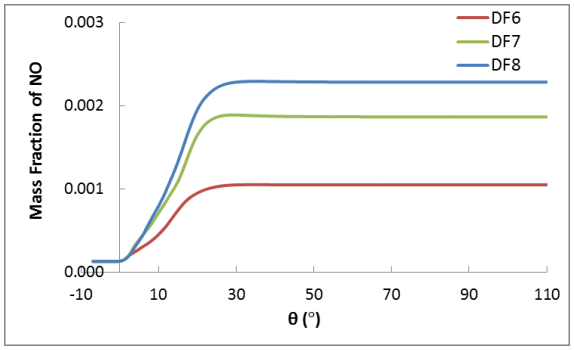

Figure 6.49 Mass fraction of nitric oxide variation for different lateral angles of single-hole gas injector

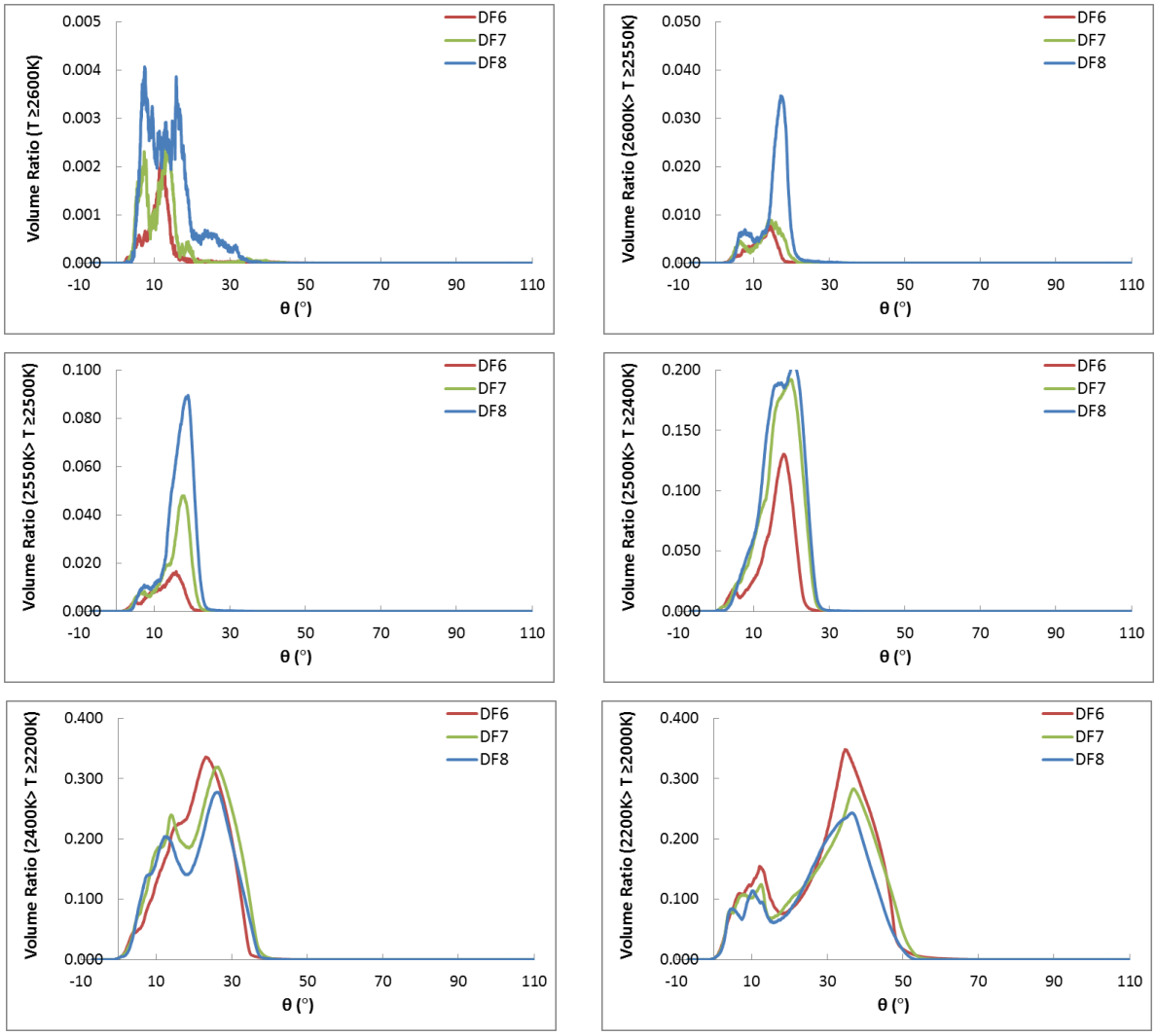

Figure 6.50 Variation of high-temperature volume ratio greater 2000 K for different lateral angles of the single-hole gas injector

6.4.4 Effects of Holes Number of Gas Injector

Three gas injectors with one, three and five holes respectively will be compared. Table 6.15 depicts that the lateral angle of the middle hole in each gas injector is -30 °, and the separation angle between holes is equal to 20 °.

Figures 6.51 ~ 6.53 and Table 6.16 demonstrate that there is no monotonous relationship between the holes number of gas injector and the pressure or temperature. Due to the greater heat release peak values (Figure 6.54) caused by the more rapidly burning rate of gas (Figure 6.56), DF10 provides the highest pressure and temperature during the early stage of gas injection. As a consequence, the lowest pressure and temperature in DF10 at late combustion process can be observed. These results demonstrate that the mixing process for the case of the 5-hole gas injector is better in comparison with the other two investigated gas injector, as depicted in Figure 6.57.

For DF8 and DF9 cases, after the early gas combustion, the gas flame contacts the cold plumes, which deteriorates the combustion process. Therefore, more gas fuel is retained and lower carbon dioxide is produced, as shown in Figures 6.55 and 6.56. For DF9, the lower temperature on the stoichiometric surface of gas plumes compared with case DF8 (single-hole gas injector). Hence, the lower in-cylinder pressure and mean temperature in the closed cycle is estimated, despite of the slightly higher heat release at late expansion stroke.

The indicated work in DF10 is found to be 3% lower than that of DF8, despite the higher peak pressure. In the three cases, Table 6.16 lists that all the methane is consumed and extremely low unburned HC and CO are emitted, due to the excellent combustion quality.

Due to the greater flame temperature and associated flame volume during the gas injection process as presented in Figures 6.58 and 6.60, DF8 produces the highest NO emissions in these three cases. DF9 achieves the minimum NO emission, but the indicated work is also considerably reduced. According to the HRR and flame temperature shown in Figures 6.54 and 6.58, the reduction of the in-cylinder pressure for DF9 is mainly due to the amount of the gas combustion retarding to the late stroke. Case DF10 produces the remarkable reduction of NO emission by 23% and maintains the similar power level to case DF8.

Table 6.15 Case parameters in the investigation of the holes number of the gas injector

	Pilot Injector			Gas Injector					
	Timing (°ATDC)	α_l (°)	β_l (°)	Timing (°ATDC)	Duration (°CA)	Holes Number	Hole Diameter (mm)	α_g (°)	β_g (°)
DF8	-1.5~3.02	15	0	0.0~11.24	11.24	1	6.03	15	-30
DF9	-1.5~3.02	15	0	0.0~11.24	11.24	3	3.48	15	-50, -30, -10
DF10	-1.5~3.02	15	0	0.0~11.24	11.24	5	2.70	15	-70, -50, -30,-10, 10

Table 6.16 Dual fuel engine performance and emissions influenced by the holes number of the gas injector

	IMEPcc (barabs)	Mass Fraction of NO (ppm)	Mass Fraction of CO (ppm)	Mass Fraction of Unburned HC (ppm)	Mass Fraction of CO_2 (ppm)
DF8	25.24	2282	18	0.0	79765
DF9	23.99	1260	13	0.0	79841
DF10	24.50	1791	6	0.0	79457

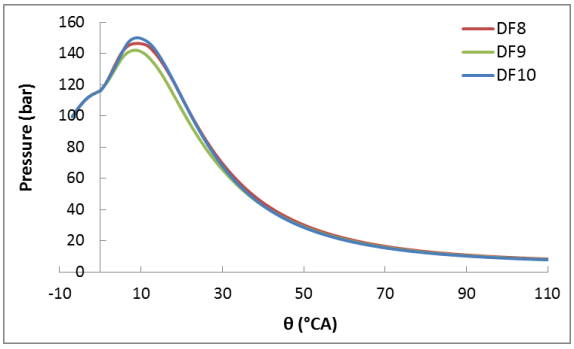

Figure 6.51 In-cylinder pressure versus the holes number of the gas injector

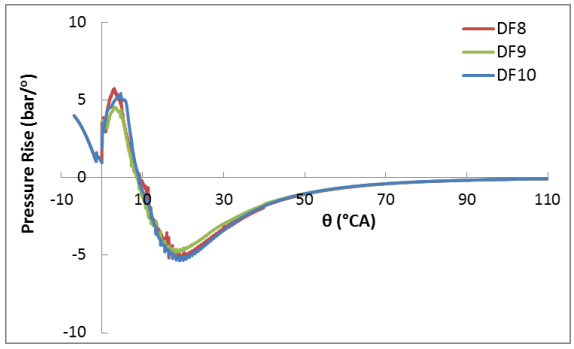

Figure 6.52 Pressure rise versus the holes number of the gas injector

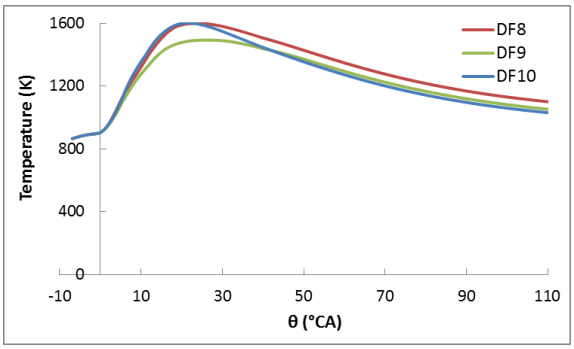

Figure 6.53 Mean temperature versus the holes number of the gas injector

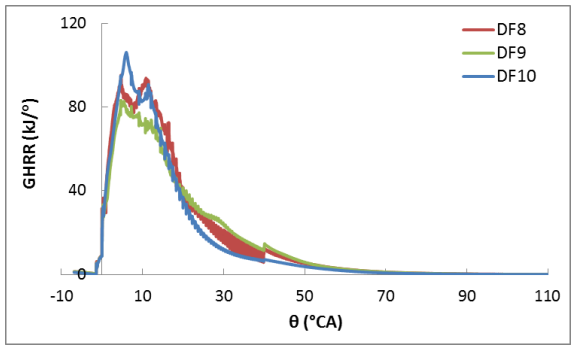

Figure 6.54 HRR versus the holes number of the gas injector

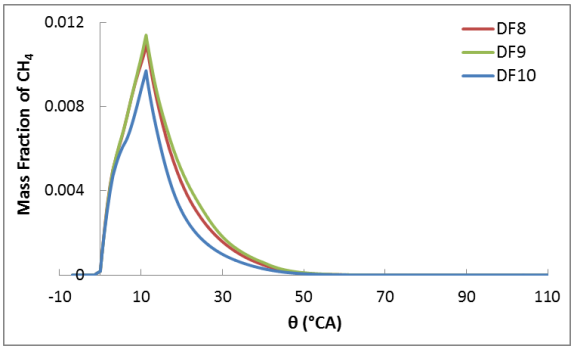

Figure 6.55 Mass fraction of methane versus the holes number of the gas injector

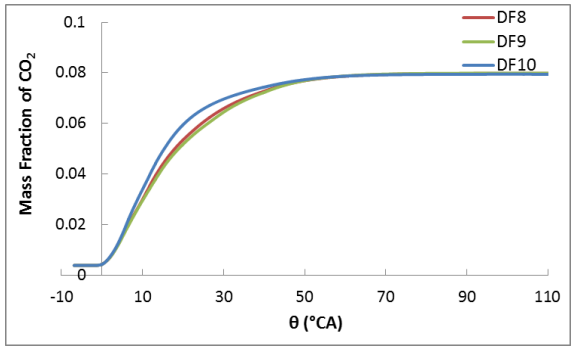

Figure 6.56 Mass fraction of carbon dioxide versus the holes number of the gas injector

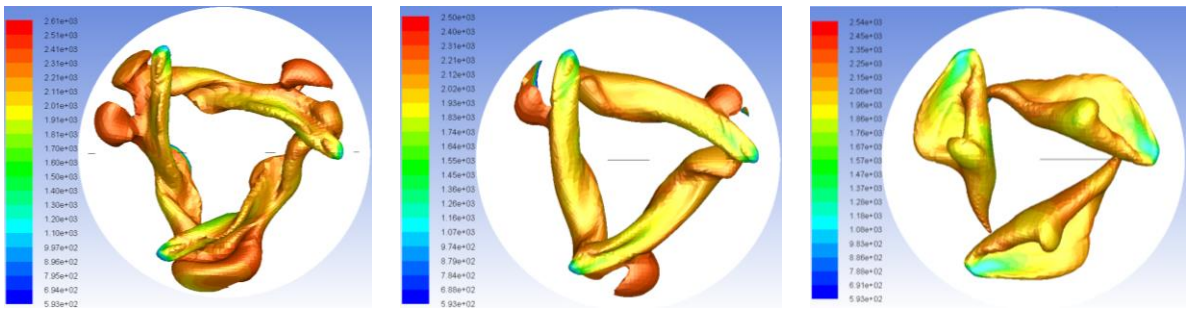

(a) Single-hole gas injector (b) Three-hole gas injector (c) Five-hole gas injector

Figure 6.57 The temperature contours on the stoichiometric surface of gas plumes at crank angle 10 °ATDC

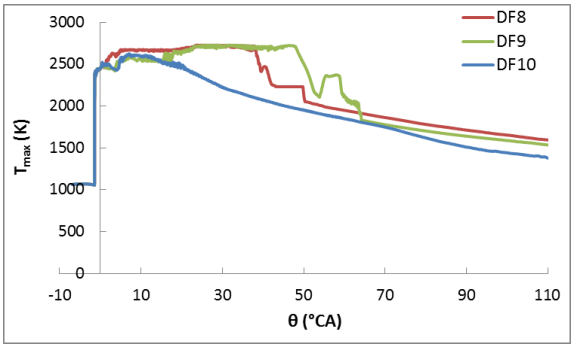

Figure 6.58 Maximum temperature versus the holes number of the gas injector

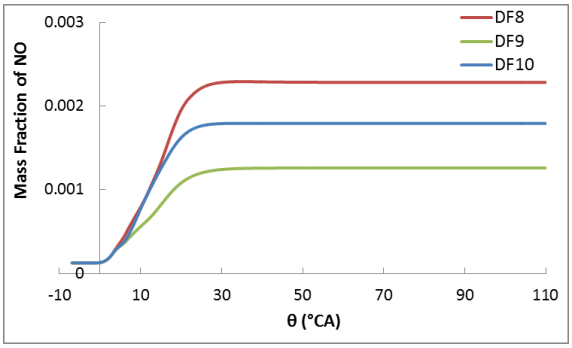

Figure 6.59 Mass fraction of nitric oxide the holes number of the gas injector

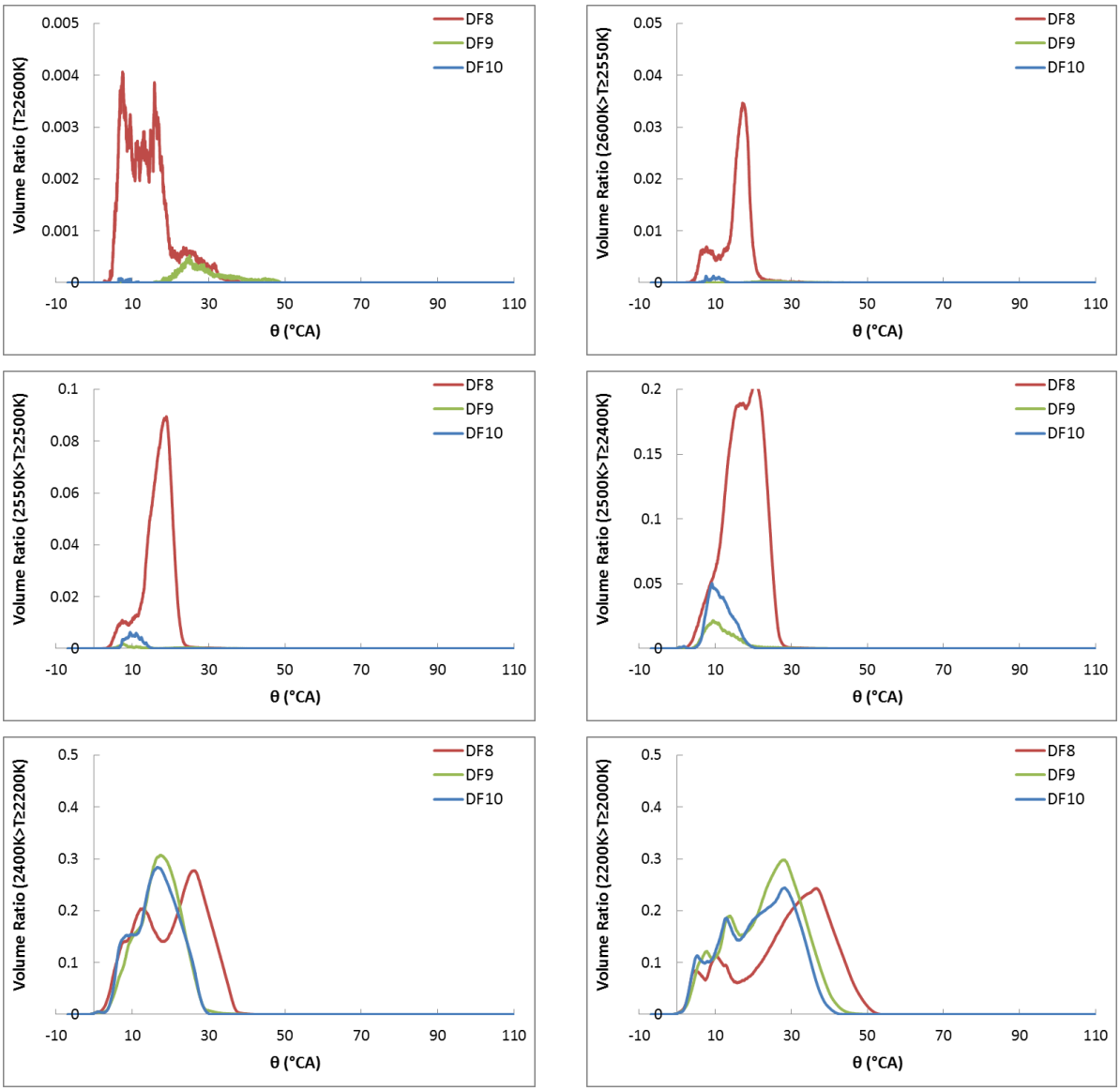

Figure 6.60 High-temperature volume ratio greater 2000 K versus the holes number of the gas injector

6.4.5 Effects of the Different Inclination Angle for Each Gas Hole

For the case DF10 with the same inclination angle 15 ° for each gas hole, two new cases DF11 and DF12 are investigated. In DF11, the inclination angle of the mid hole in 5-hole gas injector is equal to

15 °, and the separation inclination angle between holes is set to 4 °. With the same separation inclination angle to DF11, the inclination angle of mid hole in DF12 is designated to 23 °, shown in Table 6.17.

By comparing the results of cases DF10 and DF11, it can be inferred that there is no distinguishable variation in the engine performance, combustion quality and gaseous pollutant formations caused by the change of the inclination angle for each hole in 5-hole gas injector, provided in Table 6.18 and Figures 6.61 - 6.69.

For an 8 ° increase in the inclination angle for each gas hole (DF12), the engine performance and emissions are shown in Table 6.18. The pressure variation provided in Figure 6.61 demonstrates that the in-cylinder peak pressure exhibits a slight increase in DF12, as well as the peak of the mass-averaged temperature shown in Figure 6.63. In terms of the mean temperature variation shown in Figure 6.63, it can be concluded that the in-cylinder mean pressure at late combustion process in DF12 slightly declines, compared to DF11. Based on the HRR curves in Figure 6.64, it is inferred that the increase of the inclination angle of gas hole in DF12 can improve the gaseous combustion quality, which benefits the reduction of methane slip shown in Figure 6.65. The production of CO_2 will marginally increase during the combustion process presented in Figure 6.66. The NO formation in DF12 is remarkably increased, attributed to the higher maximum temperature and the larger high-temperature volume greater than 2000 K. Table 6.18 shows that the NO emission in DF12 is higher than that of DF11 by 11%.

Table 6.17 Cases parameters for the investigation of the inclination angle of the gas hole

	Pilot Injector			Gas Injector				
	Timing (°ATDC)	α_l (°)	β_l (°)	Timing (°ATDC)	Duration (°CA)	Holes Number	α_g (°)	β_g (°)
DF10	-1.5~3.02	15	0	0.0~11.24	11.24	5	15	-70
							15	-50
							15	-30
							15	-10
							15	10
DF11	-1.5~3.02	15	0	0.0~11.24	11.24	5	23	-70
							19	-50
							15	-30
							11	-10
							7	10
DF12	-1.5~3.02	23	0	0.0~11.24	11.24	5	31	-70
							27	-50
							23	-30
							19	-10
							15	10

Table 6.18 Dual fuel engine performance and emissions affected by the gas-hole inclination angle

	IMEPcc (barabs)	Mass Fraction of NO (ppm)	Mass Fraction of CO (ppm)	Mass Fraction of Unburned HC (ppm)	Mass Fraction of CO_2 (ppm)
DF10	24.50	1791	6	0.0	79457
DF11	24.51	1820	4	0.0	79489
DF12	24.56	2019	61	0.0	79518

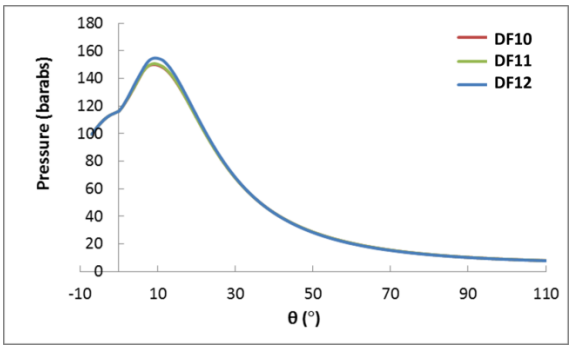

Figure 6.61 In-cylinder pressure curves versus the inclination angle of 5-hole gas injector

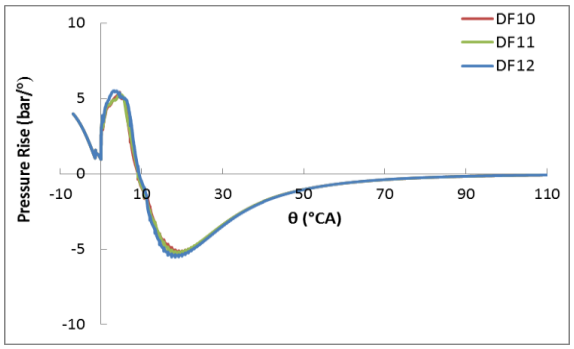

Figure 6.62 Pressure rise curves versus the inclination angle of 5-hole gas injector

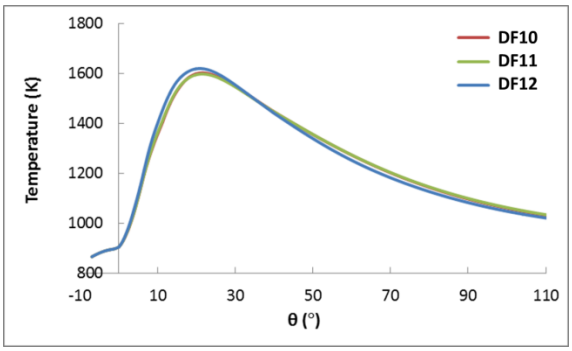

Figure 6.63 Mean temperature curves versus the inclination angle of the 5-hole gas injector

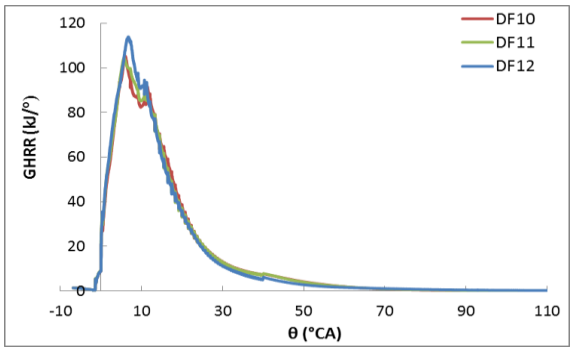

Figure 6.64 HRR curves versus the inclination angle of the 5-hole gas injector

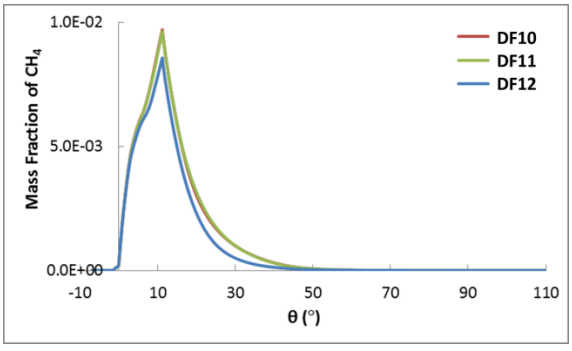

Figure 6.65 Mass fraction of methane versus the inclination angle of the 5-hole gas injector

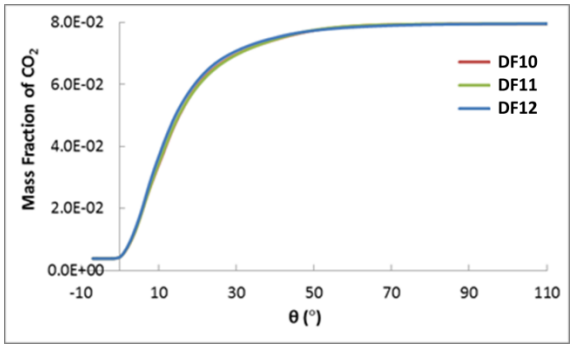

Figure 6.66 Mass fraction of carbon dioxide versus the inclination angle of the 5-hole gas injector

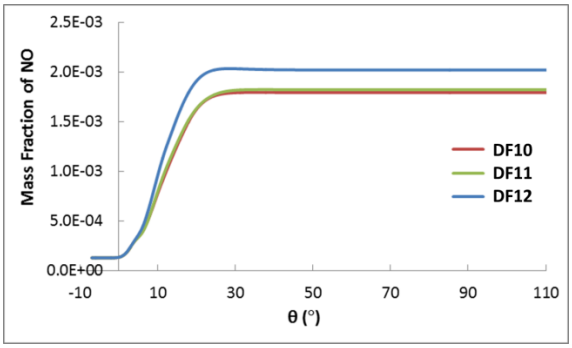

Figure 6.67 Mass fraction of nitric oixde versus the inclination angle of the 5-hole gas injector

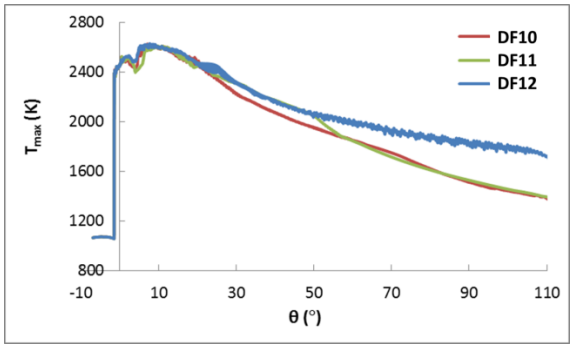

Figure 6.68 Maximum temperature versus the inclination angle of the 5-hole gas injector

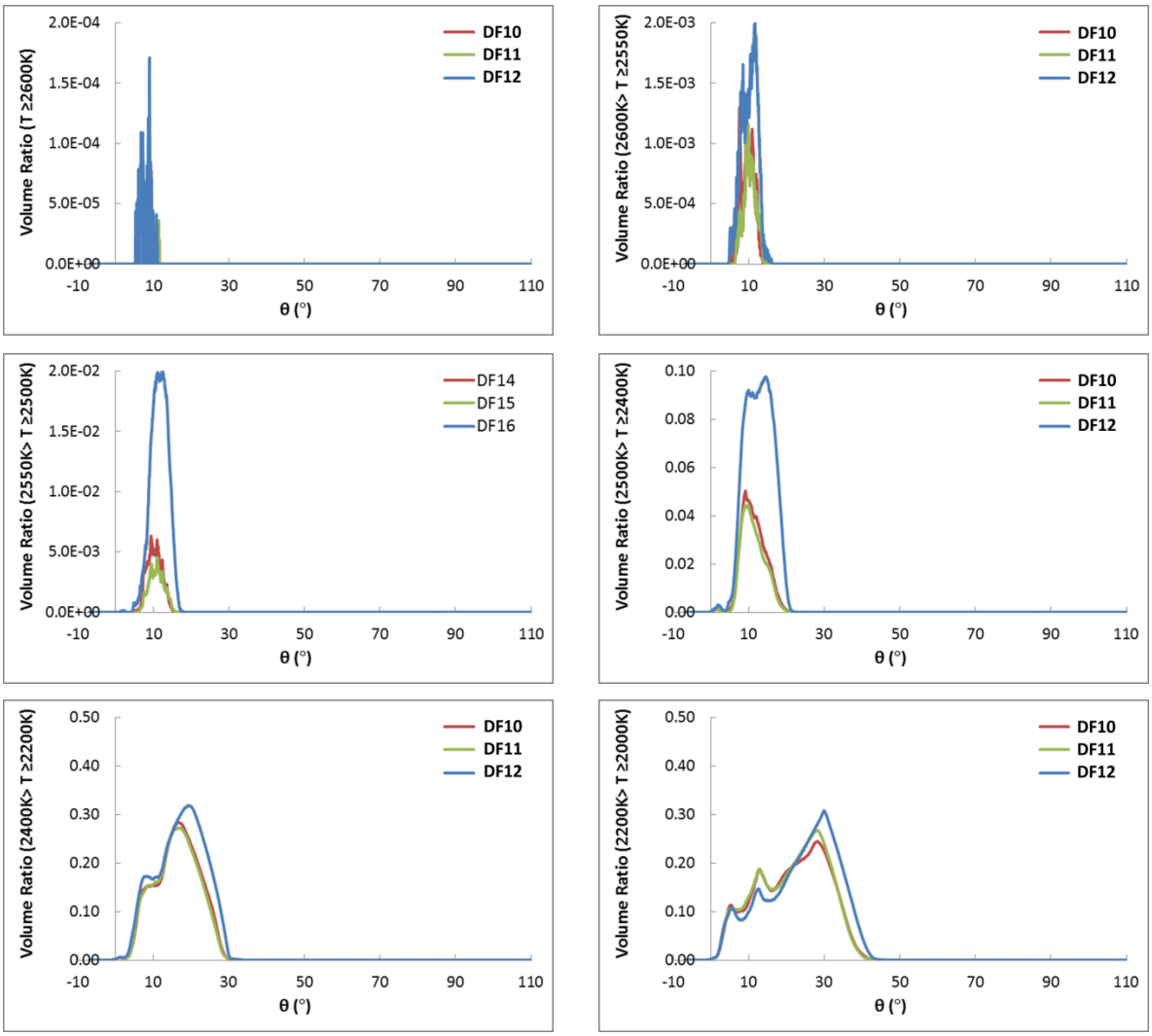

Figure 6.69 High-temperature volume ratio greater than 2000K versus the inclination angle of the 5-hole gas injector

6.5 Recommended Set of Design Parameters

Apart from the above-mentioned cases, the four additional cases also are investigated and the simulation results are evaluated to comment on the recommended parameters, as shown in Table 6.19 and Table 6.20.

Generally, in the same engine supplied by the same mass and type of fuel, the higher IMEPcc implies the higher CO_2 production and NO emission, due to the improvement of the fuel combustion process. As a consequence, the optimisation of engine settings for increasing the IMEPcc and simultaneously reducing CO_2 and NO emissions is a compromising process. For the investigated engine, the associated results are plotted for all the investigated cases as shown in Figure 6.70.

With respect to the diesel mode, the IMEPcc was estimated about 24.74 bar. In order to maintain the same engine output, the similar level of IMEPcc in the dual fuel operation needs to be met. Hence, DF8, DF10, DF11 and DF12 are the preferable choice, which are summarized in Table 6.21. Table 6.21 depicts that all the methane is consumed in these four cases, as well as the unburned HC. Despite of the notable in-cylinder lower peak pressure (Figure 6.71) caused by the relatively unfavourable mixing process and the flame surface impinging on the cold gas plumes, DF8 with three one-hole gas injectors still has a higher IMEPcc due to the longer combustion duration (Figure 6.72), which also results in the 25% increments of the NO emission, compared to DF11. The cases DF10, DF11 and DF12 achieves the similar engine power, whilst the NO emission for DF12 is noticeable higher of 12% than that of DF10 or DF11. By comparing the case DF10 with DF11, both indicated work IMEPcc and gaseous emissions approach together. Table 6.21 lists that the more slightly complete combustion takes place in case DF11. In the presented work, the design parameters of the dual fuel injection parameters will be recommended for the investigation of the full-cycle operating processes under 75% load in the large two-stroke dual fuel marine engine.

Table 6.19 New cases for the investigation of the recommended parameters

	Pilot Injector			Gas Injector				
	Timing (°ATDC)	α_l (°)	β_l (°)	Timing (°ATDC)	Duration (°CA)	Holes Number	α_g (°)	β_g (°)
DF13	-1.5~3.02	15	0	0.0~11.24	11.24	3	15	-20, 0, 20
DF14	-1.5~3.02	15	0	0.0~11.24	11.24	3	15	-35, -15, 5
DF15	-1.5~3.02	15	0	0.0~11.24	11.24	5	15	-40, -20, 0, 20, 40
DF16	-1.5~3.02	15	0	0.0~11.24	11.24	5	15	-55, -35, -15, 5, 25

Table 6.20 Dual fuel engine performance and gaseous emissions for the new cases

	IMEPcc (barabs)	Mass Fraction of NO (ppm)	Mass Fraction of CO (ppm)	Mass Fraction of Unburned HC (ppm)	Mass Fraction of CO_2 (ppm)
DF13	21.45	631	7353	219	67334
DF14	23.69	1024	447	1	79153
DF15	21.13	813	7820	312	65835
DF16	22.16	1087	5954	263	69061

Table 6.21 Dual fuel engine performance and emissions affected by the gas-hole inclination angle

	IMEPcc (bar)	Mass Fraction of NO (ppm)	Mass Fraction of CO (ppm)	Mass Fraction of Unburned HC (ppm)	Mass Fraction of CO_2 (ppm)
DF8	25.24	2282	18	0.0	79765
DF10	24.50	1791	6	0.0	79457
DF11	24.51	1820	4	0.0	79489
DF12	24.56	2019	61	0.0	79518

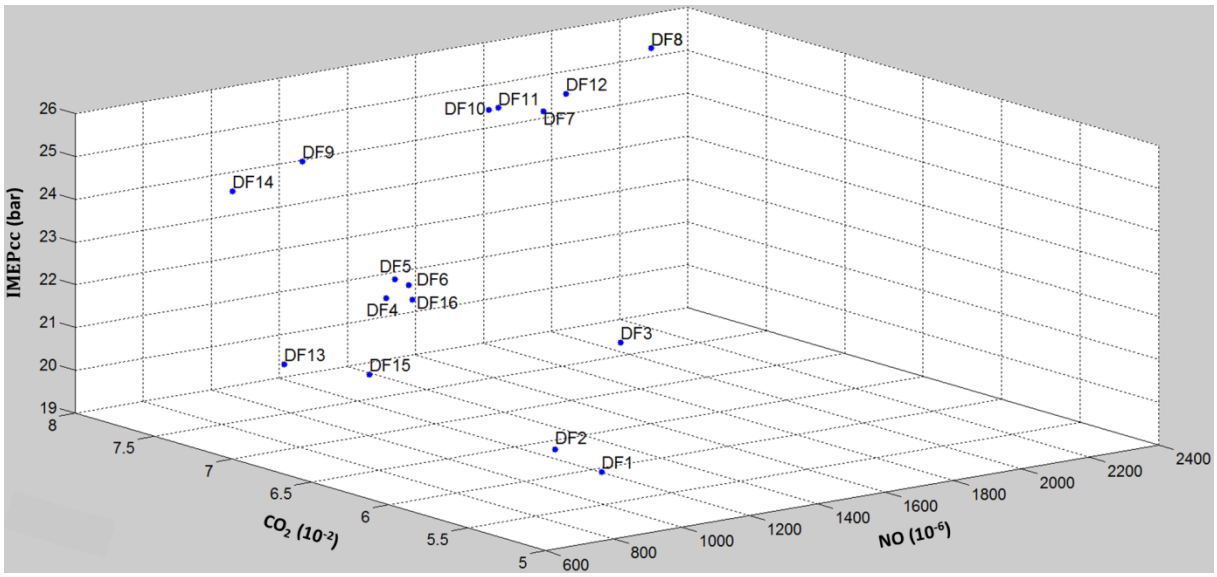

Figure 6.70 The evaluated cases scattered by the IMEPcc, CO_2 production and NO emission

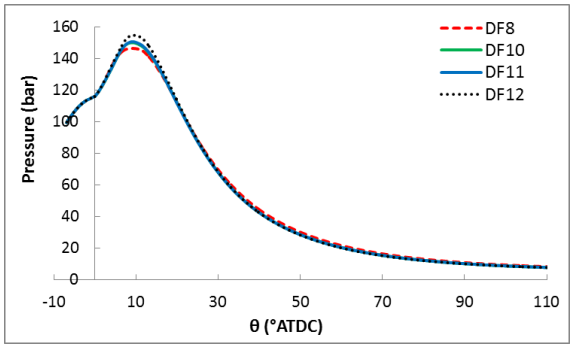

Figure 6.71 In-cylinder pressure curved by crank angle in the recommended cases

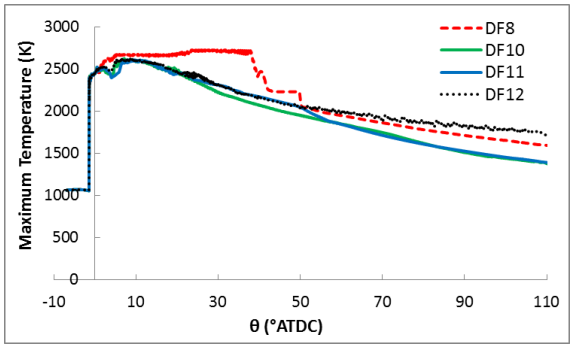

Figure 6.72 Maximum temperture curved by crank angle in the recommended cases

6.6 Conclusions

By using the validated CFD model, the parametric investigation of the dual fuel operation in the large two-stroke marine engine S60ME under 75% load is conducted, including the dual fuel injection timing, gas injection duration, holes number of the gas injector, and the gas injection direction. The main findings of this study are summarised as follows:

- Advancing the gas injection start in the vicinity of TDC can significantly benefit the engine power, unburned HC and CO emissions. In this case, the NO and CO_2 will also inevitably increase, due to the improvement of the gaseous combustion process.
- Shortening of the gas injection duration from 11.24 ℃A to 17.32 ℃A, does not cause a remarkable change in the engine performance and gaseous emissions. However, it can notably affect the peak pressure, temperature and heat release rate during the gaseous combustion process. The cold gas plumes impingement on the flame surface results in incomplete gas combustion takes place and generates increased unburned HC and CO emissions.
- The lateral angle of the gas injector is a parameter that affects the engine power and elimination of the HC emissions. Varying the lateral angle changes from 0 ° to 30 °, increases the indicated pressure IMEPcc by 12%, and reduces the HC emissions, whilst substantially increasing the NO and CO_2 emissions.
- The increase of the holes number in the gas injector does not affect the engine power, due to the reduction of the gaseous combustion duration. The case of the 5-hole gas injectors not only can maintain the similar level of engine output, but also noticeably reduce the NO formation, because of the improvement of gas mixing process and limiting the contact of the cold gas plumes on the gas flame surface.
- Gas injection direction towards the piston can slightly improve the gas combustion process, which causes the increase of the peak pressure, temperature and heat release during the gas

injection process. This however just marginally affects the engine power and gaseous emissions except for the NO emissions which change by 13% with comparison of cases DF10 and DF12.

- For comprising on the contradictory objectives of retaining the engine power, NO and CO_2 emissions, the settings of the investigated case DF11 shown in Table 6.22 are recommended for the dual fuel operation under 75% load in the large two-stroke marine engine S60ME.

Table 6.22 Recommended set of design parameters for the dual fuel operation under 75% load

	Injectors number	Holes Parameters in One Injector			Injected Mass (kg/rev)	Injection Start (°ATDC)	Injection End (°ATDC)
		Holes Number	Inclination Angle (°)	Lateral Angle (°)			
Pilot	3	1	15	0	0.00193	-1.5	3.02
Gas	3	5	23	-70	0.0380	0.0	11.24
			19	-50			
			15	-30			
			11	-10			
			7	10			

Chapter 7 Comparison of the Full-Cycle Internal Operations of 2-S Marine Engine under The diesel and Dual Fuel Modes

7.1 Introduction

Based on the recommended case settings in Chapter 6, the full-cycle operating processes of the two-stroke developed marine engine S60ME under dual fuel mode at 75% load are investigated by using the developed CFD models and the results are compared with that of the normal diesel operation. The liquid fuel injectors for the diesel operation and the pilot fuel injectors and gas injectors for the dual fuel operation of the marine engine S60ME are listed in Table 7.1.

Table 7.1 The parameters of engine S60MC injectors in each cylinder under dual fuel and the diesel modes at 75% engine load

	Dual Fuel Mode		The diesel Mode
	Pilot	Gas	Liquid
Injectors Number	3	3	2
Holes Number in the injector	5	5	5
Injected Mass (kg/rev)	0.00193	0.0380	0.0472
Injection Start (°ATDC)	-1.5	0.0	-0.9
Injection End (°ATDC)	3.02	11.24	15.1

7.2 Closed-Cycle Processes

7.2.1 Liquid Fuel/Dual Fuel Injection Processes

7.2.1.1 Dual Fuel Operation

For the dual fuel mode, three one-hole pilot fuel injectors and three five-hole gas injectors are installed on the engine cylinder head. Hence, there are three ignition kernels to be simulated, in which the three liquid streams consisting of the carbon dioxide (CO_2) and water (H_2O) are injected. It seems that there is no significant change in the pilot fuel (liquid) penetration as the gas injection starts, as shown in Figure 7.1. Based on the description of the ignition kernel models, the mass fraction of the pilot fuel vapour can be regarded as the sum of the CO_2 and H_2O evaporated from the pilot streams. The pilot fuel evaporating process results are illustrated in Figure 7.2. It must be noted that the mass fraction of CO_2 and H_2O (illustrated by the lightly blue colour in Figure 7.2) is attributed to the trapped CO_2 and H_2O after the scavenging processes in the previous engine cycle.

Figure 7.3 depicts the sharp rise of the mean diameter of the droplets at the early stage of pilot fuel injection, which implies a similar variation of the pilot fuel (liquid) penetration. Figure 7.4 demonstrates that the pilot fuel injection and evaporation rates almost coincide, which signifies that

most of pilot fuel evaporates immediately. Due to the accumulation of the pilot droplets resulted from the relatively large droplets at the early stage of pilot spray shown in Figure 7.3, the substantial increase of the evaporation rate can be observed at the start of the evaporation process.

The gas jets evolution of the three employed five-hole injectors is shown in Figure 7.5. At the start of gas injection, the three stoichiometric gas surfaces created by the pilot fuel combustion can be distinguished. Before the three gas plumes contact each other, the vortex head of gas jet is produced and followed by the flat tails derived from the five-hole gas injectors and entrained with the ambient air. It seems that the vortex-head temperature is higher than that of the following tails on the stoichiometric surface of gas jet. As the vortex head impinges on the cold root of the gas plumes, the strong interactions between them take place, where the gas plumes severely wrinkle and touch the cylinder head, and the vortex heads are gradually shaped as spikes. As shown in Figure 7.5, the mixing-limited process of gas plumes still continues after the gas injection end (at 5 ℃A).

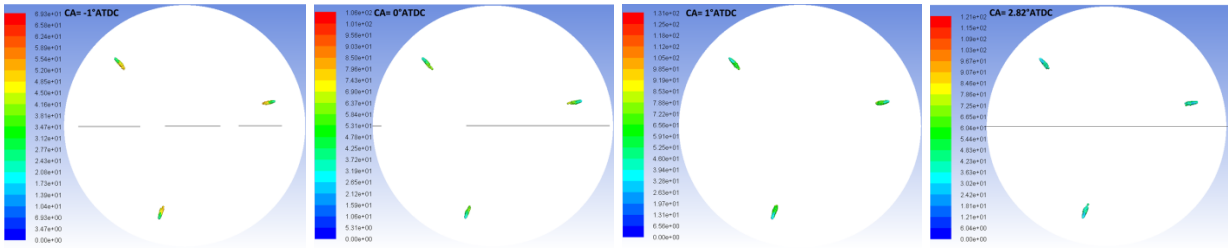

Figure 7.1 Pilot sprays viewed by the constant diameter for each droplet and velocity contours on the droplets' surface under dual fuel mode

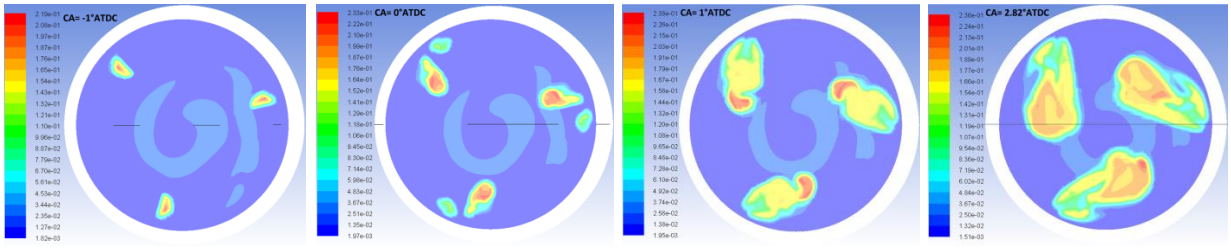

Figure 7.2 The contours of the mass fraction sum of the CO_2 and H_2O under dual fuel mode

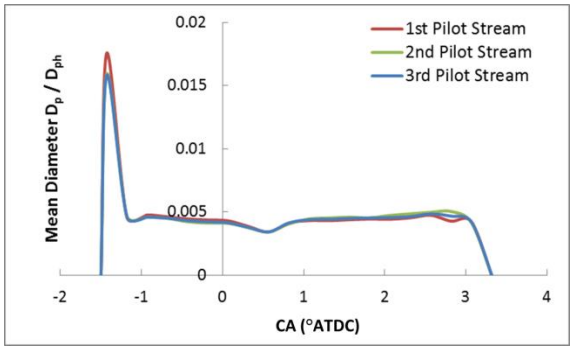

Figure 7.3 Mean diameter of the droplets normalized by the pilot hole diameter

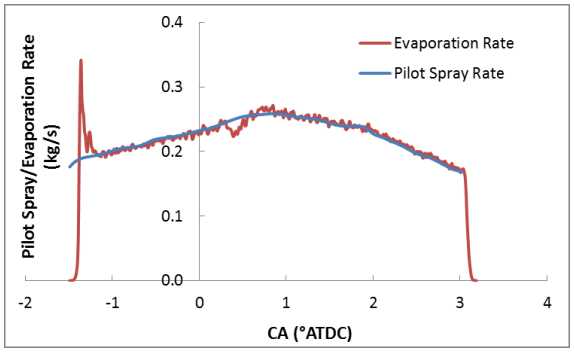

Figure 7.4 The spray rate of pilot fuel and the evaporation rate as a function of the crank angle

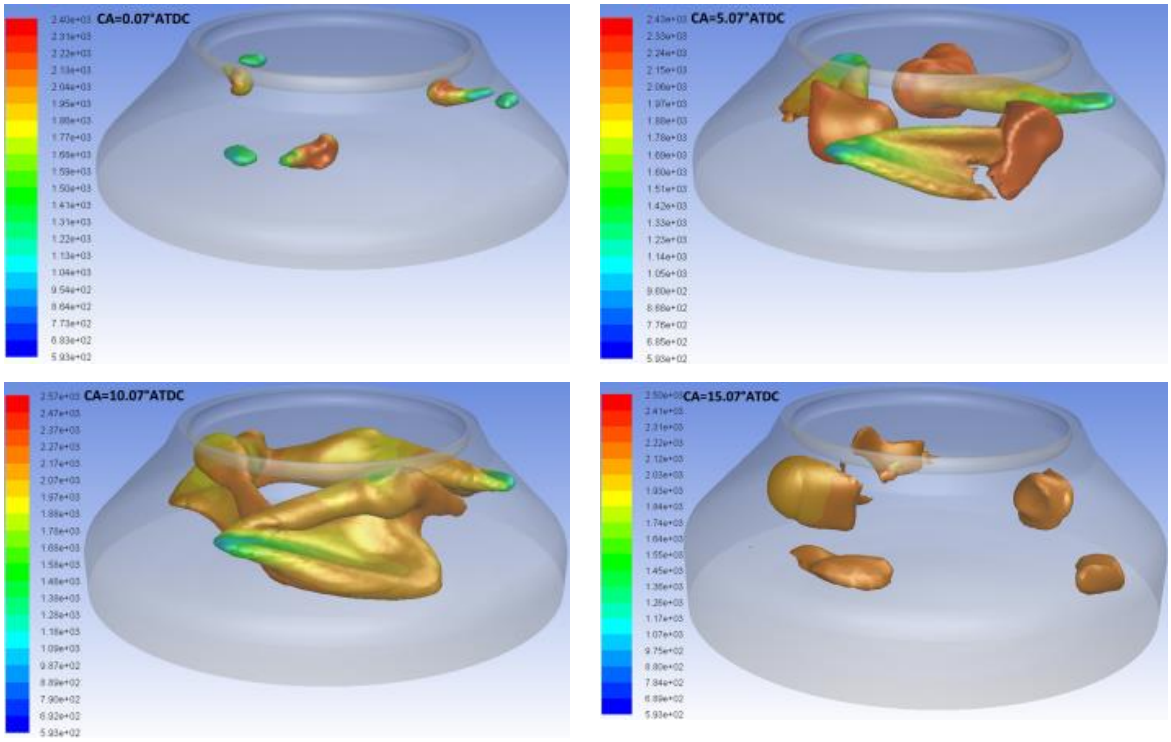

Figure 7.5 The temperature contours on the stoichiometric surface of the injected gas under dual fuel operation

7.2.1.2 Comparison with the diesel Mode

Figure 7.6 depicts the liquid fuel penetration injected by the two five-hole liquid injectors in the normal diesel, which shows that the liquid penetration does not remarkably change in the presented graphs. The vapour plumes shown in Figure 7.7 present the quite difference between the diesel and the dual fuel operations, where the temperature on the stoichiometric surface is far lower than the flame temperature. Moreover, the size of the vapour plumes appears to be thinner and smaller, due to the faster burning rate and mixing process under normal diesel mode.

Figure 7.8 shows the identical variation of mean diameter of the droplets under the diesel and dual fuel operating modes. For the diesel mode, the mean diameter of the droplets significantly increases after the liquid injection finishes, as most of the tiny droplets have been consumed. For the dual fuel operation, at the end of the pilot injection, the gas combustion has commenced, thus the high-temperature gas flame results in the evaporation all of the liquid fuel droplets.

The comparison of the liquid spray rate and evaporation rate variations with the crank angle illustrated in Figure 7.9 demonstrates that the most of the injected fuel amount is almost instantly evaporated, despite the existence of the droplets shortly after the end of liquid injection which causes a considerable increase in the mean diameter of the retained droplets as depicted in Figure 7.8.

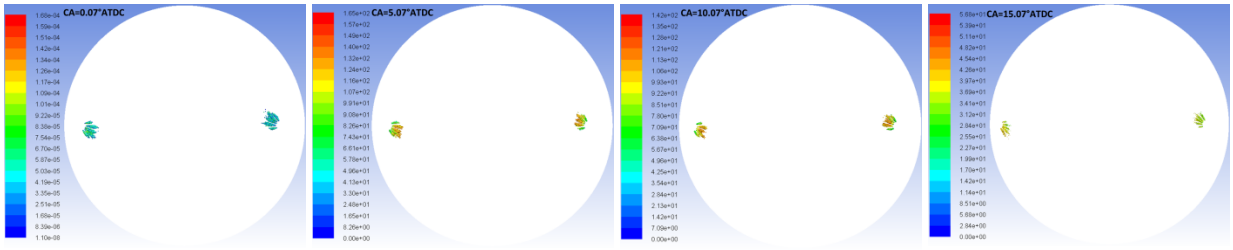

Figure 7.6 Droplets tracks viewed as the constant diameter and the velocity contours on the droplets' surface under the diesel mode

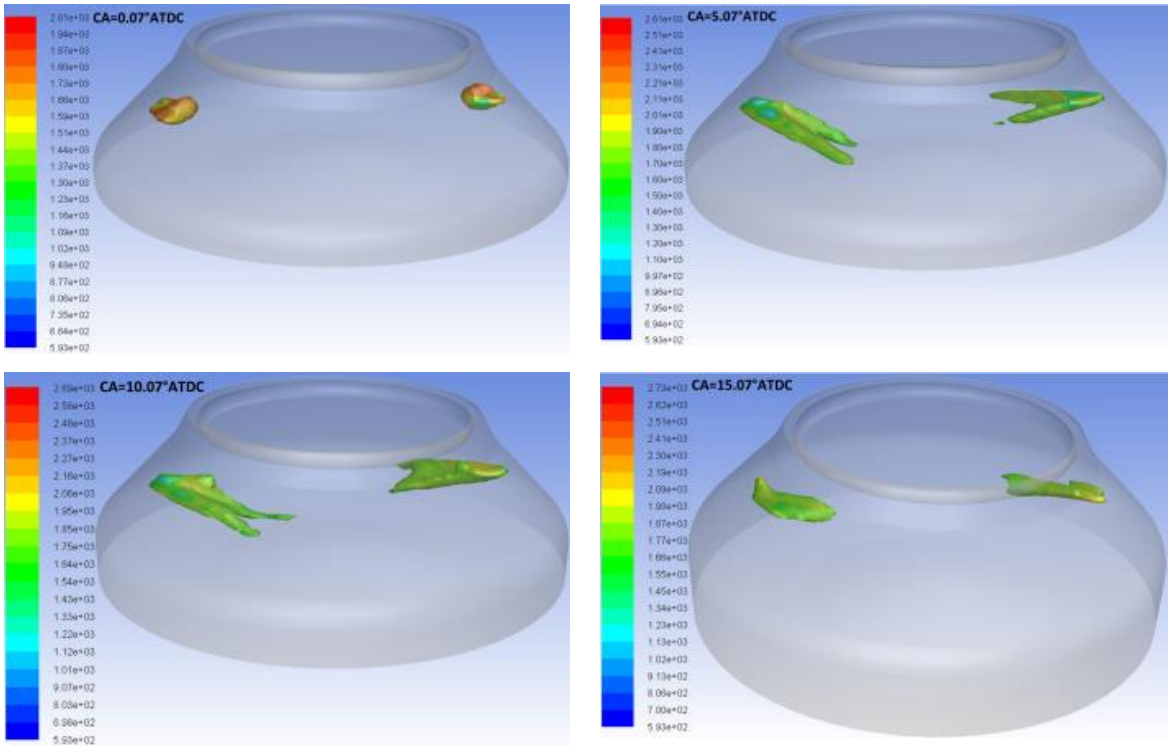

Figure 7.7 Temperature contours on the stoichiometric surface of the fuel vapour under the diesel mode

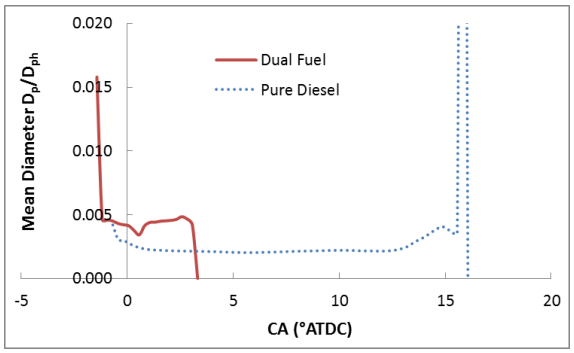

Figure 7.8 Mean diameter of the droplets normalized by the hole diameter of the liquid injector

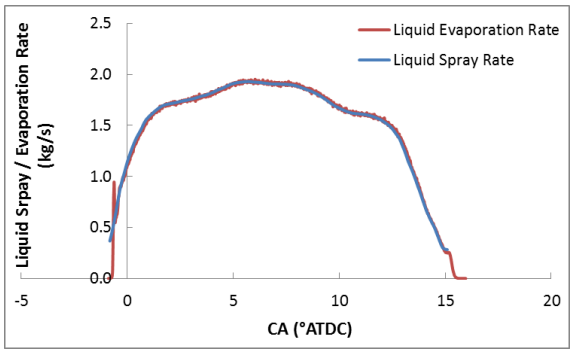

Figure 7.9 The liquid spray rate and evaporation rate under the diesel operation

7.2.2 Combustion process

7.2.2.1 Temporal and Spatial Distributions on the Flame Structure

The local equilibrium ratio (EQ) represents the current fuel-air ratio in the cylinder. The in-cylinder temperature (T) - equilibrium ratio (EQ) variations at crank angle values equal to 0.0 °ATDC, 5.07 °ATDC, 10.07 °ATDC and 15.07 °ATDC for the dual fuel and the diesel modes, respectively are illustrated in Figure 7.10. The ambient air is represented by the low temperature – lean equilibrium ratio regime, which also can be observed near the cylinder walls. Apparently, the fuel –air mixing rate near the fuel injectors is characterised by the low temperature – high equilibrium ratio. The diffusion flame located at the high temperature region takes place at lean fuel conditions. Comparing to the diesel operation, the broad maps of the temperature versus equilibrium ratio for the dual fuel mode can be seen, due to the higher injection rate and lower burning rate of the gas. It implies the richer fuel – air combustion for the dual fuel mode than that of the diesel mode.

As the conserved scalar, the mixture fraction expresses the element distribution derived from the injection fuel and the related productions. At the early stage of fuel injection shown in Figure 7.11, the maximum temperature for the dual fuel mode is much higher than that of the diesel operation, signifying the stronger diffusion combustion. At the stable and late fuel combustion process, the reversed trend about the maximum in-cylinder temperature can be observed.

Apart from the mixture fraction, the spatial distributions of the species OH, CH_2O and CO_2 for the dual fuel and the diesel modes are illustrated in Figure 7.12 and Figure 7.13, where the radical OH signifies the high temperature related to the diffusion flame, CH_2O distribution can demonstrate the low temperature reaction zone. The mixture fraction has the similar distribution with the one of CO_2, both of which magnitude is reversed, based on the element conservation. In the core of the gas/vapour plumes, the low OH and high CH_2O concentration can be seen, especially near the nozzle exit. Regarding the high - OH and low - CH_2O zones, the noticeable disparity between the dual fuel and the diesel operating modes is found. For the dual fuel mode, due to the diffusion combustion of the injected gas, the high-temperature flame is located in the vicinity of the stoichiometric surface, where there exists high concentration of OH radical and low concentration of CH_2O. On the contrary, the high CH_2O concentration occurs near the stoichiometric surface for the diesel operation, owing to the heat transfer due to the liquid fuel evaporation. Therefore, the high-concentration OH is not observed close to the stoichiometric surface of the fuel vapour, but downstream the vapour plumes due to the transportation by the strong swirling flow and the high-speed liquid sprays. In addition, in terms of the mixture fraction distribution shown in Figure 7.12, the slight accumulation of the gas fuel and the related products near the cylinder walls in Figure 7.11 is mainly caused by the hot head of one gas plume impinging on the root of another gas plume.

The comparison of the temperature distributions for the dual fuel and diesel modes are shown in Figure 7.14 and Figure 7.15. These results demonstrate that the diesel operation fuelled by the liquid oil has a higher flame temperature than the dual fuel, which primarily uses the methane as fuel, except for the early stage of fuel injection. At the early gas injection stage, the higher flame temperature observed in dual fuel mode than that of the diesel mode is attributed to the pilot fuel ignition combustion. Moreover, the locations of the flame temperature for these two investigated operating modes are quite different. For the diesel operation, the diffusion flame is strongly transported by the swirling flow in the cylinder, similarly to the flame developed in the dual fuel after the gas injection is finished. However, during the gas injection process for the dual fuel mode, the high-temperature flame is observed primarily near the gas-plume heads shown in Figure 7.14.

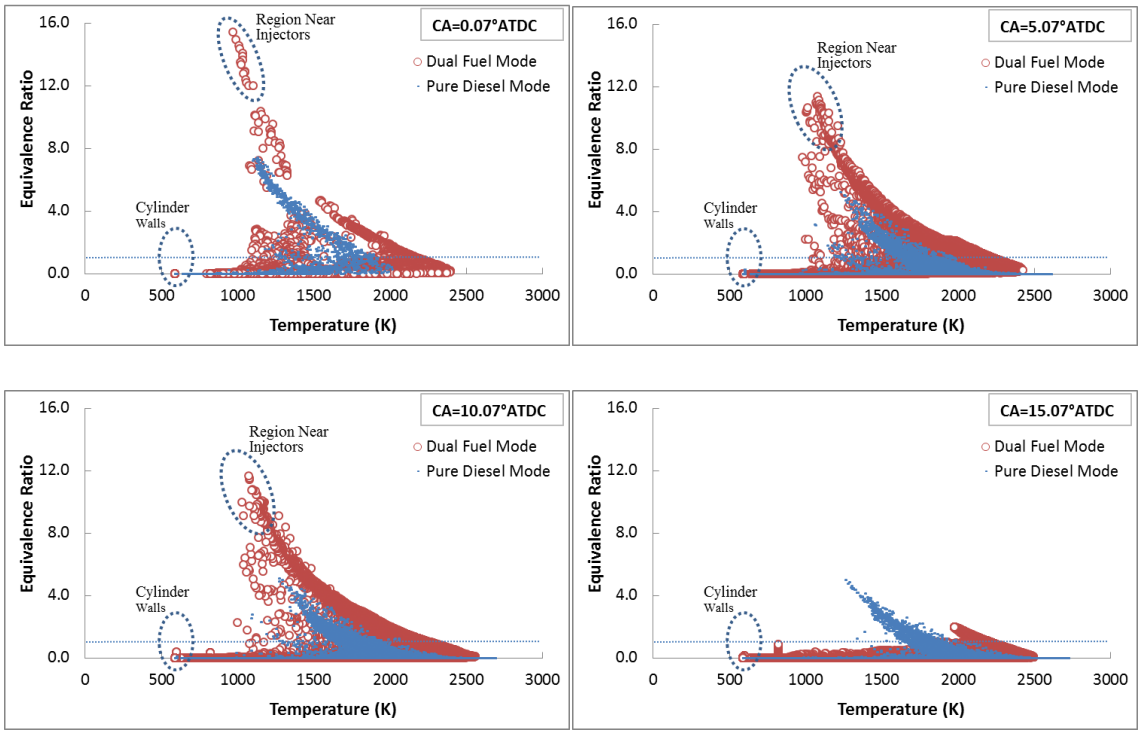

Figure 7.10 The maps of the local temperature and equilibrium ratio as a function of the crank angle

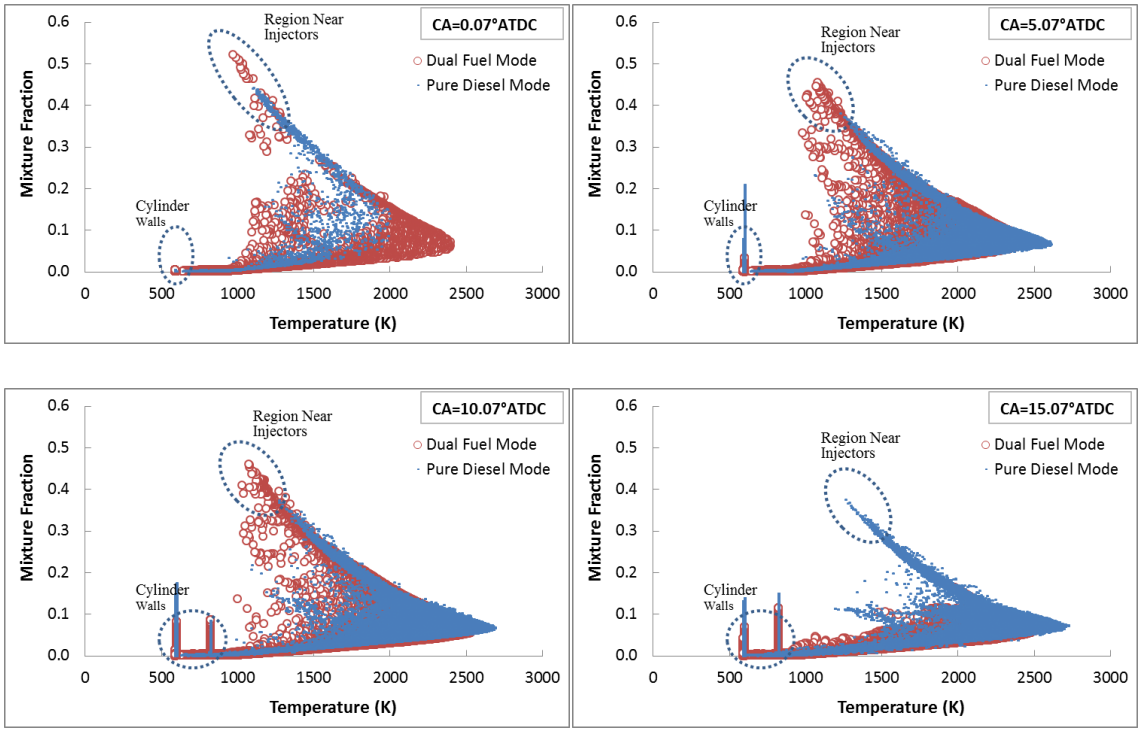

Figure 7.11 The maps of the local temperature and mean mixture fraction as a function of the crank angle

(a) Mixture Fraction (b) OH (c) CH_2O (d) CO_2

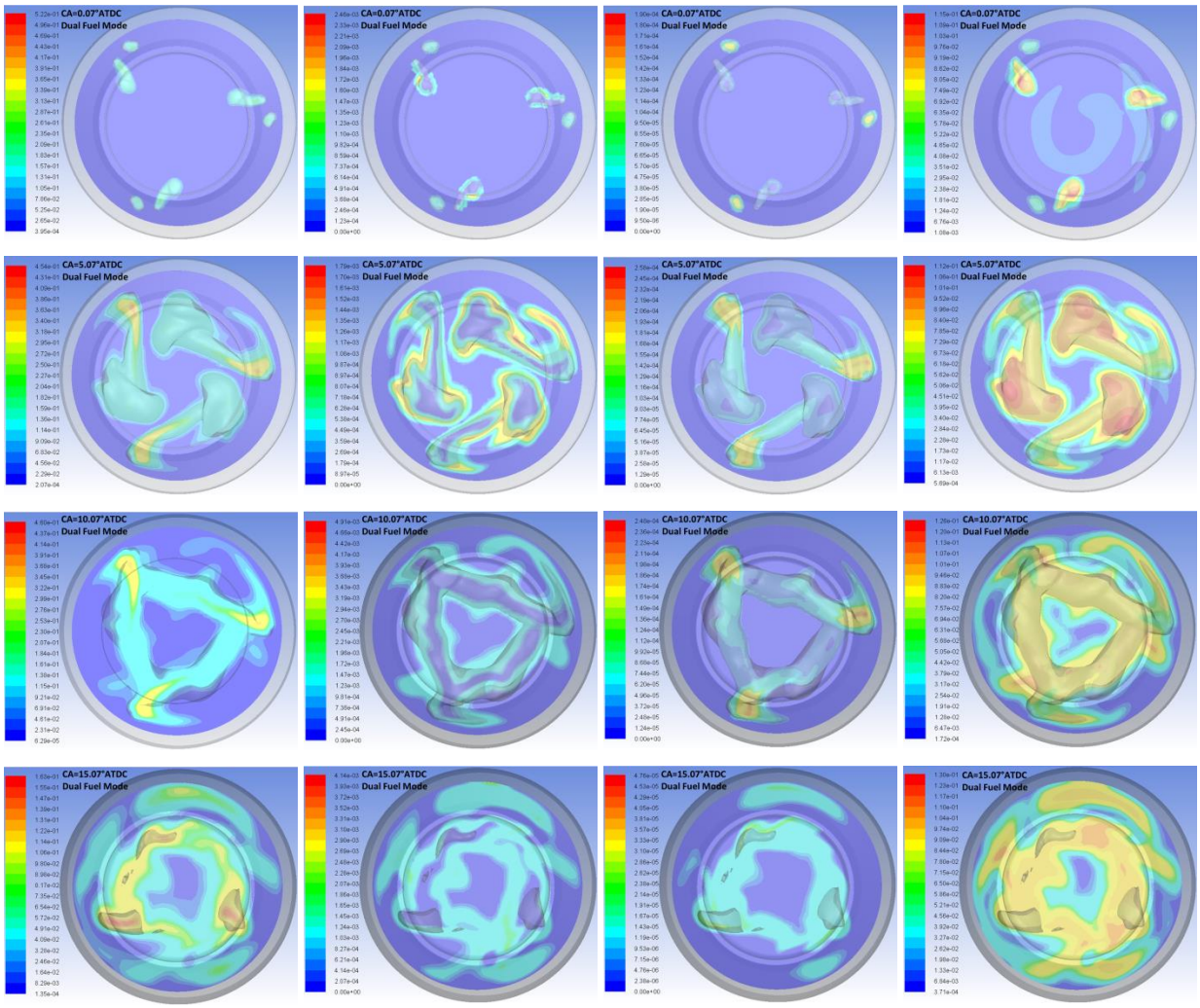

Figure 7.12 The species mass fraction distributions including mixture fraction, OH, $CH_2O$and CO_2 for the dual fuel mode

(a) Mixture Fraction (b) OH (c) CH_2O (d) CO_2

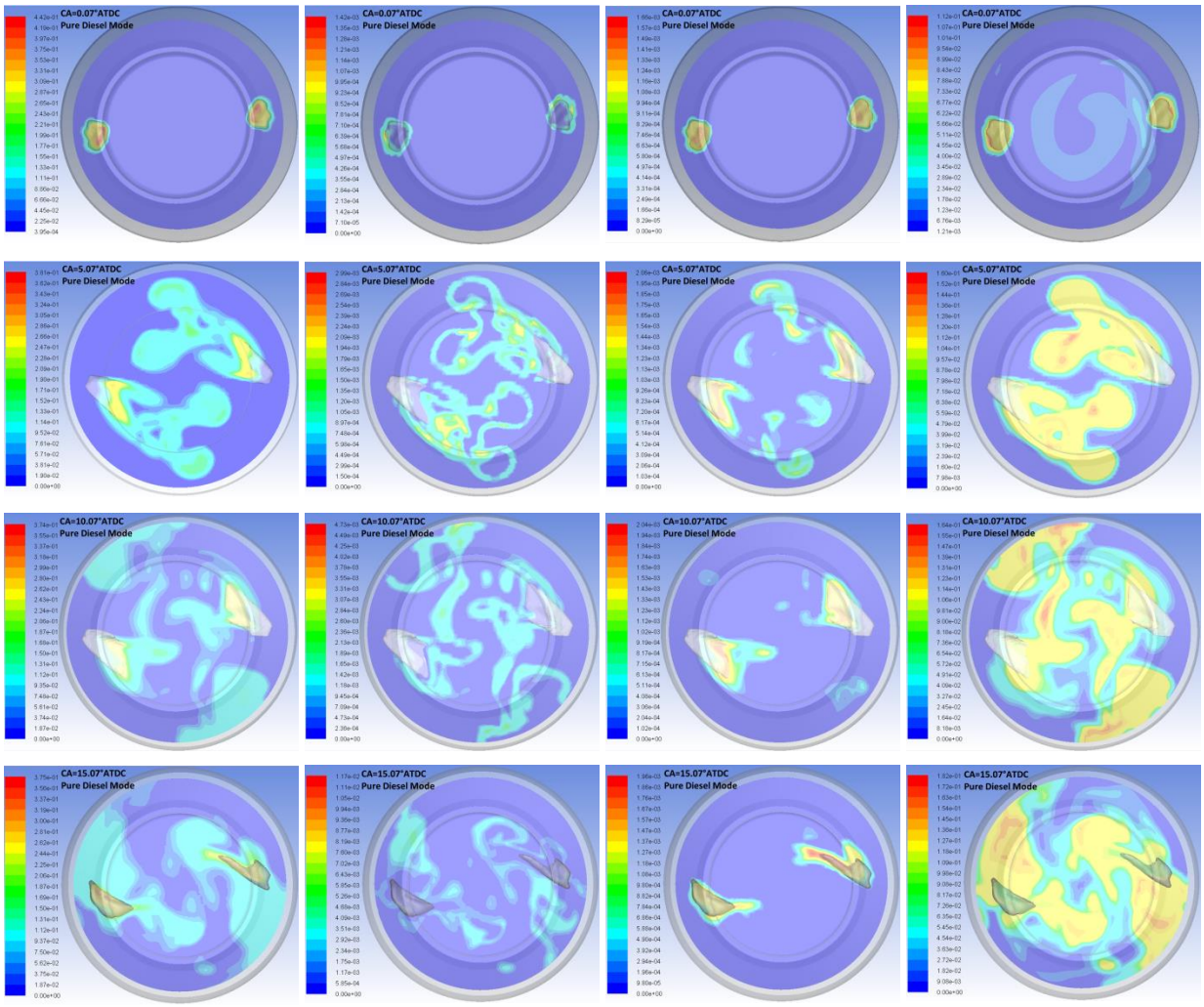

Figure 7.13 The species mass fraction distributions including mixture fraction, OH, $CH_2O$and CO_2 for the diesel mode

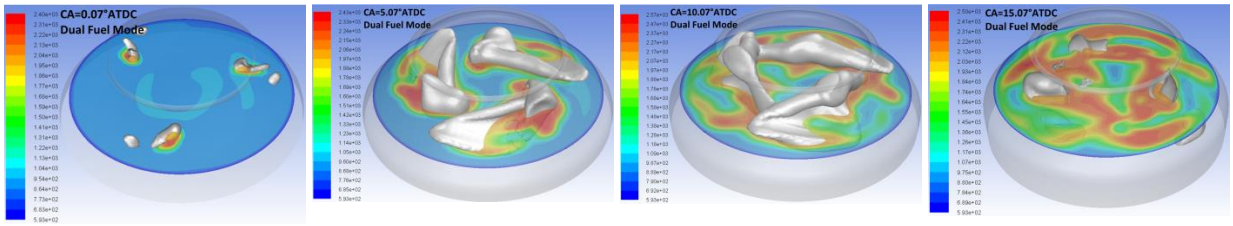

Figure 7.14 The spatial distributions of in-cylinder temperature as a function of the crank angle for the dual fuel operation

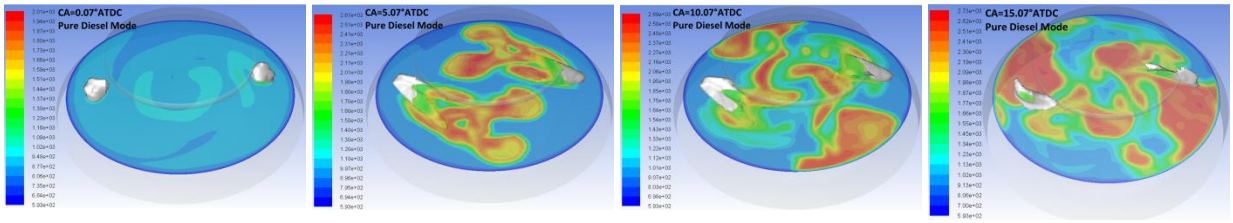

Figure 7.15 The spatial distributions of in-cylinder temperature as a function of the crank angle for the diesel mode

7.2.2.2 In-Cylinder Pressure, Temperature and Heat Release Rate

The derived mean in-cylinder temperature by mass-averaging the calculated local temperature is shown in Figure 7.16. The comparison depicts that the mean temperature for the dual fuel operation is slightly higher than that of the diesel operation, followed by the reversed variation between the two modes after the end of the gas injection, and the results at the late expansion stroke coincide. As expected, the similar trends for the in-cylinder pressure can be observed for both operating modes in Figure 7.17. The peak pressure of the dual fuel mode is slightly higher than that of the diesel mode.

Figure 7.17 also compares the experimental in-cylinder pressure and CFD results for the diesel mode. The results show that the numerical simulation excellently matches the experimental results in the closed cycle. In detailed, The CFD slightly underestimates the maximum cylinder pressure by 1.8%. For the indicated work IMEPcc, the difference between the CFD and the experiment is within 0.1%.

Two definitions of heat release rate are compared, including GHRR and AHRR. AHRR denotes the actual heat release rate that accounts for the evaporation heat loss of liquid fuel, as well as the change of the mixture molecular weight (MW) and in-cylinder mass detailed in Appendix F, in terms of the first law of thermodynamics. The gross heat release rate (GHRR) is calculated by the following equation [119]:

$$GHRR = \frac{dQ_{net}}{dCA} - \frac{dQ_w}{dCA} = \frac{C_v}{R}\left(P\frac{dV}{dCA} + V\frac{dP}{dCA} - \frac{PV}{m}\frac{dm}{dCA}\right) + P\frac{dV}{dCA} - \frac{dQ_w}{dCA} \quad (7.1)$$

Figure 7.18 demonstrates the estimated variations of GHRR and AHRR. The detailed comparison of the each term in the definitions of HRR shows that such difference primarily comes from the calculation of the specific heat capacity C_V of the mixture illustrated in Figure 7.19, which is caused by the intermediates produced by the fuel combustion. As a consequence, the AHRR will be applied to investigate the heat release of the injected fuel, because the AHRR can more precisely predict the real heat release of the fuel combustion.

The AHRR for the dual fuel operation fast increases till its maximum value observed at 5.62 °ATDC, and then gradually decreases. Figure 7.21 illustrates that this variation is due to the gas-plume hot head impinging on the cold root of the gas plumes.

For the diesel operation, the heat release rate AHRR variation with the crank angle is remarkably different with that of dual fuel operation, as shown in Figure 7.20. The two peaks and one valley between them are observed. Before the first peak at 6 °ATDC, the AHRR fast increases, whilst the HRR peak value is almost the same to that of dual fuel operation. The following reduction of the AHRR values is due to the less fuel vapor retained in the engine chamber as shown in Figure 7.22. After 9 °ATDC, the liquid fuel injection increases the AHRR until to its peak at 11.3 °ATDC,

attributed to the increases of the in-cylinder diesel vapour and the associated flame temperature presented by the maximum temperature illustrated in Figure 7.22.

The heat release loss through the cylinder walls shown in Figure 7.23 also clearly demonstrates the change of the HRRs for the dual fuel and diesel modes. The high-temperature flame transported and the hotter mixture accumulating near the cylinder walls causes the greater heat loss for the diesel operation than that of the dual fuel operation, by observing the Figure 7.21 and Figure 7.24.

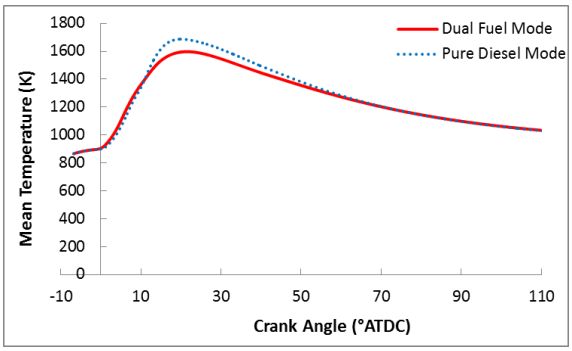

Figure 7.16 Mass-averaged temperature curved by crank angle for the dual fuel and the diesel modes

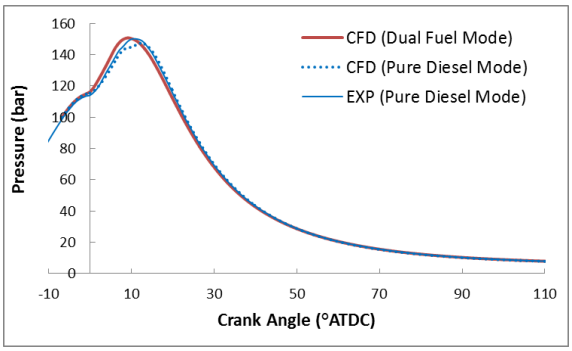

Figure 7.17 In-cylinder temperature curved by crank angle for the dual fuel and the diesel modes

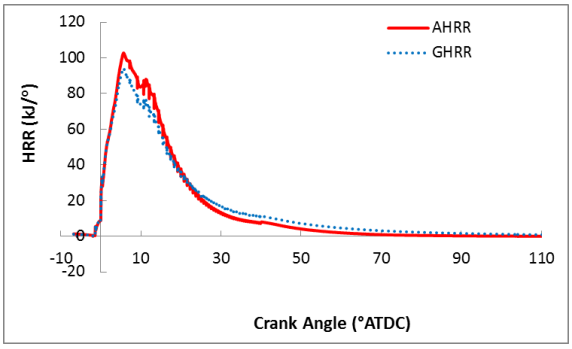

Figure 7.18 The comparison of two HRR definitions for the dual fuel mode

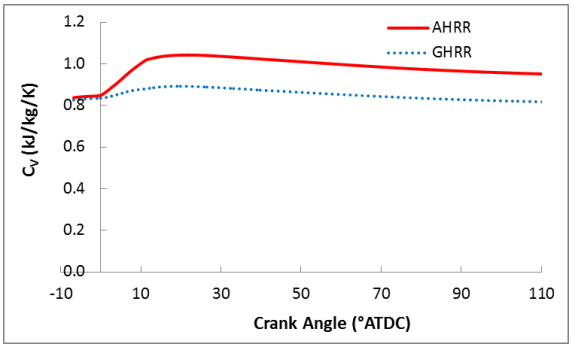

Figure 7.19 Specific heat capacity CV defined in AHRR and GHRR for the dual fuel operation

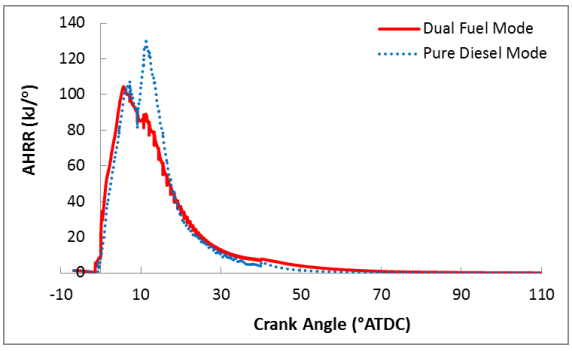

Figure 7.20 The AHRR curves for the dual fuel and the diesel operations

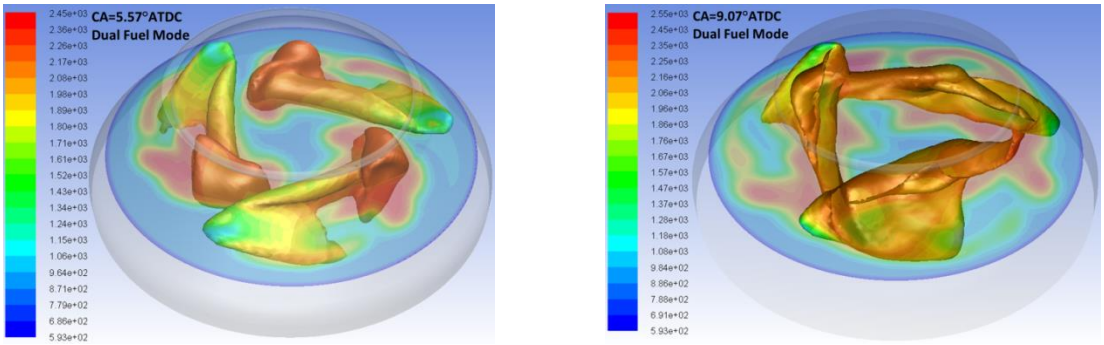

Figure 7.21 Gas plumes and temperature distribution at crank angle 5.57 °ATDC and 9.07 °ATDC for the dual fuel mode

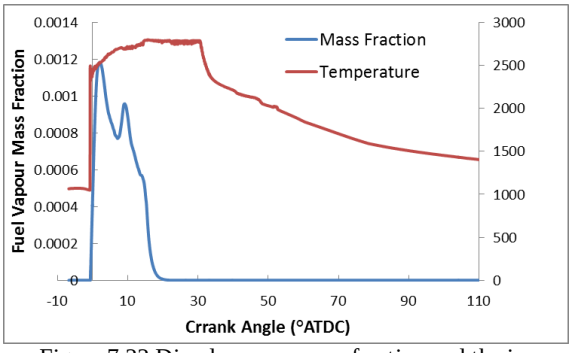

Figure 7.22 Diesel vapour mass fraction and the in-cylinder maximum temperature for the diesel mode

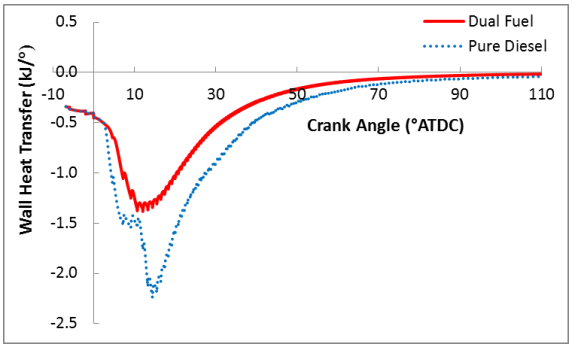

Figure 7.23 Heat transfer through the wall for the dual fuel and the diesel operations

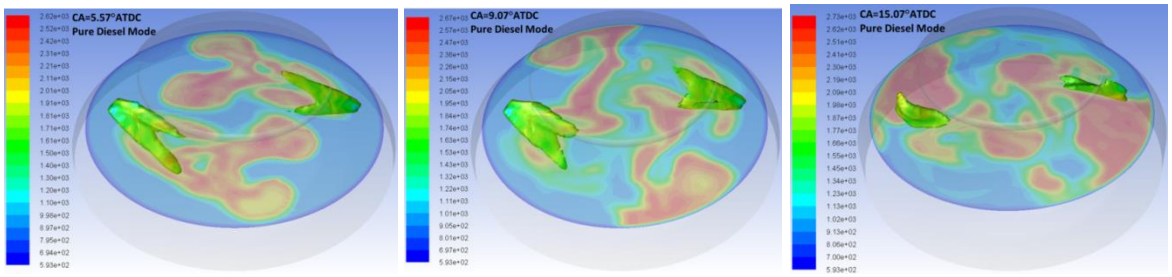

Figure 7.24 Liquid vapour plumes and temperature distribution at crank angle 5.57 °ATDC, 9.07 °ATDC and 15.07 °ATDC for the diesel mode

7.2.3 Gaseous Emissions

The results shown in Figure 7.25 demonstrate that there is no unburned fuel for both the dual fuel and the diesel modes. Comparing the diesel mode, the dual fuel mode has a much slower burning rate of the injected fuel.

Due to the lower C/H ratio of the methane and less injected gas mass for the dual fuel, the CO_2 emission is significantly lower than that produced for the diesel mode. Figure 7.26 depicts that each cylinder operated by dual fuel under 75% engine load will emit 0.115 kg CO_2, which is lower than the one of the diesel operation by 21%.

Similar variation of the NO formation with the crank angle can be observed in Figure 7.27. In the period of the gas injection process, the dual fuel operation creates slightly higher NO than that of the

diesel operation. The much greater growth rate of the NO formation is found for the diesel mode. After the fuel is completely consumed, the production rate of NO almost approach zero. At EVO, the NO emission for the dual fuel mode is about 1820 ppm, which is 31% lower than that of the diesel mode.

It is well known that the NO formation is substantially dependent of the in-cylinder temperature. Figure 7.28 depicts that the maximum temperature for the dual fuel mode is remarkably lower than that of the diesel mode, despite the marginally higher maximum temperature in the early stage of the gas injection due to the pilot fuel combustion. ANSYS Fluent [45] indicates that the production rate of NO is significantly dominated by the high temperature greater than 1800 K. The associated volume ratio at temperature greater than 1800 K is shown in Figure 7.29, which demonstrates that the NO reduction for the dual fuel operation is mainly due to the decrease of the flame temperature and the high-temperature volume ranging from 2000 K to 2400 K.

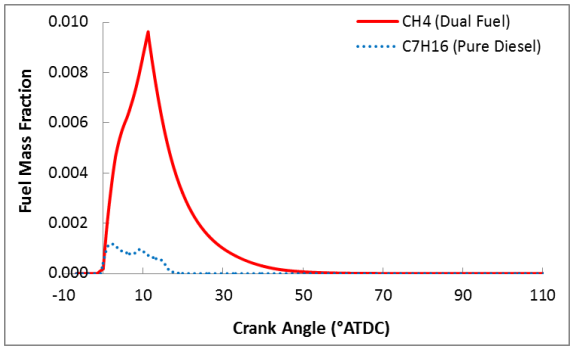

Figure 7.25 Mass fraction of the injected gas fuel / vapour in the cylinder for the dual fuel and the diesel modes

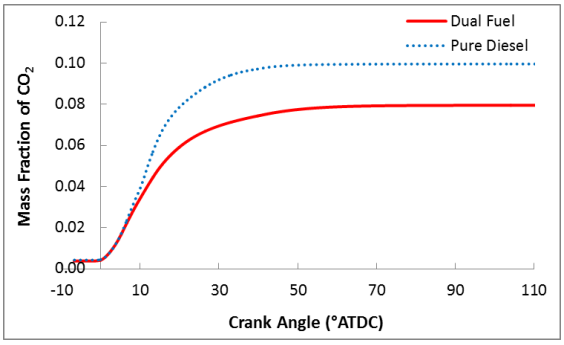

Figure 7.26 Mass fraction of carbon dioxide in the cylinder for the dual fuel and the diesel modes

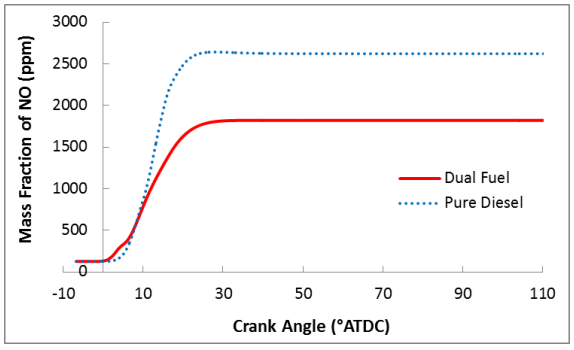

Figure 7.27 Mass fraction of nitric oxide in the cylinder for the dual fuel and the diesel modes

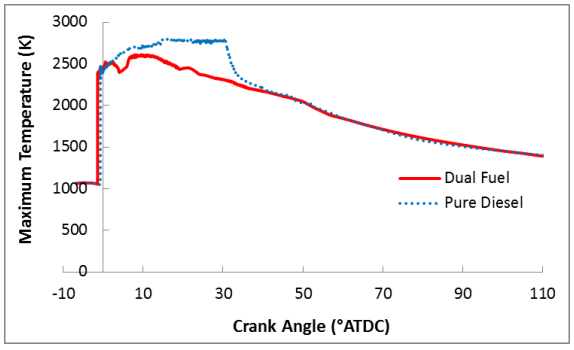

Figure 7.28 In-cylinder maximum temperature for the dual fuel and the diesel modes

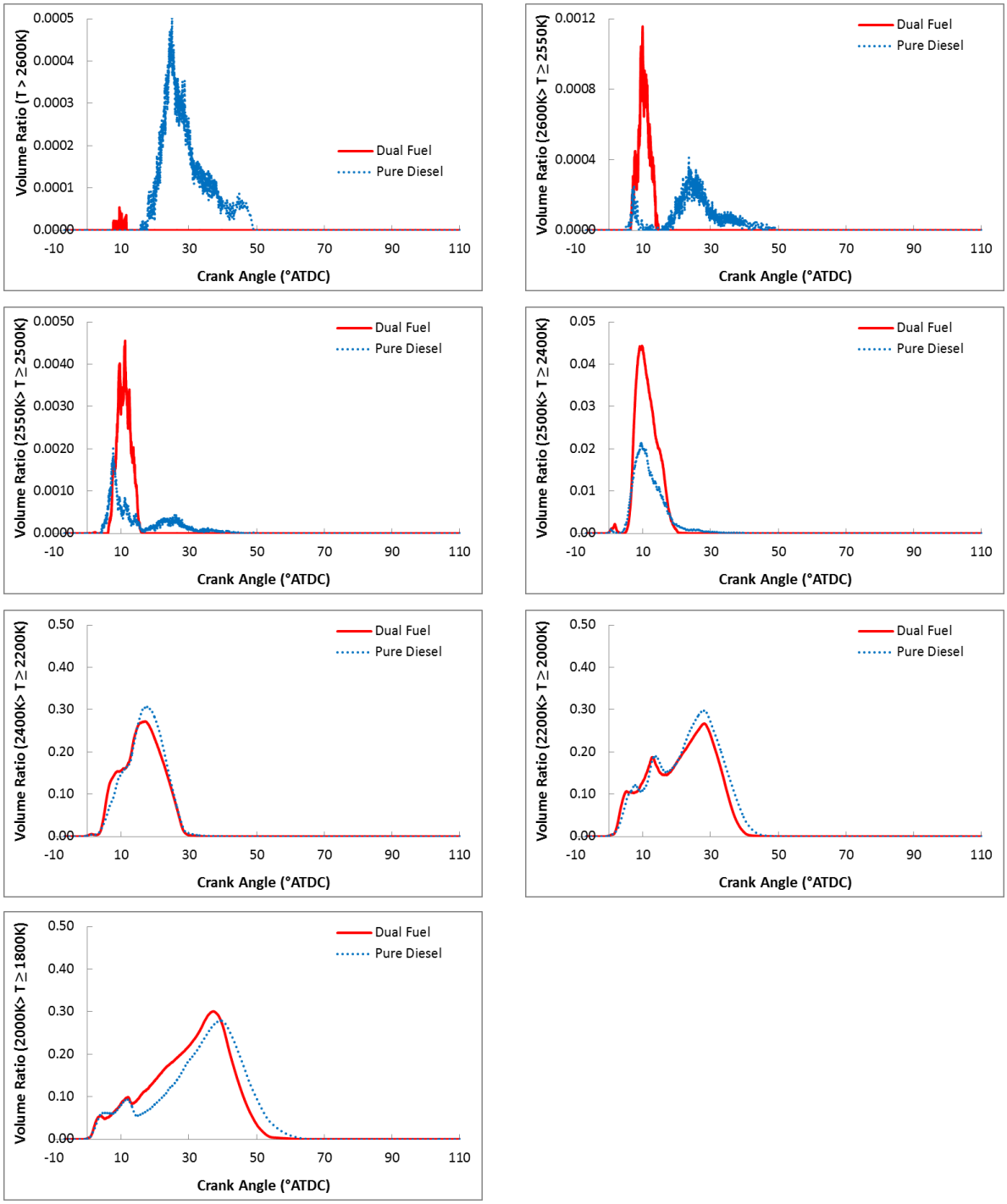

Figure 7.29 The comparisons of the volume ratio greater than 1800 K for the dual fuel and the diesel modes

7.3 Blowout and Scavenging Processes

7.3.1 Flow Visualization

The flow visualization for the diesel operation will be qualitatively analysed, due to almost the same visualization for the dual fuel and the diesel modes during the blowout and the scavenging processes.

Figure 7.30 describes the spatial distributions of the axial velocity in the engine cylinder at various crank angle position from the exhaust valve opening (EVO) to the exhaust valve closing (EVC). In the cylinder cycle before the EVO, the uniformed distribution of the negative axial velocity caused by the piston downward moving is observed. At the EVO, the cylinder exhaust gas starts to blow out from the cylinder through the exhaust valve port with swirling flow. When the exhaust valve opens, the blowout is dominated, due to the high in-cylinder pressure, whilst the slightly reversed flow in the vicinity of the exhaust duct can be found. When the scavenging ports open, the fresh air enters into the cylinder and the several recirculation zones are generated by the pre-swirling flow through the scavenging ports, leading the formation of the complicated vortices within the cylinder. Moreover, the central negative zone (downward velocity) gradually moves up due to the scavenge air flow. As the piston proceeds towards the bottom dead centre (BDC), this central zone expands along the axial direction and highly non-uniform recirculation zones are created. The negative axial velocity representing the recirculation zones still exists in the region underneath the exhaust valve, even when the exhaust valve closes. This can result in trapping the burned gas, causing a reduction of the scavenging efficiency.

The mixture fraction distributions in the cylinder are shown in Figure 7.31. In terms of the definition of the mixture fraction, the fresh air is denoted by mixture fraction values equal to zero. As the scavenging ports open, the fresh air enters into the cylinder and mixes with the burned gas. When the piston arrives at the BDC and reverses its motion, the fresh air moves towards the cylinder head region, subsequently expelling the burned gas. Figure 7.31 at 286 °ATDC demonstrates that the burned gas cannot be discharged entirely after EVC, some of which is still trapped in the cylinder.

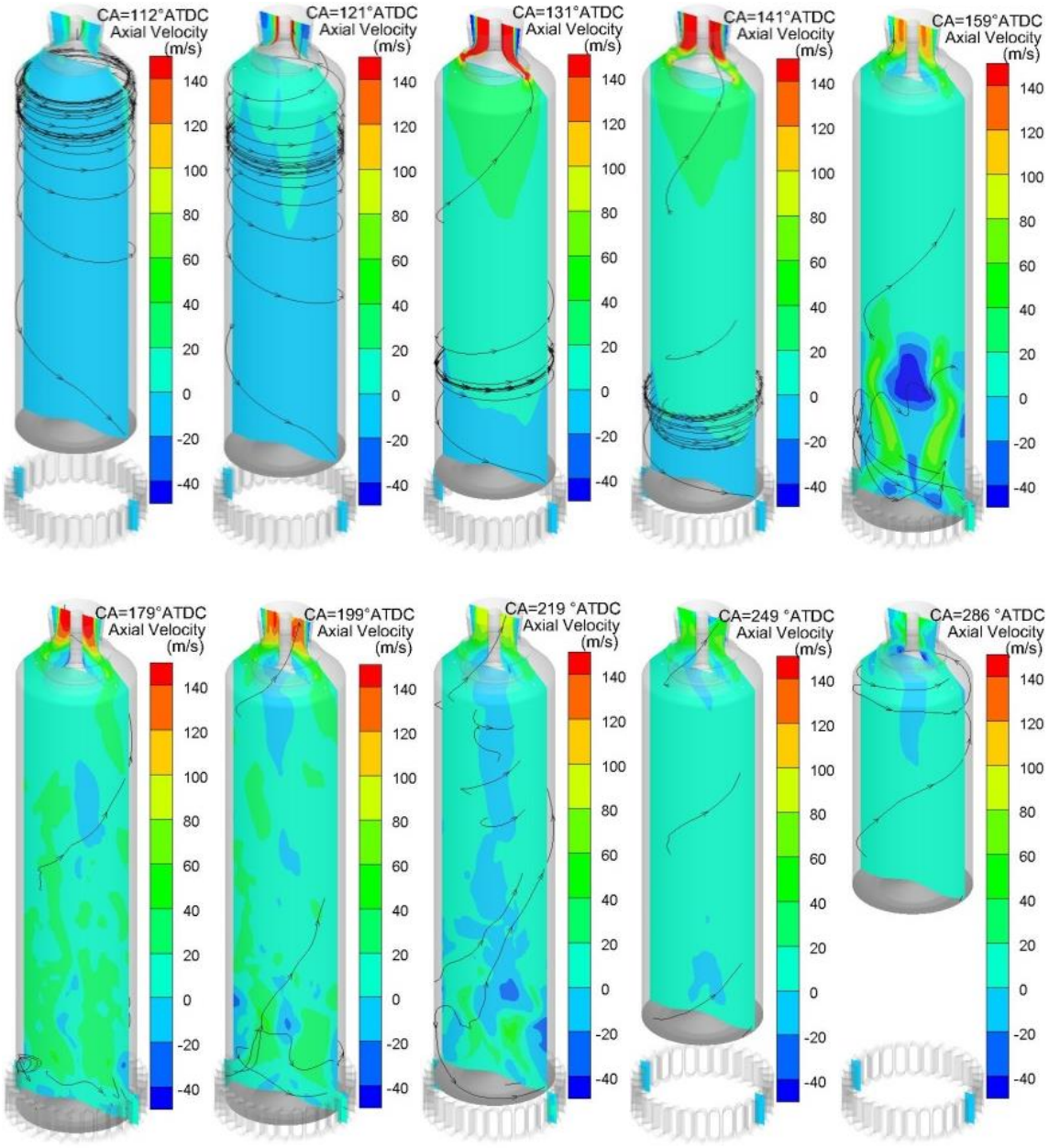

Figure 7.30 Axial Velocity Contours and streamlines as a function of crank angle

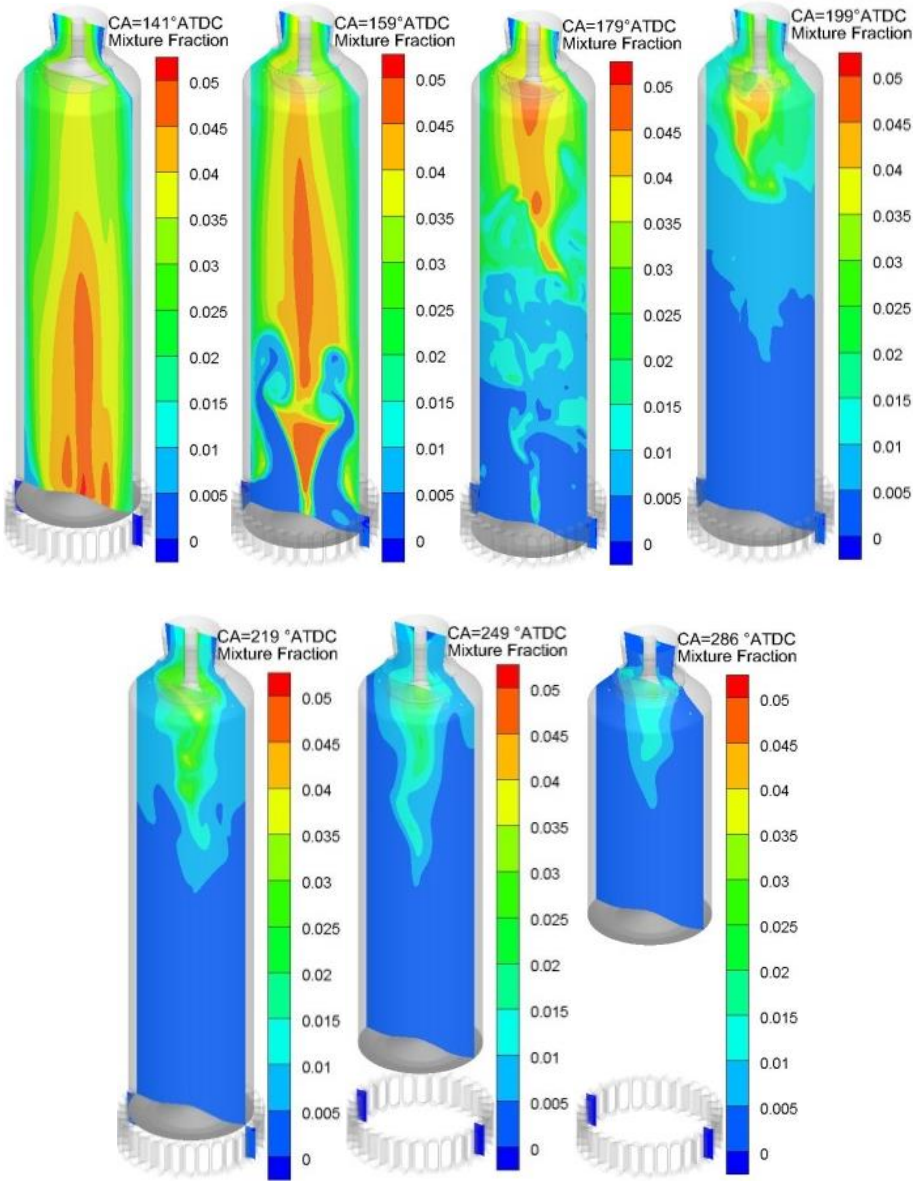

Figure 7.31 The spatial and temporal distributions of the mixture fraction in scavenging process

7.3.2 In-Cylinder Mean Velocity and Momentum

The flow field in the blowdown and scavenging processes is evaluated on the basis of the mass-integrated velocity components in the cylinder, named as axial momentum G and angular momentum L_Z respectively:

$$G = \int_{\Omega} \rho V_z d\Omega \tag{7.2}$$

$$L_Z = \int_{\Omega} r\rho V_t d\Omega \tag{7.3}$$

Where Ω is the cylinder volume, and V_t is the tangential velocity and V_r is the radial velocity defined by the following equations:

$$V_t = \frac{1}{\sqrt{x^2+y^2}}(-yV_x + xV_y) \tag{7.4}$$

$$V_r = \frac{1}{\sqrt{x^2+y^2}}(xV_x + yV_y) \tag{7.5}$$

And the mass-averaged axial velocity $\bar{V}_Z$, radial velocity $\bar{V}_r$ and tangential velocity $\bar{V}_t$ can be evaluated by the following equations:

$$\bar{V}_Z = \frac{\int_\Omega \rho V_z d\Omega}{\int_\Omega \rho d\Omega} \tag{7.6}$$

$$\bar{V}_r = \frac{\int_\Omega \rho V_r d\Omega}{\int_\Omega \rho d\Omega} \tag{7.7}$$

$$\bar{V}_t = \frac{\int_\Omega \rho V_t d\Omega}{\int_\Omega \rho d\Omega} \tag{7.8}$$

Based on the equations (7.6) - (7.8), the change of the cylinder momentums caused by the fuel injection, the fuel combustion and the blowout and scavenging processes can be easily quantified, in conjunction with the cylinder mass.

Figure 7.32 shows that almost the same averaged axial cylinder velocity is obtained in the diesel and the DF operating modes. In the closed cycle ranging from -45 °ATDC to 45 °ATDC, the in-cylinder averaged axial velocity follows the piston moving speed. In the late expansion stroke, the downwards in-cylinder velocity primarily caused by piston motion is observed, where its minimum value is about -6.26 m/s at 67.6 °ATDC (whereas the piston moving speed is -8.40 m/s). As the exhaust valve opens, the in-cylinder burned gas gradually blows out, leading the sharp increase of the averaged axial velocity from negative to positive values, until it reaches the local peak of 16.1 m/s closely before the SPO. The scavenging ports opening further causes the steep reduction of the averaged upward velocity until 145.2 °ATDC. As the in-cylinder pressure retains its minimum values (shown in Figure 7.33), the upwards velocity sharply rises again, due to the increasing opening of the scavenging ports and the associated increase of the air flow rate entering the cylinder. Close to the BDC, the averaged axial velocity reaches 18.6 m/s, accompanied by the notable fluctuation resulted from the vortices induced by the fresh air charge. Subsequently, the in-cylinder averaged axial velocity still reduces due to the scavenging ports closing and the stop of the incoming fresh air. Shortly after the SPC, the in-cylinder axial velocity is significantly affected by the piston moving, where the local peak occurs at 286 °ATDC. The following variation is similar to the piston speed variation, even after EVC.

The in-cylinder average radial velocity variations calculated for the dual fuel and the diesel operating modes are quite similar during the burned gas blowing out and scavenging processes, as shown in Figure 7.34. The magnitude of the in-cylinder radial velocity is far less than the in-cylinder axial velocity, except during the scavenging ports opening.

The dual fuel and diesel modes also exhibit the similar variations of the in-cylinder average tangential velocities, as shown in Figure 7.35. The liquid fuel injection and combustion generates the higher in-cylinder tangential velocity for the diesel mode than that of the dual fuel mode in the closed cycle, which results in the similar change from the EVO to the SPO. As the increasing opening of the scavenging ports, the results between these two operating modes almost coincide before the TDC. The maximum average in-cylinder tangential velocities for both operating modes are equal to 16.7 m/s at 166 °ATDC.

According to the momentum conservation, the required force and the angular moment passing through the scavenging ports can be estimated from the in-cylinder results in Figures 7.36 and 7.37. It can be seen that the axial momentum variation primarily follows the in-cylinder axial velocity. The difference between the local peak shortly after the SPO and the maximum of the axial momentum close to the BDC is relatively enlarged due to the increase of the cylinder mass (Figure 7.37) delivered from the fresh air. It can be found that the visible difference of axial momentum between dual fuel and diesel modes close to the BDC is due to the mass change caused by the fresh air charge.

The angular momentum (defined by equation 7.3) is notably different by the in-cylinder averaged tangential velocity, as shown in Figure 7.38. The remarkable difference between the diesel and the dual fuel modes is also exhibited. From the fuel injection end to the EVO, the approximately linear reduction can be observed, attributed to the wall friction [126]. After the EVO, the reduction of the angular momentum is still retained, followed by the rapid decrease due to the exhaust valve opening. The minimum of angular momentum values of 1.9 kg·m^2 and 2.1 kg·m^2 at 147 °ATDC (shortly after SPO) respectively are calculated for the dual fuel and the diesel modes. Due to the increase of the tangential velocity and fresh air charge, the angular momentum increases until 195 °ATDC, whilst the dual fuel mode exhibits the lower angular momentum than the diesel mode. The maximum value for the dual fuel operation is equal to 4.8 kg·m^2, which is 8% lower than that of the diesel operation. As the scavenging ports start to close, the angular momentum reduces, resulting in smaller derivation of the angular momentum variations for the dual fuel and the diesel modes. After EVC, the angular momentum reduces gradually due to the wall friction, and the similar variations are calculated for the dual fuel and diesel modes.

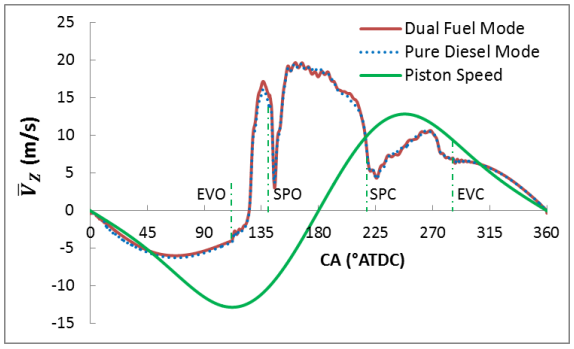

Figure 7.32 Mass-averaged axial velocity against crank angle for the dual fuel and the diesel operations

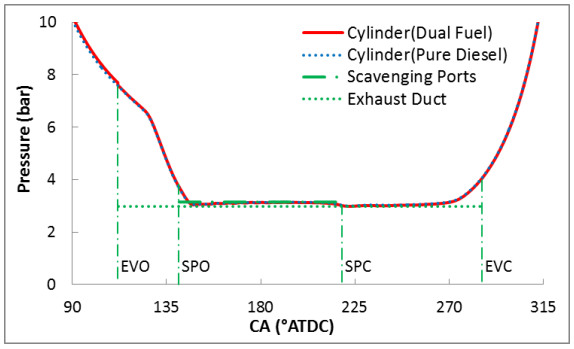

Figure 7.33 Pressure curves in the blowingdown and scavenging processes for the dual fuel and the diesel operations

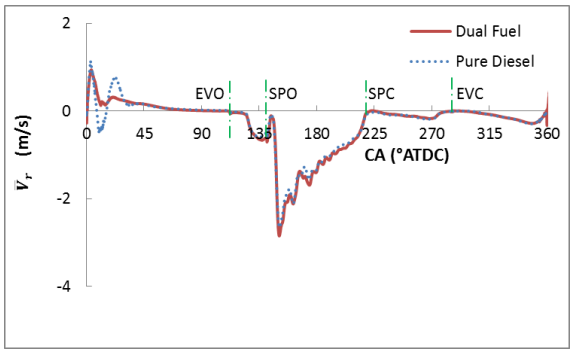

Figure 7.34 Mass-averaged radial velocity against crank angle for the dual fuel and the diesel operations

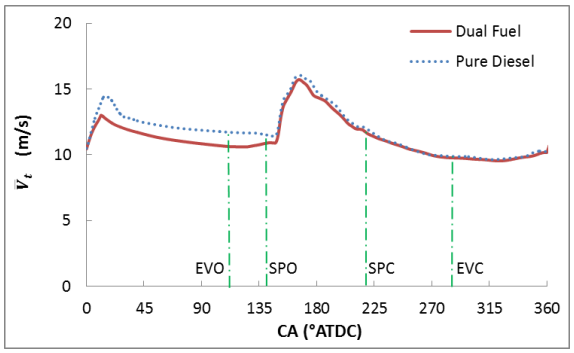

Figure 7.35 Mass-averaged tangential velocity against crank angle for the dual fuel and the diesel operations

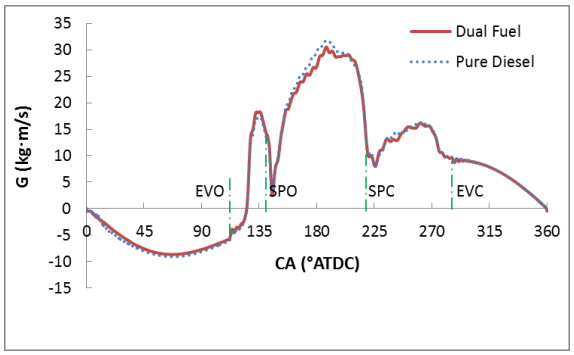

Figure 7.36 Axial momentum against crank angle for the dual fuel and the diesel operations

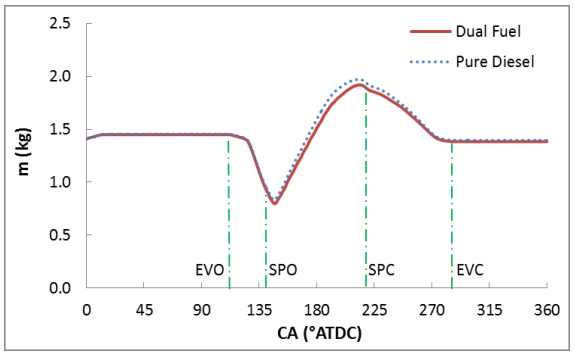

Figure 7.37 Mixture mass in-cylinder against crank angle for the dual fuel and the diesel operations

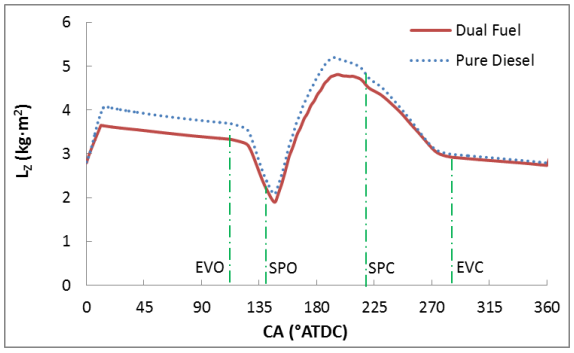

Figure 7.38 Angular momentum against crank angle for the dual fuel and the diesel operations

7.3.3 Mass Flow Rate

The pressure difference between the scavenge air receiver and the cylinder shown in Figure 7.33 causes the fresh air flow through the scavenging ports. Figure 7.39 depicts that the scavenging air mass flow rates variations for the dual fuel and the diesel modes are prettily similar. At the early stage of the scavenging ports opening, due to the negative pressure difference (the cylinder pressure higher than scavenging air receiver pressure), the back flow occurs, with the minimum value being about -2.87 kg/s. Owing to the rapid decrease of the cylinder pressure caused by the burned gas blow down process, the mass flow rate of fresh air charge quickly increases to 19.68 kg/s at 157.3 °ATDC. Then, the mass flow oscillations are estimated due to the respective oscillations in the cylinder pressure attributed to the induced vortices. 10 °CA after the BDC, the oscillations fast decrease, as well as the scavenging air flow rate.

The exhaust valve opening causes the cylinder burned gas blowdown, as shown in Figure 7.40. It can be seen that the flow rates through the exhaust valve for the dual fuel and the diesel modes are almost the same, due to the similar pressure difference between the cylinder and the exhaust port. At 134 °ATDC (corresponding to the half of the exhaust valve opening), the flow rate reaches the maximum value of 17.9kg/s. As the exhaust valve opens further, the associated flow rate decreases, due to the shaper reduction of the cylinder pressure. 7.3 °CA after the SPO, the local minimum value of 3.2 kg/s is observed. The scavenging ports opening benefits the burned gas blowing down. 5 °CA after the SPC, the flow rate through the exhaust valve reaches the local minimum again. The following variations are dominated by the piston moving upward and the exhaust valve lifting, which causes the increasing and the subsequent reduction of the flow rate through the exhaust valve.

Figures 7.41 and 7.42 illustrate the flow rate of the oxygen (O_2) and the carbon dioxide (CO_2) through the exhaust valve respectively. Before the BDC, the duel fuel mode exhibits the slightly higher flow rate of the oxygen than the diesel mode. After the BDC, the reversed variation of the O_2flow rate for these two operating modes is observed. With respect to the CO_2 in the cylinder mixture through the exhaust valve, the notably lower CO_2 for the dual fuel mode than that of the diesel mode is emitted, because the less CO_2 is produced for the methane combustion. Attributed to the burned gas mostly blowing down after the SPC, the CO_2 emitted from the exhaust valve for both two operating modes almost coincides.

In terms of the results in Figure 7.41 and Figure 7.42, the mass ratio of the emitted oxygen and carbon dioxide is demonstrated in Figure 7.43. It can be observed that the mass ratio significantly increase at 5 °CA after the BDC, which implies the O_2 derived from the fresh air starts to emit. Subsequently, the flow rate of the burned gas and the fresh air through the exhaust valve can be estimated, as shown in

Figures 7.44 and 7.45. The calculations illustrate that the slightly higher burned gas and the lower fresh air for the dual fuel mode than that of the diesel mode is exhausted from the exhaust valve.

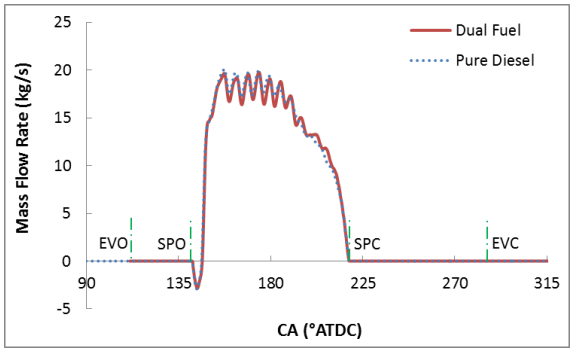

Figure 7.39 Mass flow rate through scavenging ports for the dual fuel and the diesel modes

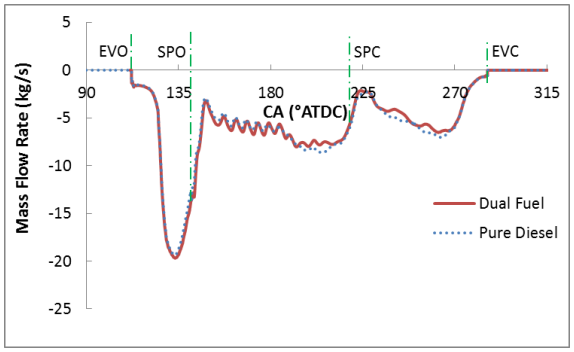

Figure 7.40 Mass flow rate through exhaust valve for the dual fuel and the diesel modes

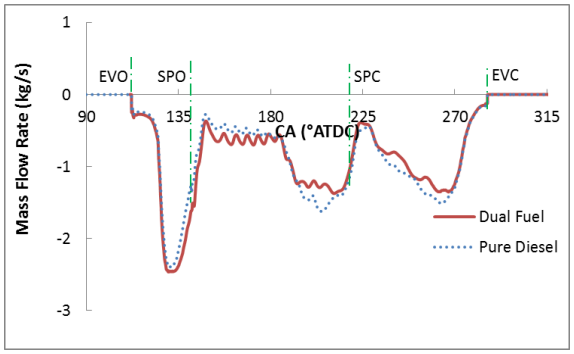

Figure 7.41 Mass flow rate of oxygen through exhaust valve for the dual fuel and the diesel modes

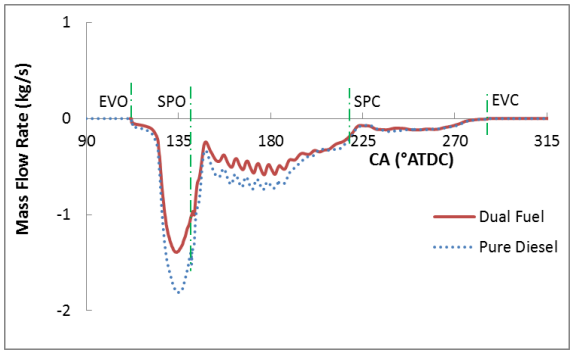

Figure 7.42 Mass flow rate of carbon dioxide through exhaust valve for the dual fuel and the diesel modes

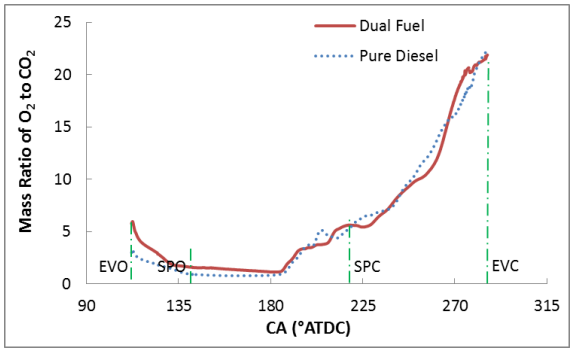

Figure 7.43 Mass ratio of oxygen to carbon dioxide through exhaust valve for the dual fuel and the diesel modes

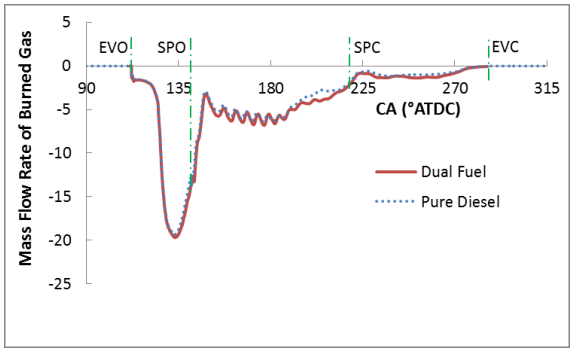

Figure 7.44 Mass flow rate of burned gas through exhaust valve for the dual fuel and the diesel modes

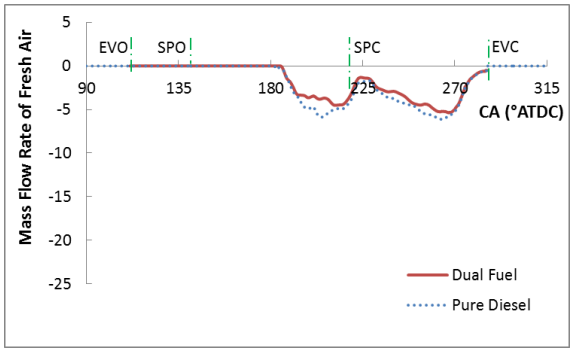

Figure 7.45 Mass flow rate of fresh air through exhaust valve for the dual fuel and the diesel modes

7.3.4 Scavenging Parameters

The scavenging parameters (Appendix G) for the dual fuel and the diesel modes will be compared, involving the delivery ratio, the charging efficiency, the scavenging efficiency and the relative charge efficiency.

Figures 7.46 - 7.50 present the above-mentioned scavenging parameters variations as a function of the delivery ratio. The comparison of the dual fuel and the diesel operations shows that the charging efficiency and retaining efficiency variations almost coincide for both modes. Due to the observable difference of the retained fresh air in the cylinder (shown in Figure 7.51) and the total mass of the cylinder charge (shown in Figure 7.37), the dual fuel mode obtains a slight higher scavenging efficiency and a lower relative charge efficiency, compared to the diesel mode. Moreover, this deviation is gradually enlarged as the increase of the delivery ratio. At the SPC, the scavenging efficiency for the dual fuel mode reaches 90.9%, and is higher by 4.2% than the respective value obtained for the diesel mode.

In Figures 7.46 - 7.49, the scavenging parameters are also estimated for the perfect mixing and the perfect displacement. As expected, all the scavenging parameters of CFD results for both fuel modes fall in the range of the results assumed by perfect mixing and perfect displacement, except the retaining efficiency. Furthermore, the scavenging parameters under both modes are much closer to the calculation for the perfect displacement than that of the perfect mixing, which is also demonstrated in the flow visualizations in Figure 7.31. For values of the delivery ratio lower than 0.7, the charging efficiency and the scavenging efficiency for both modes almost coincide with the results of the perfect displacement. When the delivery ratio increases, the deviation of the actual CFD and the perfect displacement also increases. At the SPC, the scavenging efficiency of the perfect displacement model reaches 100%, higher than CFD results for the dual fuel mode by 9.1%. To be noted, the retaining efficiencies of the perfect mixing model and perfect displacement model close to zero delivery ratio approach the infinite, which is caused by the back flow near the scavenging ports.

Obviously, as the scavenging process in the cylinder is closer to the perfect displacement, the higher scavenging efficiency can be achieved. The comparison of the dual fuel mode and the diesel mode indicates that the lower mass of CO_2 produced by the fuel combustion leads to the scavenging process closer to the perfect displacement. As a consequence, one of the ways to improve the scavenging efficiency is to reduce the mass of the produce derived from the fuel combustion.

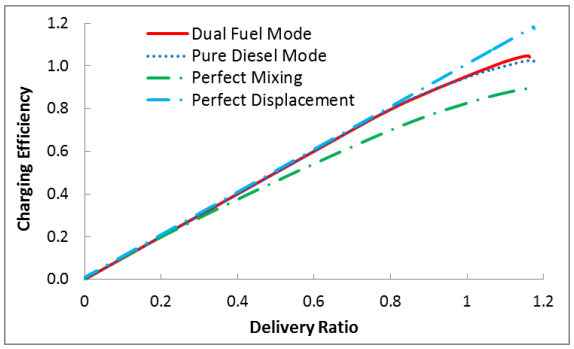

Figure 7.46 Charging efficiency as a function of the delivery ratio

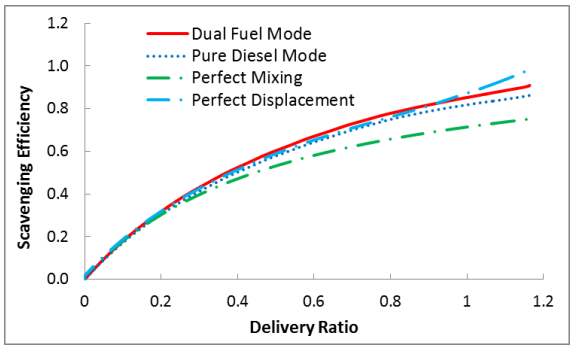

Figure 7.47 Scavenging efficiency as a function of the delivery ratio. Perfect mixing and perfect displacement assumed under the diesel condition

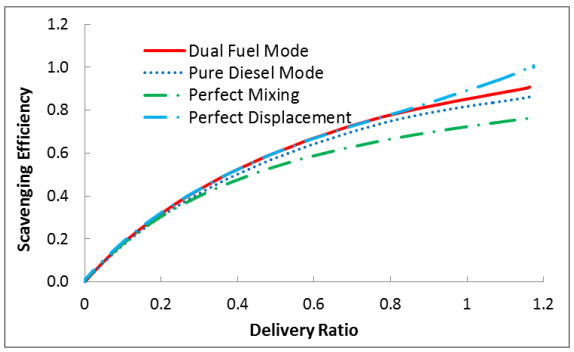

Figure 7.48 Scavenging efficiency as a function of the delivery ratio. Perfect mixing and perfect displacement assumed under dual fuel condition

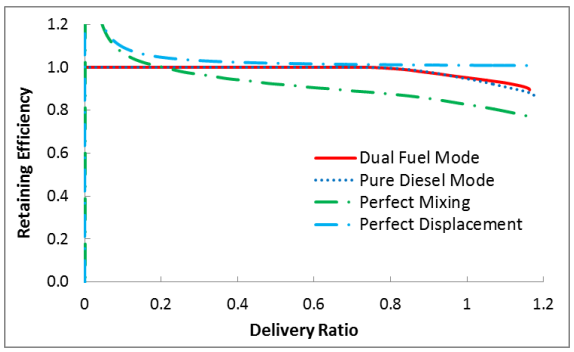

Figure 7.49 Retaining efficiency as a function of the delivery ratio

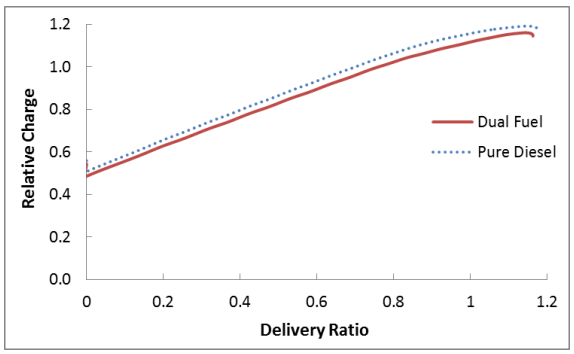

Figure 7.50 Relative charge as a function of the delivery ratio

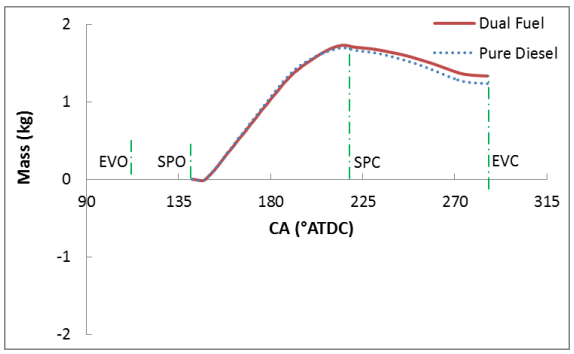

Figure 7.51 Retained mass of the fresh air charge for the dual fuel and the diesel modes

7.4 Conclusions

In this chapter, the full-cycle operating processes in the large 2-stroke marine engine for the dual fuel and the diesel modes under 75% engine load is investigated by using the developed CFD model. The main findings are summarised as follows:

- During the gas injection process for the dual fuel mode, the high-temperature flame is observed primarily near the stoichiometric surface of the gas plumes, whist the diesel mode exhibits the diffusion flame is located downstream the vapour plumes due to the transportation by the strong swirling flow and the high-speed liquid sprays.
- The diesel operation fuelled by the liquid oil has a higher flame temperature than the dual fuel, which primarily uses the methane as fuel, except for the early stage of fuel injection.
- For the diesel mode, the heat release rate AHRR variation with the crank angle is remarkably different with that of the dual fuel mode. The two peaks and one valley between them are observed. Before the first peak at 6 °ATDC, the AHRR fast increases, whilst the HRR peak value is almost the same to that of the dual fuel mode. The following reduction of the AHRR values is due to the less fuel vapor retained in the engine chamber. After 9 °ATDC, the liquid fuel injection increases the AHRR until to its peak at 11.3 °ATDC, attributed to the increases of the in-cylinder diesel vapor and the associated flame temperature.
- Gas emissions show that both modes have no unburned fuel before the EVC. The emitted CO_2 for the dual fuel mode is lower than the diesel mode by 21%. The NO emissions for the dual fuel mode reach 1820 ppm at the EVO, which is 31% lower than that of the diesel mode.
- Due to the observable difference of the retained fresh air mass and the total mass of the cylinder charge, the dual fuel mode obtains a slight higher scavenging efficiency, compared to the diesel mode. At the SPC, the scavenging efficiency for the dual fuel mode reaches 90.9%, and is higher by 4.2% than the respective value obtained for the diesel mode.
- As the scavenging process in the cylinder is closer to the perfect displacement, the higher scavenging efficiency is achieved. Consequently, the reduction of the carbon dioxide (CO_2) produced by the fuel combustion can be beneficial of the improvement of the scavenging efficiency.

Chapter 8 Conclusions and Recommendations

8.1 Summary and Conclusions

The objective of this research was to numerically investigate the whole-cycle operating processes in the 2-stroke marine dual fuel engine with the high-pressure gas direct injection type. For addressing this objective, the following work was conducted:

- The critical review was conducted, involving the CFD models and the related investigation in the operating processes of a 2-stroke marine engine and the HPGI engine.
- In terms of the characteristics of the 2-s dual fuel marine engine S60ME, the sub-models released by ANSYS Fluent were customized and developed. The spray process of liquid/pilot fuel was modelled, taking into account the variable Thermophysical liquid fuel properties with the high temperature and pressure. The conserving-equation sources approach was developed, considering the effects of the barrel-shaped shocks patterns near the nozzle exit. The non-premixed dual fuel combustion model was developed, in which the pilot fuel combustion was treated as the ignition kernel, accounting for the heat loss of pilot fuel evaporation and CO_2 and H_2O produced by the pilot fuel combustion.
- The validation of the developed CFD models was performed. The breakup and evaporation processes of the droplets were validated, by comparing the simulation results with the measured liquid and vapour penetration, as well as the temporal and special distributions of the vapour concentration in the SANDIA experiment,. Implementing the grid convergence by using ITTC procedure [116], the feasible grid density was recommended, compromising the computational cost and the accuracy, and the associated CFD results were validated by the measured penetrations of nitrogen injection under two pressure ratios values. The developed non-premixed dual fuel combustion models and the rate constants in the extended Zeldovich mechanism were validated, according to the published measurements of the derived HRR and NOx emissions in RCEM [9].
- In order to determine the injection and geometric parameters of dual fuel operation for the 75% engine load in the marine engine S60ME [5], the parametric investigation of dual fuel injection in the closed cycle was conducted with the aim to maintain the power level and reducing the NO and CO_2 emissions. The investigated parameters included the dual fuel injection timing, the gas injection duration, the lateral angle of gas nozzle, the holes number of gas injector, and the different inclination angle for each gas hole. Subsequently, the design parameters for 75% engine load were recommended.
- By using the developed CFD models, the full-cycle operating processes for the 75% engine load of the large two-stroke marine engine S60ME were investigated. With the comparison of

the dual fuel and the diesel modes, the in-depth understanding of the effects of the fuel injection, combustion, blowdown and scavenging processes on the engine performance and NO emission was obtained and the main difference between these two operating modes were studied.

Based on the above-mentioned investigation, the following conclusions are drawn:

- The customized liquid fuel injection model could adequately evaluate the liquid penetration and the vapour evolution in the SANDIA chamber. The developed high-pressure gas injection model sufficiently predicted the gas jet tip penetration.
- Regarding the non-premixed dual fuel combustion model, the steady diffusion flamelet model and the extended Zeldovich Mechanism with the rate constants according to Hanson and Salimian [95] were recommended, which could sufficiently evaluate the effects of the change of the fuel operation from the diesel mode to the dual fuel diesel mode, the pilot fuel injection timing and the reduction of the oxygen content in the charge air on the heat release rate (HRR) and the NO emissions in RCEM.
- The most significant parameter for the parametric study of the marine engine S60ME under 75% load was the lateral angle of the gas injectors. Varying the lateral angle from 0° to 30°, increased the cylinder indicated pressure (IMEPcc) by 12%, and reduced the HC emissions, whilst substantially increasing the NO and CO_2 emissions.
- For comprising on the contradictory objectives of retaining the engine power, NO and CO_2 emissions for the dual fuel operation for 75% load in the marine engine S60ME, the design settings of the dual fuel injection were recommended as follows:

Table 8.1 Recommended set of design parameters for the dual fuel operation for 75% load

	Injectors number	Holes Parameters in One Injector			Injected Mass (kg/rev)	Injection Start (°ATDC)	Injection End (°ATDC)
		Holes Number	Inclination Angle (°)	Lateral Angle (°)			
Pilot	3	1	15	0	0.00193	-1.5	3.02
Gas	3	5	23	-70	0.0380	0.0	11.24
			19	-50			
			15	-30			
			11	-10			

- By comparing the S60ME engine dual fuel and the diesel operating mode for the 75% load, the combustion processes indicated that the diesel mode achieves the higher flame temperature than the dual fuel mode. Moreover, the diffusion flame for the diesel mode was located downstream the vapour flumes, whilst the dual fuel mode exhibited the high-temperature flame in the vicinity of the stoichiometric surface of the gas plumes.

- The dual fuel mode for the engine S60ME could provide the same power to the diesel mode for 75% load. The results showed that both operating modes had no unburned HC emitted, whereas the carbon dioxide (CO_2) and nitrogen oxide (NO) emissions for the dual fuel mode were lower by 21% and 31% than that of the diesel mode, respectively.
- Due to the higher retained fresh air mass and the lower total mass of the cylinder charge, the scavenging efficiency for the dual fuel mode was 4.2% higher than that of the diesel mode. The investigation of the scavenging process with the perfect displacement and the perfect mixing indicated that the less CO_2 emissions produced by the dual fuel combustion is the reason of the higher scavenging efficiency for the dual fuel operating mode .

As the investigation of the internal operations in the large two-stroke dual fuel marine engine, the innovations and the main findings are summarized as follows:

- ANSYS Fluent operation for the simulation of the full-cycle operating processes in the marine is extremely high challenge, including the combination and cancellation of the extern zone (scavenging ports and the exhaust duct) with the cylinder zone, dynamic meshing caused by the piston moving and the exhaust valve lifting, the automatically time-step adjustment and the link of the personal codes (the developed models and the post-processing codes in the parallel) into ANSYS Fluent. As a consequence, operating ANSYS Fluent and integrating ANSYS Fluent with my developed models was a creation for the simulation of the full-cycle operation in a dual fuel engine.
- Combining the shock tube theory with the pseudo-diameter concept, the conserving-equation sources approach was developed to simulate the high-pressure gas direct injection into the engine combustion chamber, accounting for the effects of the expansion fan inside the gas nozzle and the barrel-shaped shocks patterns close to the nozzle exit.
- The dual fuel non-premixed combustion model was developed, by regarding the pilot fuel combustion as an ignition kernel, which involved the steady diffusion flamelet model and the extended Zeldovich mechanism.
- The parametric investigation of the dual fuel injection at 75% load of the large 2-s marine engine was conducted by the developed dual fuel combustion models. The study demonstrated the most important dual fuel injection parameter of deteriorating the gas fuel combustion process and derating the engine power.
- Numerical investigation of the whole-cycle operating processes at 75% load of the large 2-s marine engine S60ME indicated the diffusion flame difference between the dual fuel mode and the diesel mode and the reason that causes the higher scavenging efficiency for the dual fuel mode than that of the diesel mode.

8.2 Future Work

For the further investigation of the large 2-stroke marine engine S60ME, the following work is recommended in the future:

- In the thesis, the investigated dual fuel mode in the marine engine S60ME is the minor pilot fuel mode, where the amount of the pilot fuel is about 5% of the total fuel mass. In the future, the effects of the pilot fuel up to 50% of the total fuel on the full-cycle operating processes and the engine performance and the gas emissions should be investigated.
- As expected, the dual fuel injection parameters for the different engine load should be slightly different, in order to retain the engine power and reduce the gas emissions. The dual fuel injection parameters feasible to the different engine load in the marine engine S60ME should proceed, particularly for the dual fuel injection timing.
- Apart from the methane, natural gas primarily includes the ethane and propane. The effects of the various gas fuel quality on the gas combustion characteristics and the emissions should be studied, as well as the skeletal chemical mechanism.
- Apart from the natural gas, other alternative fuels and their chemical mechanisms in the marine engine will be studied, such as the biodiesel, methanol, biogas, synthetic fuel, etc.

Due to the limits of the developed dual fuel combustion model in the thesis, the following work for the improvement of the dual fuel combustion model is recommended:

- As the increment of the pilot fuel up to 50% in the dual fuel engine, the current developed dual fuel combustion model based on the single mixture-fraction approach is not applicable, due to the strong interaction between the liquid fuel injection and the gas fuel injection. The two-mixure-fractions approach embedded in the variable chemical mechanisms is an alternative method to solve the dual fuel operation with the similar level of the liquid fuel and the gas fuel.
- For the precise prediction of the low chemistry, strongly instantaneous state or long residence time of the fuel combustion such as NOx formation, low-temperature CO oxidation and split-injections, the unsteady diffusion flammlet model should be developed in the future. And, the more complicated chemical kinetics of the NOx formation such as the super-extended Zeldovich mechanism [127] should be directly added to the fuel chemical reactions, rather than the extended Zeldovich mechanism.
- When the pilot fuel injection timing and the gas fuel injection timing is extremely close, the diffusion combustion is not dominated in the dual fuel combustion process. Due to the feasible simulation in the premixed, partial premixed and non-premixed combustion,

Conditional Moment Closure (CMC) method should be developed in the future, in case that the diffusion combustion does not prevail.

References

[1] IMO. (2016). *Revised MARPOL Annex VI* [Online]. Available: http://www.imo.org/en/OurWork/Environment/PollutionPrevention/AirPollution/Pages/Air-Pollution.aspx.

[2] M. Ott, "Low pressure gas engines - The industry standard," in the International Council on Combustion engines CIMAC, Athens Greece, 22 January 2015.

[3] N. Kjemtrup, "Gas 2-stroke marine engine design and operation," in the International Council on Combustion engines CIMAC, Athens Greece, 22 January 2015.

[4] WÄRTSILÄ. (2015). *WÄRTSILÄ low-speed dual-fuel solution. Energy Environment Economy* [Online]. Available: http://www.cedervall.com/docs/default-source/product-files/engines-generating-sets/low-speed-generation-x-engines/brochure-o-e-wartsila-dual-fual-low-speed.pdf?sfvrsn=4.

[5] MAN Diesel & Turbo. (2016). *CEAS engine data report 5S60ME-C8.5-GI (methane) with high load tuning* [Online]. Available: http://marine.man.eu/two-stroke/ceas.

[6] BusinessDictionary. (2017). *Octane number definition* [Online]. Available: http://www.businessdictionary.com/definition/Octane-number.html.

[7] T. Korakianitis et al., "Diesel and rapeseed methyl ester (RME) pilot fuels for hydrogen and natural gas dual-fuel combustion in compression–ignition engines," Fuel, vol. 90, No. 7, pp. 2384-2395, July 2011.

[8] M. M. Abdelaal et al., "Effect of adding oxygen to the intake air on a dual-fuel engine performance, emissions, and knock tendency," Energy, vol. 61, pp. 612-620, 2013.

[9] D. Imhof et al., "High-pressure natural gas injection (GI) marine engine research with a Rapid Compression Expansion Machine," in the International Council on Combustion engines CIMAC, Shanghai China, 2013.

[10] MAN Diesel & Turbo, "MAN Diesel & Turbo's Mature Gas Technology: a Closer Look - Low and medium speed segments offer multiple proven solutions," DIESELFACTS, pp. 6-6, 2016.

[11] L. Haraldson, "LNG as a fuel for environmentally friendly shipping retrofit perspective," in the 33rd Motorship Propulsion & Emissions Conference, Copenhagen, 11-12 May 2011.

[12] R. D. Reitz and F. V. Bracco, "Mechanisms of breakup of round liquid jets," The Encyclopedia of Fluid Mechanics, vol. 3, pp. 223–249, 1986.

[13] P. J. O'Rourke and A. A. Amsden, "The TAB method for numerical calculation of spray droplet breakup," SAE Technical Paper 872089, 1987.

[14] S. P. Lin and R. D. Reitz, "Drop and spray formation from a liquid jet," Annu. Rev. Fluid Mech., vol. 30, pp. 85-105, 1998.

[15] J. C. Beale and R. D. Reitz, "Modeling spray atomization with the Kelvin-Helmholtz/Rayleigh-Taylor hybrid model," Atomization and Sprays, vol. 9, pp. 623–650, 1999.

[16] S. V. Apte et al., "LES of atomizing spray with stochastic modelling of secondary breakup," International Journal of Multiphase Flow, vol. 29, pp. 1503 –1522, 2003.

[17] S. B. Dam, "Experimental and numerical investigations of sprays in two stroke diesel engines," Ph.D. dissertation, Technical University of Denmark, 2007.

[18] B. F. Magnussen and B. H. Hjertager, "On mathematical models of turbulent combustion with special emphasis on soot formation and combustion," in the 16th Symp. (Int'l.) on Combustion, 1976.

[19] N. Peters, "Laminar diffusion Flamelet models in non-premixed turbulent combustion," Prog. Energy Combust. Sci., vol. 10, pp. 319-339, 1984.

[20] R. W. Bilger, "Turbulent jet diffusion flames," Prog. Energy Combust. Sci., vol. 1, pp. 87-109, 1993.

[21] A.Y. Klimenko and R.W. Bilger, "Conditional moment closure for turbulent combustion," Progress in Energy and Combustion Science, vol. 25, pp. 595–687, 1999.

[22] H. Barths et al., "Simulation of combustion in direct injection diesel engines using a Eulerian particle flamelet model," Proceeding of the Combustion Institute, Vol. 28, pp. 1161-1168, 2000.

[23] B. Andr éet al., "Experimental exploration of underexpanded supersonic jets," Shock Waves, vol. 24, pp. 21–32, 2014.

[24] P. L. Eggins and D. A. Jackson, "Laser-Doppler velocity measurements in an under-expanded free jet," J. Phys. D: Appl. Phys., vol. 7, 1974.

[25] P. Ouellette, "Direct injection of natural gas for the diesel engine fueling," Ph. D. dissertation, University of British Columbia, 1996.

[26] J. S. Turner, "The 'starting plume' in neutral surroundings," Journal of Fluid Mechanics, vol. 13, pp. 356-68, 1962.

[27] P. Ouellette and P. G. Hill, “Turbulent transient gas injections,” Journal of Fluids Engineering, vol. 122, page 743, 2000.

[28] P. G. Hill and B. Douville, “Analysis of combustion in diesel engines fuelled by directly injected natural gas,” Journal of Engineering for Gas Turbines and Power, vol. 122, pp. 141-149, 2000.

[29] A. Hajialimohammadi et al., “Ultra high speed investigation of gaseous jet injected by a single-hole injector and proposing of an analytical method for pressure loss prediction during transient injection,” Fuel, vol. 184, pp. 100-109, 2016.

[30] M. Choi et al., “Numerical and experimental study of gaseous fuel injection for CNG direct injection,” Fuel, vol. 140, pp. 693-700, 2015.

[31] R. P. Hessel et al., “Gaseous fuel injection modeling using a gaseous sphere injection methodology,” SAE Technical Paper 2006-01-3265, 2006.

[32] M. Vångö, “CFD modelling of direct gas injection using a Lagrangian Particle Tracking approach,” LUP Student Papers, Lund University Libraries, 2015.

[33] S. G. Chuech et al., “Structure of turbulent sonic underexpanded free jets,” AIAA Journal, vol. 27, No. 5, May 1989.

[34] P. S. Cumber et al., “Predictions of the structure of turbulent, highly underexpanded jets,” ASME, vol. 117, pp. 599-604, Dec. 1995.

[35] M. J. Jennings and F. R. Jeske, “Analysis of the injection process in direct injected natural gas engines: Part I—study of unconfined and in-cylinder plume behaviour,” ASME, vol. 116, pp. 806-813, Oct. 1994.

[36] M. J. Jennings and F. R. Jeske, “Analysis of the injection process in direct injected natural gas engines: Part II—Effects of injector and combustion chamber design,” ASME, vol. 116, pp. 799-805, Oct. 1994.

[37] B. J. Gribben et al., “Numerical study of shock-reflection hysteresis in an underexpanded jet,” AIAA Journal, vol. 38, No. 2, Feb. 2000.

[38] Y. Li et al., “Characteristic and computational fluid dynamics modelling of high-pressure gas jet injection,” J. Eng. Gas Turbines Power, vol. 126, No. 1, pp. 192-197, 2004.

[39] A. Hajialimohammadi et al., “Experimental and Numerical Investigation on the macroscopic characteristics of the jet discharging from gaseous direct injector,” Journal of Mechanical Science and Technology, vol. 28, No. 2, pp. 773~781, 2014.

[40] B. Yadollahi and M. Boroomand, "The effect of combustion chamber geometry on injection and mixture preparation in a CNG direct injection SI engine," Fuel, vol. 107, No. 5, pp. 52–62, 2013.

[41] G. P. Mctaggart-Cowan, "Pollutant formation in a gaseous-fuelled, direct injection engine," Ph.D. dissertation, University of British Columbia, 2006.

[42] L. Muniz and M. G. Mungal, "Instantaneous flame-stabilization velocities in lifted-jet diffusion flames," Combustion and Flame, vol. 111, pp. 16-31, 1997.

[43] G. Li et al., "Optimization study of pilot-ignited natural gas direct-injection in diesel engines," Journal of Fuels and Lubricants, vol.108, No. 4, 1999.

[44] B. Jin, "Conditional source-term estimation method for turbulent reacting flow," Ph.D. Dissertation, the University of British Columbia, Dec. 2007.

[45] ANSYS Inc. (2015). *ANSYS Fluent theory guide release 15.0* [Online]. Available: http://ishare.iask.sina.com.cn/f/35269373.html.

[46] C. M. Cha et al., "Modelling extinction and re-ignition in turbulent non-premixed combustion using a doubly conditional moment closure approach," Physics of Fluids, vol. 13, No. 12, pp. 3824–3834, 2001.

[47] I. S. Kim, "Conditional moment closure for non-premixed turbulent combustion," Ph.D. Dissertation, St Edmund's College, Dec. 2004.

[48] I. Han and K. Y. Huh. (2004). *Conditional moment closure modelling of turbulent spray combustion in a direct injection diesel engine* [Online]. Available: https://www.erc.wisc.edu/documents/6-KIVAUsers_CMC_engine.pdf.

[49] K. M. Pang et al., "Numerical investigation of soot formation and oxidation processes under large two-stroke marine diesel engine-like conditions using integrated CFD-chemical kinetics," Applied Energy, vol. 169, pp. 874–887, 2016.

[50] F. Tao et al., "Nine-step phenomenological diesel soot model validated over a wide range of engine conditions," Int. J. Therm. Sci., vol. 48, pp.1223–1234, 2007.

[51] W. L. Easley and A. M. Mellor, "NO decomposition in diesel engines," SAE paper 1999- 01-3546, 1999.

[52] X. Sun, "Effect of different combustion models and alternative fuels on two-stroke marine diesel engine performance," Applied Thermal Engineering, vol. 115, pp. 597–606, 2017.

[53] A. Obeidat et al., "Influence of piston displacement on the scavenging and swirling flow in two-stroke diesel engines," in the 23rd Nordic Seminar on Computational Mechanics, 2010.

[54] M. I. Lamas and C. G. R. Vidal, "Computational fluid dynamics analysis of the scavenging process in the MAN B&W 7S50MC two-stroke marine diesel engine," Journal of Ship Research, vol. 56, No. 3, pp. 154–161, Sep. 2012.

[55] C. S. Hemmingsen et al., "Swirling flow in a two-stroke marine diesel engine," in the Proceedings of the 26th Nordic Seminar on Computational Mechanics, 2013.

[56] E. Sigurdsson, "Scavenging flow in a two-stroke diesel engine," M.S. thesis, Technical University of Denmark, 2011.

[57] E. Sigurdsson et al., "Numerical analysis of the scavenge flow and convective heat transfer in large two-stroke marine diesel engines," Applied Energy, vol. 123, pp. 37–46, 2014.

[58] B. Douville, "Performance, emissions and combustion characteristics of natural gas fuelling of diesel engines," M.S. thesis, the University of British Columbia, 1994.

[59] C. R. Larson, "Injection study of a diesel engine fuelled with pilot-ignited, directly-injected natural gas," M.S. thesis, the University of British Columbia, 2003.

[60] G. P. McTaggart-Cowan et al., "Effects of operating condition on particulate matter and nitrogen oxides emissions from a heavy-duty direct injection natural gase engine using cooled exhaust gas recirculation," Int. J. Engine Res., vol. 5, No. 6, 2004.

[61] G. P. McTaggart-Cowan et al., "Hydrogen-methane blend fuelling of a heavy-duty, direct-injection engine," in the International Mechanical Engineering Congress and Exposition ASME, Seattle, Washington, USA, Nov. 11-15, 2007.

[62] G. P. McTaggart-Cowan et al., "The influence of fuel composition on a heavy-duty, natural-gas direct-injection engine," Fuel, vol. 89, pp. 752–759, 2010.

[63] B. S. Brown, "High-pressure direct-injection of natural gas with entrained diesel into a compression-ignition engine," M.S. thesis, the University of British Columbia, 2008.

[64] M. Li et al., "Experimental investigation on performance and heat release analysis of a pilot ignited direct injection natural gas engine," Energy, vol. 90, pp. 1251-1260, 2015.

[65] Q. Zhang et al., "Combustion process and emissions of a heavy-duty engine fuelled with directly injected natural gas and pilot diesel," Applied Energy, vol.157, pp.217–228, 2015.

[66] T. Tsuboi and H. G. Wagner, "Homogeneous thermal oxidation of methane in reflected shock waves," in the 15th International Symposium on Combustion, 1974.

[67] G. Li et al., "Modeling HPDI natural gas heavey duty engine combustion," in the Proceedings of ICEF2005, ASME Internal Combustion Engine Division 2005 Fall Technical Conference, Ottawa, Canada, Sep. 11-14, 2005.

[68] M. P. Halstead et al., "The autoignition of hydrocarbon fuels at high temperatures and pressures—Fitting of a mathematical model," Combustion Flame, vol. 30, pp. 45-60, 1977.

[69] W. G. Lee and D. Montgomery, "Numerical investigation of the performance of a high pressure direct injection (HPDI) natural gas engine," in the Proceedings of the ASME 2014 Internal Combustion Engine Division Fall Technical Conference, Columbus, IN, USA, October 19-22, 2014.

[70] A. Patel et al., "Development and Validation of a Reduced Reaction Mechanism for HCCI Engine Simulations," SAE Technical Paper No. 2004-01-0558, 2004.

[71] M. Li et al., "Effects of hydrogen addition on the performance of pilot-ignition direct-injection natural gas engine: a numerical study," Energy Fuels, vol. 31, pp. 4407-4423, 2017.

[72] *CONVERGE CFD Software* [Online]. Available: https://convergecfd.com/applications/internal-combustion-engines.

[73] Q. Wang et al., "Effects of injection rate on combustion and emissions of a pilot ignited direct injection natural gas engine," Journal of Mechanical Science and Technology, vol. 31, No. 4, pp.1969~1978, 2017.

[74] O. Colin and A. Benkenida, "The 3-Zones extended coherent flame model (ECFM3Z) for computing premixed/diffusion combustion," Oil & Gas Science and Technology – Rev. IFP, vol. 59, No. 6, pp. 593-609, 2004.

[75] V. K. Duggal et al., "Development of the high-pressure direct-injected, ultralow-NOx natural gas engine," NREL/SR-540-35911, 2004.

[76] Y. Gao, et al., "Numerical simulations of natural gas injection pressure effects on a direct injected, pilot ignited, natural gas engine," Applied Mechanics and Materials, vol. 510, pp. 179-184, 2014.

[77] I. O. Hinze, *Turbulence*, McGraw-Hill Publishing Co., New York, 1975.

[78] S. A. Orszag et al., "Renormalization group modelling and turbulence simulations," in International Conference on Near-Wall Turbulent Flows, Tempe, Arizona, 1993.

[79] D. Y. Peng and D. B. Robinson, "A New Two-Constant Equation of State," Industrial and Engineering Chemistry: Fundamentals, vol. 15, pp. 59-64, 1976.

[80] W. Jin, "CFD modelling and validation of a large 2-stroke marine diesel engine," Ph.D. Dissertation, University of Strathclyde, 2014.

[81] A. D. Gosman and E. Ioannides, "Aspects of computer simulation of liquid-fuelled combustors," J. Energy, vol. 7, No. 6, pp. 482-490, 1983.

[82] A. B. Liu et al., "Modelling the effects of drop drag and breakup on fuel sprays," SAE Technical Paper 930072, 1993.

[83] P. J. O'Rourke and A. A. Amsden, "The TAB method for numerical calculation of spray droplet breakup," SAE Technical Paper 872089, 1987.

[84] V. G. Levich, *Physicochemical hydrodynamics*. Prentice Hall, 1962.

[85] R. D. Reitz, "Mechanisms of atomization processes in high-pressure vaporizing sprays," Atomization and Spray Technology, vol. 3, pp. 309–337, 1987.

[86] W. E. Ranz and W. R. Marshall, "Vaporation from drops, Part I," Chem. Eng. Prog., vol. 48, No. 3, pp. 141-146, 1952.

[87] W. E. Ranz and W. R. Marshall, "Vaporation from drops, Part I and PII," Chem. Eng. Prog., vol. 48, No. 4, pp. 173-180, 1952.

[88] R. S. Miller et al., "Evaluation of equilibrium and non-equilibrium evaporation models for many droplet gas-Liquid flow simulations," International Journal of Multiphase Flow, vol. 24, No. 6, pp. 1025 –1055, 1998.

[89] S. S. Sazhin, "Advanced models of fuel droplet heating and evaporation," Progress in Energy and Combustion Science, Elsevier Science, vol. 32, pp. 162–214, 2006.

[90] K. K. Y. Kuo, *Principles of combustion*. John Wiley and Sons, New York, 1986.

[91] Y. R. Sivathanu and G. M. Faeth, "Generalized state relationships for scalar properties in non-premixed hydrocarbon/airFlames," Combustion and Flame, vol. 82, pp. 211–230, 1990.

[92] W. P. Jones and J. H.Whitelaw, "Calculation methods for reacting turbulent flows: a review," Combustion and Flame, vol. 48, pp. 1–26, 1982.

[93] F. A. Williams and S. N. B. MURTHY, Ed., *Turbulent mixing in non-reactive and reactive flows*. Plenum, 1975, pp. 189-189.

[94] P. C. Melte and D. T. Pratt, "Measurement of atomic oxygen and nitrogen oxides in jet stirred combustion," in 15th Symposium on Combustion, 1974, pp. 1061-1070.

[95] R. K. Hanson and S. Salimian, "Survey of rate constants in H/N/O systems," In W. C. Gardiner, Combustion Chemistry, vol. 361, 1984.

[96] A. A.Westenberg, Comb. Sci. Tech., vol. 4, No. 59, 1971.

[97] C.Westbrook and F. Dryer, "Chemical kinetic modelling of hydrocarbon combustion," Prog. Energy Comb. Sci., vol. 1, 1984.

[98] D. L. Baulch et al., "Evaluated kinetic data for combustion modelling," J. Physical and Chemical Reference Data, vol. 21, No. 3, 1992.

[99] R. W. Bilger and S. H. Starner, "On reduced mechanism for methane-air combustion in nonpremixed flames," Combustion and Flame, vol. 80, pp. 135-149, 1990.

[100] M. A. Patterson and R. D. Reitz, "Modeling the effects of fuel spray characteristics on diesel engine combustion and emission," SAE Paper, 1998.

[101] Y. Wakuri et al., "Studies on the penetration of fuel spray in a diesel engine," Bulletin of JSME, vol. 3, No. 9, 1960.

[102] J. D. Naber and D. L. Sieber, "Effects of gas density and vaporization on penetration and dispersion of diesel sprays," SAE 960034, 1996.

[103] D.L. Sieber, "Scaling liquid-phase fuel penetration in diesel sprays based on mixing-limited vaporation," SAE 1999-01-0528, 1999.

[104] J. D. Anderson, *Fundamentals of aerodynamics*. Second Ed. McGraw-Hill Inc., ISBN 0-07-001679-8, 1991.

[105] C. L. Rasmussen et al., "Sensitizing effects of NOx on CH_4 oxidation at high pressure," Combustion and Flame, vol. 154, pp. 529-545, 2008.

[106] ECN. (2016). *Engine Combustion Network* [Online]. Available: https://ecn.sandia.gov/.

[107] D.L. Sieber, "Liquid-phase fuel penetration in diesel sprays," SAE Paper 980809, 1998.

[108] N. Nordin, "Modelling spray combustion CECOST spray course notes," Chalmers University, 2003.

[109] ANSYS Inc. (2015). *ANSYS Fluent user guide release 15.0* [Online]. Available: https://www.ansys.com/.

[110] J. Abraham, "What is adequate resolution in the numerical computations of transient jets?" SAE 970051, 1997.

[111] P. Beard et al., "Extension of Lagrangian-Eulerian spray modelling: application to high pressure evaporating diesel sprays," SAE 2000-01-1893, 2000.

[112] R. Steiner et al., "3D-simulation of DI diesel combustion applying a progress variable approach accounting for complex chemistry," SAE 2004-01-0106, 2004.

[113] R. Saini and A. De., "Simulation of non-reacting transient N-Dodecane spray in a high-pressure combustion vessel," in ASME 2015 Gas Turbine India Conference, Hyderabad, India, December 2-3 2015.

[114] N. Nordin, "Complex chemistry modelling of diesel spray combustion," Ph.D. dissertation, Chalmers University, 2000.

[115] Ryosuke Ishibashi and Daisuke Tsuru. An optical investigation of combustion process of a direct high-pressure injection of natural gas. J. Mar. Sci. Technol., DOI 10.1007/s00773-016-0422-x, 2016.

[116] *CFD general uncertainty analysis in CFD verification and validation methodology and procedures*, ITTC – Quality Mannual 7.5-03-01-01, 2002.

[117] John W. Slater. (2008). *Examining Spatial (Grid) Convergence* [Online]. Available: https://www.grc.nasa.gov/WWW/wind/valid/tutorial/spatconv.html.

[118] J. B. Heywood, *Internal combustion engine fundamentals*. McGraw-Hill Series in Mechanical Engineering, 1988.

[119] R. G. Papagiannakis and D. T. Hountalas, "Experimental investigation concerning the effect of natural gas percentage on performance and emissions of a DI dual fuel diesel engine," Applied Thermal Engineering, vol. 23, pp. 353-365, 2003.

[120] G. S. Zhu and S. K. Aggarwal, "Fuel droplet evaporation in a supercritical environment," Transactions of the ASME, vol. 124, pp. 762-770, 2002.

[121] NIST. (2016). *Chemical and Engineering* [Online]. Available: http://webbook.nist.gov/chemistry.

[122] A. Manuel and D. E. Rosner, "Multicomponent fuel droplet vaporization and combustion using spectral theory for a continuous mixture," Combustion and Flame, vol. 135, pp.271-284, 2003.

[123] A. E. Y. M. Elwardany, "Modelling of multi-component fuel droplets heating and evaporation," Ph.D. dissertation, University of Brighton, UK, 2012.

[124] B. E. Poling et al., *The properties of gases and liquids*. Fifth Ed. McGRAW-HILL, 2000.

[125] R. Yang et al., "Numerical investigation of the gas injection process in large marine DF engines," in International Conference on Maritime Safety and Operations, Glasgow, UK, 13th – 14th October 2016.

[126] E. Sigurdsson, "Scavenging flow in a two-stroke diesel engine," M.S. thesis, Technical University of Denmark, 2011.

[127] S. Woolridge, "An experimental and theoretical study into nitric oxide production at elevated pressures and temperatures," Ph.D. dissertation, Loughborough University, May 2007.

Appendix A: Skeletal Chemical Kinetics Mechanism of n-Heptane with Rate Data

Source: ANSYS Fluent [45].

The reaction rate coefficients are formed by the following expression.

$$k = AT^{b}e^{-E_0/T} \quad \text{(A-1)}$$

Table A.1 Rate coefficients of the skeleton chemical reactions of n-heptane

Reaction Number	Reactions	A (cm^3 mol/s)	b (-)	E_0 (K)
R1	C7H16 + H= C7H15-2 + H2	4.380e+07	2.0	4760.0
R2	C7H16 + OH = C7H15-2 + H2O	9.700e+09	1.3	1690.0
R3	C7H16 + HO2 = C7H15-2 + H2O2	1.650e+13	0.0	16950.0
R4	C7H16 + O2 = C7H15-2 + HO2	2.000e+15	0.0	47380.0
R5	C7H15-2 + O2 = C7H15O2	1.560e+12	0.0	0.0
R6	C7H15O2 + O2 = C7KET12 + OH	4.500e+14	0.0	18232.712
R7	C7KET12 = C5H11CO + CH2O +OH	9.530e+14	0.0	4.110e+4
R8	C5H11CO = C2H4 + C3H7 +CO	9.84E+15	0.0	4.02E+04
R9	C7H15-2 = C2H5 +C2H4 +C3H6	7.045E+14	0.0	3.46E+04
R10	C3H7 = C2H4 + CH3	9.600e+13	0.0	30950.0
R11	C3H7 = C3H6 + H	1.250e+14	0.0	36900.0
R12	C3H6 + CH3 = C3H5 +CH4	9.000e+12	0.0	8480.0
R13	C3H5 + O2 = C3H4 + HO2	6.000e+11	0.0	10000.0
R14	C3H4 + OH = C2H3 +CH2O	1.000e+12	0.0	0.0
R15	C3H4 + OH = C2H4 +HCO	1.000e+12	0.0	0.0
R16	CH3 + HO2 = CH3O + OH	5.000e+13	0.0	0.0
R17	CH3 + OH = CH2 +H2O	7.500e+06	2.0	5000.0
R18	CH2 + OH = CH2O + H	2.500e+13	0.0	0.0
R19	CH2 + O2 = HCO + OH	4.300e+10	0.0	-500.0
R20	CH2 + O2 = CO2 +H2	6.900e+11	0.0	500.0
R21	CH2 + O2 = CO + H2O	2.000e+10	0.0	-1000.0
R22	CH2 + O2 = CH2O + O	5.000e+13	0.0	9000.0
R23	CH2 + O2 = CO2 + H + H	1.600e+12	0.0	1000.0
R24	CH2 + O2 = CO + OH +H	8.600e+10	0.0	-500.0
R25	CH3O + CO = CH3 + CO2	1.570e+14	0.0	11800.0
R26	CO + OH = CO2 +H	8.987e+07	1.38	5232.877
R27	O + OH = O2 + H	4.000e+14	-0.5	0.0
R28	H + HO2 = OH + OH	1.700e+14	0.0	875.0
R29	OH + OH = O + H2O	6.000e+08	1.30	0.0
R30	H + O2 + M = HO2 + M	3.600e+17	-0.72	0.0
R31	H2O2 + M = OH + OH + M	1.000e+16	0.0	45500.0
R32	H2 + OH = H2O + H	1.170e+09	1.30	3626.0
R33	HO2 + HO2 = H2O2 + O2	3.000e+12	0.0	0.0
R34	CH2O + OH = HCO + H2O	5.563e+10	1.095	-76.517
R35	CH2O + HO2 = HCO + H2O2	3.000e+12	0.0	8000.0
R36	HCO + O2 = HO2 + CO	3.300e+13	-0.4	0.0
R37	HCO + M = H + CO +M	1.591E+18	0.95	56712.329
R38	CH3 + CH3O = CH4 + CH2O	4.300e+14	0.0	0.0

Reaction Number	Reactions	A (cm^3 mol/s)	b (-)	E_0 (K)
R39	C2H4 + OH = CH2O + CH3	6.000e+13	0.0	960.0
R40	C2H4 + OH = C2H3 + H2O	8.020e+13	0.0	5955.0
R41	C2H3 + O2 = CH2O + HCO	4.000e+12	0.0	-250.0
R42	C2H3 + HCO = C2H4 + CO	6.034e+13	0.0	0.0
R43	C2H5 + O2 = C2H4 + HO2	2.000e+10	0.0	-2200.0
R44	CH4 + O2 = CH3 + HO2	7.900e+13	0.0	56000.0
R45	OH + HO2 = H2O + O2	7.50E+12	0.0	0.0
R46	CH3 + O2 = CH2O + OH	3.80E+11	0.0	9000.0
R47	CH4 + H = CH3 + H2	6.600e+08	1.6	10840.0
R48	CH4 + OH = CH3 + H2O	1.600e+06	2.1	2460.0
R49	CH4 + O = CH3 + OH	1.020e+09	1.5	8604
R50	CH4 + HO2 = CH3 + H2O2	9.000e+11	0.0	18700.0
R51	CH4 + CH2 = CH3 +CH3	4.000e+12	0.0	-570.0
R52	C3H6 = C2H3 +CH3	3.150e+15	0.0	85500.0

Appendix B: Skeletal Chemical Kinetics Mechanism of Methane with Rate Data

Source: R. W. Bilger and S. H. Starner [99].

The reaction rate coefficients are formed by the following expression.

$$k = AT^{b}e^{-E_0/T} \quad \text{(B-1)}$$

Table B.1 Rate coefficients of the skeleton chemical reactions of methane

Reaction Number	Reactions	A (cm^3 mol/s)	b (-)	E_0 (K)
R1	CH4 + M = CH3 + H + M	6.300e+14	0.0	104000.0
R2	CH4 + O2 = CH3 + HO2	7.900e+13	0.0	56000.0
R3	CH4 + H = CH3 +H2	2.200e+04	3.0	8750.0
R4	CH4 + O = CH3 + OH	1.600e+06	2.36	7400.0
R5	CH4 + OH = CH3 + H2O	1.600e+06	2.1	2460.0
R6	CH3 + O = CH2O + H	6.800e+13	0.0	0.0
R7	CH3 + OH = CH2O + H2	1.000e+12	0.0	0.0
R8	CH3 + OH = CH2 + H2O	1.500e+13	0.0	5000.0
R9	CH3 + H = CH2 + H2	9.000e+13	0.0	15100.0
R10	CH2 + H = CH + H2	1.400e+19	-2.0	0.0
R11	CH2 + OH = CH2O + H	2.500e+13	0.0	0.0
R12	CH2 + OH = CH + H2O	4.500e+13	0.0	3000.0
R13	CH + O2 = HCO + O	3.300e+13	0.0	0.0
R14	CH + O = CO + H	5.700e+13	0.0	0.0
R15	CH + OH = HCO + H	3.000e+13	0.0	0.0
R16	CH + CO2 = HCO + CO	3.400e+12	0.0	690.0
R17	CH2 + CO2 = CH2O + CO	1.100e+11	0.0	1000.0
R18	CH2 + O = CO + H + H	3.000e+13	0.0	0.0
R19	CH2 + O = CO + H2	5.000e+13	0.0	0.0
R20	CH2 + O2 = CO2 + H + H	1.600e+12	0.0	1000.0
R21	CH2 + O2 = CH2O + O	5.000e+13	0.0	9000.0
R22	CH2 + O2 = CO2 + H2	6.900e+11	0.0	500.0
R23	CH2 + O2 = CO + H2O	1.900e+10	0.0	-1000.0
R24	CH2 + O2 = CO + OH + H	8.600e+10	0.0	-500.0
R25	CH2 + O2 = HCO + OH	4.300e+10	0.0	-500.0
R26	CH2O + OH = HCO + H2O	3.430e+09	1.18	-447.0
R27	CH2O + H = HCO + H2	2.190e+08	1.77	3000.0
R28	CH2O + M = HCO + H + M	3.310e+16	0.0	81000.0
R29	CH2O + O = HCO + OH	1.810e+13	0.0	3082.0
R30	HCO + OH = CO +H2O	5.000e+12	0.0	0.0
R31	HCO + M = H + CO + M	1.600e+14	0.0	14700.0
R32	HCO + H = CO + H2	4.000e+13	0.0	0.0
R33	HCO + O = CO2 + H	1.000e+13	0.0	0.0
R34	HCO + O2 = HO2 + CO	3.300e+13	-0.4	0.0
R35	CO + O + M = CO2 + M	3.200e+13	0.0	-4200.0
R36	CO + OH = CO2 + H	1.510e+07	1.3	-758.0
R37	CO + O2 = CO2 + O	1.600e+13	0.0	41000.0
R38	HO2 + CO = CO2 + OH	5.800e+13	0.0	22934.0

Reaction Number	Reactions	A (cm^3 mol/s)	b (-)	E_0 (K)
R39	H2 + O2 = OH +OH	1.700e+13	0.0	47780.0
R40	OH + H2 = H2O + H	1.170e+09	1.3	3626.0
R41	H + O2 = OH + O	5.130e+16	-0.816	16507.0
R42	O + H2 = OH + H	1.800e+10	1.0	8826.0
R43	H + O2 + M = HO2 + M	3.610e+17	-0.72	0.0
R44	OH + HO2 = H2O + O2	7.500e+12	0.0	0.0
R45	H + HO2 = OH + OH	1.400e+14	0.0	1073.0
R46	O + HO2 = O2 + OH	1.400e+13	0.0	1073.0
R47	OH + OH = O + H2O	6.000e+08	1.3	0.0
R48	H + H + M = H2 + M	1.000e+18	-1.0	0.0
R49	H + H + H2 = H2 + H2	9.200e+16	-0.6	0.0
R50	H + H + H2O = H2 + H2O	6.000e+19	-1.25	0.0
R51	H + H + CO2 = H2 + CO2	5.490e+20	-2.0	0.0
R52	H + OH + M = H2O + M	1.600e+22	-2.0	0.0
R53	H + O + M = OH + M	6.200e+16	-0.6	0.0
R54	H + HO2 = H2 + O2	1.250e+13	0.0	0.0
R55	HO2 + HO2 = H2O2 + O2	2.000e+12	0.0	0.0
R56	H2O2 + M = OH + OH + M	1.300e+17	0.0	45500.0
R57	H2O2 + H = HO2 + H2	1.600e+12	0.0	3800.0
R58	H2O2 + OH = H2O +HO2	1.000e+13	0.0	1800.0

Appendix C: Thermophysical Properties of Species

Source: ANSYS Fluent [45].

The species heat capacity C_{Pi} is expressed by the polynomials, and the enthalpy H_i^0 and entropy S_i^0 are given under the standard state.

$$C_{Pi} = a_0 + a_1 T + a_2 T^2 + a_3 T^3 + a_4 T^4 \quad \text{(C-1)}$$

Table C.1 Heat capacity for the temperature ranging from 300 K to 1000 K and standard state enthalpy

Species	C_{Pi} ($T \in [300,1000]$) (J/kg/K)					H_i^0 (J/kmol)
	a_0	a_1	a_2	a_3	a_4	
C7H16*[1]	-105.2412	7.088941	-0.004359018	1.352027e-06	-1.679354e-10	-1.885058e+08
C7H15O2	150.5127	5.289519	-0.003256771	1.040712e-06	-1.391091e-10	-1.324353e+08
C7H15-2 *[2]	-3.177978	6.342671	-0.00341533	7.817454e-07	-4.12683e-11	5439680
C7KET12	33.12588	5.756191	-0.004355801	1.710449e-06	-2.746507e-10	-3.554621e+08
C5H11CO	179.849	5.181025	-0.003137264	9.499283e-07	-1.148108e-10	-9.368801e+07
C3H7	202.9066	5.015393	0.0004592534	-3.783848e-06	1.808655e-09	1.004983e+08
C3H6 *[3]	77.96856	5.712222	-0.003060271	7.682235e-07	-6.676076e-11	1.945731e+07
C3H5	766.7935	1.919874	0.004905753	-7.400916e-06	3.007953e-09	1.689965e+08
C3H4	542.2719	2.515658	0.00384758	-7.164891e-06	3.182428e-09	1.909161e+08
C2H5	769.7902	2.49448	0.001264484	2.671735e-07	-1.123707e-09	1.172256e+08
C2H4	-255.3206	8.287035	-0.01004308	8.254402e-06	-2.886032e-09	5.246394e+07
C2H3	756.0228	2.266116	0.0006486105	-4.06295e-07	-3.642225e-10	2.86251e+08
CH4	403.5915	9.057485	-0.01442533	1.580545e-05	-6.343159e-09	-7.489298e+07
CH3O	564.2706	1.933389	0.001430223	-1.976533e-06	5.560744e-10	1.630347e+07
CH3	1344.049	6.15169	-0.009291711	8.968806e-06	-3.243352e-09	1.456979e+08
CH2O	457.6447	3.497672	-0.005228377	5.676579e-06	-2.329643e-09	-1.159143e+08
CH2	2230.041	0.687475	0.0001475685	5.216637e-07	-4.346252e-10	3.86989e+08
CH	2043.758	1.32381	-0.003279023	3.661858e-06	-1.24887e-09	5.941752e+08
CO2	429.9304	1.87448	-0.001966491	1.297256e-06	-3.99997e-10	-3.935428e+08
CO	968.3951	0.4487901	-0.001152223	1.656891e-06	-7.346408e-10	-1.105397e+08
HCO	830.4301	1.776181	-0.002757208	3.122569e-06	-1.310797e-09	4.351684e+07
H2O2	828.3263	1.605741	-3.629875e-05	-1.130704e-06	6.04122e-10	-1.361066e+08
H2O	1563.082	1.60376	-0.002932794	3.216112e-06	-1.156831e-09	-2.418428e+08
H2	13602.86	3.402418	-0.003358523	-3.908069e-07	1.705396e-09	2447.8
HO2	750.6475	1.258659	-0.0009549455	5.930169e-07	-2.037611e-10	1.045585e+07
H	20622.11	–	–	–	–	2.179771e+08
OH	1778.142	0.09048502	-0.000819423	1.167027e-06	-4.12186e-10	3.898569e+07
O2	834.8264	0.2929579	-0.0001495637	3.413884e-07	-2.278358e-10	-847.7932
O	1531.158	-0.8512987	0.001258127	-8.329426e-07	2.021861e-10	2.49195e+08
N2	979.043	0.4179638	-0.001176279	1.674394e-06	-7.256297e-10	1428.898

*[1]: The temperature is between 300 K and 1391 K;
*[2]: The temperature is between 300 K and 1382 K;
*[3]: The temperature is between 300 K and 1388 K.

Table C.2 Heat capacity for the temperature ranging from 1000 K to 5000 K and standard state entropy

Species	C_{Pi} ($T \in [1000,5000]$) (J/kg/K)					S_i^0 (J/kmol/K)
	a_0	a_1	a_2	a_3	a_4	
C7H16*[1]	1843.261	2.884808	-0.0009824724	1.520903e-07	-8.806064e-12	427558.8
C7H15O2	1578.162	2.222632	-0.0007632779	1.188039e-07	-6.904453e-12	511999.3
C7H15-2 *[2]	1813.543	2.710018	-0.0009159026	1.411122e-07	-8.145139e-12	451869.9
C7KET12	1691.875	1.743912	-0.0006003922	9.36317e-08	-5.449595e-12	529448.1
C5H11CO	1633.337	2.100254	-0.0007168342	1.11155e-07	-6.444197e-12	427265.9
C3H7	1486.307	3.095877	-0.001019466	1.472252e-07	-7.601106e-12	289459.2
C3H6 *[3]	1583.802	2.707328	-0.0009212214	1.425063e-07	-8.246446e-12	267004.6
C3H5	1325.432	2.695399	-0.0009682889	1.562657e-07	-9.350858e-12	274552.9
C3H4	1310.909	2.310478	-0.000822389	1.319083e-07	-7.859913e-12	243628.4
C2H5	2057.144	1.855047	-0.0001839022	-6.71711e-08	1.110291e-11	251635.8
C2H4	1045.724	3.403882	-0.001309484	2.324918e-07	-1.560945e-11	219170.2
C2H3	1824.048	1.235123	-0.0001219443	-4.430697e-08	7.312352e-12	231518.9
CH4	872.4818	5.305564	-0.002008329	3.516705e-07	-2.333949e-11	186057.7
CH3O*[4]	1010.23	2.108843	-0.0007116686	1.056748e-07	-5.659884e-12	228480.6
CH3	1572.777	3.394334	-0.001233393	2.093215e-07	-1.356058e-11	194048.5
CH2O	829.4896	1.850072	-0.0007279632	1.311728e-07	-8.895527e-12	218606.8
CH2*[5]	2155.457	1.145807	-9.999675e-05	-5.986109e-08	1.071832e-11	195482.4
CH	1402.583	1.494647	-0.0004507608	5.75255e-08	-2.46196e-12	182929.3
CO2	841.3793	0.5932413	-0.0002415177	4.522744e-08	-3.15314e-12	213734.7
CO	897.9353	0.428234	-0.0001671401	3.023459e-08	-2.051381e-12	197546.3
HCO	1019.23	0.9585742	-0.0003825062	7.07869e-08	-4.910529e-12	224528.2
H2O2	1117.837	1.059898	-0.0003604639	5.741517e-08	-3.499447e-12	232877.6
H2O	1233.238	1.410528	-0.0004029155	5.542789e-08	-2.949834e-12	188713.3
H2	12337.89	2.887361	-0.0002323629	-3.807492e-08	6.527937e-12	130593.6
HO2	1025.778	0.5368697	-0.0001337112	1.53967e-08	-7.156845e-13	228992
H	20622.11	–	–	–	–	114603.8
OH	1409.274	0.4956992	-0.0001113092	1.063133e-08	-2.506085e-13	183602.6
O2	960.7523	0.1594126	-3.270885e-05	4.612764e-09	-2.952832e-13	205041.6
O	1321.021	-0.01431711	-1.61242e-06	2.365034e-09	-2.269927e-13	160943.6
N2	868.6229	0.4416296	-0.000168723	2.996788e-08	-2.004386e-12	191509.4

*[1]: The temperature is between 1391 K and 500 0K;
*[2]: The temperature is between 1382 K and 5000 K;
*[3]: The temperature is between 1388 K and 500 0K;
*[4]: The temperature is between 1388 K and 3000 K;
*[5]: The temperature is between 1388 K and 4000 K.

Appendix D: Liquid Fuel Properties in SANDIA Chamber

1. Density

The liquid fuel NHPT comprised of 100% n-heptane is used to investigate the liquid fuel injection process [106]. Under the high-pressure and variable temperature, the fuel density should change accordingly, which directly influences the fuel injection process. In the SANDIA chamber, the density of droplets left from the liquid injector should be the function of the surrounding temperature, illustrated in Figure D.1.

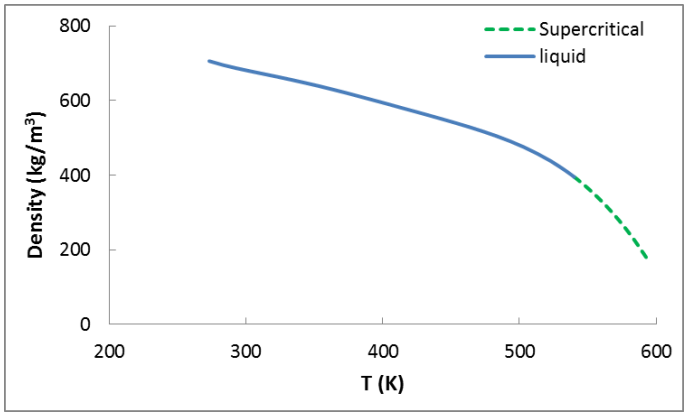

Figure D.1 The variation of density with the liquid temperature under isobaric condition [121]

2. Specific Heat Ratio

The specific heat C_{pl} of liquid is an importance parameter that effects the heat exchange between the droplet and chamber environment. In the SANDIA chamber [106], the specific heat ratio of the liquid n-heptane curved by the temperature is shown in Figure D.2.

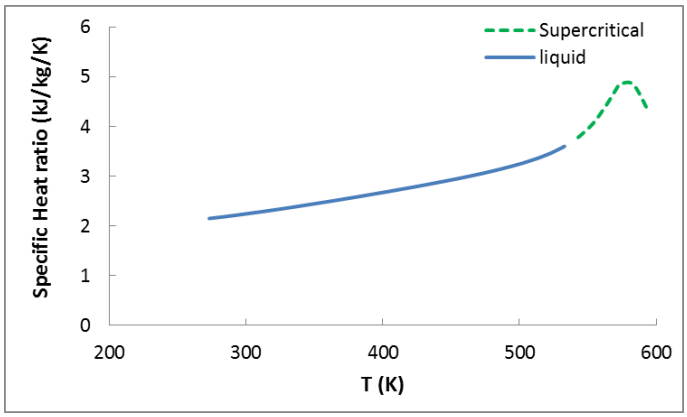

Figure D.2 Specific heat ratio of liquid against temperature at ambient high pressure at SANDIA [121]

3. Viscosity

The liquid viscosity varies with the temperature in SANDIA chamber [106] as illustrated in Figure D.3.

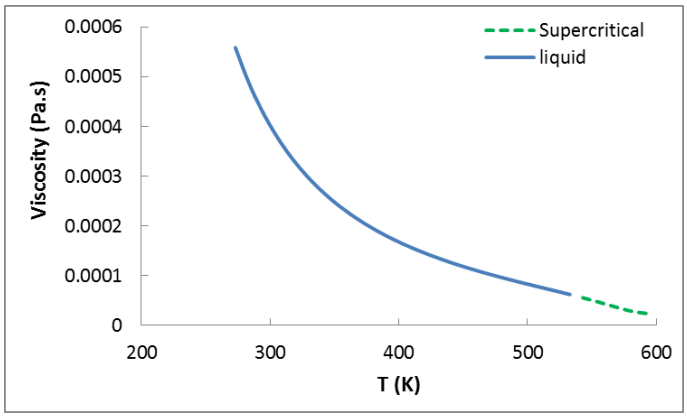

Figure D.3 Liquid viscosity against temperature at ambient high pressure at SANDIA [121]

4. Saturation Vapour Pressure

Saturation vapour pressure is used to calculate the vapour concentration at the droplet surface in the evaporation process according to equation (3.58). Based on the Anoine equation [123], the saturation vapour pressure P_{sat} can be looked as the function of the carbon number n of the fuel.

$$P_{sat} = exp\left(A - \frac{B}{T_s - C}\right) \tag{D.1}$$

Where T_s is the droplet surface temperature, and the three coefficients can be estimated by using the power law of the carbon number n of the fuel [123].

$$A = 6.318n^{0.05091} \tag{D.2}$$

$$B = 1178n^{0.4652} \tag{D.3}$$

$$C = 9.467n^{0.9143} \tag{D.4}$$

The results at the SANDIA chamber conditions are plotted in Figure D.4.

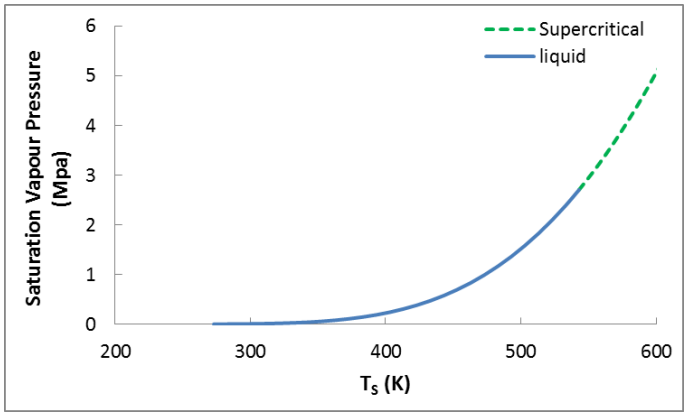

Figure D.4 Saturation vapour pressure against droplet surface temperature

5. Latent Heat of Evaporation

Substituting saturation vapour pressure P_{sat} calculated by the equation (D.1) into the Clausius-Clapeyron equation [122], the latent heat of liquid fuel vaporization per mass unit can be written as,

$$L_H = \frac{B \cdot R_u \cdot T^2}{M_W (T-C)^2} \qquad \text{(D.5)}$$

Where R_u and M_W are the universal gas constant in unit kJ/kmol/K and molecular weight in unit kg/kmol.

Based on the equation (D.5), the latent heat of n-heptane curved by the temperature is shown in Figure D.5.

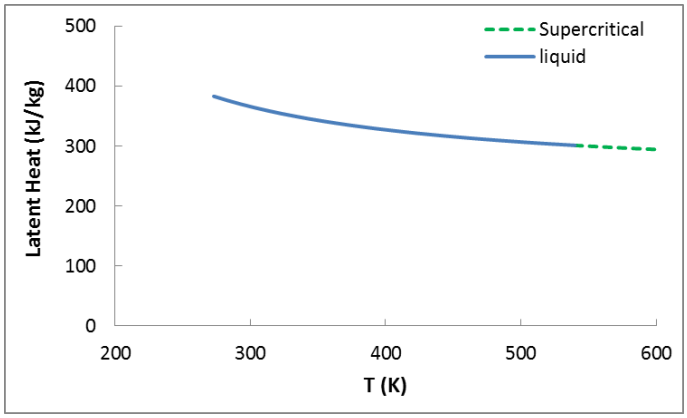

Figure D.5 Latent heat of droplet evaporation against the liquid temperature

6. Boiling Temperature

As expectation, the boiling temperature of the liquid droplets is determined by the chamber pressure. The results illustrated in Figure D.6, shows that the boiling lines evaluated by the three models coincide well before the critical point, while the significant discrepancy can be observed in the

supercritical condition [120]. In this section, the boiling temperature T_b of liquid n-heptane is predicted, based on the SRK-EOS model which is reasonable agreement with the experiment [120].

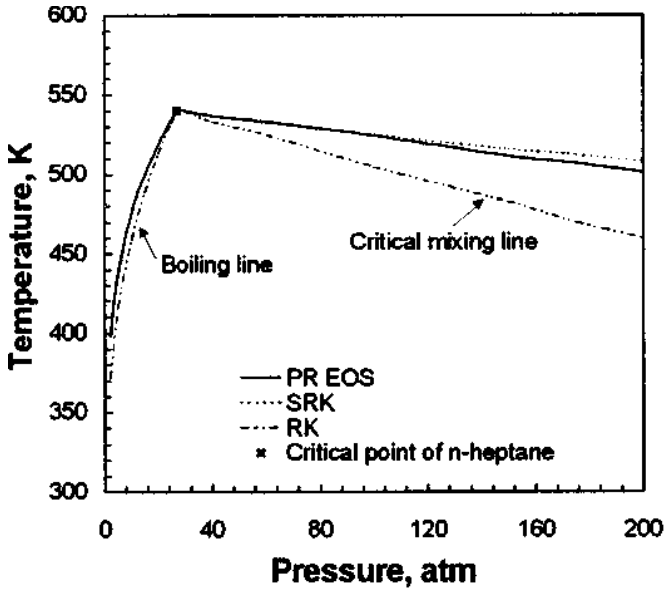

Figure D.6 Pressure and temperature plots for n-heptane & nitrogen system in phase equilibrium [120]

7. Binary Diffusion

Binary diffusion coefficient $D_{i,m}$ determines the mass transfer through the droplet surface during the liquid evaporation by means of Sherwood number correlation [45]. It can be estimated by using the Wilke-Lee formula [124].

$$D_{i,m} = \frac{\left[3.03 - \left(0.98/M_{va}^{1/2}\right)\right]10^{-7}T^{3/2}}{p M_{va}^{1/2} \sigma_{va}^2 \Omega_D(T^*)} \quad \text{(D.6)}$$

Where, the calculations of the mean molecular weight M_{va} of vapour and air, minimal distance σ_{va} between molecules, normalized temperature T^* and collision integral Ω_D are formulated as follows.

$$M_{va} = 2\left(\frac{1}{M_v} + \frac{1}{M_a}\right)^{-1} \quad \text{(D.7)}$$

$$\sigma_{va} = (\sigma_v + \sigma_a)/2 \quad \text{(D.8)}$$

$$T^* = k_B T/\varepsilon_{va} \quad \text{(D.9)}$$

$$\varepsilon_{va} = \sqrt{\varepsilon_v \varepsilon_a} \quad \text{(D.10)}$$

$$\Omega_D = \frac{1.06036}{(T^*)^{0.15610}} + \frac{0.19300}{\exp(0.47635T^*)} + \frac{1.03587}{\exp(1.52996T^*)} + \frac{1.76474}{\exp(3.89411T^*)} \quad \text{(D.11)}$$

The definitions and estimations of the parameters involved in the equations (D.6) ~ (D.11), list in Table D.1. Subsequently, the resulting Binary diffusion coefficient of droplet varied with the surrounding temperature is predicted in Figure D.7.

Table D.1 The parameters for the estimation of binary diffusion in DPM model [123]

Parameters	Sym.	Unit	—
Molecular Weight of Fuel Vapour	M_v	g/mol	100.204
Molecular Weight of Ambient Air	M_a	g/mol	28.68
Characteristic Lennard-Jones Length of Fuel Vapour	σ_v	Å	5.949
Characteristic Lennard-Jones Length of Ambient Air	σ_a	Å	3.617
Characteristic Lennard-Jones Energy of Fuel Vapour	ε_v/k_B	K	399.3
Characteristic Lennard-Jones Energy of Ambient Air	ε_a/k_B	K	97.0

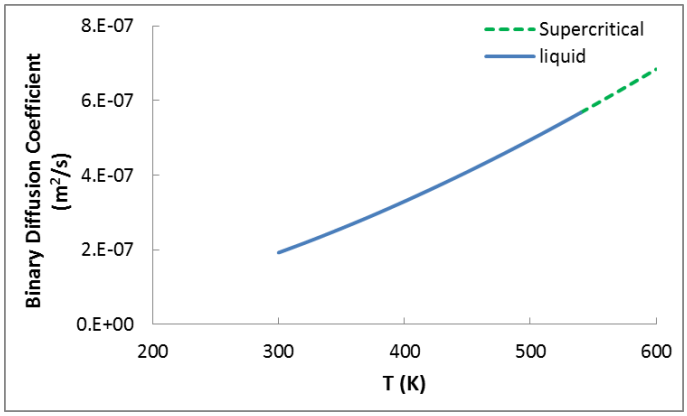

Figure D.7 Binary diffusion coefficient of droplet varied with the surrounding temperature

Appendix E Estimation of the High-Pressure Gas Injection Velocity

When the injector needle opens, the high-pressure gas pushes the low-pressure air forward, and a high-compression shock wave is created, as schematically shown in Figure E.1. The shock wave propagating with a Mach number greater than one causes the pressure and temperature jump in the chamber working medium. The contact surface separating the gas and chamber air propagates in a relatively low speed. Meanwhile, the expansion fan travels in the reversed direction, which consists of a series of expansion waves in the nozzle. To simplify the mathematical description of the gas injection process, the following assumptions are employed:

a. The nozzle is considered to be an infinitely long tube;

b. One-dimension flow is considered;

c. There is no heat loss;

d. The fluid viscosity in the nozzle is neglected;

e. Normal shock is generated as the gas injection starts.

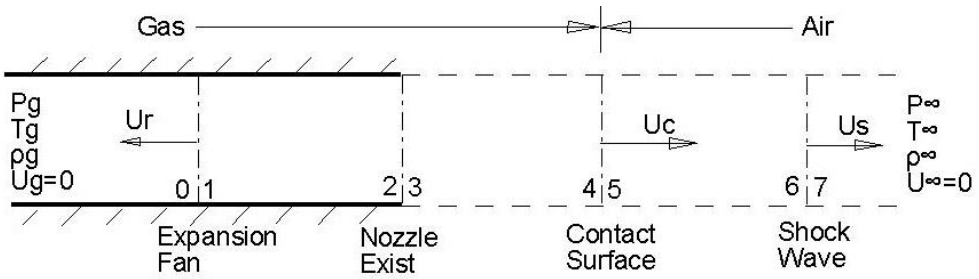

Figure E.1 Schematic diagram of the shock tube

Fixing the coordinate on the expansion fan, the steady flow can be observed near the expansion wave, in which the mass, momentum, energy, and ideal gas equations of state are expressed by the following equations:

$$\rho U_r = (\rho + d\rho)(U_r + du) \tag{E.1}$$

$$P + \rho U_r^2 = P + dP + (\rho + d\rho)(U_r + du) \tag{E.2}$$

$$C_{Pg}T + \frac{1}{2}U_r^2 = C_{Pg}(T + dT) + \frac{1}{2}(U_r + du)^2 \tag{E.3}$$

$$dP = \rho R_{mg} dT + R_{mg} T d\rho \tag{E.4}$$

Combining the above four differential equations and ignoring the higher-order terms, the following formulae can be obtained:

$$\frac{P}{\rho^{\gamma_g}} = const \tag{E.5}$$

$$U_r = \sqrt{\frac{dP}{d\rho}} \tag{E.6}$$

$$a = \sqrt{\gamma_g R_{mg} T} \tag{E.7}$$

$$a + \frac{\gamma_g - 1}{2} u = const \tag{E.8}$$

Where, the relationship between the specific heat ratio γ_g, specific heat capacity under constant pressure C_{Pg} and universal gas constant in unit mass R_{mg} is shown as follows,

$$C_{Pg} = \frac{\gamma_g}{\gamma_g - 1} R_{mg} \tag{E.9}$$

These equations indicate isentropic flow within the nozzle, where the propagation speed U_r of expansion wave is equal to the local sound speed.

Fixing the coordinate on the contact surface, the following relationship can be achieved:

$$P_3 = P_4 = P_5 = P_6 \tag{E.10}$$

$$u_3 = u_4 = u_5 = u_6 = U_C \tag{E.11}$$

Substituting the equation (E.11) into the equation (E.8) and the isentropic equations (E.5) and (E.7), the relationship between the injection velocity U_3 at the nozzle exit and the pressure P_6 closely in front of shock wave can be obtained:

$$u_3 = \frac{2\sqrt{\gamma_g R_{mg} T_g}}{\gamma_g - 1} \left[1 - \left(\frac{P_6}{P_g} \right)^{(\gamma_g - 1)/2\gamma_g} \right] \tag{E.12}$$

Fixing the coorrdinate on the shock wave, the corresponding equations are shown below,

$$\rho_6 (u_6 - U_S) = \rho_\infty (-U_S) \tag{E.13}$$

$$P_6 + \rho_6 (u_6 - U_S)^2 = P_\infty + \rho_\infty U_S^2 \tag{E.14}$$

$$C_{P\infty} T_6 + \frac{1}{2} (u_6 - U_S)^2 = C_{P\infty} T_\infty + \frac{1}{2} U_S^2 \tag{E.15}$$

$$P_6 = \rho_6 R_{m\infty} T_6 \tag{E.16}$$

Accordingly, the following equation is achieved,

$$u_3 = (P_6 - P_\infty)\sqrt{\frac{2}{\rho_\infty\left[\left(\gamma_\infty+1\right)P_6+\left(\gamma_\infty-1\right)P_\infty\right]}} \quad \text{(E.17)}$$

Combining the equation (E.12) with the equation (E.17), theoretical gas velocity u_3 at nozzle exit and pressure P_6 are solved, where the gas injection velocity U_g is equal to u_3. The pseudo diameter will also change accordingly,

$$U_g = u_3 \quad \text{(E.18)}$$

$$d_{ps} = d_n\sqrt{\frac{P_6}{P_a}} \quad \text{(E.19)}$$

Appendix F: Definition of the Actual Heat Release Rate (AHRR)

Applying the first law of thermodynamics, the following equation is obtained represented the closed system energy:

$$dQ_W + dQ_{ch} + \sum h_i dm_i = dU_S + dW + E_{ev} \quad \text{(D-1)}$$

Where,

dQ_W: Heat transfer to the cylinder wall;

dQ_{ch}: Heat released by the fuel combustion;

$\sum h_i dm_i$: Sensible energy due to the fuel addition and crevice loss;

dU_S: Change of internal energy in the closed system;

dW: Piston work;

E_{ev}: Evaporating heat for the liquid fuel.

The change of internal energy dU_S can be divided into two terms, which is expressed below,

$$dU_S = d(mu) = udm + mC_v dT \quad \text{(D-2)}$$

The piston work dW is calculated, based on the in-cylinder pressure and the corresponding cylinder volume dV.

$$dW = PdV \quad \text{(D-3)}$$

The latent heat of liquid fuel is a function of the local temperature. The evaporating heat E_{ev} is estimated by the following equation:

$$E_{ev} = L_H dm_l = L_H(dm - dm_g + dm_{cr}) \quad \text{(D-4)}$$

Where, dm, dm_g, dm_l and dm_{cr} represent the change of the total mass, the injected gas mass, the evaporating mass of liquid/pilot fuel and the mass escaped to the crevice.

The term $\sum h_i dm_i$ is derived from the fuel addition and the crevice effect, as shown in the following:

$$\sum h_i dm_i = h_l dm_l + h_g dm_g - h_S dm_{cr} = h_l dm + (h_g - h_l) dm_g + (h_l - h_S) dm_{cr} \quad \text{(D-5)}$$

Where, the sensible enthalpy of the vapour of liquid/pilot fuel, the injected gas and the mixture in-cylinder are symbolized by h_l, h_g and h_S.

Substituting the equations (D.2) – (D.5) to the equation (D.1), the following equation is derived:

$$dQ_{ch} = mC_v dT + PdV + (u - h_l + L_H)dm + \left(h_l - h_g - L_H\right)dm_g + (h_S - h_l + L_H)dm_{cr} - dQ_W \quad \text{(D-6)}$$

Ideal State of Gas:

$$\mathrm{PV = nRT = mR_mT} \quad \text{(D-7)}$$

Based on the equation (D-7), the following can be obtained.

$$PdV + VdP = mR_m dT + RTd\left(\frac{m}{M_w}\right) = mR_m dT + R_m T dm - R_m T\frac{m}{M_w}dM_w \quad \text{(D-8)}$$

Hence,

$$mdT = \frac{P}{m}dV + \frac{V}{R_m}dP - Tdm + T\frac{m}{M_w}dM_w \quad \text{(D-9)}$$

Substituting equation (D-9) to equation (D-6) in conjunction with the ideal state equation of the mixture, the heat release form the actual fuel combustion can be expressed as follows:

$$\frac{dQ_{ch}}{d\theta} = \left(\frac{C_v}{R_m} + 1\right)P\frac{dV}{d\theta} + \frac{C_v}{R_m}V\frac{dP}{d\theta} - \frac{PV}{m}\frac{C_v}{R_m}\frac{dm}{d\theta} + \frac{C_v}{R_m}\frac{PV}{M_W}\frac{dM_W}{d\theta} + (u - h_l + L_H)\frac{dm}{d\theta} + \left(h_l - h_g - L_H\right)\frac{dm_g}{d\theta} + (h_S - h_l + L_H)\frac{dm_{cr}}{d\theta} - \frac{dQ_W}{d\theta} \quad \text{(D-10)}$$

In equation (D-10), the variables can be computed according to the following equations:

$$M_W = \left(\sum\frac{Y_i}{M_{Wi}}\right)^{-1} \quad \text{(D-11)}$$

$$C_P = \sum C_{Pi}Y_i \quad \text{(D-12)}$$

$$R_m = R/M_W \quad \text{(D-13)}$$

$$C_v = C_P - R_m \quad \text{(D-14)}$$

$$h_S = \sum Y_i \int_{T_{ref}}^{T} C_{Pi}dT \quad \text{(D-15)}$$

$$u = m\left[h_S - R_m\left(T - T_{ref}\right)\right] \quad \text{(D-16)}$$

$$L_H = \frac{B \cdot R_u \cdot T^2}{M_{Wl}(T-C)^2} \quad \text{(D-17)}$$

$$h_l = Y_l \int_{T_{ref}}^{\bar{T}_l} C_{Pl} dT \quad \text{(D-18)}$$

$$h_g = Y_g \int_{T_{ref}}^{T_{g0}} C_{Pg} dT \quad \text{(D-19)}$$

Where,

Y_i: Mass fraction of species i in the mixture;

Y_l: Vapour mass fraction of the liquid fuel;

Y_g: Mass fraction of the injected gas;

M_{Wi}: Molecular weight of species i in the mixture;

M_{Wl}: Molecular weight of liquid fuel;

R: Universal constant of gas equal to 8.3145 J/(mol.K);

C_{Pi}: Specific heat ratio under constant pressure of species i;

C_{Pl}: Specific heat ratio under constant pressure of the vapour of injected liquid fuel;

C_{Pg}: Specific heat ratio under constant pressure of the injected gas;

T_{ref}: Reference temperature equal to 298.15 K;

$\bar{T}_l$: Mean evaporating temperature of the liquid fuel;

T_{g0}: Initial temperature of injected gas;

T: Mean temperature in-cylinder;

P: Mean pressure in-cylinder;

V: Cylinder volume;

θ: Crank angle.

Most of researchers including [119] assumed that the compositions of the mixture have no change, as the fuel injection and combustion. The resulted net heat release rate (NHRR) and gross heat release rate (GHRR) are defined by the following equations:

$$\frac{dQ_{net}}{d\theta} = \frac{C_v}{R}\left(P\frac{dV}{d\theta} + V\frac{dP}{d\theta} - \frac{PV}{m}\frac{dm}{d\theta}\right) + P\frac{dV}{d\theta} \quad \text{(D-20)}$$

$$\frac{dQ_{gross}}{d\theta} = \frac{dQ_{net}}{d\theta} - \frac{dQ_W}{d\theta} \quad \text{(D-21)}$$

Apart from neglecting the change of the mean molecular weight of the mixture, Heywood [118] also ignored the mass addition caused by the fuel injection. As a consequence, the heat release rate involving the crevice effect can be expressed [118].

$$\frac{dQ_{ch}}{d\theta} = \left(\frac{C_v}{R_m} + 1\right)P\frac{dV}{d\theta} + \left(\frac{C_v}{R_m}\right)V\frac{dP}{d\theta} + (h_S - u + C_vT)\frac{dm_{cr}}{d\theta} - \frac{dQ_W}{d\theta} \quad \text{(D-22)}$$

In the presented thesis, the crevice effect is neglected, but the compositions of the mixture and mass addition caused by dual fuel injection and the combustion are considered. The actual heat release rate (AHRR) derived from equation (D-10) can be reduced as following:

$$AHRR = \left(\frac{C_v}{R_m} + 1\right)P\frac{dV}{d\theta} + \frac{C_v}{R_m}V\frac{dP}{d\theta} - \frac{PV}{m}\frac{C_v}{R_m}\frac{dm}{d\theta} + \frac{C_v}{R_m}\frac{PV}{M_W}\frac{dM_W}{d\theta} + (u - h_l + L_H)\frac{dm}{d\theta} + \left(h_l - h_g - L_H\right)\frac{dm_g}{d\theta} - \frac{dQ_W}{d\theta} \quad \text{(D-23)}$$

Appendix G: Definition of the scavenging parameters

Source: Sigurdsson [126].

The characteristics of the scavenging process can be described by the following parameters:

$$\Lambda = \frac{M_{Totscav}}{M_{Dsref}} \tag{G.1}$$

$$\eta_{ch} = \frac{M_{Retscav}}{M_{Dsref}} \tag{G.2}$$

$$\eta_{sc} = \frac{M_{Retscav}}{M_{Cych}} \tag{G.3}$$

$$\eta_{rt} = \frac{M_{Retscav}}{M_{Totscav}} \tag{G.4}$$

$$\eta_{rc} = \frac{M_{Cych}}{M_{Dsref}} \tag{G.5}$$

where,

Λ: delivery ratio;

η_{ch}: charging efficiency;

η_{sc}: scavenging efficiency;

η_{rt}: retaining efficiency;

η_{rc}: relative charge;

$M_{Totscav}$: delivered fresh mass;

M_{Dsref}: reference mass;

$M_{Retscav}$: retained fresh mass;

M_{Cych}: total mass of the cylinder charge.

And, the reference mass M_{Dsref} can be calculated by using the following equation:

$$M_{Dsref} = \rho_a V_d \tag{G.5}$$

where,

ρ_a: air density at scavenging box conditions;

V_d: displaced volume.

In terms of the above equations, the relationship between the charging efficiency η_{ch}, delivery ratio Λ and the retaining efficiency η_{rt} can be obtained,

$$\eta_{ch} = \Lambda \eta_{rt} \tag{G.6}$$

Also, the charging efficiency η_{ch} is related to the relative charge η_{rc} and scavenging efficiency η_{sc}.

$$\eta_{ch} = \eta_{rc}\eta_{sc} \tag{G.7}$$